ANALYTICAL CAMERA POSE ESTIMATION AND INVERSE MODELLING OF HIGH ORDER RADIAL LENS DISTORTION POLYNOMIALS FOR CLOSE RANGE PHOTOGRAMMETRY

By
GUY BLANCHARD IKOKOU
IKKGUY001

Thesis submitted to the University of Cape Town in fulfilment of the requirements for the degree of Doctor of Philosophy in Engineering (Geomatics)

SUPERVISOR:

Dr. Moreblessings Shoko

CO-SUPERVISOR:
Dr. Naa Dedei Tagoe

Department of Architecture, Planning and Geomatics

Faculty of Engineering and Built Environment
University of Cape Town

November 2024

He who knows all the answers has not been asked all the questions."

— Confucius—

University of Cape Town

The copyright of this thesis vests in the author. No quotation from it or information derived from it is to be published without full acknowledgement of the source. The thesis is to be used for private study or non-commercial research purposes only.

Published by the University of Cape Town (UCT) in terms of the non-exclusive license granted to UCT by the author.

University of Cape Town

The copyright of this thesis vests in the author, no quotation from it or information derived from it to be published without full acknowledgment of the source. The thesis is to be used for private study or non-commercial research purposes only.

DECLARATION

I, Guy Blanchard Ikokou, hereby declare that the work from which this dissertation thesis was derived is my own original work and has not been submitted to any other tertiary education institutions in the country or outside South Africa. I have acknowledged all resources used in this work which were not produced by me and have used proper citation in the reference list.

I empower the University of Cape Town to reproduce partially or fully this work for research purposes only.

Date: November 2024

Guy Blanchard Ikokou

ACKNOWLEDGEMENT

To the Almighty GOD for this PhD opportunity and for the patience and strengths gained along this PhD journey full of challenges.

To my lovely wife Catherine, thank you for your priceless and selfless love and support.
To my wonderful daughters, Virginie Daniella, Joyce Daisy.
To my siblings, Malone, Anouchka Phanie, Leticia Bernice, Praxede, Omer-Arsene, Joelle, Landry, Julie-Kelene, thank you for your love and support.

To Dr. Moreblessings Shoko for your supervision, regular follow ups and encouragements.
To my co-supervisor Dr. Naa Dedei Tagoe, thank you for your suggestions, advices.

My heartfelt thanks to Prof Julian Smit, for your technical guidance, mentorship during many years of this PhD research.

My further thanks to my colleagues in the Geomatics Department at Tshwane University of Technology for your encouragements.

My thanks to the Dean of teaching and Learning of the Faculty of Engineering and Built Environment at Tshwane University of Technology for the support.

In Loving Memory of my late father Daniel Mouangoye and my late mother Anne Marie Kelemoye for your priceless love and supports during this PhD journey that you could not witness the completion as you had always wished.

ABSTRACT

Camera calibration aims at estimating intrinsic and extrinsic camera parameters that accurately describe the projection of points from the 3D scene to the 2D image sensor. The absence of numerical estimates of parameters describing the camera internal and external geometry can prevent absolute readjustment of bundles of rays that project 3D points from the scene onto the image plane. When information derived from photographs is used for metric purposes, small imaging errors can significantly affect the accuracy of derived information. Current analytical methods for camera pose calibration failed to exploit the intrinsic geometric properties associated with each camera parameter within the structures of individual coefficients of the projective transformation matrix. This resulted in these methods being prone to parameter coupling, sign ambiguity, and multiple roots associated with some of the parameters. In the same way, recursive reversions methods proposed to compute inverses of radial distortion coefficients in order to correct radial distortions were found not suitable for high-degree radial distortion polynomials and failed to model the inverse profiles of severe barrel, pincushion, and moustache distortions inherent to consumer-grade cameras used in close range photogrammetry. This PhD research successfully developed two analytical calibration systems. The first calibration system decomposed the coefficients of the projective transformation matrix into nineteen robust equations that independently estimate individual parameters describing the internal geometry of the camera as well as its location and orientation in a 3D scene. The second calibration system, based on the concept of forced differential equation, successfully modelled inverse coefficients of high-order quintic, sextic, and octic radial distortion polynomials and reduced the effects of severe barrel, pincushion, and moustache radial distortions on distorted points. The experimental results demonstrate that both developed calibration strategies achieved root mean square reprojection errors of 0.0843 and 0.057 pixels, respectively. These values are substantially lower than those reported by several current state-of-the-art methods, which exhibit average errors around 3.63 pixels. Such a significant reduction in error by nearly two orders of magnitude not only confirms the high accuracy of the proposed approaches but also underscores their suitability for close-range photogrammetry applications where sub-pixel precision is essential. In practical terms, this level of accuracy enables more reliable 3D reconstructions and measurements in scenarios where even small deviations can lead to substantial errors. These results affirm the reliability and effectiveness of the proposed calibration strategies, making them well-suited for high-precision 3D reconstruction, industrial metrology, cultural heritage documentation, and other close-range imaging tasks where geometric accuracy is paramount.

Table of Contents

List of Tables

List of Figures

CHAPTER 1

INTRODUCTION

1.1 Research Motivation

Camera calibration consists of computing exterior and interior camera parameters that accurately map 3D-object points from the world coordinate space into a 2D image coordinate space. Frequently, lenses integrated into Digital Single-Lens Reflex (DSLR) and other consumer-grade digital cameras exhibit flaws resulting from imperfections in lens design and manufacture and the lens-camera assembly. As a result, they show a variety of lens distortions due to the low reliability and durability of internal geometry information over time and between successive images (**Sasián, 2019; Clédat et al., 2020**; **Andaru et al., 2022**). Lens distortions can be classified into three categories: radial, decentring, and thin prism (**Tang et al.,2017**). Radial distortion is the most dominant and the focus of this research. The absence of camera internal geometry information such as the focal length or effective focal lengths, the coordinates of the principal point, and inverse radial distortion coefficients, as well as the absence of camera external geometry information describing camera location and orientation in 3D space, can prevent absolute readjustment of a bundle of rays that projected the 3D points from the scene onto the 2D image plane and can lead to a bad metric representation of the scene (**Abdullah et al., 2019; Syafiq et al., 2022**). Digital photogrammetry has made remarkable progress during the last decade in developing new mathematical models for camera calibration. As the number of photogrammetric applications grows and technology advances, camera calibration has become more complex. With the recent significant improvements in digital image quality, one might argue that camera calibration would appear less important. However, when information derived from the imagery is used for metric purposes and not as a tool for general visualization or qualitative analysis, small imaging errors can significantly affect the accuracy of derived information. The widespread adoption of consumer-grade cameras in photogrammetric workflows has amplified the need for precise calibration of camera parameters to ensure metric reliability. Unlike traditional metric cameras, consumer-grade imaging systems lack geometric stability and are prone to optical inconsistencies, which complicates accurate camera pose estimation and the modelling of lens distortions. This shift toward accessible and cost-effective imaging solutions introduces critical challenges, particularly in the accurate determination of camera position and orientation within a 3D environment and in the correction of radial lens distortions using inverse polynomial models. The inherent variability in the optical and mechanical properties of consumer-grade cameras further exacerbates these challenges, making conventional calibration techniques insufficient. As a result, there is a pressing need for more robust, mathematically sophisticated calibration algorithms capable of addressing the inconsistencies and unpredictability of these devices. The increasing diversity of consumer-grade imaging platforms has thus rendered camera calibration a more complex and demanding task in modern photogrammetric applications.

1.2 Research Background

Some of the earliest camera calibration works can be grouped into multiple-view and single-view. The multiple-view approach uses point correspondence between two or more images, such as the work proposed by **Perez et al. (2020).** A key component in Multiview camera calibration

approaches is the fundamental matrix. The fundamental matrix as a 3×3 matrix that describes the geometric relationship between two uncalibrated images of the same scene, Perez **et al. (2020)** used multiple-view images to describe the relationship between distortion parameters and the fundamental matrices in a linear model for 3D reconstruction. **Vera et al. (2020)** emphasize that the distortion centre is central when establishing the relationship between distortion parameters and the fundamental matrix and is the basis for correcting lens distortions. **Cai et al. (2020)** advocated that parameters describing camera geometry and describing image geometry could better be estimated by matching point features from images taken at different views. Multiview camera calibration approaches generally involve capturing the calibration object from multiple spatially distributed camera positions, ideally with variations in angle, height, distance, and camera rotation. This approach increases the diversity of projection geometries and ensures that each calibration parameter, both intrinsic and extrinsic, is sufficiently constrained by the data. To minimize the dependency between camera parameters when using the multiple view technique, **Dai et al. (2023)** emphasize the importance of acquiring calibration images from varied camera positions, specifically different heights, angles, and rotations, to improve the robustness of parameter estimation. This diversity in camera viewpoints introduces a richer set of geometric constraints, which helps decouple the estimation of intrinsic parameters such as focal length and coordinates of the principal point from extrinsic parameters such as rotation and translation. When calibration images cover a wide range of perspectives, the solution space is better conditioned, reducing parameter correlation and improving the numerical stability of the calibration process. This strategy is particularly valuable in mitigating issues related to parameter degeneracy or ambiguous solutions, especially when using non-metric or consumer-grade cameras. In contrast, Xiao **et al. (2019)** earlier argued that 3D ground control points should be integrated into multi-view calibration approaches, and establishing the correspondence between 3D scene control points and their corresponding on the images can lead to good estimates of camera parameters that map the 3D space onto the 2D image plane.

Since the multi-view techniques do not need particular conditions about the calibration objects, such as the straightness of lines, they can be used in many applications, such as accident scene reconstruction, but the disadvantage is that they rely on multiple images, which are sometimes not available. Authors such as **Zhang et al. (2019) and Hu et al. (2023)** expressed their scepticisms about multi-view techniques in terms of the number of images available and the accuracy of the approaches due to measurement errors originating from the difficulty to establish accurate geometric relationships between the various coordinate systems. The authors instead advocated for the use of single image-based calibration approaches. Single-view methods generally rely on the property of the perspective camera model that stipulates that the projection of any 3D straight line from the scene onto the image plane produces a straight line. Any deviation from this property is attributed to lens distortion. One common strategy in this method is the computation of undistorted points from their respective distorted counterparts on the images and then minimizing the residual errors based on the collinearity of the undistorted points. However, linear minimization approaches do not always guarantee calibrated camera parameters' accuracy, as **Tsai (1987)** pointed out**.** The author also suggested that the accuracy of estimated parameters could be improved by breaking down the calibration process into two stages while considering a single-view approach. The first stage of the solution could estimate initial estimates of a few parameters, and then the second stage enables estimating and refining all the parameters together through an optimization process. However, the accuracy of the proposed parameter optimization scheme depends on the accuracy of the coordinates of the principal point, and an accurate estimation of the coordinates of the principal point cannot be modelled using a weak perspective camera model and could exacerbate severe radial distortions within the image (**Tomaselli and Bervegliera, 2014**; **Luhmann et al., 2016**).

Modelling severe radial distortions remains extremely difficult, especially without considering well-elaborated polynomial functions that can capture several distortion profiles. Attempts to analytically compute inverse coefficients of large polynomial functions have been discouraged by some authors with the hypothesis that any such solutions would introduce numerical instabilities to the estimated distortion coefficients (**Diaz-Ramirez, 2021**). Methods to correct radial distortions from distorted points can be classified into four categories. The first category of solutions approximates the polynomial function by expanding a Taylor series by estimating the first derivative at certain coordinates (**Liao et al., 2019; Zhu et al., 2021**). This type of polynomial approximation offers an interpolated solution that may extrapolate radial distortion profiles. The second group is the iterative approach that requires initial estimates of radial distortion coefficients, which would then be refined through non-linear optimization algorithms. The accuracy of such a solution relies on the user-defined number of iterations, which is determined by trial-and-error strategy and makes the optimization algorithm convergence at the correct maxima very subjective. The third category of solutions is estimating distortion coefficients and storing the estimated values in a look-up table for further radial distortion corrections. Although the accuracy of the technique remains debatable, it requires a lot of processing time and computer memory space. The fourth category of solutions is the semi-analytical exact formula proposed by **Drap and Lefevre (2016),** which computes inverse undistorted coefficients from distorted coefficients in a recursive manner and then refines the computed inverse coefficients through an intense iteration process. This solution requires intense series manipulation and a large number of iterations to achieve successful results, and this also adds some subjectivity in terms of the convergence point of the optimization algorithm.

Techniques that analytically compute parameters describing camera location and orientation in 3D space, except for lens distortions, need to be improved (**Rodehorst et al., 2008; Zheng et al., 2020**). From the computer vision literature, among the earliest attempts to analytically solve the parameters describing the internal geometry of the camera as well as the parameters describing the location and orientation of the camera in 3D was the work of **Ganapathy (1984).** The strategy relies on decomposing the projective transformation matrix to establish non-linear equations to solve the camera parameters (**Oniga et al., 2015**). To simplify the solution, the approach did not rely on an upper triangular camera matrix, which is generally used in photogrammetry**.** The solution is also not very stringent, with the various geometric constraints imposed by the projective transformation matrix on individual camera parameters not being considered **(Faugeras and Toscani, 1986)**. Variations of this analytical approach were also discussed in the works of **Roumie et al. (2018)** and **Kim et al. (2023)**.

Despite the extensive efforts dedicated to improving camera calibration through both multi-view and single-view strategies, significant challenges remain in analytically decoupling and accurately estimating individual camera parameters, particularly under conditions of severe radial distortions and geometric ambiguity. The limitations of current calibration techniques, including parameter coupling, numerical instabilities, and dependency on iterative optimization, underscore the need for robust analytical methods that can independently model both camera geometry and distortion effects. These unresolved issues establish a critical foundation for this study's problem statements.

1.3 **Problem Statement**

With the increase in the need for highly accurate metrics from digital photographs, several camera calibration strategies have been developed for photogrammetry applications. Iterative computation techniques have been the most used approaches to recovering parameters describing

the internal geometry of the camera and parameters describing the camera location and orientation in the 3D space. Iterative calibration methods are, in general, part of a two-step camera calibration scheme that requires very accurate initial estimates of the parameters to be calibrated in the first phase to run the optimization algorithm to refine all the parameters together in the second phase **(Usamentiaga et al., 2019).** Optimization algorithms generally attempt to maximize (or minimize) a function by starting from the initial estimate and following step by step a path to what looks like the best solution. However, without accurate initial estimates of parameters, optimization algorithms can converge at wrong maxima meaning the algorithm can get stuck at a local maximum or incorrect solution called the global maximum (**Qi et al., 2010**). From this, there is a suggestion that analytical camera calibration could offer more stable and reliable results in terms of accuracy of calibrated parameters since the strategy does not only require initial estimates of parameters but also decouples the calibration of radial lens distortion from the calibration of other camera parameters **(Hong et al., 2015).** The analytical decomposition of the projective transformation matrix can be defined as mathematically breaking apart the projective transformation matrix into linear and nonlinear equations that contain the intrinsic and extrinsic parameters of the camera. The analytical decomposition of the projective transformation matrix provides an effective means of recovering both the intrinsic parameters that define the camera's internal geometry (excluding radial lens distortion) and the extrinsic parameters that describe the camera's position and orientation in three-dimensional space. This approach yields a closed-form solution for the estimation of camera parameters, offering computational efficiency and mathematical rigor (**Cai et al., 2020**). Although the decomposition strategy offers closed-form solutions through linear and non-linear equations, many critical problems affecting calibrated parameters' accuracy and the approach's applicability in close-range photogrammetry still need to be solved. The decomposition solution of the projective transformation matrix proposed by **Ganapathy (1984)** mostly uses intermediate parameters to solve for the final camera parameters due to the difficulty of developing straightforward algorithms that can independently estimate individual parameters while preserving the various geometric constraints associated with each parameter. This can lead to numerically unstable solutions containing parameter coupling errors (**Faraji, 2021; Su et al., 2022).** The camera matrix and the rotation matrix used in the formulation of the solution were designed for computer vision applications and not for close-range photogrammetry applications **(Alturki and Loomis, 2016).** Ganapathy's proposed approach also suffers from parameter coupling, multiple roots, and sign ambiguities. Other analytical decomposition approaches proposed in **Roumie et al. (2018)** and **Kim et al. (2023)** also suffer from similar accuracy limitations. For the past decades, there has been a need in the photogrammetry literature for mathematical algorithms that analytically compute individual parameters describing camera location and orientation in 3D space and the internal geometry of the camera (**Heikkila and Silven, 1997; Aicardi et al., 2018).** New fully analytical closed-form decomposition solutions to independently calibrate the parameters of camera location and orientation in a 3D scene are desired for close-range photogrammetry. Correction of radial distortion is also very important in digital photogrammetry, where highly accurate metrics derived from photographs are needed. Initially modelled by a general polynomial function introduced by **Brown (1971),** radial lens distortions can now be modelled using division and rational models due to the difficulty of computing polynomial inverse models. Division and rational models offer formulation advantages because of the few terms they contain **(Santana-Cedrés et al., 2016)**. Although a handful of rational and division models offer analytical inverse formulas, the majority achieve

inversion only locally through iterative processes **(Larsson et al., 2019)**. In addition, rational and division distortion models impose numerical constraints on the distortion coefficients present in their denominator terms, as the denominator must remain non-zero to avoid instability. Moreover, the common assumption in these models that the principal point is located at the center of the image does not necessarily lead to accurate modelling of radial lens distortions. In contrast, polynomial radial distortion models provide greater numerical stability and flexibility in capturing distortion effects. Although their algebraic inversion can be challenging, polynomial functions are capable of representing both symmetric and asymmetric radial distortions with high precision. However, increasing the polynomial order does not always guarantee a better fit; excessively high orders may introduce numerical instability or overfitting. Therefore, selecting an appropriate polynomial degree is essential to balancing model flexibility and robustness (**Tang et al., 2017**). Approaches to computing inverse formulations of high-order polynomial models have attracted little attention among the photogrammetry community for many decades due to the complexity of the task since ordinary series reversion strategies are not suitable for the formulation structures of radial distortion polynomial models. Among the computer vision community, the first approach to algebraically compute inverse coefficients of radial distortion polynomial models from original coefficients is the semi-analytical strategy proposed by **Drap and Lefevre (2016)**. The strategy recursively computes inverse radial distortion coefficients and then refines the coefficients' respective numerical estimates through an intense iterative process. However, many problems related to the formulation and accuracy of this approach remain unsolved. The inverse distortion coefficients presented in the approach seem rigid and formulated for a specific polynomial structure. The excessive number of iterations required by the approach to achieve optimal estimates of inverse coefficients can introduce numerical instabilities since the exact number of iterations that will guarantee the optimization algorithm to converge at the correct maxima is not known a priori. Moreover, little is known about how the proposed algorithms can deal with severe barrel radial distortions (where straight lines curve outward from the center), pincushion radial distortions (where straight lines curve inward toward the center), and moustache radial distortions (combining both barrel and pincushion distortions) common to consumer-grade digital cameras. From these, further investigations are needed on the strategy's effectiveness to deal with severe barrel, pincushion, and moustache radial distortion profiles. Given the limitations of existing computer vision approaches for polynomial reversion, particularly in effectively correcting complex radial distortions such as severe barrel, pincushion, and moustache distortions modelled by high-order polynomials, there is a clear need for the development of a fully analytical calibration framework. Such a system should be capable of reliably computing the inverse radial distortion coefficients and accurately modelling the inverse of radial distortion polynomials. Addressing this gap is essential for enhancing the precision and robustness of photogrammetric workflows involving non-linear and high-magnitude lens distortions. To the best of my knowledge, such a fully analytical, robust strategy is yet to be developed.

1.4 Research Questions

From the problem statement, this PhD research seeks to answer the following specific questions:

i) Current camera calibration approaches, particularly in close-range photogrammetry, predominantly rely on iterative numerical methods such as optimization-based

techniques and bundle adjustment. While effective, these methods often suffer from significant drawbacks, including convergence to local minima, parameter coupling, ambiguity in solutions, and high computational demands, making them less suitable for real-time or resource-constrained applications. To address these limitations, can a fully analytical and deterministic camera calibration system, based on the decomposition of the projective transformation matrix, be developed to accurately estimate both intrinsic and extrinsic camera parameters for close-range photogrammetry applications, addressing the limitations of current iterative and non-geometric methods?

ii) Can the mathematical algorithms produced by the new analytical camera calibration system minimize parameter coupling errors, sign ambiguity, multiple parameter roots, and preserve geometric constraints imposed by the internal structure of the projective transformation matrix on individual camera parameters?

iii) Can the newly developed analytical calibration system, based on the decomposition of the projective transformation matrix, accurately estimate camera orientation and interior geometry parameters from a single image of a planar checkerboard pattern and achieve root mean square and standard deviation reprojection errors that are comparable to or lower than those of established calibration methods?

iv) Can a non-iterative, analytically grounded technique based on differential geometric principles be developed to accurately compute the inverse of high-order radial distortion polynomial models, thereby overcoming the instability and convergence issues observed in traditional series reversion methods?

v) Can the newly developed inverse radial distortion coefficients successfully model the inverse curves of moderate, severe barrel, and moustache radial distortion profiles and achieve minimal residual errors (root mean square error and maximum deviation) when compared to existing iterative strategies?

1.5 **Research Aims and Objectives**

This research aims to develop fully analytical camera calibration systems to estimate accurate parameters describing the camera pose and non-iterative inverse modelling of high-order radial distortion polynomial functions for close-range photogrammetry applications. To achieve this, the following five objectives are proposed:

i) To design a structurally decomposed projective transformation matrix that explicitly isolates and constrains each intrinsic and extrinsic camera parameter by exploiting the algebraic properties of matrix coefficients, with the goal of minimizing parameter coupling and sign ambiguity.

ii) To develop analytical algorithms for accurately estimating both the camera's pose (orientation and position) and its internal geometric parameters (principal point and effective focal lengths), by independently resolving each parameter through structured linear and non-linear equations derived from the projective transformation matrix. The method will be validated using standard reprojection error thresholds commonly applied in close-range photogrammetry.

iii) To develop and validate a fully analytical series reversion strategy for high-order radial distortion polynomial models that eliminates the need for iterative approximations. This method addresses the limitations of existing recursive techniques, which often suffer from convergence issues and reduced accuracy when modelling complex distortion profiles such as severe barrel, pincushion, and moustache distortions. The proposed approach will be formulated under well-defined mathematical assumptions, including radial symmetry and a known polynomial degree. Its effectiveness will be evaluated using reprojection error, root mean square error (RMSE), and maximum deviation metrics, with results benchmarked against those of established methods.

iv) To construct analytical algorithms based on differential modelling to directly compute inverse radial distortion coefficients from forward polynomial models, ensuring compatibility with polynomials of varying degrees and distortion profiles. The method is designed to overcome the limitations of existing iterative approaches, which often struggle with convergence and accuracy when modelling complex distortion patterns such as severe barrel, pincushion, and moustache. By operating under clearly defined mathematical assumptions such as known polynomial degree and radial symmetry, the strategy aims to achieve precise inverse solutions. Performance will be rigorously evaluated using quantitative metrics such as reprojection error, root mean square error (RMSE), and residual error, and will be benchmarked against conventional calibration approaches to validate its effectiveness and robustness.

v) To evaluate the accuracy and practical effectiveness of the analytically derived inverse radial distortion coefficients by validating their ability to accurately reconstruct inverse distortion profiles for common lens distortion types, including barrel, pincushion, and moustache distortions. This evaluation will involve both graphical profile comparisons and quantitative performance metrics, such as reprojection error and root mean square error (RMSE), benchmarked against current semi analytical strategies.

1.6 **Thesis organization**

This research work is organized into five chapters as follows:

Chapter 2: Literature Review

This chapter provides an extensive review of foundational theories and existing methodologies in camera calibration, with a focus on both iterative and analytical approaches. It begins by examining essential concepts in point coordinates, vector transformations, and the geometry of the pinhole camera model. The chapter then explores various calibration strategies for estimating intrinsic parameters such as the distortion centre, focal lengths, and principal point, as well as extrinsic parameters including the translation vector and rotation matrix. It analyses **Tsai's (1987)** iterative calibration method, highlighting its approach to parameter estimation and potential for parameter coupling. The analytical calibration framework by **Seedahmed (2006)** is reviewed, emphasizing its geometric constraints and limitations, particularly the requirement for a priori focal length values and the assumption that the distortion centre lies at the image center. **Liu et al.'s (2008)** technique is examined, with attention to the calibration plane geometry and the influence of distortion centre constraints. The chapter also evaluates the Direct Linear Transformation (DLT) algorithm for estimating the projective transformation matrix and its coefficients while identifying risks associated with parameter interdependencies, especially in aspect ratio calibration and translation vector recovery. **Wang et al.'s (2016)** iterative method is assessed for its assumption about the origin of the world coordinate system and its inclusion of

distortion coefficients in the camera matrix. A detailed analysis of **Ganapathy's (1984)** decomposition approach is provided, including its modification of the upper triangular camera matrix and its derivation of both linear and nonlinear calibration equations. Variants of this analytical approach, such as those by **Roumie et al. (2018)** and **Kim et al. (2023),** are reviewed with a focus on parameter coupling effects, geometric constraints, and sign ambiguity issues. Further, the chapter explores QR decomposition and Cholesky factorization techniques, particularly those proposed by **Labuz et al. (1991)** and **Wang et al. (2022),** examining their limitations and accuracy implications, especially regarding the computation of the skew factor, principal point coordinates, and focal lengths. The relationship between projective transformation matrix scaling and numerical stability is critically assessed. Recent developments in deep learning-based calibration are explored, such as the approaches proposed in **Guo et al. (2017)** and **Lee et al. (2020)** that use convolutional neural networks and LSTMs. Additionally, various methods for modelling and correcting radial lens distortions are analysed, including division and rational models, polynomial function models, Taylor series approximations, look-up table strategies, and the semi-analytical inverse polynomial approach proposed by **Drap and Lefevre (2016)**. Throughout the chapter, emphasis is placed on the risks of parameter coupling, numerical instability, and geometric formulation limitations in existing calibration methods, thereby laying the groundwork for the development of a more robust analytical calibration approach.

Chapter 3: Analytical and Robust Camera Pose Estimation Model from a Single View Image for Close Range Photogrammetry

This chapter presents a non-iterative decomposition solution in the context of analytical camera pose calibration. In its first part, the chapter discusses some relevant solutions while pointing out the various areas of improvement and presents the need to improve these existing theories. In the second part of the chapter, a projective transformation matrix is formulated from the standard rigid body transformation matrix and the upper triangular camera matrix.
In the third part, a decomposition solution is developed to independently calibrate individual camera parameters through linear and non-linear equations that consider the geometric constraints imposed by the geometric structure of the projective transformation matrix and minimize parameter coupling and sign ambiguities. The data and methodology used to compute the twelve coefficients of the projective transformation matrix through the DLT algorithm are presented. A revisited decomposition solution from **Ganapathy's** original solution is developed in this chapter. The direct linear transform decomposition solutions proposed in **Roumie et al. (2018)** and **Kim et al. (2023)** are implemented and tested in this chapter. The QR decomposition camera calibration solution originally proposed by **Labuz et al. (1991)** and Cholesky factorization proposed in **Wang et al., (2022)** are also implemented and tested in this chapter. The aim of implementing these five solutions is to assess the performance of the newly developed fully analytical approach in calibrating the same camera parameters considered in this study. The accuracy of individual camera parameters calibrated through each of the five calibration methods is assessed against the newly proposed strategy through metrics such as the reprojection and root mean square error measures.

Chapter 4: Development of Fully Analytical Algorithms for Computation of Inverse Coefficients of High-order Radial Distortion Polynomials

This chapter provides a brief background on radial distortion correction methods. Some modelling of radial distortion through polynomial functions is discussed. Some limitations of the semi-analytic exact formula solution for radial distortion corrections are recalled in this chapter. The equipment, data, and methodology used to compute radial distortion coefficients are explained and presented. This chapter presents the methodology of developing a fully analytical series reversion algorithm for the general quintic radial distortion model. The algorithms to estimate inverse coefficients of a general quintic radial distortion polynomial are developed and presented. The methodologies of developing a fully analytical series reversion algorithm for a sixth and eight-degree polynomial radial distortion models are explained and presented. Individual algorithms to compute inverse coefficients of the sixth and eighth-degree radial distortion polynomials are developed and presented.
Numerical accuracy evaluations of the derived inverse distortion coefficients are undertaken in this chapter. Assessments of the quality of inverse curves of radial distortion polynomials formulated from the derived inverse coefficients are also performed. Distorted points measured from captured "distorted" photographs are corrected from barrel, pincushion, and moustache distortions using the respectively developed inverse polynomial models. The radial distortion correction results are evaluated through some error metrics to assess the performance of the newly proposed algorithms against the semi-analytical radial distortion approach.

Chapter 5: Research summary and conclusion

In the first part of this chapter, a general summary of each chapter of this thesis is provided. This summary discusses the camera calibration results for the camera pose estimation and the calibration of the parameters of the camera's internal geometry. Additional results to illustrate the performance of the newly proposed decomposition solution are also discussed, and relations to existing literature are presented. Additional illustrations of the performance of the newly developed analytical approach for inverse modelling of radial distortion polynomial models are presented and discussed. The findings of this research work are discussed. The limitations of the research work are discussed in this chapter, and suggestions for future works are presented. The research aims' achievement and research questions' answers are discussed.

1.7 Research Contributions

The contributions of this study are multifaceted. Firstly, it introduces a calibration framework capable of handling complex imaging scenarios with high accuracy, solidifying its relevance in photogrammetric measurements, 3D modelling, and computational imaging. Secondly, by analytically deriving inverse models for complex radial distortions, it significantly expands the methodological toolkit available for high-accuracy analytical radial distortion corrections. These advancements enrich the body of literature by providing scalable, theoretically grounded solutions that transcend the computational inefficiencies and limitations of existing methods. Thirdly, the development of a Python-based implementation makes the calibration of parameters describing camera internal geometry as well as parameters describing camera location and orientation in a 3D scene accessible to researchers and practitioners, fostering broader adoption in real-world applications. Furthermore, this research has been disseminated through two accredited conference publications presented at the 2019 ISPRS Geospatial Week, highlighting its practical impact and aligning with global standards in geospatial sciences. By bridging theoretical innovation with computational applicability, this PhD research contributes a novel,

scalable paradigm for precision imaging, ensuring robust performance across diverse fields such as 3D modelling, 3D scene reconstruction, remote sensing, autonomous navigation, and computer vision. These contributions collectively lay a solid foundation for future advancements in camera calibration and distortion correction, advancing the state of the art in imaging science and technology.

CHAPTER 2

LITERATURE REVIEW

2.1. Introduction

This chapter critically examines two principal areas of focus within the broader context of camera pose estimation as well as the estimation of the coordinates of the principal point and the camera effective focal lengths in photogrammetry: (i) the decomposition of the projective transformation matrix for camera parameter calibration and (ii) the analytical and semi-analytical correction of radial lens distortion through the reversion of polynomial distortion models. Each subsection of the chapter explores the extent to which existing methodologies, predominantly developed in the field of computer vision, address these challenges and evaluates their applicability and limitations in photogrammetric contexts. This review is essential for identifying theoretical and practical gaps in current literature and for establishing a foundation upon which this thesis builds its contributions to more robust and geometrically consistent calibration and distortion correction strategies tailored to photogrammetry applications.

2.2. Fundamentals of Vector Transformation

2.2.1. Homogeneous coordinates theory

In classical geometry, the Cartesian coordinate system represents points in space using fixed (x, y, z) coordinates relative to perpendicular axes. This system is intuitive and widely used for many geometric computations. However, when dealing with large-dimensional matrices and performing projective transformations in 3D space, particularly in the context of projective geometry, the Cartesian system becomes inadequate due to its inability to represent points at infinity and its limitations in handling perspective transformations efficiently (**Wegman and Said, 2010).** To overcome these issues, a more general coordinate representation known as the homogeneous coordinate system has been introduced, which incorporates an additional dimension referred to as the weight (**Zahneisen and Ernst, 2016).** This representation enables the use of linear algebra techniques for modelling projective transformations, allowing points and lines to be expressed as vectors that can be projected from one plane to another using transformation matrices (**Vakhitov et al., 2016**). The transformation of a line or point vector in homogeneous coordinates from one coordinate system to another requires some alignment between their respective coordinate axes to ensure the segment or line transformation is done accurately (**Lee and Jung, 2019**). It should be noted that the rigid body transformation is of high importance in the camera calibration task (**Chai et al., 2019**). The rigid body transformation

generally consists of a translation between the origins of coordinate systems and three rotations of the x, y and z axes of one coordinate system around the respective axes of the other fixed coordinate system (**Bartl et al., 2021**). The transformation of a point or line vector through a matrix is mostly done from the right to the left side convention (**Xu et al., 2017; Liu et al., 2017**). Assuming a point vector has the following coordinates in the 3D space x_1, x_2, x_3 while the expected output coordinates after the transformation are noted by y_1, y_2 and y_3, the transformation of homogeneous coordinates through a given matrix can be summarized as follows:

$$\begin{bmatrix} r_1 & r_2 & r_3 & 0 \\ r_4 & r_5 & r_6 & 0 \\ r_7 & r_8 & r_9 & 0 \\ 0 & 0 & 0 & 1 \end{bmatrix} \begin{bmatrix} x_1 \\ x_2 \\ x_3 \\ 1 \end{bmatrix} = \begin{bmatrix} y_1 \\ y_2 \\ y_3 \\ 1 \end{bmatrix} = \begin{bmatrix} r_1x_1 + r_2x_2 + r_3x_3 \\ r_4x_1 + r_5x_2 + r_6x_3 \\ r_7x_1 + r_8x_2 + r_9x_3 \\ 1 \end{bmatrix} \quad \textbf{[2-1]}$$

It must be pointed out here that the fundamental nature of the vector $X(x_1, x_2, x_3)$ remained unaffected despite the change of the coordinate system (**Allmendinger, 2015**). One of the most used matrices in camera calibration is the rotation matrix, which holds a number of properties useful for camera pose estimation. Since the inverse of a rotation matrix is equal to its transpose, it becomes easier to recover, for instance, the original coordinates x_1, x_2, x_3 of the vector X from those of $Y(y_1, y_2, y_3)$ as follows:

$$\begin{bmatrix} r_1 & r_4 & r_7 & 0 \\ r_2 & r_5 & r_8 & 0 \\ r_3 & r_6 & r_9 & 0 \\ 0 & 0 & 0 & 1 \end{bmatrix} \begin{bmatrix} y_1 \\ y_2 \\ y_3 \\ 1 \end{bmatrix} = \begin{bmatrix} x_1 \\ x_2 \\ x_3 \\ 1 \end{bmatrix} = \begin{bmatrix} r_1y_1 + r_4y_2 + r_7y_3 \\ r_2y_1 + r_5y_2 + r_8y_3 \\ r_3y_1 + r_6y_2 + r_9y_3 \\ 1 \end{bmatrix} \quad \textbf{[2-2]}$$

It is also important to note that from the formulation equation **[2-2]** the Cartesian coordinates of the original vector X can be recovered by dividing the first three rows on both sides of **[2-2]** by the last row, which is in this case reduced to unity.

2.2.2. The Pinhole Camera Projection Model

The pinhole camera model describes the projection geometry of an object from the three-dimensional plane onto the two-dimensional image plane in the absence of lens distortions. This model is the cornerstone of camera calibration algorithms for non-curved lenses (**Chen et al., 2018; Juarez-Salazar et al., 2020).** In a pinhole projection geometry, all light rays intersect at a single point generally labeled as the projection center or the lens center **(Zhao et al., 2016; Khomutenko et al., 2015),** as illustrated in Figure 2-1 by the point. O_c.

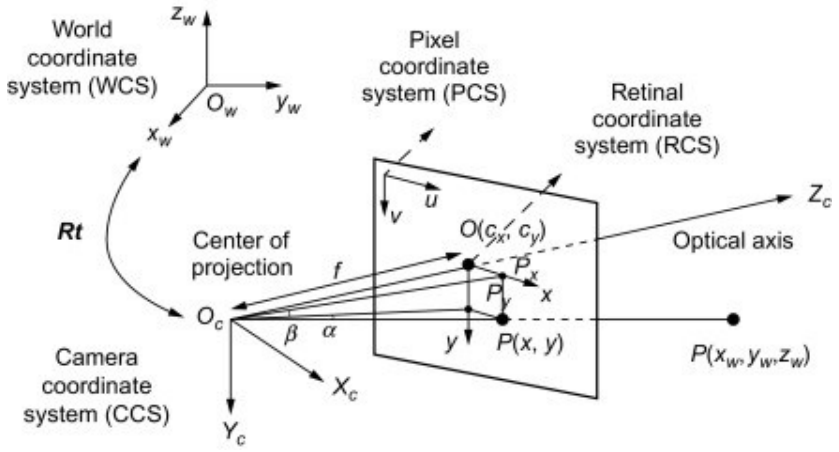

Figure 0-1: Illustration of the pinhole camera geometry (Huang et al.,2018)

An observation of Figure 2-1 shows that the projection center O_c is the center of a three-dimensional camera coordinate system with its X_c, Y_c and Z_c axes. The X_c axis of the camera coordinate system generally points toward the right direction and parallel to the vertical image plane (**Cornic et al., 2016**), while the Y_c axis points downward and parallel to the image plane (**Huang et al., 2018**; **Zhao et al., 2020**), and the Z_c axis is pointing in the viewing direction and projected along the optical axis (**Chen and Pan, 2020**). Although the above orientations of the camera coordinate axes are widely used, the X_c axis of the camera coordinate system can also be oriented in the left direction parallel to the vertical image plane while the Y_c axis is maintained in the downward direction (**Lei et al., 2020**). Earlier, **Dehkharghani and Pleshkova (2014)** and **Lu (2018)** proposed a camera coordinate system with the X_c axis having a similar orientation as that in the work of **Lei et al. (2020)**, while the camera Y_c axis is oriented in the upward direction and parallel to the image plane. In contrast, **Zhu et al. (2019)** proposed a camera coordinate system with the Z_c axis pointing downward and parallel to the image plane. The camera Y_c axis shares the same direction as the optical axis and maintains its orientation towards the right-hand side. The sequence between the translation and rotation processes in a rigid body transformation is not binding, as it can depend on the analyst's preferences. The optical axis from the projection center intersects the image plane at a crucial point, the origin of another coordinate system called the retinal coordinate system (**Feng and Pan, 2018**). The axes of this coordinate system are parallel to those of the lens-centered camera coordinate system, and this alignment facilitates the projection from the 3D camera coordinates onto the image plane because no additional axes' rotation is required; only a scaling transformation is needed (**Schramm et al., 2021**). The normal pinhole projection has the image plane located behind the projection center, which creates some computational challenges considering the inverted orientation of the image. However, an upright-oriented image would eliminate numerical ambiguities that may be introduced by the negative measure of the image (**Stankiewicz et al., 2018**). To achieve an upright image orientation, the image plane is brought forward in front of the projection center at a distance equivalent to the lens focal distance **(Semeniuta, 2016; Juarez-Salazar and Díaz-Ramírez, 2020).** In addition, there seems to be no convention adopted on the sign of the focal length, as some authors would use its negated value by considering the displacement from the projection center to the image plane located behind it as positive, while moving the plane in front of the projection center would be considered a negative displacement (**Khalil, 2011**). In the absence of lens distortion in the pinhole camera model, the 3D world point, its projected image

representation, and the projection center must lie on the same line. This alignment is the foundation of the collinearity equations useful for estimating parameters of the camera transformation matrix **(El-Ashmawy, 2015; Luhmann et al., 2016)**. Since the 3D world points are transformed to a two-dimensional point on the image plane, it is expected to derive only two collinear equations relating the camera coordinates x_c and y_c to the image coordinates x_p and y_p. In the instance of a negative focal length and the assumption that the principal point is the center of the image, the collinearity equations are formulated as follows:

$$\begin{cases} x_p = -f\dfrac{(x_w - x_0)r_{11} + (y_w - y_0)r_{12} + (z_w - z_0)r_{13}}{(x_w - x_0)r_{31} + (y_w - y_0)r_{32} + (z_w - z_0)r_{33}} \\ y_p = -f\dfrac{(x_w - x_0)r_{21} + (y_w - y_0)r_{22} + (z_w - z_0)r_{23}}{(x_w - x_0)r_{31} + (y_w - y_0)r_{32} + (z_w - z_0)r_{33}} \end{cases} \quad \textbf{[2-3]}$$

The coordinates x_0, y_0 and z_0 are the coordinates of the origin of the camera coordinate system. Formulating the collinearity equations in **[2-3]** is a special case where the translation between the camera and world coordinate systems' origins is performed before the axes rotation phase **(Elnima, 2015; Tjahjadi et al., 2017)**. When the translation procedure is performed after a rotation of coordinate systems' axes, the translation coefficients along the x and y directions are generally added as the last terms of the respective numerator expressions of collinearity equations, while the last coefficient of the translation vector is added as the last component of the denominator expression. Image coordinates derived from equation **[2-3]** are generally in world units. However, a fourth coordinate system is needed to convert the world unit measures to the corresponding pixel measures. This fourth image coordinate system originates from the top left corner of the image plane (**Yan et al., 2016; Boby and Saha, 2016**). The choice of the top left corner of the image frame as the origin of the image pixel coordinate system is not always a unanimous one, as authors such as **Liang et al. (2020)** opted to have the bottom right corner of the image frame as the origin of the image pixel coordinates. A general formulation of the conversion from image world units to pixel units is given as follows **(Tang et al., 2019):**

$$\begin{bmatrix} u \\ v \\ 1 \end{bmatrix} = \begin{bmatrix} \alpha_x & \lambda & u_0 \\ 0 & \alpha_y & v_0 \\ 0 & 0 & 1 \end{bmatrix} \begin{bmatrix} x_p \\ y_p \\ 1 \end{bmatrix} \quad \textbf{[2-4]}$$

The parameters a_x and a_y are the effective focal lengths and are usually ratios of focal length by the pixel's length and width, respectively. The parameter λ is the skew factor and is generally considered zero, assuming that current lens systems produce square or rectangular image frames with an angle of $\frac{\pi}{2}$ between the image pixel coordinate system u and v axes **(Yan et al., 2016).** The parameters u_0 and v_0 are the coordinates of the origin of the image coordinate system in pixels.

2.3. Modelling Camera Location and Orientation through the Pinhole Camera Geometry

The success of the projection from the 3D world coordinate system to the intermediate 3D camera coordinate system cannot be separated from the success of the last rotation performed during the

rigid body transformation. The last rotation of the rigid body transformation can either align the camera coordinate frame's Z_c axis with the world coordinate system's Z_ω axis, as performed by **Lopez et al. (2019),** and the projection of the 3D world plane onto the 3D vertical camera plane passing through the lens centre is done through a simple scaling process by the inverse of the distance from the 3D world scene to the camera lens generally denoted Z_ω (**Moru and Borro, 2020**). The last rotation can also align the camera Z_c axis with the world Y_ω axis, as reported in **Ganaphaty (1984).** In such instances, the projection from the 3D world plane onto the 3D camera plans is done through scaling by the Y_ω coordinate of the world point viewed from the camera coordinate system. The conversion from the 3D camera coordinates to the 2D image retinal coordinates is done using equation **[2-3],** in contrast to authors such as **Tsai (1987)**, **Rojtberg and Kuijper (2018), Lelowicz (2019),** and **Liu et al. (2019)**.

2.3.1. Tsai's Camera Parameters Modelling

Tsai (1987) applied the translation between the two coordinate systems' origins post-rotation using the coefficients t_x, t_y and t_z of the translation vector. For the scaling of camera coordinates in order to achieve retinal coordinates, the author considered the same scaling factor; however, to convert retinal image coordinates from world units to pixel units, the author applied two different scaling factors to each retinal image coordinate through the following homogeneous matrix transformation:

$$\begin{bmatrix} u \\ v \\ 1 \end{bmatrix} = \begin{bmatrix} s_x d_x^{-1} & 0 & c_x \\ 0 & d_y^{-1} & c_y \\ 0 & 0 & 1 \end{bmatrix} \begin{bmatrix} x_d \\ y_d \\ 1 \end{bmatrix} \qquad \textbf{[2-5]}$$

The measures c_x and c_y represent the origin of the pixel coordinate system, d_x and d_y are the horizontal and vertical distances between centres of adjacent cells in the CCD array, while the parameter s_x is a scaling factor introduced by the image capture hardware. The approach algebraically estimates the components of the camera matrix through simple linear equations, while the parameters describing camera location and orientation are recuperated using non-linear optimization techniques. This requires accurate initial estimates of these parameters, which are generally difficult to obtain (**Ruszczynski, 2011**). Additionally, **Zhang et al. (2018**) argued that Tsai's approach could not handle severe radial lens distortions and assumed the distortion centre as the principal point, which is not always the case for consumer-grade digital cameras (**Li et al., 2015**). Since projective geometry does not preserve angles in the two planes, Tsai's calibration strategy will likely introduce numerical errors in estimating camera location and orientation (**Tang et al., 2021**).

2.3.2. Seedahmed's Camera Parameters Modelling

Seedahmed (2006) proposed a calibration method that constrains 3D scene calibration points and the origin of the 3D world coordinate system to lie on the same planar surface to simplify the collinearity equations, as also reported in the works of **Semeniuta (2016)** and of **Lai et al. (2018**). The crucial advantage of this constraint is that the Z coordinates of all the points lying on the planar surface are reduced to zero, resulting in the 3D calibration points being only defined by their X and Y coordinates while their nullified third coordinates are set to unity to

accommodate the homogeneous representation of the point vectors being transformed. The second advantage is that while the third-world points' coordinates are nullified, the 3×4 projective transformation matrix loses its third column, which is then replaced by the coefficients of the translation vector (**Lari et al., 2014; Jiang et al., (2019)**. Another advantage of the proposed approach is that during the solution estimation, the number of unknown exterior parameters can be reduced by scaling both collinearity equations by the third coefficient of the translation vector; this scaling, however, does not change the fundamental property of the rigid body transformation matrix when the column vector being transformed is in a homogeneous representation form (**Abdel-Aziz et al., 2015**). Scaling the elements of the projective transformation matrix renders the extraction of individual parameters very difficult due to the resulting concatenations within the matrix (**Vladimirov and Koceski, 2019; Barrett et al., 2020**). To mitigate this difficulty, orthogonal decomposition solutions have been proposed (**Imakura and Yamamoto, 2019**). However, since orthogonal decomposition techniques suffer from parameter coupling, **Seedahmed** instead proposed an algebraic decomposition solution slightly similar to the method earlier proposed by **Ganaphati (1984).** The cornerstone of the proposed solution is to first compute the twelve coefficients of the projective transformation matrix using the DLT algorithm. The general transformation from a 3D scene point to a 2D image point through the projective transformation matrix is given as follows:

$$\begin{bmatrix} x \\ y \\ 1 \end{bmatrix} = \begin{bmatrix} \varphi_{11} & \varphi_{12} & \varphi_{13} \\ \varphi_{21} & \varphi_{22} & \varphi_{23} \\ \varphi_{31} & \varphi_{32} & 1 \end{bmatrix} \begin{bmatrix} X \\ Y \\ 1 \end{bmatrix} = \lambda \begin{bmatrix} 1 & 0 & -c_x f^{-1} \\ 0 & 1 & -c_y f^{-1} \\ 0 & 0 & -f^{-1} \end{bmatrix} \begin{bmatrix} r_{11} & r_{21} & -\left(X_0 r_{11} + Y_0 r_{21} + Z_0 r_{31}\right) \\ r_{12} & r_{22} & -\left(X_0 r_{12} + Y_0 r_{22} + Z_0 r_{32}\right) \\ r_{13} & r_{23} & -\left(X_0 r_{13} + Y_0 r_{23} + Z_0 r_{33}\right) \end{bmatrix} \begin{bmatrix} X \\ Y \\ 1 \end{bmatrix} \quad \textbf{[2-6]}$$

Once the components of the matrix on the left side of **[2.6]** are estimated, the next step of the strategy is to construct a "twin" projective transformation matrix, which has as foundation the transpose of the commonly used rotation matrix based on Euler's three rotations (**Wang et al., 2018**). An example of such a rotation matrix can be found in the work of **Uygur et al. (2020**). In contrast to the equation **[2-3],** the collinearity equations proposed in **Seedahmed (2006)** account for the coordinates of the principal point and also maintain a negative focal length to justify the displacement of the image plane from its location behind the centre of the projection (considered positive) to the front location as presented in the work of **Lichti et al. (2020**). The collinearity equations constituting the foundation of the "twin" projective transformation matrix are formulated as follows:

$$x - c_x = -f \frac{r_{11}X + r_{21}Y - r_{11}X_0 - r_{21}Y_0 - Z_0}{r_{13}X + r_{23}Y - r_{13}X_0 - r_{23}Y_0 - r_{33}Z_0} \quad \textbf{[2-7]}$$

$$y - c_y = -f \frac{r_{12}X + r_{22}Y - r_{12}X_0 - r_{22}Y_0 - r_{32}Z_0}{r_{13}X + r_{23}Y - r_{13}X_0 - r_{23}Y_0 - r_{33}Z_0} \quad \textbf{[2-8]}$$

Both the above equations can be reformulated into a matrix representation after isolating the focal length as a scaling factor and then shifting the coordinates of the principal point c_x and c_y to the right side of the equality sign to achieve the following:

$$\begin{bmatrix} x \\ y \\ 1 \end{bmatrix} = f \begin{bmatrix} 1 & 0 & -c_x f^{-1} \\ 0 & 1 & -c_y f^{-1} \\ 0 & 0 & -f^{-1} \end{bmatrix} \begin{bmatrix} r_{11} & r_{21} & -\left(X_0 r_{11} + Y_0 r_{21} + r_{31} Z_0\right) \\ r_{12} & r_{22} & -\left(X_0 r_{12} + Y_0 r_{22} + r_{32} Z_0\right) \\ r_{13} & r_{23} & -\left(X_0 r_{13} + Y_0 r_{23} + r_{33} Z_0\right) \end{bmatrix} \begin{bmatrix} X \\ Y \\ 1 \end{bmatrix} \quad \textbf{[2-9]}$$

The value zero attributed to the first coefficients of the second column of the first 3×3 matrix is the skew factor due to the orthogonality between the 2D image coordinate axes (**Halloran et al.,**

2020). If one denotes the first matrix on the left as k and the matrix containing the rotation matrix coefficients as M the expression in **[2-9]** can be summarized as follows:

$$p(x, y, 1) = f \bullet k \bullet M \bullet P(X, Y, 1) \qquad \textbf{[2-10]}$$

A comparison between the general transformation from 3D point to 2D image points in **[2-6]** and that in **[2-10]** reveals the first shortcoming of the modelling proposed by Seedahmed in **[2-9],** which assumes that the scale factor λ is equal to the focal length, which does not always hold true, as supported in the works of **An et al. (2018), Liu et al. (2021),** and **Chen et al. (2021**). One suggestion to the author would be to consider the image coordinates in **[2-9]** as non-measurable image coordinates that are still located on the image plane, resulting in the extraction of the focal length as a scale factor from the image coordinates, which can then be eliminated if **[2-9]** is reformulated as follows:

$$\lambda \begin{bmatrix} x_i \\ y_i \\ 1 \end{bmatrix} = f \begin{bmatrix} xf^{-1} \\ yf^{-1} \\ 1 \end{bmatrix} = f \begin{bmatrix} 1 & 0 & -c_x f^{-1} \\ 0 & 1 & -c_y f^{-1} \\ 0 & 0 & -f^{-1} \end{bmatrix} \begin{bmatrix} r_{11} & r_{21} & -(X_0 r_{11} + Y_0 r_{21} + r_{31} Z_0) \\ r_{12} & r_{22} & -(X_0 r_{12} + Y_0 r_{22} + r_{32} Z_0) \\ r_{13} & r_{23} & -(X_0 r_{13} + Y_0 r_{23} + r_{33} Z_0) \end{bmatrix} \begin{bmatrix} X \\ Y \\ 1 \end{bmatrix} \qquad \textbf{[2-11]}$$

Where x , y represent the non-measurable image coordinates and x_i and y_i the measurable image coordinates in world units. From **[2-10],** the author can relate **[2-6]** to the expression on the right side of the equality sign in **[2-10]** after eliminating the focal length since it is a common factor on both sides of **[2-11].** The camera matrix containing the inverse focal length and the coordinates of the principal point can be eliminated by calculating its inverse since it has a non-zero discriminant. The multiplication will transform the coefficients of the last column of the matrix on the right side of **[2-11]** to some well-structured negated sums of products of its original coefficients with the coordinates of the principal point c_x and c_y. The inverse of the scaling parameter λ can be eliminated in the remaining expression by normalizing both sides of the remaining equality, and the three rotation angles can easily be retrieved after substituting the coefficients of the remaining two columns of the rotation matrix in the resulting expression. The second shortcoming of the proposed method is that the estimation of the parameters describing the camera position X_0, Y_0 and Z_0 can only be performed under the assumptions that the focal length is known a priori and the coordinates of the principal point are at the centre of the image, which does not always hold true for consumer-grade digital cameras. The third shortcoming of the approach is that the proposed camera geometry does not reflect the horizontal projection plane when considering the transpose of the commonly used Euler rotation matrix. In fact, to simulate the horizontal plane of the aerial survey, only the vertical plane XY passing through the principal point had to be rotated by an angle $\frac{\pi}{2}$ in the anticlockwise direction considered as positive orientation, while the horizontal plane containing the XZ plane also had to be rotated $\frac{\pi}{2}$ in the anticlockwise direction to construct the perfect horizontal plane of the camera with the camera Z axis now pointing downward.

2.3.3. Liu's Modelling of Camera Parameters

Liu et al. (2008) proposed a different approach than that of **Seedahmed (2006)** in the sense that it extends the number of parameters estimated during the calibration process and it considered non-coplanar calibration points. The method also differs from **Seedahmed (2006)** in the sense that the final estimates of parameters are optimized through the minimization of a cost

function. The proposed technique offers a two-stage approach where intrinsic parameters are first estimated under the constraints that the principal point is located at the centre of the image while neglecting the influence of lens distortion. To relate 3D world points' coordinates to their respective image buffer coordinates, the following transformation is considered:

$$\begin{bmatrix} x_f \\ y_f \\ 1 \end{bmatrix} = \begin{bmatrix} s & 0 & u_0 \\ 0 & 1 & v_0 \\ 0 & 0 & 1 \end{bmatrix} \begin{bmatrix} fd_x^{-1} & 0 & 0 \\ 0 & fd_y^{-1} & 0 \\ 0 & 0 & 1 \end{bmatrix} \begin{bmatrix} r_{11} & r_{12} & r_{13} & t_x \\ r_{21} & r_{22} & r_{23} & t_y \\ r_{31} & r_{32} & r_{33} & t_z \end{bmatrix} \begin{bmatrix} X \\ Y \\ Z \\ 1 \end{bmatrix} \quad \textbf{[2-12]}$$

The parameters f, u_0, v_0 and s represent the intrinsic characteristics of the camera, where f denotes the focal length, (u_0, v_0) are the coordinates of the principal point, and s represents the aspect ratio. The parameters d_x and d_y define the physical pixel dimensions in the x and y directions, respectively. The elements $r_{11}, r_{12}, r_{13} \ldots . r_{33}$ correspond to the components of the rotation matrix that describes the camera's exterior orientation, while t_x, t_y and t_z define the translation vector, indicating the camera's position in three-dimensional space. It can be observed from **[2-12]** that unlike the formulations presented in the works of **Li et al. (2017)** and **Lei et al. (2020),** the matrix on the left uses the same value of the focal length f for the scaling of x and y coordinates. Reformulating the matrix multiplication on the right side of the equality sign leads to the following simplified equation:

$$\begin{bmatrix} x_f \\ y_f \\ 1 \end{bmatrix} = \begin{bmatrix} r_{11} fsd_x^{-1} + u_0 r_{31} & r_{12} fsd_x^{-1} + u_0 r_{32} & r_{13} fsd_x^{-1} + u_0 r_{33} \\ r_{21} fd_y^{-1} + v_0 r_{31} & r_{22} fd_y^{-1} + v_0 r_{32} & r_{23} fd_y^{-1} + v_0 r_{33} \\ r_{31} & r_{32} & r_{33} \end{bmatrix} \begin{bmatrix} X \\ Y \\ Z \end{bmatrix} + \begin{bmatrix} t_x \\ t_y \\ t_z \end{bmatrix} \quad \textbf{[2-13]}$$

From **[2-13]** two collinearity equations that relate the image buffer pixel coordinates to the 3D world coordinates can be expressed as follows:

$$x_f = \frac{\left(r_{11} fsd_x^{-1} + u_0 r_{31}\right) X + \left(r_{12} fsd_x^{-1} + u_0 r_{32}\right) Y + \left(r_{13} fsd_x^{-1} + u_0 r_{33}\right) Z + t_x}{r_{31} X + r_{32} Y + r_{33} Z + t_z} \quad \textbf{[2-14]}$$

$$y_f = \frac{\left(r_{21} fd_y^{-1} + v_0 r_{31}\right) X + \left(r_{22} fd_y^{-1} + v_0 r_{32}\right) Y + \left(r_{23} fd_y^{-1} + v_0 r_{33}\right) Z + t_y}{r_{31} X + r_{32} Y + r_{33} Z + t_z} \quad \textbf{[2-15]}$$

It can be observed that the above formulations of x and y buffer coordinates do not account for the arbitrary scaling factor. It has been reported in the works of **Lu and Cai (2020)** and **Cheng and Matsuoka (2021)** that the radial alignment constraint used in the solution proposed by **Liu et al. (2008)** imposes the 3D world point, its undistorted projection on the image frame, and the projection centre to lie on a straight line, and the following equalities hold true under this constraint:

$$\frac{y_f}{y_c} = \frac{f}{z_c} \quad \textbf{[2-16]}$$

$$\frac{x_f}{x_c} = \frac{f}{z_c} \quad \textbf{[2-17]}$$

The coordinates x_c, y_c and z_c are the camera coordinates computed through the rigid body transformation. From **[2-16]** and **[2-17],** the following equality is derived:

$$\frac{x_f}{x_c} = \frac{y_f}{y_c} \qquad \textbf{[2-18]}$$

Reformulating **[2-18]** as cross multiplications leads to the following:

$$x_f \times y_c = x_c \times y_f \qquad \textbf{[2-19]}$$

Dividing both sides of **[2-19]** by $y_c \times y_f$ leads to the following radial alignment constraint:

$$\frac{x_f}{y_f} = \frac{x_c}{y_c} \qquad \textbf{[2-20]}$$

Expressing the ratio on the left in **[2-20]** as a function of **[2-14]** and **[2-15]** leads to the following:

$$\frac{x_f}{y_f} = \frac{\left(fsd_x^{-1}r_{11} + u_0 r_{31}\right)X + \left(fsd_x^{-1}r_{12} + u_0 r_{32}\right)Y + \left(fsd_x^{-1}r_{13} + u_0 r_{33}\right)Z + t_x}{\left(fd_y^{-1}r_{21} + v_0 r_{31}\right)X + \left(fd_y^{-1}r_{22} + v_0 r_{32}\right)Y + \left(fd_y^{-1}r_{23} + v_0 r_{33}\right)Z + t_y} \qquad \textbf{[2-21]}$$

After some rearrangements and factorization, the expression in **[2-21]** can be reformulated as follows:

$$\frac{x_f}{y_f} = \frac{fsd_x^{-1}\left(r_{11}X + r_{12}Y + r_{13}Z\right) + u_0\left(r_{31}X + r_{32}Y + r_{33}Z\right) + t_x}{fd_y^{-1}\left(r_{21}X + r_{22}Y + r_{23}Z\right) + v_0\left(r_{31}X + v_0 r_{32}Y + v_0 r_{33}Z\right) + t_y} \qquad \textbf{[2-22]}$$

Posing $R_1 = r_{11} + r_{12} + r_{13}$, $R_2 = r_{21} + r_{22} + r_{23}$, $R_3 = r_{31} + r_{32} + r_{33}$ and $p = \begin{bmatrix} X & Y & Z \end{bmatrix}$, the expression in **[2-22]** can be simplified after linearization to the following:

$$\left[fd_y^{-1}R_2 + v_0 R_3\right]x_f P + x_f t_y = \left[fsd_x^{-1}R_1 + u_0 R_3\right]y_f P + y_f t_x \qquad \textbf{[2-23]}$$

From **[2-23],** the authors defined the following homographic relationships:

$$H_1 = \frac{fsR_1}{d_x} + u_0 R_3 \qquad \textbf{[2-24]}$$

$$H_2 = \frac{fR_2}{d_y} + v_0 R_3 \qquad \textbf{[2-25]}$$

Substituting **[2-24]** and **[2-25]** into **[2-23]** leads to the following equation:

$$\left(y_f P + y_f - x_f P - x_f\right)\begin{bmatrix} H_1 \\ t_x \\ H_2 \\ t_y \end{bmatrix}^T = 0 \qquad \textbf{[2-26]}$$

Using techniques such as the Singular Value Decomposition approach, the parameters H_1, H_2, t_x and t_z can be recovered. Squaring both sides of expressions **[2-24]** and **[2-25]** leads to the following equivalences:

$$\|H_1\|^2 = \left(\frac{fsR_1}{d_x} + u_0 R_3\right)^2 = \frac{f^2 s^2}{d_x^2} + u_0^2 + \frac{2u_0 fsR_3 R_1}{d_x} = \frac{s^2 f^2}{d_x^2} + u_0^2 \qquad \textbf{[2-27]}$$

$$\|H_2\|^2 = \left(\frac{fR_2}{d_y} + v_0 R_3\right)^2 = \frac{f^2}{d_y^2} + v_0^2 + \frac{2v_0 fR_2 R_3}{d_y} = \frac{f^2}{d_y^2} + v_0^2 \qquad \textbf{[2-28]}$$

Multiplying both sides **[2-28]** by d_y^2 enables the authors to estimate the focal length as follows:

$$f = d_y\sqrt{\|H_2\|^2 - v_0^2} \qquad \textbf{[2-29]}$$

The formulation **[2-29]** exhibits a shortfall of the proposed solution because the presented algorithm does not satisfy the constraint in **[2-27].** Indeed, simultaneously extracting a more representative estimate of f from **[2-27]** and **[2-28]** can be tricky if enough attention is not paid when analysing **[2-27].** The author could have dealt with this drawback by changing the sequence of estimation of the focal length and the aspect ratio parameters**.** Since the parameters H_1 and H_2 are assumed known from the solution of **[2-26],** the squared focal length could have been isolated from **[2-27]** then substituted into **[2-28]** to estimate the aspect ratio independently from the focal length measure**.** Once the aspect ratio has been estimated, the authors could have added both equations **[2-27]** and **[2-28]** to extract a more representative estimate of f that satisfies **[2-27]** and **[2-28].** Equation **[2-29]** can introduce numerical instability if included in an optimization algorithm such as the LM used by the authors to optimize the intrinsic camera parameters, as the iteration would converge at the wrong maximum. Furthermore, estimating the aspect ratio by multiplying both sides of **[2-27]** by d_x^2 does not improve the solution, as any inaccuracy in the estimation of f will propagate into the aspect ratio parameter when considering the strategy proposed by the authors, which is formulated as follows:

$$s = \frac{d_x\sqrt{\|H_1\|^2 - u_0^2}}{f} \qquad \textbf{[2-30]}$$

Once the intrinsic camera parameters have been estimated, given the image pixel coordinates x_f and y_f, the authors recovered the image coordinates in world units by multiplying the pixel coordinates by the inverse of the camera projective matrix as follows:

$$\begin{bmatrix} x_i \\ y_i \\ 1 \end{bmatrix} = \begin{bmatrix} fsd_x^{-1} & 0 & u_0 \\ 0 & fd_y^{-1} & v_0 \\ 0 & 0 & 1 \end{bmatrix}^{-1} \begin{bmatrix} x_f \\ y_f \\ 1 \end{bmatrix} \quad \textbf{[2-31]}$$

The Direct Linear Transformation (DLT) is a widely used algorithm in camera calibration and 3D reconstruction for estimating the elements of the projective transformation matrix. It relies on known correspondences between 3D world calibration points and their 2D image projections. By establishing a system of linear equations from these correspondences, the DLT algorithm computes the transformation matrix that maps world coordinates to image coordinates under a pinhole camera model. An analysis of the above transformation exposes another shortfall of the calibration strategy. In fact, 3D world calibration points are projected into an image plane to produce measurable, distorted coordinates. However, from the radial alignment equation derived in **[2-14]** and **[2-15],** lens distortion was not considered, thus the image coordinates obtained through **[2-31]** actually amount to undistorted coordinates rather than the measurable distorted coordinates. This can undermine the accuracy of the solution of the projective transformation through the DLT algorithm. From the results of the DLT procedure, the authors estimated the first two rows of the rotation matrix, which enabled them to recover the last row of the matrix using the orthogonality property of the axes of the rotation matrix through cross-products. This proposed estimation procedure has the inconvenient of being time-consuming. The last row of the rotation matrix could also be recovered in a straightforward manner once the coefficients of the projective transformation matrix have been obtained since the components of the inverse camera matrix in **[2-31]** are already known from **[2-29]** and **[2-30]**. Multiplying the camera matrix on the left side in **[2-12]** by the coefficients of the translation column vector leads to the following:

$$\begin{bmatrix} fsd_x^{-1} & 0 & u_0 \\ 0 & fd_y^{-1} & v_0 \\ 0 & 0 & 1 \end{bmatrix} \begin{bmatrix} t_x \\ t_y \\ t_z \end{bmatrix} = \begin{bmatrix} fsd_x^{-1}t_x + u_0 t_z \\ fd_y^{-1}t_y + v_0 t_z \\ t_z \end{bmatrix} \quad \textbf{[2-32]}$$

From the above the authors extracted the following equations:

$$sft_x d_x^{-1} + u_0 t_z = t_x \quad \textbf{[2-33]}$$

$$ft_y d_y^{-1} + v_0 t_z = t_y \quad \textbf{[2-34]}$$

Assuming that the coordinates of the origin of the image coordinate frame are located at the centre of the image, the authors isolated the z component of the translation vector as follows:

$$\frac{t_x - sft_x d_x^{-1}}{u_0} = t_z \quad \textbf{[2-35]}$$

$$\frac{t_y - t_y d_y^{-1}}{v_0} = t_z \quad \textbf{[2-36]}$$

Adding the above equations leads to the following:

$$T_z = 0.5\left(\frac{T_x - sfT_x d_x^{-1}}{u_0} + \frac{T_y - T_y d_y^{-1}}{v_0}\right) \quad \textbf{[2-37]}$$

It can be argued that the parameter estimated in **[2-37]** does not satisfy the constraints imposed by **[2-12]** since the dot product of the column vectors $\begin{bmatrix} t_x & t_y & t_z \end{bmatrix}^T$ with the last row of the camera matrix in **[2-12]** leads to a value of t_z equal to unity. Moreover, the formulation in **[2-32]** from which **[2-33]** and **[2-34]** were derived does not have any clear geometrical meaning. Furthermore, the formulations in **[2-35]** and **[2-36]** do not hold true for a principal point with coordinates very close to zero. To deal with these drawbacks, the authors could have expanded the equation in **[2-12]** as follows:

$$\begin{bmatrix} x_f \\ y_f \\ 1 \end{bmatrix} = \begin{bmatrix} fsd_x^{-1} & 0 & u_0 \\ 0 & fd_y^{-1} & v_0 \\ 0 & 0 & 1 \end{bmatrix} \begin{bmatrix} Xr_{11} + Yr_{12} + Zr_{13} + t_x \\ r_{21}X + r_{22}Y + r_{23}Z + t_y \\ r_{31}X + r_{32}Y + r_{33}Z + t_z \end{bmatrix} \quad \textbf{[2-38]}$$

From **[2-38]** the following equations can be derived:

$$x_f = \frac{fsd_x^{-1}\left(Xr_{11} + Yr_{12} + Zr_{13} + t_x\right) + u_0\left(r_{31}X + r_{32}Y + r_{33}Z\right) + u_0 t_z}{r_{31}X + r_{32}Y + r_{33}Z + t_z} \quad \textbf{[2-39]}$$

$$y_f = \frac{fd_y^{-1}\left(r_{21}X + r_{22}Y + r_{23}Z + t_y\right) + v_0\left(r_{31}X + r_{32}Y + r_{33}Z\right) + v_0 t_z}{r_{31}X + r_{32}Y + r_{33}Z + t_z} \quad \textbf{[2-40]}$$

Expanding **[2-39]** leads to the following:

$$fsd_x^{-1}\left(Xr_{11} + Yr_{12} + Zr_{13} + t_x\right) + u_0\left(r_{31}X + r_{32}Y + r_{33}Z\right) - x_f\left(r_{31}X + r_{32}Y + r_{33}Z\right) = \left(x_f - u_0\right)t_z \quad \textbf{[2-41]}$$

Similarly, from **[2-40]** the following is derived:

$$fd_y^{-1}\left(r_{21}X + r_{22}Y + r_{23}Z + t_y\right) + v_0\left(r_{31}X + r_{32}Y + r_{33}Z\right) - y_f\left(r_{31}X + r_{32}Y + r_{33}Z\right) = \left(y_f - v_0\right)t_z \quad \textbf{[2-42]}$$

Adding **[2-41]** and **[2-42]** enables to estimate the third component of the translation vector as follows:

$$t_z = \frac{fsd_x^{-1}\left(Xr_{11} + Yr_{12} + Zr_{13} + t_x\right) + fd_y^{-1}\left(r_{21}X + r_{22}Y + r_{23}Z + t_y\right)}{\left(x_f - u_0 + y_f - v_0\right)} + \frac{\left(r_{31}X + r_{32}Y + r_{33}Z\right)\left(u_0 + v_0\right) + \left(r_{31}X + r_{32}Y + r_{33}Z\right)\left(-x_f - y_f\right)}{\left(x_f - u_0 + y_f - v_0\right)} \quad \textbf{[2-43]}$$

The expression **[2-43]** is more numerically stable than that proposed by the authors in **[2-37],** even with a near zero shift of the principal point from the image centre. Finally, two more limitations were identified in relation to the handling of radial distortion. One first drawback is

that the approach only considered one coefficient, while another limitation is the formulation of the cost function to be optimized using the LM algorithm to enhance the accuracy of the radial distortion coefficient, which is formulated as follows:

$$y_{di}\left(1+\kappa_1 r_{di}^2\right)=\frac{r_{21}X+r_{22}Y+r_{23}Z+t_y}{r_{31}X+r_{32}Y+r_{33}Z+t_z} \qquad \textbf{[2-44]}$$

It can be observed that the expression on the right resembles the collinear equation associated with the image y_i coordinate, but the expression lacks its scaling by the camera constant f as generally formulated (**El-Ashmawy, 2021**). Furthermore, the cost function in **[2-44]** contains the third coefficient of the translation vector t_z estimated through the very subjective equation **[2-37],** and initializing the coefficient of radial distortion to zero does not always guarantee convergence of the optimization algorithm at the right maxima, especially for images where radial distortions are observables.

2.3.4. Wang's Camera Parameters Modelling

Wang et al. (2016) proposed a four-step iterative camera calibration approach in which initial values of some of the camera's intrinsic and extrinsic parameters are estimated under certain geometric constraints. Once the partial estimation of parameters is performed, these values are refined through a maximum likelihood optimization. One strength of the proposed approach is the reduced number of exterior orientation parameters to be estimated thanks to the co-planar geometry between the 3D calibration points and the origin of the 3D world coordinate frame. The conversion from world 3D coordinates to 3D camera coordinates is done through a rigid body transformation in which the rotation matrix is different from those in **Tsai (1987)**, **Seedhamed (2006),** and **Liu et al. (2008)** and formulated as follows:

$$R=\begin{bmatrix} \cos\beta\cos\gamma-\sin\gamma\sin\alpha\sin\beta & \sin\beta\cos\alpha & \sin\beta\cos\gamma+\sin\gamma\sin\alpha\cos\beta \\ -\cos\beta\sin\gamma-\sin\gamma\sin\alpha\sin\beta & \cos\alpha\cos\gamma & -\sin\beta\sin\gamma+\sin\alpha\cos\beta\cos\gamma \\ -\sin\beta\cos\alpha & -\sin\alpha & \cos\beta\cos\alpha \end{bmatrix} \qquad \textbf{[2-45]}$$

From the coplanar geometry between the 3D calibration points and the origin of their coordinate frame, the rigid body transformation can be reduced to the following:

$$\begin{bmatrix} x_c \\ y_c \\ z_c \end{bmatrix}=\begin{bmatrix} \cos\beta\cos\gamma-\sin\gamma\sin\alpha\sin\beta & \sin\beta\cos\alpha & t_x \\ -\cos\beta\sin\gamma-\sin\gamma\sin\alpha\sin\beta & \cos\alpha\cos\gamma & t_y \\ -\sin\beta\cos\alpha & -\sin\alpha & t_z \end{bmatrix}\begin{bmatrix} X_\omega \\ Y_\omega \\ 1 \end{bmatrix} \qquad \textbf{[2-46]}$$

To transform the camera coordinates to image pixel coordinates, it is necessary to incorporate a camera projection matrix into the transformation in **[2-46],** and the authors proposed the following structure of the matrix:

$$C=\begin{bmatrix} f_x & s & c_x \\ 0 & f_y & c_y \\ \kappa_1 & \kappa_2 & 1 \end{bmatrix} \qquad \textbf{[2-47]}$$

The parameters f_x and f_y are the estimates of the effective focal length in the x and y directions, respectively (**Bell et al., 2016**), and the coordinates (c_x, c_y) define the location of the principal point on the image plane. It can be observed that the first problem with the proposed calibration solution is the fact that the first two coefficients of radial distortion are components of the last row of the camera projective matrix, and this seems to have no geometric meaning since these parameters are assigned the role of scaling factors which is not how the radial distortion is applied on image coordinates. With the assumption of a planar calibration object set in a parallel orientation with reference to the image plane, the values of the Euler angles α and β can approach a zero value, respectively. From these simplifications, the authors reformulated the transformation in **[2-46]** as follows:

$$\begin{bmatrix} x_c \\ y_c \\ z_c \end{bmatrix} = \begin{bmatrix} \cos\gamma & \beta & t_x \\ -\sin\gamma & \cos\gamma & t_y \\ -\beta & -\alpha & t_z \end{bmatrix} \begin{bmatrix} X_\omega \\ Y_\omega \\ 1 \end{bmatrix} \quad \textbf{[2-48]}$$

From the similar triangle property, the undistorted image coordinates can be related to the camera coordinates in **[2-46]** through the following equations:

$$x_u = \frac{f_x x_c}{z_c} \quad \textbf{[2-49]}$$

$$y_u = \frac{f_y y_c}{z_c} \quad \textbf{[2-50]}$$

Assuming the coefficients of radial distortion and the aspect ratio in **[2-47]** are replaced by zeros to achieve the traditional structure of a camera projective matrix, transforming the undistorted coordinates in **[2-49]** and **[2-50]** to their respective image pixel coordinates can be done with the use of **[2-47]** as follows (**An et al., 2018**):

$$\lambda \begin{bmatrix} u \\ v \\ 1 \end{bmatrix} = \begin{bmatrix} f_x & 0 & c_x \\ 0 & f_y & c_y \\ 0 & 0 & 1 \end{bmatrix} \begin{bmatrix} f_x x_c z_c^{-1} \\ f_y y_c z_c^{-1} \\ 1 \end{bmatrix} \quad \textbf{[2-51]}$$

The parameter λ is the scale factor, the quantities (u, v) are the image coordinates in pixel units. From **[2-51],** the individual expressions of image pixel coordinates can be isolated as follows:

$$u = \frac{f_x x_c}{z_c} + c_x \quad \textbf{[2-52]}$$

$$v = \frac{f_y y_c}{z_c} + c_y \quad \textbf{[2-53]}$$

One problem with equations in **[2-52]** and **[2-53]** as formulated by the authors is that in the occurrence of the coordinates of the principal points c_x and c_y being equal to zero, these equations become equal to those in **[2-49]** and **[2-50],** which assume the conversion from world unit coordinates to the corresponding pixel measure is held by the coordinates of the principal point c_x and c_y , which does not hold true in projective geometry. The conversion generally relies on pixel width and length dimensions d_x and d_y respectively (**Narazaki et al., 2021; Xu et al., 2021**). Also, equating the effective focal lengths f_x and f_y to the distance from the camera projection centre to the image plane can lead to image projection errors as the normalized coordinates will not be coplanar, and this can be observed in the following formulations proposed by the authors:

$$x_n = \frac{u - c_x}{f_x} \qquad \textbf{[2-54]}$$

$$y_n = \frac{v - c_y}{f_y} \qquad \textbf{[2-55]}$$

Indeed, the above coordinates are not measurable on the same image plan. One strategy to improve the above formulations is to introduce the pixel dimensions d_x and d_y into equations **[2-54]** and **[2-55]** by decomposing the effective focal lengths in the x and y directions as ratios of pixel dimensions over the focal length f as follows:

$$f_x = f^{-1} d_x \qquad \textbf{[2-56]}$$

$$f_y = f^{-1} d_y \qquad \textbf{[2-57]}$$

Substituting **[2-56]** and **[2-57]** into **[2-54]** and **[2-55]** would lead to the correct formulation of the conversion from the image world unit to the image pixel unit. As a result of this correction, the normalized image point will correctly be projected on the image plane located at a distance f from the camera projection centre and this can be formulated as follows:

$$\begin{bmatrix} x_n \\ y_n \\ 1 \end{bmatrix} = \begin{bmatrix} a_x^{-1}\left(u - c_x\right) f^{-1} \\ a_y^{-1}\left(u - c_y\right) f^{-1} \\ 1 \end{bmatrix} \qquad \textbf{[2-58]}$$

The normalized image coordinates estimated through **[2-58]** now lie on the same normalized image plan. Up to this stage of the solution, none of the exterior orientation parameters have been estimated yet; thus, for this purpose, both sides of the equation **[2-48]** can be multiplied by the camera projective matrix in **[2-51]** produces the following after some rearrangements:

$$\begin{bmatrix} 1 & 0 & c_x \\ 0 & 1 & c_y \\ 0 & 0 & 1 \end{bmatrix} \begin{bmatrix} f_x & 0 & 0 \\ 0 & f_y & 0 \\ 0 & 0 & 1 \end{bmatrix} \begin{bmatrix} x_c \\ y_c \\ z_c \end{bmatrix} = \begin{bmatrix} f_x & 0 & c_x \\ 0 & f_y & c_y \\ 0 & 0 & 1 \end{bmatrix} \begin{bmatrix} \cos\gamma & \beta & t_x \\ -\sin\gamma & \cos\gamma & t_y \\ -\beta & -\alpha & t_z \end{bmatrix} \begin{bmatrix} X_\omega \\ Y_\omega \\ 1 \end{bmatrix} \qquad \textbf{[2-59]}$$

Expanding both sides of **[2-59]** leads to the following equations:

$$\frac{f_x x_c}{z_c} + c_x = f_x \frac{X_\omega \cos\gamma + \beta Y_\omega + t_x}{-\beta X_\omega - \alpha Y_\omega + t_z} \quad \textbf{[2-60]}$$

$$\frac{f_y y_c}{z_c} + c_y = f_y \frac{-X_\omega \sin\gamma + \cos\gamma Y_\omega + t_y}{-\beta X_\omega - \alpha Y_\omega + t_z} \quad \textbf{[2-61]}$$

It can be observed that the expressions on the left in **[2-60]** and **[2-61]** correspond to **[2-51]** and **[2-52],** and this allows to reformulate **[2-60]** and **[2-61]** as follows:

$$u = f_x \frac{X_\omega \cos\gamma + \beta Y_\omega + t_x}{-\beta X_\omega - \alpha Y_\omega + t_z} \quad \textbf{[2-62]}$$

$$v = f_y \frac{-X_\omega \sin\gamma + \cos\gamma Y_\omega + t_y}{-\beta X_\omega - \alpha Y_\omega + t_z} \quad \textbf{[2-63]}$$

In the original versions of **[2-62]** and **[2-63],** the authors possibly omitted unintentionally to disregard certain parameters and angles considering the geometrical advantage of the co-planarity constraint of 3D calibration points and the origin of their coordinate frame. However, this omission only has implications on numerical parameter estimates and not on the general solution strategy proposed. Linearizing the above equations leads to the following:

$$-u\alpha Y_\omega - u\beta X_\omega - f_x t_x + u t_z = f_x X_\omega \cos\gamma + f_x \beta Y_\omega \quad \textbf{[2-64]}$$

$$-v\alpha Y_\omega - v\beta X_\omega - f_y t_y + v t_z = f_y X_\omega \sin\gamma + f_y \cos\gamma Y_\omega \quad \textbf{[2-65]}$$

With more than five 3D calibration points and their undistorted projections, the authors proposed solving the parameters α, β and t_z through an absolutely determined system of equations. However, one issue with the above formulations is that the first and second parameters of the translation vector t_x, t_y and the Euler angle γ are not yet estimated at this stage; thus, a pre-processing of each of the above equations is required to eliminate these parameters and only retain t_z and this can easily be achieved with simple algebraic operations. Furthermore, equation **[2-64]** will provide a set of solutions for α, β, t_z and equation **[2-65]** will produce another set of solutions, and there were no clear insights on how the optimal estimates of these parameters were selected from the multiple roots. In order to recover the initial estimates for the parameters γ, t_x, t_y both sides of **[2-49]** and **[2-50]** can be multiplied by the quartic expression of the radial distortion polynomial, which then leads to the following equations:

$$x_u \left(\kappa_1 r^2 + \kappa_2 r^4\right) = \frac{f_x x_c}{z_c}\left(\kappa_1 r^2 + \kappa_2 r^4\right) \quad \textbf{[2-66]}$$

$$y_u\left(\kappa_1 r^2+\kappa_2 r^4\right)=\frac{f_y y_c}{z_c}\left(\kappa_1 r^2+\kappa_2 r^4\right) \quad \textbf{[2-67]}$$

The above can be reformulated as follows:

$$x_d=f_x\frac{X_\omega\cos\gamma+\beta Y_\omega+t_x}{-\beta X_\omega-\alpha Y_\omega+t_z}\left(\kappa_1 r^2+\kappa_2 r^4\right) \quad \textbf{[2-68]}$$

$$y_d=f_y\frac{-X_\omega\sin\gamma+\cos\gamma Y_\omega+t_y}{-\beta X_\omega-\alpha Y_\omega+t_z}\left(\kappa_1 r^2+\kappa_2 r^4\right) \quad \textbf{[2-69]}$$

Applying the radial alignment constraint using **[2-68]** and **[2-69]** produces the following equation:

$$\frac{x_d}{y_d}=\frac{f_x}{f_y}\frac{\left(X_\omega\cos\gamma+\beta Y_\omega+t_x\right)}{\left(-X_\omega\sin\gamma+\cos\gamma Y_\omega+t_y\right)} \quad \textbf{[2-70]}$$

It can be observed that the effective focal lengths are still not estimated, and this makes challenging the extraction of γ , t_x , t_y . To address the challenge, the authors seem to have attributed equal value to the parameters f_x and f_y to simplify the expansion of **[2-70].** Extracting the parameter t_x as a factor from the numerator and denominator in **[2-70]** leads to the following after simplification:

$$\frac{x_d}{y_d}=\frac{X_\omega\dfrac{\cos\gamma}{t_x}+\dfrac{\beta}{t_x}Y_\omega+1}{\left(-X_\omega\dfrac{\sin\gamma}{t_x}+\dfrac{\cos\gamma}{t_x}Y_\omega+\dfrac{t_y}{t_x}\right)} \quad \textbf{[2-71]}$$

Expanding **[2-71]** leads to the following:

$$\left(-x_d X_\omega\right)\frac{\sin\gamma}{t_x}+\left(x_d Y_\omega-y_d X_\omega\right)\frac{\cos\gamma}{t_x}+\left(x_d\right)\frac{t_y}{t_x}-\frac{\beta y_d Y_\omega}{t_x}=y_d \quad \textbf{[2-72]}$$

From the constraint that $\beta\approx-0$ the equation **[2-72]** can be reformulated as follows:

$$\left(-x_d X_\omega\right)\frac{\sin\gamma}{t_x}+\left(x_d Y_\omega-y_d X_\omega\right)\frac{\cos\gamma}{t_x}+\left(x_d\right)\frac{t_y}{t_x}=y_d \quad \textbf{[2-73]}$$

Formulating **[2-73]** in a matrix form leads to the following:

$$\begin{bmatrix} -x_d X_\omega & x_d Y_\omega - y_d X_\omega & x_d \end{bmatrix}^T \begin{bmatrix} \frac{\sin\gamma}{t_x} \\ \frac{\cos\gamma}{t_x} \\ \frac{t_y}{t_x} \end{bmatrix} = y_d \qquad \textbf{[2-74]}$$

To solve the parameters in the numerators and denominators of the column vector in **[2-74],** the authors suggested three-variable linear least squares solution. The first challenge with the solution is the parameter coupling that may introduce numerical errors. In case any error occurs when estimating t_x ,the error will propagate to $\sin\gamma$ and $\cos\gamma$. The second problem is that all variables in numerators and denominators in the column vector are unknown, and the least squares solution will only provide numerical estimates of these ratios, and the challenge to separate them will remain, as in reality, the system has four unknown parameters, which are t_x , t_y , $\cos\gamma$ and $\sin\gamma$. One solution that can be suggested to the authors is to formulate a fourth equation that would enable them to express the parameter t_y as a function t_x . However, this would require defining a vector $A = \begin{bmatrix} a_1 & a_2 & a_3 \end{bmatrix}$ that would relate the elements of the row vector and those of the column vector in **[2-74]** as follows:

$$\begin{bmatrix} -x_d X_\omega & 0 & 0 \\ 0 & x_d Y_\omega - y_d X_\omega & 0 \\ 0 & 0 & x_d \end{bmatrix} \begin{bmatrix} \frac{\sin\gamma}{t_x} \\ \frac{\cos\gamma}{t_x} \\ \frac{t_y}{t_x} \end{bmatrix} = \begin{bmatrix} a_1 \\ a_2 \\ a_3 \end{bmatrix} \qquad \textbf{[2-75]}$$

From **[2-75],** once t_y is estimated as a function of t_x , with coefficients of the column vector A already known, the expressions of $\sin\gamma$ and $\cos\gamma$ can be simplified as follows:

$$\sin\gamma = \frac{-a_1}{x_d X_\omega t_x} \qquad \textbf{[2-76]}$$

$$\cos\gamma = \frac{a_2}{t_x \left(x_d Y_\omega - y_d X_\omega \right)} \qquad \textbf{[2-77]}$$

Instead of estimating individual values of γ through **[2-76]** and **[2-77]** and then taking the average, the optimal estimate of the angles can be extracted from the tangent function as follows :

$$\tan\gamma = \frac{-a_1 \left(x_d Y_\omega - y_d X_\omega \right)}{a_2 x_d X_\omega} \qquad \textbf{[2-78]}$$

Once $\kappa_1, \kappa_2, \alpha, \beta, \gamma, t_x, t_y, t_z$ are estimated, the remaining parameters c_x, c_y, f_x, f_y and the scale factor S can be recovered through a nonlinear optimization process that estimates the maximum likelihood of parameters by minimizing the distance between distorted points and their distortion-free counterparts as follows:

$$\min \sum_{i}^{m} \sum_{j}^{n} \left\| m_{ij} - \hat{m}\left(A, R_i, T_i, M_j\right) \right\|^2 \qquad \textbf{[2-79]}$$

The iteration of the minimization of **[2-79]** was performed using the Levenberg-Marquardt algorithm. Since optimization solutions for camera calibration require good initial estimates of the camera's intrinsic and extrinsic parameters, which are very difficult to obtain, it becomes clear that analytical solutions to the problem of accurate calibration of camera pose in a 3D scene are needed.

2.3.5. Ganapathy's Camera Parameters Modelling

Analytical solutions to the camera pose problem generally involve the derivation of non-linear equations that need to be solved to extract the various camera parameters embedded within their coefficients, and solving such equations has been reported to be very difficult (**Ganapathy, 1984**; **Henrichsen, 2000**). When recovering the elements describing the orientation and location of the camera in the 3D scene, most of the camera's intrinsic parameters should be separated from the main matrix. To achieve this, one solution would require developing reverse perspective models that map from the image plane to the 3D scene. One of the few attempts to offer analytical solutions to the camera calibration pose problem was earlier proposed by **Ganapathy (1984).** The author presented a camera projective matrix derived from similar triangle properties. However, one particularity of the proposed camera matrix in contrast to the traditional Euler rotations is that the camera coordinate frames Y_C axis is aligned with the world Z_ω axis in the last rotation. From this geometry, the relationship between the 3D camera coordinates and the image pixel coordinates is formulated as follows:

$$u = f\frac{a_u x_c}{y_c} + u_0 \qquad \textbf{[2-80]}$$

$$v = f\frac{a_v z_c}{y_c} + v_0 \qquad \textbf{[2-81]}$$

By posing: $fa_u = f_u$ and $fa_v = f_v$ the expressions **[2-80]** and **[2-81]** can be simplified as follows:

$$u = f_u\frac{x_c}{y_c} + u_0 \qquad \textbf{[2-82]}$$

$$v = f_v\frac{z_c}{y_c} + v_0 \qquad \textbf{[2-83]}$$

Where f_u and f_v represent the effective focal lengths in the x and y directions and u_0, v_0 are the coordinates of the origin of the image pixel coordinate frame. Equations **[2-82]** and **[2-83]** enable us to formulate the camera projective matrix as follows:

$$C = \begin{bmatrix} f_u & u_0 & 0 & 0 \\ 0 & v_0 & f_v & 0 \\ 0 & 1 & 0 & 0 \end{bmatrix} \quad \textbf{[2-84]}$$

The advantage of the formulation **[2-84]** over those in **[2-82]** and **[2-83]** is that it allows the reader to notice that the intrinsic parameters cannot be solved using QR decomposition methods because the matrix is not upper triangular. The relationship between the 3D camera coordinates and their 3D world counterparts is established through a rigid body transformation matrix. The first component of the rigid body transformation is a 4×4 displacement matrix formulated by the author as follows:

$$D = \begin{bmatrix} 1 & 0 & 0 & -X_0 \\ 0 & 1 & 0 & -Y_0 \\ 0 & 0 & 1 & -Z_0 \\ 0 & 0 & 0 & 1 \end{bmatrix} \quad \textbf{[2-85]}$$

Where X_0 , Y_0 and Z_0 define the camera location in 3D space and are related to the parameters of the translation vector $\begin{bmatrix} t_x & t_y & t_z \end{bmatrix}^T$. Once the origin of the camera and world coordinate frames' have been aligned through **[2-85],** a rotation is performed. The primary rotation modifies the orientation of the camera $X_C - Y_C$ plane by an angle θ around its Z_C axis. The results are two new camera axes X_{2C}, Y_{2C} and a new $Y_{2C} - Z_C$ plane. In contrast to the traditional Euler rotation sequence, the newly created $Y_{2C} - Z_C$ plane is rotated around the new X_{2C} axis by an angle ϕ. From the above, it can be observed that the camera Y_C has been involved in both previous rotations. It can be argued that these two first rotations aimed at aligning the 3D camera coordinate frame's Y_C axis with the 3D world coordinate frame's Z_ω axis. With the camera Y_C axis aligned with the world Z_ω axis, a swing rotation of the camera's new $Z_{2C} - X_{2C}$ plane around the new Y_{2C} axis is performed by an angle ψ . To formulate the rotation matrix R of the rigid body transformation, the resulting matrix from the rotation around the camera Y_C axis is multiplied by the resulting matrix from the rotation around the camera X_{2C} axis, and then the matrix product is multiplied by the resulting matrix from the swing rotation around the Z_{2C} axis. The resulting matrix proposed by the author is formulated as follows:

$$R = R_3 \times R_2 \times R_1 = \begin{bmatrix} \cos\theta\cos\psi - \sin\theta\sin\psi\sin\phi & \sin\theta\cos\psi + \cos\theta\sin\psi\sin\phi & -\cos\phi\sin\psi & 0 \\ -\sin\theta\cos\phi & \cos\theta\cos\phi & \sin\phi & 0 \\ \cos\theta\sin\psi + \sin\phi\cos\psi\sin\theta & \sin\theta\sin\psi - \cos\theta\sin\phi\cos\psi & \cos\phi\cos\psi & 0 \\ 0 & 0 & 0 & 1 \end{bmatrix} \quad \textbf{[2-86]}$$

The three angles ψ, ϕ, θ define the orientation of the camera coordinate frame axes around those of a fixed 3D world coordinate frame. Adding the coefficients of the translation vector in the last column results in a rigid body transformation matrix that accounts for homogeneous coordinates and is formulated as follows:

$$M = \begin{bmatrix} \cos\theta\cos\psi - \sin\theta\sin\psi\sin\phi & \sin\theta\cos\psi + \cos\theta\sin\psi\sin\phi & -\cos\phi\sin\psi & t_x \\ -\sin\theta\cos\phi & \cos\theta\cos\phi & \sin\phi & t_y \\ \cos\theta\sin\psi + \sin\phi\cos\psi\sin\theta & \sin\theta\sin\psi - \cos\theta\sin\phi\cos\psi & \cos\phi\cos\psi & t_z \\ 0 & 0 & 0 & 1 \end{bmatrix} \quad \textbf{[2-87]}$$

Let's simplify the matrix M in **[2-87]** as follows:

$$M = \begin{bmatrix} r_{11} & r_{12} & r_{13} & t_x \\ r_{21} & r_{22} & r_{23} & t_y \\ r_{31} & r_{32} & r_{33} & t_z \\ 0 & 0 & 0 & 1 \end{bmatrix} \quad \textbf{[2-88]}$$

Multiplying the camera projective matrix in **[2-84]** by **[2-88]** leads to the following simplified formulation of the transformation matrix from 3D world points to 2D image pixel points:

$$P = \begin{bmatrix} f_u r_{11} + u_0 r_{21} & f_u r_{12} + u_0 r_{22} & f_u r_{13} + u_0 r_{23} & f_u t_x + u_0 t_y \\ f_v r_{31} + v_0 r_{21} & f_v r_{32} + v_0 r_{22} & f_v r_{33} + v_0 r_{23} & f_v t_z + v_0 t_y \\ r_{21} & r_{22} & r_{23} & t_y \end{bmatrix} \quad \textbf{[2-89]}$$

To estimate each coefficient of P ,the author proposed a decomposition of **[2-89]** in order to calibrate the following 16 parameters: $f_u, f_v, r_{11}, r_{21}, u_0, r_{31}, v_0, r_{12}, r_{22}, r_{32}, r_{13}, r_{23}, r_{33}, t_x, t_y, t_z$.

However, before decomposition, let's denote $C = \begin{bmatrix} c_{11} & c_{12} & c_{13} & c_{14} \\ c_{21} & c_{22} & c_{23} & c_{24} \\ c_{31} & c_{32} & c_{33} & c_{34} \\ 0 & 0 & 0 & 1 \end{bmatrix}$ an experimentally computed projective transformation matrix estimated through direct linear transform as proposed in Tsai **(1987).** Equating cell by cell P and C, leads to the following nonlinear equations:

$$c_{11} = f_u r_{11} + u_0 r_{21} \; ; \; c_{12} = f_u r_{12} + u_0 r_{22} \; ; c_{13} = f_u r_{13} + u_0 r_{23} \; ; c_{14} = f_u t_x + u_0 t_y \quad \textbf{[2-90.1]}$$

$$c_{21} = f_v r_{31} + v_0 r_{21}; \; c_{22} = f_v r_{32} + v_0 r_{22} \; ; c_{23} = f_v r_{33} + v_0 r_{23} \; ; c_{24} = f_v t_z + v_0 t_y \quad \textbf{[2-90.2]}$$

$$c_{31} = r_{21}; \;\; c_{32} = r_{22} \; ; \; c_{33} = r_{23} \; ; \;\; c_{34} = t_y \quad \textbf{[2-90.3]}$$

Substituting the parameters in **[2-87]** into the twelve equations in **[2-90.1]- [2-90.3]** leads to the following decomposition:

$$c_{11} = f_u\left(\cos\theta\cos\psi - \sin\theta\sin\psi\sin\phi\right) - u_0\left(\sin\theta\cos\phi\right) \quad \textbf{[2-91.1]}$$

$$c_{12} = f_u\left(\sin\theta\cos\psi + \cos\theta\sin\psi\sin\phi\right) + u_0\left(\cos\theta\cos\phi\right) \quad \textbf{[2-91.2]}$$

$$c_{13} = f_u\left(-\cos\phi\sin\psi\right) + u_0\left(\sin\phi\right) \quad \textbf{[2-91.3]}$$

$$c_{14} = t_x f_u + u_0 t_y \quad \textbf{[2-91.4]}$$

$$c_{21} = f_v\left(\cos\theta\sin\psi + \sin\phi\cos\psi\sin\theta\right) - v_0\left(\sin\theta\cos\phi\right) \quad \textbf{[2-91.5]}$$

$$c_{22} = f_v\left(\sin\theta\sin\psi - \cos\theta\sin\phi\cos\psi\right) + v_0\left(\cos\theta\cos\phi\right) \quad \textbf{[2-91.6]}$$

$$c_{23} = f_v\left(\cos\phi\cos\psi\right) + v_0\left(\sin\phi\right) \quad \textbf{[2-91.7]}$$

$$c_{24} = f_v t_z + v_0 t_y \quad \textbf{[2-91.8]}$$

$$c_{31} = -\sin\theta\cos\phi \quad \textbf{[2-91.9]}$$

$$c_{32} = \cos\theta\cos\phi \quad \textbf{[2-91.10]}$$

$$c_{33} = \sin\phi \quad \textbf{[2-91.11]}$$

$$c_{34} = t_y \quad \textbf{[2-91.12]}$$

To simplify the solutions of the above respective equations, **Ganapathy (1984)** suggested a scaling of each element of the matrix in **[2-89]** by the coefficient t_y^{-1}. The above author argued that this does not change the numerical outcome of the transformation as long as the point being transformed has its coordinates formulated in a homogeneous coordinate form. However, earlier, **Faugeras and Toscani (1986)** reported that proceeding as such would lead to absurd solutions since camera intrinsic parameters, depend on the geometry of 3D world points. This study aligns with that opinion since a QR decomposition solution of the scaled transformation matrix in **[2-89]** will lead to a camera projective matrix with coefficients not estimated from the concatenation of 3D world points and their corresponding 2D image point coordinates. This will result in the integrity of the original coefficients of the matrix being altered by the scaling process. Furthermore, the other challenge with the scaling process is that the equality between matrices P and c no longer holds true unless all elements c_{11}, c_{12}, c_{33} of the matrix c are also scaled by the coefficient c_{34}. For the remaining analysis of this camera calibration solution, it is assumed that the coefficients of the matrix c were not scaled by c_{34} as supported by the author in his publication. From the proposed scaling strategy, the following expressions were considered by the author:

$$c_{31} = \frac{r_{21}}{t_y} \quad \textbf{[2-92.1]}$$

$$c_{32} = \frac{r_{22}}{t_y} \quad \textbf{[2-92.2]}$$

$$c_{33} = \frac{r_{23}}{t_y} \quad \textbf{[2-92.3]}$$

Squaring both sides of **[2-92.1] – [2-91.3]** then adding the three equations leads to the following:

$$t_y^2\left(c_{31}^2 + c_{32}^2 + c_{33}^2\right) = r_{21}^2 + r_{22}^2 + r_{23}^2 \quad \textbf{[2-93]}$$

Using the orthonormal property of the axes of a rotation matrix, the second coefficient of the translation vector t_y can be isolated from **[2-93]** as follows when only considering the positive value:

$$t_y = \frac{\sqrt{c_{31}^2 + c_{32}^2 + c_{33}^2}}{c_{31}^2 + c_{32}^2 + c_{33}^2} \quad \textbf{[2-94]}$$

For more insight on the demonstration of the positive sign of t_y the reader is directed to the appendix A of the author's original paper. However, the weakness of the provided solution in **[2-94]** is its lack of uniqueness; the formulation does not consider the constraints c_{14} and c_{24} from which two more distinct values of t_y can be estimated. From **[2-94],** the coefficients of the

second row of the rotation matrix in **[2-87]** and involved in equations **[2-92.1]–[2-92.3]** can be retrieved as follows:

$$r_{21} = \frac{c_{31}\sqrt{c_{31}^2 + c_{32}^2 + c_{33}^2}}{c_{31}^2 + c_{32}^2 + c_{33}^2} \quad \textbf{[2-95.1]}$$

$$r_{22} = \frac{c_{32}\sqrt{c_{31}^2 + c_{32}^2 + c_{33}^2}}{c_{31}^2 + c_{32}^2 + c_{33}^2} \quad \textbf{[2-95.2]}$$

$$r_{23} = \frac{c_{33}\sqrt{c_{31}^2 + c_{32}^2 + c_{33}^2}}{c_{31}^2 + c_{32}^2 + c_{33}^2} \quad \textbf{[2-95.3]}$$

It can be observed that any inaccuracy associated with the calibration of the second coefficient of the translation vector t_y would spread through the parameters r_{21}, r_{22}, and r_{23}.

Let ρ_1, ρ_2 and ρ_3 be the resulting expressions when respectively multiplying both sides of **[2-95.1], [2-95.2]** and **[2-95.3]** by t_y^2 and formulated as follows:

$$\rho_1 = -\frac{\sin\theta\cos\phi}{t_y} t_y^2 \quad \textbf{[2-96.1]}$$

$$\rho_2 = \frac{\cos\theta\cos\phi}{t_y} t_y^2 \quad \textbf{[2-96.2]}$$

$$\rho_3 = \frac{\sin\phi}{t_y} t_y^2 \quad \textbf{[2-96.3]}$$

Let δ_1 be the expression obtained after multiplying both sides of **[2-96-2]** by c_{11} and δ_2 the expressions obtained after multiplying both sides of **[2-96.1]** by c_{12} and formulated as follows:

$$\delta_1 = \frac{\cos\theta\cos\phi}{t_y} t_y^2 \times \frac{f_u\left(\cos\theta\cos\psi - \sin\theta\sin\psi\sin\phi\right) - u_0\left(\sin\theta\cos\phi\right)}{t_y} \quad \textbf{[2-97.1]}$$

$$\delta_2 = -\frac{\sin\theta\cos\phi}{t_y} t_y^2 \times \frac{f_u\left(\sin\theta\cos\psi + \cos\theta\sin\psi\sin\phi\right) + u_0\left(\cos\theta\cos\phi\right)}{t_y} \quad \textbf{[2-97.2]}$$

Let ∂_1 be a quantity obtained after subtracting **[2-97.2]** from **[2-97.1]** and reduced as follows:

$$\partial_1 = \delta_1 - \delta_2 = f_u\cos\phi\cos\psi\cos\theta\times\cos\theta + f_u\cos\phi\cos\psi\sin\theta\times\sin\theta \quad \textbf{[2-98]}$$

After some factorization and simplification, the following equation is obtained:

$$\partial_1 = f_u\cos\phi\cos\psi\left(\cos\theta^2 + \sin\theta^2\right) = f_u\cos\phi\cos\psi \quad \textbf{[2-99]}$$

Let δ_3 be the expression obtained after multiplying **[2-96.3]** by c_{12}, and δ_4 be the expression obtained after multiplying **[2-96.2]** by c_{13} and formulated as follows:

$$\delta_3 = \frac{\sin\phi}{t_y} t_y^2 \times \frac{f_u\left(\sin\theta\cos\psi + \cos\theta\sin\psi\sin\phi\right) + u_0\left(\cos\theta\cos\phi\right)}{t_y} \quad \textbf{[2-100.1]}$$

$$\delta_4 = \frac{\cos\theta\cos\phi}{t_y} t_y^2 \times \frac{f_u\left(-\cos\phi\sin\psi\right) + u_0\left(\sin\phi\right)}{t_y} \quad \textbf{[2-100.2]}$$

Let ∂_2 be the result of subtracting **[2-100.1]** from **[2-100.2]** and estimated as follows:

$$\partial_2 = f_u \sin\phi\sin\theta\cos\psi + f_u\cos\theta\sin\psi = f_u\left(\sin\phi\sin\theta\cos\psi + \cos\theta\sin\psi\right) \quad \textbf{[2-101]}$$

Let δ_5 be the result of the multiplication of **[2-96.1]** by c_{13} and δ_6 be the result of the multiplication of **[2-96.2]** by c_{11} and formulated as follows:

$$\delta_5 = f_u\cos\phi^2\sin\theta\sin\psi - \sin\theta\cos\phi\left(\sin\phi\right)u_0 \quad \textbf{[2-102.1]}$$

$$\delta_6 = f_u\sin\phi\cos\theta\cos\psi - f_u\sin\phi^2\sin\theta\sin\psi - u_0\sin\phi\cos\phi\sin\theta \quad \textbf{[2-102.2]}$$

Subtracting **[2-102.2]** from **[2-102.1]** produced the quantity ∂_3 formulated as follows:

$$\partial_3 = f_u\left(\sin\theta\sin\psi - \sin\phi\cos\theta\cos\psi\right) \quad \textbf{[2-103]}$$

Squaring both sides of **[2-99], [2-101]** and **[2-103]** leads to the following:

$$\partial_1^2 + \partial_2^2 + \partial_3^2 = f_u^2\cos\psi^2 + f_u{}^2\sin\psi^2 = f_u{}^2 \quad \textbf{[2-104]}$$

From **[2-104]** the first effective focal length can be extracted as follows:

$$f_u = \pm\sqrt{\partial_1^2 + \partial_2^2 + \partial_3^2} \quad \textbf{[2-105]}$$

From **[2-80]** and **[2-81],** the value to consider is the positive estimate. However, it can be observed from **[2-91.1]–[2-91.2]** that only the first three constraints were considered in estimating the parameter f_u; neglecting the last constraint may weaken the accuracy of its numerical value. Moreover, knowing the estimate of f_u enables us to recover the trigonometric expressions in **[2-99], [2-101],** and **[2-103],** but not the three Euler rotation angles. With knowledge of r_{31}, r_{32}, r_{33} which are the trigonometric parts of **[2-101], [2-103],** and **[2-99],** respectively, there is ground to estimate the parameters f_v and v_0 . Assuming that among equations **[2-91.5]–[2-91.7]** one is redundant, the author suggested the solution of the parameters f_v and v_0 through a system of two linear equations. From this assumption, one first concern arises from the lack of clarity to determine which among the selected equations, is not the redundant formulation of the others. The second concern is that an observation of equations **[2-91.1] – [2-91.12]** reveals that the constraint in equation **[2-91.8]** was not considered when formulating the solutions of the parameters f_v and v_0 . This may result in their values not being representative of the correct internal geometry of the camera.

With r_{21}, r_{22}, r_{23} recuperated from **[2-95.1]- [2-95.3]** after the estimation of the parameter t_y and the parameters r_{31}, r_{32}, r_{33} recovered from **[2-101], [2-103], [2-99]** and after estimating f_u , the remaining parameters of the rotation matrix r_{11}, r_{12}, r_{13} can be recovered using the properties of the determinant of an orthogonal matrix in **[2-87]** and formulated as follows:

$$r_{11} = r_{22}\times r_{33} - r_{23}\times r_{32} \quad \textbf{[2-106.1]}$$

$$r_{12} = r_{21}\times r_{33} - r_{23}\times r_{31} \quad \textbf{[2-106.2]}$$

$$r_{13} = r_{21}r_{32} - r_{22}\times r_{31} \quad \textbf{[2.106.3]}$$

With all the parameters of the rotation matrix estimated, the author proposed estimating the first coordinate of the principal point in pixel u_0 using equation **[2-91.1]**. The weakness with this proposed strategy is that there are four nonlinear constraints that the coordinate must satisfy in **[2-91.1–[2-91.4]** and considering only one or a subset of them would undermine the accuracy of the numerical estimate of this parameter. Moreover, from the estimated coordinate u_0 and the first effective focal length estimated in **[2-105],** the suggestion was made by the author to compute the first parameter of the translation vector t_x through equation **[2-91.4].** As pointed out in the earlier analysis, due to the parameter coupling, which is a major challenge in camera calibration, the numerical errors associated with the parameters t_y, f_u and u_0 will compromise the accuracy of this translation coefficient. In a similar manner, substituting the previously estimated principal point coordinate v_0 and the second effective focal length f_v into equation **[2-91.8]** will result in a compromised numerical estimate of the last coefficient of the translation vector t_z.

The recovery of the value of the Euler angle ϕ is possible from equation **[2-91.11]** as follows:

$$\phi = \sin^{-1}\left(c_{33}\right) \qquad \textbf{[2-107.1]}$$

Although the estimate in **[2-107.1]** is correct, it is not in line with the projective transformation matrix normalization suggested by the author. Under such circumstances, the solution in **[2-107-1]** would be formulated as follows:

$$\phi = \sin^{-1}\left(t_y c_{33}\right) \qquad \textbf{[2-107.2]}$$

As it can be observed, the angular estimate would be influenced by the accuracy of the parameter t_y. From **[2-91.9]** and **[2-91.10]** the angle θ can be recuperated through the tangent function as follows:

$$\theta = \tan^{-1}\left(-\frac{c_{31}}{c_{32}}\right) \qquad \textbf{[2-107.3]}$$

Since the quantities r_{13} and r_{33} have been estimated through **[2-106.3]** and **[2-99],** the remaining angle can be estimated as follows:

$$\psi = \tan^{-1}\left(-\frac{r_{13}}{r_{33}}\right) \qquad \textbf{[2-107.4]}$$

The estimates in **[2-107.3]** and **[2-107.4]** are not affected by the parameter t_y even when considering the scaling of the transformation matrix because the second coefficient of the translation vector is cancelled through the ratio formulations as both the numerator and denominator in both cases are scaled by the same parameter t_y. With the three coefficients of the translation vector estimated and the nine coefficients of the rotation matrix computed, the parameters X_0, Y_0, Z_0 in **[2-85]** defining the camera location can easily be recuperated by simple arithmetic operations.

2.3.6. Variants of Ganapathy's camera parameters modelling

Roumie et al. (2018) and **Kim et al. (2023)** proposed two variations of the calibration strategy proposed in **Ganapathy (1984)**. To calibrate the third coefficient of the translation vector t_z and

the three coefficients of the last row of the rotation matrix r_{31}, r_{32} and r_{33}, the strategies employed modified algorithms proposed by **Ganapathy (1984)** in **[2-94], [2-95-1]-[2-95.3]** as follows:

$$t_z = \frac{1}{\sqrt{c_9^2 + c_{10}^2 + c_{11}^2}} \quad \textbf{[2-108.1]}$$

$$r_{31} = \frac{c_{31}}{\sqrt{c_9^2 + c_{10}^2 + c_{11}^2}} \quad \textbf{[2-108.2]}$$

$$r_{32} = \frac{c_{32}}{\sqrt{c_9^2 + c_{10}^2 + c_{11}^2}} \quad \textbf{[2-108.3]}$$

$$r_{33} = \frac{c_{33}}{\sqrt{c_9^2 + c_{10}^2 + c_{11}^2}} \quad \textbf{[2-108.4]}$$

The approach described in **Kim et al. (2023)** associated a negative sign to the quantity on the right side of the equality sign in **[2-108.1],** while that proposed in **Roumie et al. (2018)** maintained a positive sign for this quantity. The first differences between the strategy proposed by **Ganapathy (1984)** and those proposed in **Roumie et al. (2018)** and **Kim et al. (2023)** were found in the algorithms proposed to calibrate the first effective focal length f_u. The strategy proposed in **Roumie et al. (2018)** to retrieve this coefficient first calculates the norm of the vector product between the first and third rows of the projective transformation matrix and then scales the result by the product of the coefficient t_z and the cosine of the angle between the x and y axes of the image coordinate system as follows:

$$f_u = \sin\varepsilon \times \frac{\left(c_{11} \times c_{31} + c_{12} \times c_{32} + c_{13} \times c_{33}\right)}{c_{31}^2 + c_{32}^2 + c_{33}^2} \quad \textbf{[2-108.5]}$$

Where ε, is the angle between the image x and y axes. Although the proposed algorithm mostly contains coefficients of the projective transformation matrix, the presence of the parameter $\sin\varepsilon$ in the model may introduce some numerical instabilities if the algorithms proposed to recover the coefficients of the first rows of the rotation matrix failed to produce optimal estimates of these coefficients. In such occurrences, this would result in a non-orthonormal rotation matrix. In contrast, the methodology proposed by **Kim et al. (2023)** computes this coefficient of the translation vector as the horizontal distance between the principal point's u_0 coordinate and the quantity obtained when squaring the coefficients c_{11}, c_{12}, c_{13} of the projective transformation matrix and then scaling the result by the coefficient of the translation vector t_z as follows:

$$f_u = \sqrt{\frac{\left(c_{11}^2 + c_{12}^2 + c_{13}^2\right) - \left(c_{11} \times c_{31} + c_{12}c_{32} + c_{13} \times c_{33}\right)}{c_{31}^2 + c_{32}^2 + c_{33}^2}} \quad \textbf{[2-108.6]}$$

The limitation with the above proposed algorithm is that it imposes numerical constraints on the coefficients r_{31}, r_{32} and r_{33} because if two of these coefficients are greater than c_{11}, c_{12} and c_{13}, respectively, the algorithm would not hold true.

The calibration strategy proposed by **Ganapathy (1984)** to calibrate the second coefficient of the principal point v_0 also exposed some differences with the models proposed in **Roumie et al. (2018)** and **Kim et al. (2023). Roumie et al. (2018)** and **Kim et al. (2023)** proposed a straight-

forward formulation of the model that relies solely on the coefficients of the second and third rows of the projective transformation matrix as follows:

$$v_0 = \frac{c_{21} \times c_{31} + c_{22} \times c_{32} + c_{23} \times c_{33}}{c_{31}^2 + c_{32}^2 + c_{33}^2} \quad \textbf{[2-108.7]}$$

The strength of the above-proposed algorithm is that it does not involve any parameter coupling or sign ambiguity, in contrast to the algorithm used in **Ganapathy (1984).** Furthermore**,** the formulation algorithms proposed by each of the three calibration strategies to calibrate the second effective focal length f_v were also suffering from numerical instabilities. For instance, the approach proposed in **Roumie et al. (2018)** did not consider the geometric constraints of this effective focal length as described in equations **[2-91.5]-[2-91.8].** Instead, the authors computed a ratio of the product between the pixel dimension in the y direction and the focal length divided by the sinus of the angle between the image x and y axes as follows:

$$f_v = \frac{a_x f}{\sin \varepsilon} \quad \textbf{[2-108.8]}$$

It can be observed that the algorithm in [2-10.8] did not consider any geometric constraints describing this effective focal length in **[2-91.4]-[2-91.8].** Since the orthonormality of the rotation matrix depends on the nine coefficients of this matrix, any suboptimal estimate associated with any of these nine coefficients would result in the measure of the angle ε being smaller or greater than its optimal measure of 90^0. This would result in the parameter f_v not reaching its optimal magnitude.

In contrast, the calibration strategy proposed in **Kim et al. (2023)** recovers this interior orientation coefficient by subtracting the quantity estimated in **[2-108.7]** from the norm of the vector representing the second row of the projective transformation matrix scaled by the third coefficient of the translation vector t_z as follows:

$$f_v = \sqrt{\frac{\left(c_{21}^2 + c_{22}^2 + c_{23}^2\right) - \left(c_{21}c_{31} + c_{22}c_{32} + c_{23}c_{33}\right)}{c_{31}^2 + c_{32}^2 + c_{33}^2}} \quad \textbf{[2-108.9]}$$

One limitation with the above-proposed algorithm is that it restricts the numerical magnitudes of coefficients c_{31}, c_{32} and c_{33} to fall within certain ranges. Indeed, if any two of these coefficients are larger than c_{21}, c_{22} and c_{23} the expression will result in numerical instability since the numerator of the algorithm must be equal to or greater than zero. These numerical range restrictions are also applied to the coefficients of the rotation matrix r_{31}, r_{32} and r_{33} which are directly related to the coefficients c_{31}, c_{32} and c_{33} through equations **[2-108.2]-[2-108.4]**.

The analytical calibration of the three coefficients of the rotation matrix r_{21}, r_{22} and r_{23} exposed further limitations in the strategies proposed in **Roumie et al. (2018)** and **Kim et al. (2023)**. **Roumie et al. (2018)** associated each calibration algorithm with the sinus of the angle between the image coordinate system's x and y axis as follows:

$$r_{21} = \frac{r_{31}\left(t_z^2\right)\sin \varepsilon}{a_x f} \quad \textbf{[2-108.10]}$$

$$r_{22} = \frac{r_{32}\left(t_z^2\right)\sin\varepsilon}{a_x f} \quad \textbf{[2-108-11]}$$

$$r_{23} = \frac{r_{33}\left(t_z^2\right)\sin\varepsilon}{a_x f} \quad \textbf{[2-108.12]}$$

Although the pixel dimensions and the focal length are constant measures, the above-proposed calibration algorithms suffer from parameter coupling. Any numerical inaccuracies associated with the three coefficients of the last row of the rotation matrix in **[2-108.2]-[2-108.4]** or any inaccurate calibration of the coefficients r_{11}, r_{12} and r_{13} would result in a non-orthonormal rotation matrix with the angle ε achieving a suboptimal measure. In the same way, the calibration models proposed in **Kim et al. (2023)** to estimate these three coefficients also rely on the three parameters r_{31}, r_{32} and r_{33}, in addition to the coefficients of the second row of the projective transformation matrix c_{21}, c_{22}, c_{23} as well as the second effective focal length f_v and the second coordinate of the principal point u_0, as follows:

$$r_{21} = \frac{c_{21} - v_0 r_{31}}{f_v} \quad \textbf{[2-108.13]}$$

$$r_{22} = \frac{c_{22} - v_0 r_{32}}{f_v} \quad \textbf{[2-108.14]}$$

$$r_{23} = \frac{c_{23} - v_0 r_{33}}{f_v} \quad \textbf{[2-108.15]}$$

From **[2-108.9],** it can be argued that the calibration algorithm of the parameter f_v is prone to parameter coupling errors. In addition, the algorithms to calibrate the coefficients of the translation vectors t_x, t_y were found to be similar to those proposed by **Ganapathy (1984)** in **[2-91.4]** and **[2-91.8].** However, any sign ambiguity associated with the coefficient t_z, as proposed in **Kim et al. (2023),** may undermine the accuracy of these two exterior orientation parameters. In contrast, the approach proposed by **Roumie et al. (2018)** solved simultaneously the three coefficients t_x, t_y and t_z in a system of three linear equations involving the nine coefficients of the rotation matrix and the coordinates of the camera location in the 3D scene, X_0, Y_0 and Z_0. However, the fact that the computation algorithms proposed by **Roumie et al. (2018)** to estimate the coefficients r_{21}, r_{22}, r_{23} are prone to parameter coupling errors, it can be argued that the resulting coefficients of the translation vector t_x, t_y and t_z would also be subjected to parameter coupling errors.

2.3.7. Analytical factorization of the projective transformation matrix

Several factorization approaches have been used for the calibration of camera pose. Among the mostly used strategies is the QR factorization, which formulates the first three columns of a 3×4 projective transformation matrix A into a product of an 3×3 upper triangular camera matrix and an 3×3 orthogonal rotation matrix such that:

$$\begin{bmatrix} a_1 & a_2 & a_3 \\ a_5 & a_6 & a_7 \\ a_9 & a_{10} & a_{11} \end{bmatrix} = \begin{bmatrix} q_1 & q_2 & q_3 \\ 0 & q_4 & q_5 \\ 0 & 0 & q_6 \end{bmatrix} \begin{bmatrix} r_{11} & r_{12} & r_{13} \\ r_{21} & r_{22} & r_{23} \\ r_{31} & r_{32} & r_{33} \end{bmatrix} \quad \textbf{[2-108.16]}$$

Where the coefficients $q_1, q_2, q_3, q_4, q_5, q_6$ and $r_{11}, r_{12}, r_{13} \ldots r_{33}$ are known coefficients. The parametric formulation of the projective matrix proposed by **Labuz et al. (1991)** to recover the camera interior parameters was formulated as follows:

$$c = \begin{bmatrix} \lambda f & \lambda f \tan\varphi & -\lambda\left(u_0 + f\tan\lambda\right) \\ 0 & f\sec\varphi & -v_0 \sec\lambda \\ 0 & 0 & 1 \end{bmatrix} \quad \textbf{[2-108.17]}$$

Where the parameter φ is the angle between the image x and y axes. The angle φ is generally equal to 90^0 under the perfect orthonormality of the rotation matrix and λ is a scaling factor. From the matrix Q and the parametric formulation in **[2-108.17], Labuz et al. (1991)** proposed the following solutions to recover the camera focal length and the coordinates of the principal point:

$$\varphi = \tan^{-1}\left(\frac{q_2}{q_1}\right) \quad \textbf{[2-108.18]}$$

$$f = q_4 \cos\varphi \quad \textbf{[2-108.19]}$$

$$u_0 = \frac{\left(q_2 + q_3\right)q_4}{q_1}\cos\varphi \quad \textbf{[2-108.20]}$$

$$v_0 = -q_5 \cos\varphi \quad \textbf{[2-108.21]}$$

The first formulation limitation with the proposed solution is the first coefficient of the second column of the matrix in **[2-108.17].** In the occurrence of orthogonal axes of the image sensor, the quantity $\tan\varphi$ would not be valid; this would result in numerical instabilities that would affect the focal length and the two coordinates of the principal point. To remedy this limitation, the authors could have formulated this coefficient as $\lambda f \cot\varphi$. The second limitation with the proposed solution is that it assumes the coordinates of the principal point u_0 and v_0 to be located at the centre of the image sensor, as the solution imposes the following constraints:

$$u_0 = \frac{\left(q_2 + q_3\right)q_4}{q_1}\cos 90^0 = 0 \quad \textbf{[2-108.22]}$$

$$v_0 = -q_5 \cos 90^0 = 0 \quad \textbf{[2-108.23]}$$

The above two constraints do not hold true for non-metric cameras, and these could lead to false solutions for the focal length and the coordinates of the principal point and propagate to the coefficients of the rotation matrix associated with the camera projective matrix. Furthermore, many algorithms used to compute the coefficients of a 3×4 projective transformation matrix generally produce a matrix with eleven scaled coefficients with the last coefficient of the fourth column normalized. Using the scaled coefficients of the first three columns of the projective transformation matrix could produce inaccurate estimates of the coefficients u_0, v_0 and the focal

length f since the resulting matrix Q would not be a perfect homogeneous matrix. These numerical instabilities would propagate to the estimates of the rotation matrix that is derived from these coefficients and those of the first three columns of the projective transformation matrix. The third limitation of the proposed solution in [2-108.19] is that the proposed algorithm is not suitable for cameras with rectangular pixels since the focal length in the x direction f_x is not generally equal to the focal length in the y direction f_y.

From the last column of the 3×4 projective transformation matrix, the following relationships can be established with the parameters of the rotation matrix and the three coefficients of the translation matrix as follows:

$$X_0 = -r_{11}t_x - r_{21}t_y - r_{31}t_z \quad \textbf{[2-108.24]}$$

$$Y_0 = -r_{12}t_x - r_{22}t_y - r_{32}t_z \quad \textbf{[2-108.25]}$$

$$Z_0 = -r_{13}t_x - r_{23}t_y - r_{33}t_z \quad \textbf{[2-108.26]}$$

The coordinates of camera location in a 3D scene can directly be recuperated from the coefficients of the projective transformation matrix as follows:

$$X_0 = -a_1a_4 - a_2a_8 - a_3a_{12} \quad \textbf{[2-108.27]}$$

$$Y_0 = -a_4a_5 - a_6a_8 - a_7a_{12} \quad \textbf{[2-108.28]}$$

$$Z_0 = -a_4a_9 - a_8a_{10} - a_{11}a_{12} \quad \textbf{[2-108.29]}$$

The other mostly used factorization strategy to compute parameters of camera pose is the Cholesky decomposition (**Li et al., 2015; Duan et al., 2024**). Multiplying both sides of the equation in **[2-108.16]** by the transpose of each quantity, with $q_1, q_2 \ldots q_6$ the coefficients of the upper triangular camera projective matrix, the following is obtained:

$$\begin{bmatrix} a_1 & a_2 & a_3 \\ a_5 & a_6 & a_7 \\ a_9 & a_{10} & a_{11} \end{bmatrix}\begin{bmatrix} a_1 & a_2 & a_3 \\ a_5 & a_6 & a_7 \\ a_9 & a_{10} & a_{11} \end{bmatrix}^T = \begin{bmatrix} f_x & \beta & u_0 \\ 0 & f_y & v_0 \\ 0 & 0 & 1 \end{bmatrix}\begin{bmatrix} r_{11} & r_{12} & r_{13} \\ r_{21} & r_{22} & r_{23} \\ r_{31} & r_{32} & r_{33} \end{bmatrix}\left(\begin{bmatrix} f_x & \beta & u_0 \\ 0 & f_y & v_0 \\ 0 & 0 & 1 \end{bmatrix}\begin{bmatrix} r_{11} & r_{12} & r_{13} \\ r_{21} & r_{22} & r_{23} \\ r_{31} & r_{32} & r_{33} \end{bmatrix}\right)^T \quad \textbf{[2-108.30]}$$

From the orthogonality property of the rotation matrix, the following Cholesky factorization can be derived from **[2-108.30]:**

$$\begin{bmatrix} a_1 & a_2 & a_3 \\ a_5 & a_6 & a_7 \\ a_9 & a_{10} & a_{11} \end{bmatrix}\begin{bmatrix} a_1 & a_2 & a_3 \\ a_5 & a_6 & a_7 \\ a_9 & a_{10} & a_{11} \end{bmatrix}^T = \begin{bmatrix} q_1 & q_2 & q_3 \\ 0 & q_4 & q_5 \\ 0 & 0 & q_6 \end{bmatrix}\begin{bmatrix} q_1 & q_2 & q_3 \\ 0 & q_4 & q_5 \\ 0 & 0 & q_6 \end{bmatrix}^T \quad \textbf{[2-108.31]}$$

The above equation can be simplified as follows:

$$\begin{bmatrix} a_1^2+a_2^2+a_3^2 & a_1a_5+a_2a_6+a_3a_7 & a_1a_9+a_2a_{10}+a_3a_{11} \\ a_1a_5+a_2a_6+a_3a_7 & a_5^2+a_6^2+a_7^2 & a_5a_9+a_6a_{10}+a_7a_{11} \\ a_1a_9+a_{10}a_2+a_3a_{11} & a_5a_9+a_6a_{10}+a_7a_{11} & a_9^2+a_{10}^2+a_{11}^2 \end{bmatrix} = \begin{bmatrix} f_x^2 & f_x\beta & f_xu_0 \\ f_x\beta & \beta^2+f_y^2 & \beta u_0+f_yv_0 \\ f_xu_0 & \beta u_0+f_yv_0 & u_0^2+v_0^2+1 \end{bmatrix} \quad \textbf{[2-10.32]}$$

From **[2-108.32]** the following solutions are derived:

$$u_0 = \frac{a_1a_9+a_2a_{10}+a_3a_{11}}{f_x} \quad \textbf{[2-108.33]}$$

$$v_0 = \sqrt{a_9^2+a_{10}^2+a_{11}^2-u_0^2-1} \quad \textbf{[2-108.34]}$$

$$f_x = \sqrt{a_1^2+a_2^2+a_3^2} \quad \textbf{[2-108.35]}$$

$$f_y = \sqrt{a_5^2+a_6^2+a_7^2-\beta^2} \quad \textbf{[2-108.36]}$$

$$\beta = \frac{a_1a_5+a_2a_6+a_3a_7}{f_x} \quad \textbf{[2-108.37]}$$

Due to improvements in lens manufacturing, the parameter β is generally set to zero. However, under such circumstances, the solution in [**2-108.37]** is not always true. The second limitation of the solution is that for small values of the first effective focal length, the first coordinate of the principal point u_0 would achieve very large magnitudes. This numerical instability will extend to the second coordinate of the principal point v_0 and prevent the coefficients a_9, a_{10} and a_{11} of the projective transformation matrix from holding certain numerical magnitudes. The third limitation is that any inaccurate calibration of any of the nine coefficients of the rotation matrix will undermine the accuracy of the second effective focal length f_y since the parameter β would not be equal to zero. The fourth limitation with the proposed strategy is that if the projective matrix was scaled during the recovery of its coefficients, the camera matrix would not be a perfect homogeneous matrix, and the numerical estimates of its coefficients would be compromised. From the calibrated parameters through **[2-108.33]-[2-108.37]** the coefficients of the rotation matrix and the three coefficients of the translation matrix can be recovered, as discussed earlier in this section.

2.4. Modelling Camera Location and Orientation through Learning strategies

With the development of new neural network algorithms, camera pose estimation using deep learning has been gaining momentum among the computer vision and photogrammetry community. **Guo et al., 2017,** for instance, proposed a camera pose calibration strategy based on the deep learning concept. The network architecture used in the approach consisted of two computational segments that include a convolutional neural network and a long short-term memory block. The long short-term memory block enables modelling the camera pose transition from point correspondences. Initial estimates of the camera pose are recovered through an RGB-D solver algorithm and then refined at a later stage through a loss function. Although the calibration results show good accuracy of the estimated camera pose parameters, deep learning

camera calibration suffers from a certain number of limitations. Camera pose estimation using deep neural networks is very reliant on a large number of calibration points to train the networks in order to achieve optimal accuracies, which are difficult to obtain, and this would also result in long processing times. Moreover, the generalization capability of the deep neural network to reconstruct some 3D scenes in order to perform the calibration still remains weak, and this can compromise the accuracy of the calibrated parameters. Furthermore, the accuracy of camera pose calibration through deep learning is far from meeting the standards in close-range photogrammetry compared to traditional camera pose estimation methods (**Wang et al., 2021**). **Lee et al. (2020)** proposed a camera pose estimation approach similar to that of **Guo et al. (2017)** in the sense that it uses deep learning and relies on a single image of the calibration object, which happened to be a robot, in contrast to traditional calibration surfaces containing lines and coplanar calibration points. The deep neural network implemented by the authors was initially trained on synthetic data in order to extract key points from the photograph of the calibration robot. The training of the deep network was based on the domain randomization algorithm, which offers the advantage of an interpolation algorithm in order to ensure there is no missing information during the collection of key points from the image of the calibration object. After the collection of key points from the photograph, the authors retrieved the nine coefficients of the rotation matrix as well as the three coefficients of the translation vector using a perspective n-point algorithm under the assumption that the focal length, the coordinates of the principal point, and the 3D coordinates of some calibration points on the robot are known a priori. The constraint of prior knowledge of the focal length and coordinates of the principal point in order to achieve acceptable accuracy makes this approach not suitable for consumer-grade digital cameras widely used in photogrammetry applications. Moreover, 3D annotations on calibration objects, such as robots, are very expensive, and localizing these annotations remains another challenge, and when the localization is successful, the calibration algorithm becomes rigid.

2.5. Modelling Radial Distortions with Rational and Division Model

2.5.1. Fitzgibbon's Distortion Modelling

The challenges of solving large radial distortion polynomials have led to the development of new families of models with the advantage of being solved analytically. **Fitzgibbon (2001)** proposed a division model to correct severe radial lens distortions. The model is the inverse of a three-term quadratic polynomial without the cubic term and the monomial term with the variable elevated to the power one and where the term κ_0 is set to one. This three-parameter version has been widely used to model radial distortions (**Hong et al., 2015; Santana-Cedrés et al., 2017; Yan et al., 2016; Zhang et al., 2018; Zhang et al., 2019**; **Moravec, 2020).** The commonly used formulation is given as follows:

$$F\left(r_d\right) = \frac{1}{1 + \kappa_1 r_u^2 + \kappa_2 r_u^4} \qquad \textbf{[2-109]}$$

Other studies have adopted a truncated version by dropping the quartic term, as reported in the studies of **Tang et al. (2017), Wu et al. (2017)**, **Zhang et al. (2019),** and **Weng et al. (2021**). The commonly used two-parameter inverse polynomial is given as follows:

$$f\left(r\right) = \frac{1}{1 + \kappa_1 r^2} \qquad \textbf{[2-110]}$$

The function in **[2-110]** enables to estimate the undistorted radius r_u from the distorted radius as follows (**Wu et al., 2017**; **Zhang et al., 2019**):

$$r_u = \frac{r_d}{1+\kappa_1 r_d^2} \quad \textbf{[2-111]}$$

An observation of the two-parameter division model in **[2-111]** reveals that it is invertible for values of $\kappa_1 < 0$ .This restriction makes the model suitable for barrel distortion profiles only (**Shi et al., 2018**). Moreover, for larger values of r_d in the occurrence of severe barrel distortions, the inverse polynomial equation would not hold true since it would result in model numerical instability due to the quadratic expression with the distorted radius as a variable in the equation.

2.5.2. Brauer-Burchard and Vos's (2001) Radial Distortion Modelling

To alleviate the numerical ambiguity related to solving equation **[2-110],** the term containing the first coefficient of radial distortion in the denominator can be negated (**Ma et al., 2003**) to ensure the stability of the model and produce the following:

$$f'(r) = \frac{r}{1-\kappa_1 r^2} \quad \textbf{[2-112]}$$

Expressing the distorted radius from the undistorted radius through the function $f'(r)$ in **[2-112]** gives the following:

$$r_d = \frac{r_u}{1-\kappa_1 r_u^2} \quad \textbf{[2-113]}$$

Linearizing the above model leads to the following polynomial function:

$$r_u^2(-\kappa_1 r_d) - r_u + r_d = 0 \quad \textbf{[2-114]}$$

With a discriminant of $\Delta = 1+4\kappa_1 r_d^2$ the model in **[2-112]** holds two inverse models given by the following:

$$r_u = \frac{1+\sqrt{1+4\kappa_1 r_d^2}}{-2\kappa_1 r_d} \text{ Or } r_u = \frac{1-\sqrt{1+4\kappa_1 r_d^2}}{-2\kappa_1 r_d} \quad \textbf{[2-115]}$$

In such cases when there is more than one solution, the smallest positive solution should be considered (**Ryberg et al., 2011**), and from **[2-115]** the second solution seems to satisfy this requirement after the elimination of the negative sign from the denominator and numerator and produce the following distortion function:

$$f(r) = \frac{-1+\sqrt{1+4\kappa_1 r^2}}{2\kappa_2 r} \begin{cases} \kappa_2 \neq 0 \\ \kappa_1 \geq 0.75 r_d^2 \end{cases} \quad \textbf{[2-116]}$$

A close observation of the function in **[2-115]** reveals the model is nothing else than the radial distortion division model proposed by **Brauer-Burchard and Vos (2001)**. In opposition to the model in **[2-111]** the model in **[2-116]** would work best for pincushion distortions with a positive radial distortion coefficient κ_1. However, the model restricts the coefficient to certain values, and this would undermine the correction of small distortions around the image centre where small values of the coefficient κ_1 are expected.

2.5.3. Ma et al. (2003) Division and Rational Modelling of Radial Distortion

To alleviate the limitations of the division models proposed by **Fitzgibbon (2001) and Brauer-Burchard and Vos (2001), Ma et al. (2003)** proposed three division models and three rational radial distortion models. Among the three division models proposed by **Ma et al. (2003)** are the two and three parameters of inverse polynomial functions proposed by **Fitzgibbon (2001).** The six models are summarized in equations **[2-117]-[2-120]** below:

$$f(r) = \frac{1}{1+\kappa r} \quad \textbf{[2-117]}$$

$$f(r) = \frac{1}{1+\kappa r^2} \quad \textbf{[2-118]}$$

$$f(r) = \frac{1}{1+\kappa_1 r+\kappa_2 r^2} \quad \textbf{[2-119]}$$

$$f(r) = \frac{1+\kappa_1 r}{1+\kappa_2 r^2} \quad \textbf{[2-120]}$$

$$f(r) = \frac{1+\kappa_1 r}{1+\kappa_2 r+\kappa_3 r^2} \quad \textbf{[2-121]}$$

$$f(r) = \frac{1+\kappa_1 r^2}{1+\kappa_2 r+\kappa_3 r^2} \quad \textbf{[2-122]}$$

It can be noticed that the models in **[2-117]** and **[2-118]** provide the advantage of dealing with a single particular distortion profile because of the sole distortion coefficient contained in each model. The models in **[2-119]** and **[2-120]** offer the advantage of simultaneously dealing with two distortion profiles. Observing the model in **[2-121]**, it can be noticed that the second polynomial term in the numerator has the same degree as the second polynomial term in the denominator. Additionally, in the model in **[2-122],** the second polynomial term of the numerator has a degree larger than that of the second polynomial term in the denominator. It has been reported that as long as the highest degree of a polynomial term in the denominator is smaller or equal to the highest degree term in the numerator, the contribution of the polynomial in the denominator will remain insignificant (**Ryberg et al., 2011**). Since each distortion coefficient corresponds to a certain radial distortion curve, the models in **[2-117], [2-118], [2-119], and [2-120]** can only handle one and two distortion profiles, respectively. Moreover, the models in **[2-117] and [2-122]** proposed by **Ma et al. (2003)** only deal with symmetric radial distortions, while radial distortions are not always symmetric **(Tang et al., 2017).** From the above, there is still a window for improvement of some of the current modelling of radial distortions by exploring large polynomials with analytical solutions.

2.6. Modelling Radial Lens Distortion with Polynomial Functions

Lens distortions can be classified into three categories that include radial, tangential, and thin prism distortions (**Pierré et al., 2016; Tjahjadi et al., 2019**), with tangential and thin prism distortions considered negligible due to improvements in modern lens manufacturing processes (**Li et al., 2016; He et al., 2020; Vera et al., 2020**). Radial distortions that include barrel, pincushion have attracted much attention among the photogrammetry community, while the moustache distortion profile poses a serious modelling problem since it combines both barrel and pincushion profiles (**Hamad et al., 2017; Shih and Tung, 2017; Ramírez-Hernández et al., 2020**). The radial distortion effect alters the position of image points either inward or outward

from the image centre, which is the intersection point of the optical axis and the 2D image plane (**Xing and Guo, 2020; Paiz-Reyes et al., 2020).** The negative displacement of a point is a characteristic of pincushion distortions, while a positive displacement is characteristic of barrel distortions (**Park et al., 2009**; **Thall, 2018**).

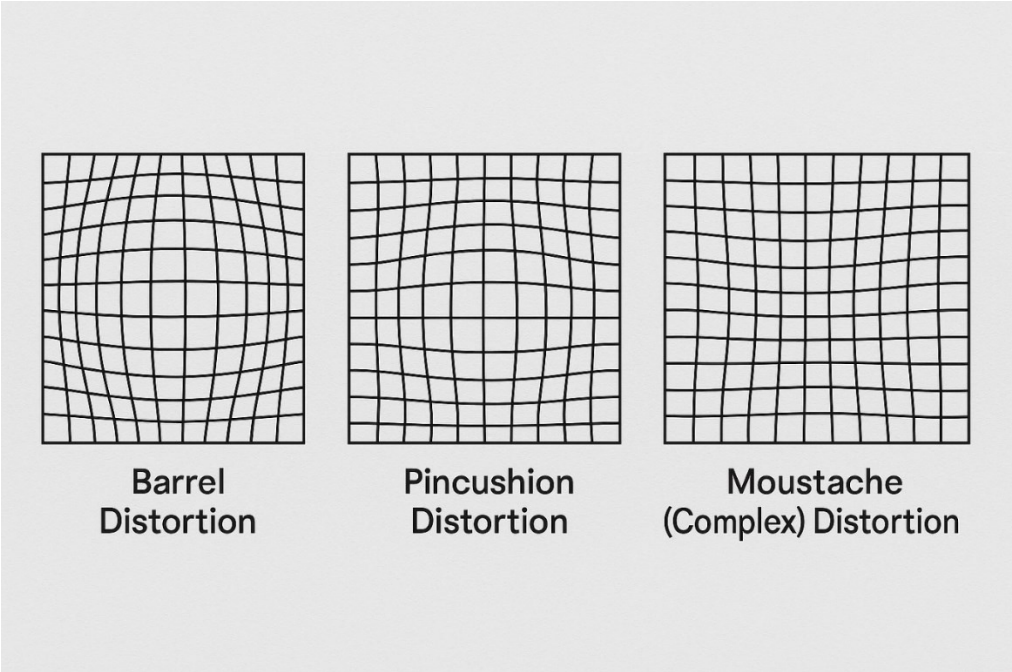

Figure 0-2: Simulated images portraying the effects of pincushion and barrel radial lens distortions

Radial lens distortions have widely been modelled through polynomial functions originally proposed by **Brown (1971)** as an odd power polynomial function for perfectly centred lenses formulated as follows:

$$f\left(r\right)=\sum_{j=2i+1}^{+\infty}\sum_{i=1}^{+\infty}\kappa_i r^j \qquad \textbf{[2-123]}$$

The model was later improved in **Fryer and Brown (1986)** and later used by authors such as **Lava et al. (2013**), **Babaei and Saadat-Seresht (2019),** to name a few. The preference of using odd-power polynomial distortion models was supported by the argument that its formulation considers negative radii and also allows expansions of spans of continuous distortion functions (**Kannala and Brandt, 2006**). Although radial lens distortions have been reported to not always be symmetrical with reference to the distortion centre **(Fryskowska et. al, 2016)**, an even power variant of the model in **[4-1]** has widely been used for lens distortion modelling (**Ju and Kang, 2014**; **Li et al., 2016**; **Wierzbicki, 2018;** and **Liao et al., 2019**). The commonly used formulation of the even power radial distortion model is given as follows:

$$f\left(r\right)=\sum_{j=2i}^{+\infty}\sum_{i=1}^{+\infty}\kappa_i r^j+\kappa_0 \qquad \textbf{[2-124]}$$

In opposition to the model in **[2-123],** the model in **[2-124]** contains a constant κ_0 that is considered a scaling factor and introduces no distortion (**Sun et al., 2016; Stapleton and Bajic, 2016**). This constant is generally set to unity, while coefficients κ_i describe the shape of the distortion curves and are responsible for the displacement of image points from their respective undistorted locations (**Tjahjadi et al., 2019; Zhu et al., 2019; and Hiba et al., 2020**). In cases where more than one term of the model in **[4-2]** is used, it has been reported that a positive sign

of all the distortion coefficients would indicate the presence of barrel distortions on the image, while a negative sign would describe pincushion distortions. Moreover, when radial distortion coefficients exhibit a mixture of positive and negative signs, there is an occurrence of moustache radial distortions (**Tang et al., 2017**). The use of depressed versions of the model in **[2-124]** has been widely suggested (**Gao and Yin 2013; Liu et al., 2016; Moravec, 2020**). Arguments have been put forward to justify the choices between odd and even power distortion polynomials; however, some authors, more specifically **Nave and Francos (2008),** suggested the use of general models that contain both even and odd power terms for modelling of severe radial distortions and formulated them as follows:

$$f(r) = \sum_{j=i+1}^{+\infty} \sum_{i=1}^{+\infty} \kappa_i r^j + 1 \qquad \textbf{[2-125]}$$

Vargas et al. (2020) proposed the use of a version of **[2-125]** with six terms and a highest power equal to five to model severe moustache radial distortions. To relate distorted image coordinates with their undistorted counterparts through the proposed quintic model is done as follows:

$$x_d = x_u + x_u \left(\sum_{j=i+1}^{5} \sum_{i=1}^{5} \kappa_i r_u^j \right) \qquad \textbf{[2-126]}$$

$$y_d = y_u + y_u \left(\sum_{j=i+1}^{5} \sum_{i=1}^{5} \kappa_i r_u^j \right) \qquad \textbf{[2-127]}$$

It can be noted from the formulations in **[2-126]** and **[2-127]** that in the absence of radial distortions, the distorted coordinates x_d and y_d are mapped as distortion-free x_u and y_u image coordinates. The radius r_u is estimated as follows:

$$r_u = \sqrt{(x_u - x_0)^2 + (y_u - y_0)^2} \qquad \textbf{[2-128]}$$

Where x_0 and y_0 represent the coordinates of the principal point. The five radial distortion coefficients $\kappa_1, \kappa_2, \kappa_3, \kappa_4$ and κ_5 in **[2-126]** and **[2-127]** were estimated by the authors using the Zhang method that needs few images of a planar calibration pattern **(Zhang, 2000)**. From the estimated coefficients, the undistorted coordinates of image points are recovered through the lookup table method. Although four of the five radial distortion coefficients estimated by the above author have negative signs that normally describe moustache radial distortions, an input of these coefficients back into a general quintic polynomial model, however, produces a pincushion distortion effect. In contrast, **Hirmiz et al. (2019)** and **Ibrahim et al. (2022)** suggested that radial barrel distortions are better modelled by three-terms depressed six-order polynomial function, reformulating the relations in **[2-126]** and **[2-127]** as the following:

$$x_d = x_u + x_u \left(\sum_{j=2i}^{6} \sum_{i=1}^{3} \kappa_i r_u^j \right) \qquad \textbf{[2-129]}$$

$$y_d = y_u + y_u \left(\sum_{j=2i}^{6} \sum_{i=1}^{3} \kappa_i r_u^j \right) \qquad \textbf{[2-130]}$$

Hirmiz et al. (2019) used an optimization approach that minimizes the distance error between distortion-free points' locations and their distorted counterparts extracted from photographed images of biological cells to solve for the radial distortion coefficients. The obtained distortion coefficients were then used in a lookup table to correct the distorted images. In contrast, **Ibrahim et al. (2022)** computed radial distortion coefficients from images of a checkerboard and applied distortion corrections to the distorted points using the camera calibration toolbox provided in

MATLAB. Although **Hirmiz et al. (2019)** suggested that coefficients beyond κ_2 have a very minimal influence in the modelling of barrel radial distortions, **Sims-Waterhouse et al. (2020)** argued that the consideration of more coefficients beyond the second one is recommended because it enables to formulate high order distortion polynomials capable of modelling severe distortions. This opinion was also shared by **Barbero-García et al. (2018)**, **Capolupo et al. (2020),** and **Janos and Benesova (2021),** who argued that some camera calibration software packages, such as Agisoft PhotoScan, can now accommodate up to four radial distortion coefficients to improve the accuracy of the camera calibration process.

2.7. Analytical Solutions for Inverse Radial Distortion Coefficients Models

Inverse radial distortion coefficients are essential to correct images from radial distortion through an inverse polynomial function. Polynomial reversion strategies are generally related to solutions of differential equations (**Zwillinger and Dobrushkin, 2021**). In recent years, inverse polynomials have also expanded to applications such as digital image processing in remote sensing (**Chen et al., 2021**). In the context of camera calibration, three strategies have been widely used, including estimating radial distortion coefficients through iteration processes that require initial estimates of the coefficients (**Abeles, 2018; Pan et al., 2022).** Estimation of inverse distortion coefficients can also be achieved through a lookup table strategy (**Li et al., 2015; Darvatkar and Bhandari, 2017**) or the computation of derivatives of the radial distortion polynomial to approximate the closest Taylor series (**Fang and Zheng, 2016; Vieira et al., 2017**). However, the above-listed techniques suffer from some limitations that may limit the performance of the reversed function to capture radial distortion profiles accurately. It can be noted, for instance, that estimating the derivative of a distortion function to approximate the nearest Taylor series, which is used as a reverse model, can only deal with minimal radial distortions, and the strategy has shown its inefficiency when it comes to dealing with severe distortions since the second and higher order terms of radial distortion polynomial functions are generally ignored **(Mallon and Whelan, 2004**; **Ma et al., 2023**). Estimating inverse coefficients of radial distortion by iteration can be subjective since it is very difficult to predict the number of iterations at which the function will converge. It also requires several images to achieve a good enough result, is time-consuming, and performs poorly when dealing with severe distortions. The constraint to impose a value of zero on the fourth radial distortion coefficient to estimate more than three inverse coefficients can lead to false solutions of inverse coefficients (**Hamed et al., 2021**). The lookup table solution similarly imposes some restrictions, such as the range within which the coefficients must belong, which can also weaken the image correction process. In addition to the above solution, **Drap and Lefevre (2016)** proposed a recursive formula to estimate inverse coefficients from radial distortion polynomials. To run the iteration process to refine the inverse coefficients, the proposed solution also imposes a numerical value of zero on the fourth radial distortion coefficient to compute coefficients beyond the third one. Among the limitations of this proposed approach is the intense series manipulation required. The other end of the approach is the rigidity of the algorithms proposed to compute the various inverse radial distortion coefficients that are only suitable for radial distortions modelled by low-degree polynomial functions. The proposed inverse algorithms cannot model severe barrel, pincushion, and moustache radial distortion profiles.

2.8. Concluding Remarks

The findings of this critical literature review exposed a lack of substantial photogrammetry literature on camera pose estimation through accurate decomposition solutions of the projective

transformation matrix. When considering techniques such as QR and Cholesky factorizations and three other existing decomposition approaches designed for computer vision applications, it was clear that camera calibration produced unsatisfying results as the different algorithms developed through these approaches lack robustness and do need to be more reliable for photogrammetry applications. To date, no significant work in the photogrammetry literature has considered the potential of preserving geometric constraints imposed by the formulation of the projective transformation matrix on individual camera parameters when independently calibrating the parameter of camera pose.

Added to this, it is perhaps predictable to say that in the background of photogrammetry literature, it was not possible to consolidate an appropriate theoretical basis of fully analytical mathematical systems that deal with the reversion of radial distortion polynomial functions and compute accurate inverse radial distortion coefficients needed for radial distortion corrections. For this reason, directions for the primary research on the analytical reversion of polynomial radial distortion models, and the computation of inverse distortion coefficients relied on a strategy extracted from the computer vision literature. This specific work, authored by **Drap and Lefevre (2016),** is referred to in this thesis as a semi-analytical approach because the second phase of the computation of inverse radial distortion coefficients involves an iterative optimization process that refines all the analytically estimated inverse radial distortion coefficients together through a cost function. However, this computer vision method offers a loose formulation framework and accuracy uncertainties, especially when it comes to dealing with complex distortion curves describing profiles such as severe barrel, pincushion, and moustache radial distortions.

CHAPTER 3

ANALYTICAL ESTIMATION OF CAMERA INTRINSIC AND EXTRINSIC PARAMETERS FROM A SINGLE IMAGE IN CLOSE-RANGE PHOTOGRAMMETRY

3.1 Introduction

Close-range photogrammetry refers to terrestrial or near-ground photogrammetric imaging conducted from relatively short distances, typically less than 300 meters from the object of interest. This domain contrasts with traditional aerial or satellite photogrammetry, where the imaging geometry is governed by greater object-to-camera distances and flight-based acquisition. Close-range applications are often performed using non-metric or consumer-grade cameras, such as DSLRs cameras or mobile phone cameras, where internal geometry is not fixed and thus requires calibration. With the development of cheap off-the-shelf digital cameras, the number of applications in close-range photogrammetry has increased drastically in the recent decade. Applications now range from building structure monitoring (**Hu et al., 2021**), landslide monitoring (**Mokhtar et al., 2021**), reconstruction of accident scenes (**Stehel et al., 2021),** and archaeological site reconstruction (**Sapirstein, 2018; Marín-Buzón et al., 2021**), to name a few. A central requirement across all these applications is the accurate estimation of camera pose parameters, which refer to the location and orientation of the camera in the 3D scene (**Semeniuta, 2016; Liu et al., 2017**). These parameters are fundamental to transforming image measurements into reliable and metrically accurate spatial data (**Luhmann et al., 2016**).

To ensure high measurement accuracy, significant research effort has been devoted to the calibration of camera systems. This includes the determination of both extrinsic parameters (camera location and orientation) and intrinsic parameters such as focal length, principal point, and lens distortion coefficients. Multi-view camera calibration, in particular, has become a standard approach in close-range photogrammetry, as it enables the estimation of radial distortion and improves pose estimation robustness by leveraging redundant observations from multiple perspectives. Several approaches available in the literature implement multi-stage optimization techniques based on well-established approaches like those of **Tsai (1984)** and **Zhang (2000)**, offering effective solutions for multi-camera setups or moving cameras across views. **Kurillo et al. (2008)** proposed a two-stage multi-camera approach that computes the camera parameters by applying the **Tsai (1984)** approach to data collected from a checkerboard calibration pattern in the first stage. In the second stage, the coefficients of the translation matrix, as well as those describing the camera orientation in a 3D scene, are estimated up to a scale factor using triangulation and then later optimized using the Levenberg-Marquardt algorithm. For more insight into the algorithm, the reader can refer to the work of **Gavin (2019). Wang et al. (2016)** proposed an approach that estimates the parameters of camera location and orientation as well as the coordinates of the principal point and the effective focal lengths under the constraint that the calibration pattern is parallel to the image plane, which results in a simplified formulation of the rotation matrix. The proposed solution starts with an equation estimating the first two Euler rotation angles and the last coefficient of the translation vector through a system of linear equations with at least five-point correspondences. The remaining two coefficients of the translation vector and the last Euler rotation angle are estimated from the radial alignment constraint using the linear least squares method. One challenge with the proposed solution is the parameter coupling, which is of great concern in photogrammetry. In addition, achieving perfect parallelism between the flat surface of the calibration object and the image plane is very difficult. **Lei et al. (2020)** instead proposed a camera pose calibration approach based on the Zhang method (**Zhang, 2000**) to estimate the initial values of parameters of camera location and orientation in a 3D scene, which are later optimized using the maximum likelihood algorithm under the constraint that the origin of the world coordinate frame is located on the planar surface of the calibration pattern. **Zhu et al. (2020)** proposed an estimation method based on the RANSAC algorithm using point correspondence from which systems of linear equations are derived and solved using Grobner basis methods while assuming the principal point to be the centre of the image. However, it has been earlier reported in **Xu et al. (2019**) that the single elimination template of the Grobner basis can lead to numerical instabilities for the estimated camera parameters. In addition, the RANSAC algorithm does not always guarantee a perfect match between image points due to the unsupervised sample selection process (**Wierzbicki, 2018**). In addition, the fact that the tool relies on user-defined settings for distance threshold, minimal number of inliers threshold, as well as the number of iterations, makes the accuracy of the output camera parameters to be very subjective because these thresholds are determined based on trial and error (**Rabin et al., 2010; Wang et al., 2013**). Another strategy to estimate the parameters of camera location and orientation in a 3D scene is by iterative point correspondence, where initial values of the camera parameters are pre-estimated through a batch processing procedure. The newly estimated parameters are refined using the Kalman filtering technique (**Chu and Yang, 2020**). Techniques estimating the parameters of camera pose relying on iterative methods have been largely criticized as unsuitable for non-metric cameras since their internal geometry is subjected to instabilities between tasks (**Abdel-Aziz et al., 2015**). The Singular Value Decomposition (SVD) method has also attracted some attention for estimating parameters of camera pose. However, the parameters computed through this strategy require further processing through optimization to achieve acceptable estimates (**Cao et al., 2018**). **Zhao et al. (2016)** and **Burger (2019)** advocated the use of the DLT algorithm to recover the

parameters of camera pose because of its simplicity in computing the coefficients of the projective transformation matrix from which the camera parameters can be extracted.

Although the above-discussed camera calibration strategies offer some robust solutions, these approaches often depend on complex optimization algorithms, external calibration patterns, and assumptions about the imaging geometry, such as planar alignment or precise image-to-pattern parallelism, which may not always be achievable in practical field settings. In contrast, the development of fully analytical camera pose calibration approaches based on a single image remains limited, despite the increasing demand for minimal-setup and flexible calibration procedures. Analytical methods are attractive because they avoid iterative optimization and can, in principle, provide closed-form solutions for camera parameters under certain constraints. Nevertheless, their adoption has been hampered by significant challenges, including nonlinear parameter coupling, sign ambiguity, multiple parameter roots, and the preservation of geometric constraints within the projective transformation matrix (**Lowe, 1987; Henrichsen, 2000**). Additionally, accurate estimation of central camera intrinsic parameters such as the coordinates of the distortion centre and the effective focal lengths during the camera pose estimation using a single image has not been adequately addressed by existing fully analytical methods.

This chapter addresses these gaps by proposing a novel, fully analytical calibration framework based on a single-view image. The approach is designed to independently estimate the full set of camera pose parameters, along with key intrinsic parameters such as the coordinates of the principal point and the effective focal lengths, thereby improving the geometric fidelity of the calibration without requiring multiple views or iterative optimization. By minimizing parameter coupling, eliminating sign ambiguities, and preserving the internal structure of the camera projection model, this method offers a scalable and theoretically grounded alternative to conventional calibration pipelines. The proposed technique is particularly suited for applications where only a single image is available, where calibration must be performed in situ with minimal equipment, or where access to multi-view data is limited.

3.2 **Methodology**

3.2.1. Formulating the Rigid Body Transformation Matrix

A rigid body transformation is a transformation that does not change the shapes and sizes of 3D objects but only changes their respective locations and orientations in the object space (**Than et al., 2017; Liu et al., 2021**). This transformation generally involves a concatenation of three rotations of the three planes composing the camera coordinate frame around the planes, making an arbitrary 3D scene coordinate system (**Miyata et. al., 2017**; **Chen et al., 2021**). The translation between the origins of the 3D scene coordinate frame, and that of the camera 3D coordinate frame is a component of the rigid body transformation process and is done either prior to or after the rotation, and any sequence has no influence on the resulting transformed column or row vector (**Cai et. al., 2020**). Concatenating the rotation matrix and the translation matrix into a single matrix only offers a computational advantage in terms of the number of operations performed on the point vector.

In this chapter, the translation between the coordinate systems' origins was performed prior to the rotation phase through a displacement matrix. To formulate the displacement matrix, a common reference point Q located in the 3D scene with coordinates $(0,0,0)$ was considered. From this reference point, the coordinates of the location of the centre of the 3D scene coordinate frame $(X_\omega, Y_\omega, Z_\omega)$ are measured, as well as those of the origin of the camera's 3D coordinate system (X_0, Y_0, Z_0). Since the coordinates of the origins of both coordinate systems are

expressed with respect to this common reference point, moving the origin of the camera coordinate system to the location of the origin of the 3D world coordinate system was achieved through the following displacement matrix:

$$T = \begin{bmatrix} 1 & 0 & 0 & -X_0 \\ 0 & 1 & 0 & -Y_0 \\ 0 & 0 & 1 & -Z_0 \end{bmatrix} \quad \textbf{[3-1]}$$

Parameters X_0, Y_0 and Z_0 describe the position of the camera in a 3D scene at the time of image capture. Once the coordinate systems' origins are superimposed, the first rotation was performed in order to transform the orientation of the camera $Y_C - Z_C$ plane to bring it to a near-parallel orientation with reference to the world coordinate frame's $Y_\omega - Z_\omega$ plane through a rotation by an angle φ around the camera X_C axis to create a new $Y_{2C} - Z_{2C}$ camera plane. This first rotation was formulated through the following matrix:

$$R_{X_c} = \begin{bmatrix} 1 & 0 & 0 \\ 0 & \cos\varphi & -\sin\varphi \\ 0 & \sin\varphi & \cos\varphi \end{bmatrix} \quad \textbf{[3-2]}$$

Where Y_{2C} and Z_{2C} represent the new camera Y and Z axes after the first rotation. The second rotation performed had the aim of modifying the orientation of the newly created $X_C - Z_{2C}$ plane by a rotation around the newly created Y_{2C} axis with an angle ϕ. This second rotation around the newly created Y_{2C} axis is represented by the second rotation matrix formulated as follows:

$$R_{Y_{2c}} = \begin{bmatrix} \cos\phi & 0 & \sin\phi \\ 0 & 1 & 0 \\ -\sin\phi & 0 & \cos\phi \end{bmatrix} \quad \textbf{[3-3]}$$

As it can be observed on the newly created $Y_{2C} - Z_{2C}$ and $X_{2C} - Z_{2C}$ planes, there is a recurrence of the camera Z_C axis; this simply means the first two rotations had as objective the alignment of the camera Z_C axis with the world Z_ω axis. With the camera Z_C axis now aligned with the world Z_ω axis, a roll rotation by an angle κ is performed to perfect the alignments between the camera coordinate system's X_{2C} , Y_{2C} axes, and the world coordinate system's X_ω and Y_ω axes, respectively. This transformation is described through the following third rotation matrix:

$$R_{Z_{2c}} = \begin{bmatrix} \cos\kappa & -\sin\kappa & 0 \\ \sin\kappa & \cos\kappa & 0 \\ 0 & 0 & 1 \end{bmatrix} \quad \textbf{[3-4]}$$

With X_{2C} the new camera X axis after the second rotation. The formulation of the rotation matrix adopted in this chapter was computed as follows:

$$R = R_{Z_{2c}} \times R_{Y_{2c}} \times R_{X_c} = \begin{bmatrix} \cos\kappa\cos\phi & \cos\kappa\sin\phi\sin\varphi - \sin\kappa\cos\varphi & \cos\kappa\sin\phi\cos\varphi + \sin\kappa\sin\varphi \\ \sin\kappa\cos\phi & \sin\kappa\sin\phi\sin\varphi + \cos\kappa\cos\varphi & \sin\kappa\sin\phi\cos\varphi - \cos\kappa\sin\varphi \\ -\sin\phi & \cos\phi\sin\varphi & \cos\phi\cos\varphi \end{bmatrix} \quad \textbf{[3-5]}$$

A simplified expression of **[3-5]** adopted in this chapter for formulation advantages is presented as follows:

$$R = \begin{bmatrix} r_{11} & r_{12} & r_{13} \\ r_{21} & r_{23} & r_{23} \\ r_{31} & r_{32} & r_{33} \end{bmatrix} \quad \textbf{[3-6]}$$

With the parameters $r_{11}, r_{12}, r_{13} \ldots r_{33}$ representing the nine coefficients of the rotation matrix that are composed of associations of trigonometric functions. From **[3-6],** a formulation of the rigid body transformation matrix R_B can be achieved by adding a fourth column filled with the three coefficients t_x, t_y and t_z of the translation matrix, respectively, as the last coefficient of the first, second, and third rows of the matrix **[3-6]** to produce the following:

$$R_B = \begin{bmatrix} r_{11} & r_{12} & r_{13} & t_x \\ r_{21} & r_{23} & r_{23} & t_y \\ r_{31} & r_{32} & r_{33} & t_z \end{bmatrix} \quad \textbf{[3-7]}$$

Similarly, another formulation of the rigid body transformation matrix can be achieved by post multiplying **[3-1]** with **[3-6]** as follows:

$$R_B = \begin{bmatrix} r_{11} & r_{12} & r_{13} \\ r_{21} & r_{23} & r_{23} \\ r_{31} & r_{32} & r_{33} \end{bmatrix} \begin{bmatrix} 1 & 0 & 0 & -X_0 \\ 0 & 1 & 0 & -Y_0 \\ 0 & 0 & 1 & -Z_0 \end{bmatrix} = \begin{bmatrix} r_{11} & r_{12} & r_{13} & -X_0 r_{11} - Y_0 r_{12} - Z_0 r_{13} \\ r_{21} & r_{23} & r_{23} & -X_0 r_{21} - Y_0 r_{23} - Z_0 r_{23} \\ r_{31} & r_{32} & r_{33} & -X_0 r_{31} - Y_0 r_{32} - Z_0 r_{33} \end{bmatrix} \quad \textbf{[3-8]}$$

A comparison of the last columns between matrices **[3-7]** and **[3-8]** shows that the coefficients of the translation vector t_x, t_y and t_z are functions of the coefficients of the rotation matrix and the parameters of the camera location in the 3D scene X_0, Y_0 and Z_0. Either of these parameters can be retrieved if the other set is known; for instance, with knowledge of the nine coefficients of the rotation matrix and the parameters of camera location, it is possible to estimate the three coefficients of the translation vector and vice versa.

3.2.2. Formulating the Camera Projective Matrix

Camera projective matrices convert the non-measurable 3D camera coordinates to measurable image coordinates that can be expressed in world units or in pixels. The matrix is usually made of a scaling factor as the first coefficient of the first row; this coefficient can be set to the camera constant f or to the effective focal length in the x direction f_x. This effective focal length measure is a ratio of the focal length over the pixel dimension in the x direction. In addition, the second coefficient of the first row is the skew factor γ, generally assumed to be zero under the assumption that the image coordinate system's axes are orthogonal, while the last coefficient of the row is the first coordinate of the principal point u_0. In contrast, the first coefficient of the second row of the matrix is set to zero to eliminate the image x coordinate, while the second coefficient of the row is the second effective focal length f_y in the y direction, and the last coefficient of this row is the second coordinate of the principal point v_0. The third row of the matrix has the first two coefficients set to zero to eliminate the x and y image coordinates, respectively, while the last coefficient is set to one to accommodate the homogeneous representation of the column vector being transformed. Some formulations of the camera

projective matrix may perform an additional scaling applied to the focal length or the effective focal length in the x direction. In contrast, others applied the parameter to the effective focal length in the y direction**.** This scaling is generally done using the aspect ratio factor, which is generally set to unity. The formulation of the camera projective matrix adopted in this chapter is as follows:

$$k = \begin{bmatrix} f_x & 0 & u_0 \\ 0 & f_y & v_0 \\ 0 & 0 & 1 \end{bmatrix} \quad \textbf{[3-9]}$$

Where $fd_x^{-1} = f_x$ and $fd_y^{-1} = f_y$ **[3-10],** are the effective focal lengths while d_x and d_y are the dimensions of a pixel in the x and y directions, respectively.

3.2.3. Formulating the Projective Transformation Matrix

Multiplying the matrix in **[3-7]** with the camera matrix in **[3-9]** produces the following formulation of the projective transformation matrix:

$$P_{TM} = \begin{bmatrix} f_x & 0 & u_0 \\ 0 & f_y & v_0 \\ 0 & 0 & 1 \end{bmatrix} \begin{bmatrix} r_{11} & r_{12} & r_{13} & t_x \\ r_{21} & r_{22} & r_{23} & t_y \\ r_{31} & r_{32} & r_{33} & t_z \end{bmatrix} = \begin{bmatrix} f_x r_{11} + u_0 r_{31} & f_x r_{12} + u_0 r_{32} & f_x r_{13} + u_0 r_{33} & f_x t_x + u_0 t_z \\ f_y r_{21} + v_0 r_{31} & f_y r_{22} + v_0 r_{32} & f_y r_{23} + v_0 r_{33} & f_y t_y + v_0 t_z \\ r_{31} & r_{32} & r_{33} & t_z \end{bmatrix} \quad \textbf{[3-11]}$$

The estimated projective transformation matrix in **[3-11]** contains 12 coefficients made of coefficients of the rotation and translation matrices, the effective focal lengths, and the coordinates of the principal point, thus making nineteen unknowns to be calibrated. The parameters of camera location in a 3D scene will also be calibrated with knowledge of the coefficients of the translation vector. Multiplying matrices in **[3-9]** and **[3-10]** gives the parametric formulation of the projective transformation matrix considered in this study as follows:

$$P_{TM} = \begin{bmatrix} f_x \cos\kappa\cos\phi - u_0 \sin\phi & f_x\begin{pmatrix}\cos\kappa\sin\phi\sin\varphi \\ -\sin\kappa\cos\varphi\end{pmatrix} + u_0\left(\cos\phi\sin\varphi\right) & f_x\begin{pmatrix}\cos\kappa\sin\phi\cos\varphi \\ +\sin\kappa\sin\varphi\end{pmatrix} + u_0\left(\cos\phi\cos\varphi\right) & f_x\begin{pmatrix}-X_0\left(\cos\kappa\cos\phi\right) \\ -Y_0\left(\cos\kappa\sin\phi\sin\varphi - \sin\kappa\cos\varphi\right) \\ -Z_0\left(\cos\kappa\sin\phi\cos\varphi + \sin\kappa\sin\varphi\right)\end{pmatrix} + u_0\begin{pmatrix}X_0\left(-\sin\phi\right) - Y_0\left(\cos\phi\sin\varphi\right) \\ -Z_0\left(\cos\phi\cos\varphi\right)\end{pmatrix} \\ f_y \sin\kappa\cos\phi - v_0\sin\phi & f_y\begin{pmatrix}\sin\kappa\sin\phi\sin\varphi \\ +\cos\kappa\cos\varphi\end{pmatrix} + v_0\left(\cos\phi\sin\varphi\right) & f_y\begin{pmatrix}\sin\kappa\sin\phi\cos\varphi \\ -\cos\kappa\sin\varphi\end{pmatrix} + v_0\left(\cos\phi\cos\varphi\right) & f_y\begin{pmatrix}-X_0\left(\sin\kappa\cos\phi\right) \\ -Y_0\left(\sin\kappa\sin\phi\sin\varphi + \cos\kappa\cos\varphi\right) \\ -Z_0\left(\sin\kappa\sin\phi\cos\varphi - \cos\kappa\sin\varphi\right)\end{pmatrix} + v_0\begin{pmatrix}X_0\left(-\sin\phi\right) - Y_0\left(\cos\phi\sin\varphi\right) \\ -Z_0\left(\cos\phi\cos\varphi\right)\end{pmatrix} \\ -\sin\phi & \cos\phi\sin\varphi & \cos\phi\cos\varphi & \begin{matrix}X_0\left(-\sin\phi\right) - Y_0\left(\cos\phi\sin\varphi\right) \\ -Z_0\left(\cos\phi\cos\varphi\right)\end{matrix} \end{bmatrix} \quad \textbf{[3-12]}$$

It can be observed from the last column of the matrix in **[3-12]** that the position of the camera in a 3D scene is directly related to the position of the principal point and the coefficients of the rotation matrix. This geometrically makes sense in a pinhole projection geometry**.** A more simplified formulation of **[3-12]** from **[3-1], [3-6]** can be expressed as follows:

$$P_{TM} = \begin{bmatrix} f_x r_{11} + u_0 r_{31} & f_x r_{12} + u_0 r_{32} & f_x r_{13} + u_0 r_{33} & f_x\left(-X_0 r_{11} - Y_0 r_{12} - Z_0 r_{13}\right) + u_0\left(-X_0 r_{31} - Y_0 r_{32} - Z_0 r_{33}\right) \\ f_y r_{21} + v_0 r_{31} & f_y r_{23} + v_0 r_{32} & f_y r_{23} + v_0 r_{33} & f_y\left(-X_0 r_{21} - Y_0 r_{23} - Z_0 r_{23}\right) + v_0\left(-X_0 r_{31} - Y_0 r_{32} - Z_0 r_{33}\right) \\ r_{31} & r_{32} & r_{33} & -X_0 r_{31} - Y_0 r_{32} - Z_0 r_{33} \end{bmatrix} \quad \textbf{[3-13]}$$

3.2.4. Proposed Fully Analytical Decomposition Solution

With at least eight 3-D world calibration points and their respective projected image points, it is possible to estimate the twelve coefficients of the projective transformation matrix using the Direct Linear Transformation algorithm. For computational advantages, let us call H the experimentally computed projective transformation matrix through the DLT algorithm with the eleven coefficients $H_1, H_2, H_3, H_4, H_5 \ldots . H_{11}$ as follows:

$$H = \begin{bmatrix} H_1 & H_2 & H_3 & H_4 \\ H_5 & H_6 & H_7 & H_8 \\ H_9 & H_{10} & H_{11} & 1 \end{bmatrix} \quad \textbf{[3-14]}$$

A direct comparison coefficient by coefficient cannot yet be established between the matrix in **[3-11]** and that in **[3-14]** because the computed projective transformation matrix H is scaled. To establish the equality between these matrices, the first scenario is to scale all the matrix coefficients in **[3-21]** by the last coefficient of the translation vector t_z. However, this scaling will result in the damages of geometric relationships that relate the various camera parameters within the projective transformation matrix. The second option is to find the estimate of the coefficient H_{12}, then rescale the coefficients $H_1, H_2, H_3, \ldots H_{11}$, before performing the inter coefficient comparison between both matrices. It can be observed in matrix **[3-11]** that the first three coefficients of the last row of the matrix are not concatenated with any other camera parameters. Thus, taking advantage of this isolation, the following equations are established:

$$\frac{r_{31}}{t_z} = H_9 \quad \textbf{[3-15.1]}$$

$$\frac{r_{32}}{t_z} = H_{10} \quad \textbf{[3-15.2]}$$

$$\frac{r_{33}}{t_z} = H_{11} \quad \textbf{[3-15.3]}$$

Elevating both sides of **[3-15.1]- [3-15.3]** to the quadratic power and then adding the results lead to the following:

$$\frac{1}{t_z^2}(r_{31}^2 + r_{32}^2 + r_{33}^2) = H_9^2 + H_{10}^2 + H_{11}^2 \quad \textbf{[3-16]}$$

From the orthogonality property of the rotation matrix, the expression in **[3-16]** can be simplified to the following:

$$t_z = \frac{1}{\sqrt{\left(H_9^2 + H_{10}^2 + H_{11}^2\right)}} \quad \textbf{[3-17]}$$

A rescaling of the matrix in **[3-14]** by **[3-17]** produces the following:

$$H = \begin{bmatrix} \frac{H_1}{\sqrt{H_9^2 + H_{10}^2 + H_{11}^2}} & \frac{H_2}{\sqrt{H_9^2 + H_{10}^2 + H_{11}^2}} & \frac{H_3}{\sqrt{H_9^2 + H_{10}^2 + H_{11}^2}} & \frac{H_4}{\sqrt{H_9^2 + H_{10}^2 + H_{11}^2}} \\ \frac{H_5}{\sqrt{H_9^2 + H_{10}^2 + H_{11}^2}} & \frac{H_6}{\sqrt{H_9^2 + H_{10}^2 + H_{11}^2}} & \frac{H_7}{\sqrt{H_9^2 + H_{10}^2 + H_{11}^2}} & \frac{H_8}{\sqrt{H_9^2 + H_{10}^2 + H_{11}^2}} \\ \frac{H_9}{\sqrt{H_9^2 + H_{10}^2 + H_{11}^2}} & \frac{H_{10}}{\sqrt{H_9^2 + H_{10}^2 + H_{11}^2}} & \frac{H_{11}}{\sqrt{H_9^2 + H_{10}^2 + H_{11}^2}} & \frac{1}{\sqrt{H_9^2 + H_{10}^2 + H_{11}^2}} \end{bmatrix} \quad \textbf{[3-18]}$$

From **[3-11]** and **[3-18]** the following twelve nonlinear equations can be formulated after simplifications:

$$f_x r_{11} + u_0 r_{31} = \frac{H_1}{\sqrt{H_9^2 + H_{10}^2 + H_{11}^2}} \quad \textbf{[3-19.1]}$$

$$f_x r_{12} + u_0 r_{32} = \frac{H_2}{\sqrt{H_9^2 + H_{10}^2 + H_{11}^2}} \quad \textbf{[3-19.2]}$$

$$f_x r_{13} + u_0 r_{33} = \frac{H_3}{\sqrt{H_9^2 + H_{10}^2 + H_{11}^2}} \quad \textbf{[3-19.3]}$$

$$f_x t_x + u_0 t_z = \frac{H_4}{\sqrt{H_9^2 + H_{10}^2 + H_{11}^2}} \quad \textbf{[3-19.4]}$$

$$f_y r_{21} + v_0 r_{31} = \frac{H_5}{\sqrt{H_9^2 + H_{10}^2 + H_{11}^2}} \quad \textbf{[3-19.5]}$$

$$f_y r_{23} + v_0 r_{32} = \frac{H_6}{\sqrt{H_9^2 + H_{10}^2 + H_{11}^2}} \quad \textbf{[3-19.6]}$$

$$f_y r_{23} + v_0 r_{33} = \frac{H_7}{\sqrt{H_9^2 + H_{10}^2 + H_{11}^2}} \quad \textbf{[3-19.7]}$$

$$f_y t_y + v_0 t_z = \frac{H_8}{\sqrt{H_9^2 + H_{10}^2 + H_{11}^2}} \quad \textbf{[3-19.8]}$$

$$r_{31} = \frac{H_9}{\sqrt{H_9^2 + H_{10}^2 + H_{11}^2}} \quad \textbf{[3-19.9]}$$

$$r_{32} = \frac{H_{10}}{\sqrt{H_9^2 + H_{10}^2 + H_{11}^2}} \quad \textbf{[3-19.10]}$$

$$r_{33} = \frac{H_{11}}{\sqrt{H_9^2 + H_{10}^2 + H_{11}^2}} \quad \textbf{[3-19.11]}$$

$$r_{34} = t_z = \frac{1}{\sqrt{H_9^2 + H_{10}^2 + H_{11}^2}} \quad \textbf{[3-19.12]}$$

Substituting the parameters in **[3-5]** into each equation in **[3-19.1]- [3-19.11]** leads to the following equations:

$$f_x \cos\kappa \cos\phi - u_0 \sin\phi = \frac{H_1}{\sqrt{H_9^2 + H_{10}^2 + H_{11}^2}} \quad \textbf{[3-20.1]}$$

$$f_x\left(\cos\kappa\sin\varphi\sin\phi-\cos\varphi\sin\kappa\right)+u_0\left(\sin\varphi\cos\phi\right)=\frac{H_2}{\sqrt{H_9^2+H_{10}^2+H_{11}^2}} \quad \textbf{[3-20.2]}$$

$$f_x\left(\cos\kappa\cos\varphi\sin\phi+\sin\varphi\sin\kappa\right)+u_0\left(\cos\varphi\cos\phi\right)=\frac{H_3}{\sqrt{H_9^2+H_{10}^2+H_{11}^2}} \quad \textbf{[3-20.3]}$$

$$f_x\begin{pmatrix}-X_0\left(\cos\kappa\cos\phi\right)\\-Y_0\left(\cos\kappa\sin\varphi\sin\phi-\cos\varphi\sin\kappa\right)\\-Z_0\left(\cos\kappa\cos\varphi\sin\phi+\sin\varphi\sin\kappa\right)\end{pmatrix}+u_0\begin{pmatrix}X_0\left(-\sin\phi\right)-Y_0\left(\sin\varphi\cos\phi\right)\\-Z_0\left(\cos\varphi\cos\phi\right)\end{pmatrix}=\frac{H_4}{\sqrt{H_9^2+H_{10}^2+H_{11}^2}} \quad \textbf{[3-20.4]}$$

$$f_y\sin\kappa\cos\phi-v_0\sin\phi=\frac{H_5}{\sqrt{H_9^2+H_{10}^2+H_{11}^2}} \quad \textbf{[3-20.5]}$$

$$f_y\left(\sin\kappa\sin\varphi\sin\phi+\cos\varphi\cos\kappa\right)+v_0\left(\sin\varphi\cos\phi\right)=\frac{H_6}{\sqrt{H_9^2+H_{10}^2+H_{11}^2}} \quad \textbf{[3-20.6]}$$

$$f_y\left(\sin\kappa\cos\varphi\sin\phi-\sin\varphi\cos\kappa\right)+v_0\left(\cos\varphi\cos\phi\right)=\frac{H_7}{\sqrt{H_9^2+H_{10}^2+H_{11}^2}} \quad \textbf{[3-20.7]}$$

$$f_y\begin{pmatrix}-X_0\left(\sin\kappa\cos\phi\right)\\-Y_0\left(\sin\kappa\sin\varphi\sin\phi+\cos\varphi\cos\kappa\right)\\-Z_0\left(\sin\kappa\cos\varphi\sin\phi-\sin\varphi\cos\kappa\right)\end{pmatrix}+v_0\begin{pmatrix}X_0\left(-\sin\phi\right)-Y_0\left(\sin\varphi\cos\phi\right)\\-Z_0\left(\cos\varphi\cos\phi\right)\end{pmatrix}=\frac{H_8}{\sqrt{H_9^2+H_{10}^2+H_{11}^2}} \quad \textbf{[3-20.8]}$$

$$-\sin\phi=\frac{H_9}{\sqrt{H_9^2+H_{10}^2+H_{11}^2}} \quad \textbf{[3-20.9]}$$

$$\sin\varphi\cos\phi=\frac{H_{10}}{\sqrt{H_9^2+H_{10}^2+H_{11}^2}} \quad \textbf{[3-20.10]}$$

$$\cos\varphi\cos\phi=\frac{H_{11}}{\sqrt{H_9^2+H_{10}^2+H_{11}^2}} \quad \textbf{[3-20.11]}$$

3.2.5. Calibration of individual camera pose parameters

A. Calibrating the third coefficient of the translation vector

From **[3-17]** the third coefficient of the translation vector was calibrated as follows:

$$t_z=\frac{1}{\sqrt{H_9^2+H_{10}^2+H_{11}^2}} \quad \textbf{[3-21]}$$

Since modern cameras produce upright images and considering that the focal is positive, the parameter estimated in **[3-21]** is of a positive sign.

B. Calibrating the three Coefficients of the Third Row of the Rotation Matrix

From **[3-19.9]- [3-19.11]** the three coefficients of the last row of the rotation matrix can be calibrated as follows:

$$r_{31} = \frac{H_9\sqrt{H_9^2 + H_{10}^2 + H_{11}^2}}{H_9^2 + H_{10}^2 + H_{11}^2} \quad \textbf{[3-22.1]}$$

$$r_{32} = \frac{H_{10}\sqrt{H_9^2 + H_{10}^2 + H_{11}^2}}{H_9^2 + H_{10}^2 + H_{11}^2} \quad \textbf{[3-22.2]}$$

$$r_{33} = \frac{H_{11}\sqrt{H_9^2 + H_{10}^2 + H_{11}^2}}{H_9^2 + H_{10}^2 + H_{11}^2} \quad \textbf{[3-22.3]}$$

Elevating the left and right sides of equations **[3-22.1]- [3-22.3]** to the power of two and then adding the respective results side by side leads to the following:

$$r_{31}^2 + r_{32}^2 + r_{33}^2 = \frac{H_9^2 + H_{10}^2 + H_{11}^2}{H_9^2 + H_{10}^2 + H_{11}^2} = 1 \quad \textbf{[3-22.4]}$$

From the results in **[3-22.4]** the last row of the rotation matrix satisfies the orthonormality property of the axes of a rotation matrix.

C. Calibrating the two first rotation angle

From **[3-20.9]** the following calibration algorithm can be derived:

$$\phi = \sin^{-1}\frac{-H_9}{\sqrt{\left(H_9^2 + H_{10}^2 + H_{11}^2\right)}} \quad \textbf{[3-23.1]}$$

It can be observed from **[3-19.2]-[3-19.8]** and **[3-19.10]-[3-19.12]** that the angle φ is associated with the coordinates of the camera location in a 3D scene X_0, Y_0, Z_0, the coordinates of the principal point u_0, v_0, the effective focal lengths f_x , f_y, as well as the other two rotation angles ϕ and κ through ten geometric constraints**.** In order to independently calibrate this angle φ while minimizing its reliance on the above-mentioned parameters, equation **[3-20.10]** can be divided by equation **[3-20.11]** to produce the following:

$$\varphi = \tan^{-1}\frac{H_{10}}{H_{11}} \quad \textbf{[3-23.2]}$$

An observation of **[3-19.1]- [3-19.9]** reveals that the angle κ is related to the coordinates of the camera location in the world reference system X_0, Y_0, Z_0, the coordinates of the principal point u_0, v_0, the effective focal lengths f_x, f_y as well as the other two rotation angles φ and ϕ through eight geometric constraints. To start the isolation of this angle from the above parameters, equation **[3-20.3]** can be multiplied with equation **[3-20.10]** to produce the following:

$$f_x \cos\varphi \sin\varphi \cos\phi \sin\phi \cos\kappa + f_x \cos\phi \sin\kappa \sin\varphi^2 + u_0 \cos\varphi \sin\varphi \cos\phi^2 = \frac{H_3 \times H_{10}}{H_9^2 + H_{10}^2 + H_{11}^2} \quad \textbf{[3-23.3]}$$

Multiplying **[3-20.2]** with **[3-20.11]** leads to the following:

$$f_x \cos\varphi \sin\varphi \cos\phi \sin\phi \cos\kappa - f_x \cos\phi \sin\kappa \cos\varphi^2 + u_0 \cos\varphi \sin\varphi \cos\phi^2 = \frac{H_2 \times H_{11}}{H_9^2 + H_{10}^2 + H_{11}^2} \quad \textbf{[3-23.4]}$$

Subtracting **[3-23.4]** from **[3-23.3]** can be formulated as follows:

$$f_x \cos\phi \sin\kappa = \frac{H_3 \times H_{10} - H_2 \times H_{11}}{H_9^2 + H_{10}^2 + H_{11}^2} \quad \textbf{[3-23.5]}$$

Similarly, multiplying **[3-20.7]** with **[3-20.10]** produces the following:

$$f_y \cos\phi \sin\phi \cos\varphi \sin\varphi \sin\kappa - f_y \cos\kappa \cos\phi \sin\varphi^2 + v_0 \sin\varphi \cos\varphi \cos\phi^2 = \frac{H_7 \times H_{10}}{H_9^2 + H_{10}^2 + H_{11}^2} \quad \textbf{[3-23.6]}$$

Multiplying **[3-20.6]** with **[3-20.11]** produces the following:

$$f_y \cos\varphi \sin\varphi \cos\phi \sin\phi \sin\kappa + f_y \cos\phi \cos\kappa \cos\varphi^2 + v_0 \cos\varphi \sin\varphi \cos\phi^2 = \frac{H_6 \times H_{11}}{H_9^2 + H_{10}^2 + H_{11}^2} \quad \textbf{[3-23.7]}$$

Subtracting **[3-23.6]** from **[3-23.7]** leads to the following formulation:

$$\frac{H_6 \times H_{11} - H_7 \times H_{10}}{H_9^2 + H_{10}^2 + H_{11}^2} = f_y \cos\kappa \cos\phi \quad \textbf{[3-23.8]}$$

Dividing **[3-23.5]** by **[3-23.8]** leads to the following:

$$\tan\kappa = \frac{f_y \left(H_3 \times H_{10} - H_2 \times H_{11}\right)}{f_x \left(H_6 \times H_{11} - H_7 \times H_{10}\right)} \quad \textbf{[3-23.9]}$$

D. Calibrating the coordinates of the principal point

Let π_1 be the quantity obtained by dividing **[3-20.9]** by t_z^2 and formulated as follows:

$$\pi_1 = \frac{-\sin\phi}{t_z^2} = \frac{H_9 \left(H_9^2 + H_{10}^2 + H_{11}^2\right)}{\sqrt{H_9^2 + H_{10}^2 + H_{11}^2}} \quad \textbf{[3-24.1]}$$

Let π_2 be the quantity obtained by dividing **[3-20.10]** by t_z^2 and formulated as follows:

$$\pi_2 = \frac{\sin\varphi \cos\phi}{t_z^2} = \frac{H_{10} \left(H_9^2 + H_{10}^2 + H_{11}^2\right)}{\sqrt{H_9^2 + H_{10}^2 + H_{11}^2}} \quad \textbf{[3-24.2]}$$

Finally let π_3 be the quantity resulting from the division of **[3-20.11]** by t_z^2 and formulated as follows:

$$\pi_3 = \frac{\cos\varphi \cos\phi}{t_z^2} = \frac{H_{11} \left(H_9^2 + H_{10}^2 + H_{11}^2\right)}{\sqrt{H_9^2 + H_{10}^2 + H_{11}^2}} \quad \textbf{[3-24.3]}$$

From **[3-20.1]- [3-20.4]** it can be observed that the first coordinate of the principal point u_0 is subjected to parameter coupling with rotation angles ϕ, φ and κ, the coordinates of the camera location X_0, Y_0, Z_0 and the first effective focal lengths f_x through four geometric constraints. To isolate this coordinate while preserving its geometric relationships with the above-mentioned parameters, equation **[3-20.1]** can be multiplied with the expression **[3-24.1]** to produce the following:

$$-f_x \cos\phi \sin\phi \cos\kappa + u_0 \sin\phi^2 = \frac{H_9 \times H_1}{H_9^2 + H_{10}^2 + H_{11}^2} \quad \textbf{[3-25.1]}$$

Multiplying **[3-20.2]** with **[3-24.2]** leads to the following formulation:

$$f_x \cos\kappa \cos\phi \sin\phi \sin\varphi^2 - f_x \cos\varphi \sin\varphi \cos\phi \sin\kappa + u_0 \cos\phi^2 \sin\varphi^2 = \frac{H_2 \times H_{10}}{H_9^2 + H_{10}^2 + H_{11}^2} \quad \textbf{[3-25.2]}$$

Similarly, multiplying **[3-20.3.]** with **[3-24.3]** produces the following:

$$f_x \cos\kappa \cos\phi \sin\phi \cos\varphi^2 + f_x \cos\varphi \sin\varphi \cos\phi \sin\kappa + u_0 \cos\varphi^2 \cos\phi^2 = \frac{H_3 \times H_{11}}{H_9^2 + H_{10}^2 + H_{11}^2} \quad \textbf{[3-25.3]}$$

Adding **[3-25.2]** to **[3-25.3]** side by side produces the following:

$$f_x \cos\kappa \cos\phi \sin\phi + u_0 \cos\phi^2 = \frac{H_2 \times H_{10} + H_3 \times H_{11}}{H_9^2 + H_{10}^2 + H_{11}^2} \quad \textbf{[3-25.4]}$$

Adding **[3-25.1]** to **[3-25.4]** leads to the following calibration of the first coordinate of the principal point:

$$u_0 = \frac{H_1 \times H_9 + H_2 \times H_{10} + H_3 \times H_{11}}{H_9^2 + H_{10}^2 + H_{11}^2} \quad \textbf{[3-25.5]}$$

It can be observed from **[3-25.5]** that the calibration of the coordinate only relies on the coefficients of the projective transformation matrix H and not those of the matrix in **[3-21].** From equations **[3-20.5]- [3-20.8]** it can be noticed that the second coordinate of the principal point v_0 is also related to the parameters of camera location X_0, Y_0, Z_0,the rotation angles ϕ, φ, κ and the effective focal length f_y through four geometric constraints, resulting in parameter coupling. To begin the isolation of this coordinate from the parameter coupling while preserving the geometric constraints that relate the coordinate to the other parameters, equation **[3-20.6]** can be multiplied with equation **[3-24.2]** to produce the following:

$$f_y \cos\phi \sin\phi \sin\kappa \sin\varphi^2 + f_y \cos\varphi \sin\varphi \cos\phi \cos\kappa + v_0 \sin\varphi^2 \cos\phi^2 = \frac{H_6 \times H_{10}}{H_9^2 + H_{10}^2 + H_{11}^2} \quad \textbf{[3-25.6]}$$

Similarly, multiplying equation **[3-20.7]** with equation [**3-24.3]** produces the following:

$$f_y \cos\phi \sin\phi \sin\kappa \cos\varphi^2 - f_y \cos\varphi \sin\varphi \cos\phi \cos\kappa + v_0 \cos\varphi^2 \cos\phi^2 = \frac{H_7 \times H_{11}}{H_9^2 + H_{10}^2 + H_{11}^2} \quad \textbf{[3-25.7]}$$

Adding **[3-25.6]** to **[3-25.7]** side by side produces the following:

$$f_y \cos\phi \sin\phi \sin\kappa + v_0 \cos\phi^2 = \frac{H_6 \times H_{10} + H_7 \times H_{11}}{H_9^2 + H_{10}^2 + H_{11}^2} \quad \textbf{[3-25.8]}$$

Similarly, multiplying equation [**3-20.5]** with equation [**3-24.1]** leads to the following:

$$-f_y \cos\phi \sin\phi \sin\kappa + v_0 \sin\phi^2 = \frac{H_5 \times H_9}{H_9^2 + H_{10}^2 + H_{11}^2} \quad \textbf{[3-25.9]}$$

Adding **[3-25.8]** and **[3-25.9]** produces the following calibration of the second coordinate of the principal point:

$$v_0 = \frac{H_6 \times H_{10} + H_7 \times H_{11} + H_5 \times H_9}{H_9^2 + H_{10}^2 + H_{11}^2} \quad \textbf{[3-25.10]}$$

Like the first coordinate of the principal point, the second coordinate is calibrated solely from the coefficients of the projective transformation matrix H.

E. Calibrating the first effective focal length and the three coefficients of the second row of the rotation matrix

From **[3-20.1]-[3-20.4]** it is observed that the first effective focal length f_x is subjected to parameter coupling through four geometric constraints that relate the parameter to the first coordinate of the principal point u_0, the three rotation angles ϕ, φ, κ and the parameters of

camera location in the 3D scene X_0 , Y_0 , Z_0 . In order to independently calibrate this parameter, the first coordinate of the principal point needs to be eliminated from the expressions in **[3-20.1]-[3-20.4].** At first inspection, this process seems very challenging. However, from an analysis of the expressions **[3-20.1]–[3-20.12]** some methodical trigonometric function manipulations are needed to achieve the above goal. First, let us consider ρ_1 to be the product obtained after multiplying the expression **[3-24.2]** with **[3-20.1]** and formulated as follows:

$$f_x \cos\kappa \sin\varphi \cos\phi^2 - u_0 \cos\phi \sin\phi \sin\varphi = \frac{H_1 \times H_{10}}{H_9^2 + H_{10}^2 + H_{11}^2} \qquad \textbf{[3-26.1]}$$

Similarly, let ρ_2 be a quantity obtained by multiplying equation **[3-20.2]** with equation **[3-24.1]** and formulated as follows:

$$-f_x \cos\kappa \sin\varphi \sin\phi^2 + f_x \cos\varphi \sin\phi \sin\kappa - u_0 \cos\phi \sin\phi \sin\varphi = \frac{H_2 \times H_9}{H_9^2 + H_{10}^2 + H_{11}^2} \qquad \textbf{[3-26.2]}$$

Subtracting **[3-26.1]** from **[3-26.2]** produces the following:

$$f_x \left(\cos\varphi \sin\phi \sin\kappa - \cos\kappa \sin\varphi\right) = \frac{H_2 \times H_9 - H_1 \times H_{10}}{H_9^2 + H_{10}^2 + H_{11}^2} \qquad \textbf{[3-26.3]}$$

From the rotation matrix in **[3-5],** the expression in **[3-26.3]** can be simplified as follows:

$$\frac{H_2 \times H_9 - H_1 \times H_{10}}{H_9^2 + H_{10}^2 + H_{11}^2} = f_x r_{23} \qquad \textbf{[3-26.4]}$$

Let ρ_3 be a quantity obtained by multiplying **[3-20.3]** with **[3-24.1]** and formulated as follows:

$$-f_x \left(\cos\kappa \cos\varphi \sin\phi^2 + \sin\phi \sin\varphi \sin\kappa\right) - u_0 \cos\phi \sin\phi \cos\varphi = \frac{H_3 \times H_9}{H_9^2 + H_{10}^2 + H_{11}^2} \qquad \textbf{[3-26.5]}$$

Similarly let ρ_4 be a quantity obtained by multiplying the expression **[3-20.1]** with **[3-24.3]** and formulated as follows:

$$f_x \cos\kappa \cos\varphi \cos\phi^2 - u_0 \cos\phi \sin\phi \cos\varphi = \frac{H_1 \times H_{11}}{H_9^2 + H_{10}^2 + H_{11}^2} \qquad \textbf{[3-26.6]}$$

Subtracting **[3-26.5]** from **[3-26.6]** produces the following:

$$f_x \left(\cos\kappa \cos\varphi + \sin\phi \sin\varphi \sin\kappa\right) = \frac{H_1 \times H_{11} - H_3 \times H_9}{H_9^2 + H_{10}^2 + H_{11}^2} \qquad \textbf{[3-26.7]}$$

From the matrix **[3-5]** the expression **[3-26.7]** is equivalent to the following:

$$\frac{H_1 \times H_{11} - H_3 \times H_9}{H_9^2 + H_{10}^2 + H_{11}^2} = f_x r_{22} \qquad \textbf{[3-26.8]}$$

Let ρ_5 be a quantity obtained by multiplying the expression **[3-20.2]** with **[3-24.4]** and formulated as follows:

$$f_x \cos\phi \sin\phi \cos\varphi \sin\varphi \cos\kappa - f_x \cos\phi \sin\kappa \cos\varphi^2 + u_0 \cos\varphi \sin\varphi \cos\phi^2 = \frac{H_2 \times H_{11}}{H_9^2 + H_{10}^2 + H_{11}^2} \qquad \textbf{[3-26.9]}$$

Finally let ρ_6 be a quantity resulting from the multiplication of equation **[3-20.3]** with equation **[3-24.2]** and formulated as follows:

$$f_x \cos\varphi \sin\varphi \cos\phi \sin\phi \cos\kappa + f_x \cos\phi \sin\kappa \sin\varphi^2 + u_0 \cos\varphi \sin\varphi \cos\phi^2 = \frac{H_3 \times H_{10}}{H_9^2 + H_{10}^2 + H_{11}^2} \qquad \textbf{[3-26.10]}$$

Subtracting **[3-26.9]** from **[3-26.10]** produces the following equality:

$$f_x \cos\phi \sin\kappa = \frac{H_3 \times H_{10} - H_2 \times H_{11}}{H_9^2 + H_{10}^2 + H_{11}^2} \quad \textbf{[3-26.11]}$$

From the matrix **[3-5],** the expression **[3-26.11]** was simplified to the following:

$$\frac{H_3 \times H_{10} - H_2 \times H_{11}}{H_9^2 + H_{10}^2 + H_{11}^2} = f_x \, \mathrm{r}_{21} \quad \textbf{[3-26.12]}$$

Elevating both sides of **[3-26.12], [3-26.8]** and **[3-26.4]** to the quadratic power and then adding the results side by side, respectively, produces the following:

$$f_x^2 \left(r_{21}^2 + r_{22}^2 + r_{23}^2\right) = \frac{\left(H_3 \times H_{10} - H_2 \times H_{11}\right)^2 + \left(H_1 \times H_{11} - H_3 \times H_9\right)^2 + \left(H_2 \times H_9 - H_1 \times H_{10}\right)^2}{H_9^2 + H_{10}^2 + H_{11}^2} \quad \textbf{[3-26.13]}$$

From the orthonormal properties of the axes of a rotation matrix, the first effective focal length can be calibrated from **[3-26.13]** as follows:

$$f_x = \pm \frac{\sqrt{\left(H_3 \times H_{10} - H_2 \times H_{11}\right)^2 + \left(H_1 \times H_{11} - H_3 \times H_9\right)^2 + \left(H_2 \times H_9 - H_1 \times H_{10}\right)^2}}{H_9^2 + H_{10}^2 + H_{11}^2} \quad \textbf{[3-26.14]}$$

With consideration that the focal length is a positive measure for modern cameras that produce upright photographs and the fact that the pixel measure in the x direction is always positive regardless of the origin of the image coordinate system in pixel being located at the top left or the bottom left corner of the image, the estimate of this parameter is consequently of positive sign. From **[3-26.12]** the first coefficient of the second row of the rotation matrix was calibrated as follows:

$$\mathrm{r}_{21} = \frac{H_3 \times H_{10} - H_2 \times H_{11}}{\sqrt{\left(H_3 \times H_{10} - H_2 \times H_{11}\right)^2 + \left(H_1 \times H_{11} - H_3 \times H_9\right)^2 + \left(H_2 \times H_9 - H_1 \times H_{10}\right)^2}} \quad \textbf{[3-26.15]}$$

Similarly, from **[3-26.8]** the second coefficient of the second row of the rotation matrix was calibrated as follows:

$$r_{22} = \frac{H_1 \times H_{11} - H_3 \times H_9}{\sqrt{\left(H_3 \times H_{10} - H_2 \times H_{11}\right)^2 + \left(H_1 \times H_{11} - H_3 \times H_9\right)^2 + \left(H_2 \times H_9 - H_1 \times H_{10}\right)^2}} \quad \textbf{[3-26.16]}$$

Finally, from **[3-26.4]** the last coefficient of the second row of the rotation matrix was calibrated as follows:

$$r_{23} = \frac{H_2 \times H_9 - H_1 \times H_{10}}{\sqrt{\left(H_3 \times H_{10} - H_2 \times H_{11}\right)^2 + \left(H_1 \times H_{11} - H_3 \times H_9\right)^2 + \left(H_2 \times H_9 - H_1 \times H_{10}\right)^2}} \quad \textbf{[3-26.17]}$$

Elevating the left and right sides of equations **[3-26.15], [3-26.16]** and **[3-26.17]** to the quadratic power and then adding the respective results leads to the following:

$$r_{21}^2 + r_{22}^2 + r_{23}^2 = \frac{\left(H_3 \times H_{10} - H_2 \times H_{11}\right)^2 + \left(H_1 \times H_{11} - H_3 \times H_9\right)^2 + \left(H_2 \times H_9 - H_1 \times H_{10}\right)^2}{\left(H_3 \times H_{10} - H_2 \times H_{11}\right)^2 + \left(H_1 \times H_{11} - H_3 \times H_9\right)^2 + \left(H_2 \times H_9 - H_1 \times H_{10}\right)^2} = 1 \quad \textbf{[3-26.18]}$$

The second row of the rotation matrix satisfies the orthonormality property of the axes of a rotation matrix with its norm equal to one.

F. Calibrating the second effective focal lengths, the three coefficients of the first row of the rotation matrix and the third rotation angle

Let λ_1 be a quantity obtained by multiplying the expression in **[3-20.6]** with that in **[3-24.3]** and formulated as follows:

$$f_y \cos\varphi \sin\varphi \cos\phi \sin\phi \sin\kappa + f_y \cos\phi \cos\kappa \cos\varphi^2 + v_0 \cos\varphi \sin\varphi \cos\phi^2 = \frac{H_6 \times H_{11}}{H_9^2 + H_{10}^2 + H_{11}^2} \quad \textbf{[3-27.1]}$$

Similarly, let λ_2 be a quantity obtained by multiplying the expression **[3-20.7]** with the expression **[3-24.2]** and formulated as follows:

$$f_y \cos\varphi \sin\varphi \cos\phi \sin\phi \sin\kappa - f_y \cos\kappa \cos\phi \sin\varphi^2 + v_0 \cos\varphi \sin\varphi \cos\phi^2 = \frac{H_7 \times H_{10}}{H_9^2 + H_{10}^2 + H_{11}^2} \quad \textbf{[3-27.2]}$$

Subtracting **[3-27.2]** from **[3-27.1]** produces the following:

$$\frac{H_6 \times H_{11} - H_7 \times H_{10}}{H_9^2 + H_{10}^2 + H_{11}^2} = f_y \cos\kappa \cos\phi \quad \textbf{[3-27.3]}$$

From the matrix **[3-5],** the expression **[3-27.3]** can be simplified as follows:

$$\frac{H_6 \times H_{11} - H_7 \times H_{10}}{H_9^2 + H_{10}^2 + H_{11}^2} = f_y \, \mathrm{r}_{11} \quad \textbf{[3-27.4]}$$

Let λ_3 be the quantity obtained by multiplying the expression **[3-20.5]** with the expression **[3-24.3]** and formulated as follows:

$$f_y \cos\varphi \sin\kappa \cos\phi^2 - v_0 \cos\phi \sin\phi \cos\varphi = \frac{H_5 \times H_{11}}{H_9^2 + H_{10}^2 + H_{11}^2} \quad \textbf{[3-27.5]}$$

Let λ_4 be a quantity obtained by multiplying the expression **[3-20.7]** with the expression **[3-24.1]** and formulated as follows:

$$-f_y \sin\kappa \cos\varphi \sin\phi^2 + f_y \cos\kappa \sin\phi \sin\varphi - v_0 \cos\phi \sin\phi \cos\varphi = \frac{H_7 \times H_9}{H_9^2 + H_{10}^2 + H_{11}^2} \quad \textbf{[3-27.6]}$$

Subtracting **[3-27.5]** from **[3-27.6]** leads to the following:

$$f_y \left(\cos\kappa \sin\phi \sin\varphi - \sin\kappa \cos\varphi\right) = \frac{H_7 \times H_9 - H_5 \times H_{11}}{H_9^2 + H_{10}^2 + H_{11}^2} \quad \textbf{[3-27.7]}$$

From the rotation matrix **[3-5],** the expression **[3-27.7]** can be simplified as follows:

$$\frac{H_7 \times H_9 - H_5 \times H_{11}}{H_9^2 + H_{10}^2 + H_{11}^2} = f_y r_{12} \quad \textbf{[3-27.8]}$$

Let λ_5 be a quantity resulting from multiplying the expression **[3-20.5]** with the expression **[3-24.2]** and formulated as follows:

$$f_y \sin\varphi \sin\kappa \cos\phi^2 - v_0 \cos\phi \sin\phi \sin\varphi = \frac{H_5 \times H_{10}}{H_9^2 + H_{10}^2 + H_{11}^2} \quad \textbf{[3-27.9]}$$

Finally, let λ_6 be a quantity obtained after multiplying the expression **[3-20.6]** with the expression **[3-24.1]** and formulated as follows:

$$-f_y \sin\kappa \sin\varphi \sin\phi^2 - f_y \cos\varphi \cos\kappa \sin\phi - v_0 \cos\phi \sin\phi \sin\varphi = \frac{H_6 \times H_9}{H_9^2 + H_{10}^2 + H_{11}^2} \quad \textbf{[3-27.10]}$$

Subtracting **[3-27.9]** from **[3-27.10]** leads to the following:

$$\frac{H_5 \times H_{10} - H_6 \times H_9}{H_9^2 + H_{10}^2 + H_{11}^2} = f_y \left(\sin\varphi \sin\kappa + \cos\varphi \cos\kappa \sin\phi \right) \quad \textbf{[3-27.11]}$$

From the rotation matrix in **[3-5],** the expression in **[3-27.11]** can be simplified as follows:

$$\frac{H_5 \times H_{10} - H_6 \times H_9}{H_9^2 + H_{10}^2 + H_{11}^2} = f_y r_{13} \quad \textbf{[3-27.12]}$$

Elevating both sides of expressions in **[3-27.4], [3-27.8]** and **[3-27.12]** to the quadratic power, then adding the results side by reside, respectively the following is obtained:

$$f_y^2 \left(r_{11}^2 + r_{12}^2 + r_{13}^2 \right) = \frac{\left(H_6 \times H_{11} - H_7 \times H_{10} \right)^2 + \left(H_7 \times H_9 - H_5 \times H_{11} \right)^2 + \left(H_5 \times H_{10} - H_6 \times H_9 \right)^2}{H_9^2 + H_{10}^2 + H_{11}^2} \quad \textbf{[3-27.13]}$$

From the orthogonality property of the rotation matrix, the second effective focal length can be calibrated as follows:

$$f_y = \frac{\sqrt{\left(H_6 \times H_{11} - H_7 \times H_{10} \right)^2 + \left(H_7 \times H_9 - H_5 \times H_{11} \right)^2 + \left(H_5 \times H_{10} - H_6 \times H_9 \right)^2}}{\sqrt{H_9^2 + H_{10}^2 + H_{11}^2}} \quad \textbf{[3-27.14]}$$

It has been reported in the work of **Ganapathy (1984)** that in general two only parameters among t_z, f_x and f_y must be positive. Since the parameters t_z and f_x are already positive, the correct value of the second effective focal length to be considered here is the negative estimate. From **[3-26.4],** the first coefficient of the first row of the rotation matrix can be calibrated as follows:

$$\mathrm{r}_{11} = \frac{H_7 \times H_{10} - H_6 \times H_{11}}{\sqrt{\left(H_6 \times H_{11} - H_7 \times H_{10} \right)^2 + \left(H_7 \times H_9 - H_5 \times H_{11} \right)^2 + \left(H_5 \times H_{10} - H_6 \times H_9 \right)^2}} \quad \textbf{[3-27.15]}$$

From **[3-27.8],** the second coefficient of the first row of the rotation matrix can be calibrated as follows:

$$r_{12} = \frac{H_5 \times H_{11} - H_7 \times H_9}{\sqrt{\left(H_6 \times H_{11} - H_7 \times H_{10} \right)^2 + \left(H_7 \times H_9 - H_5 \times H_{11} \right)^2 + \left(H_5 \times H_{10} - H_6 \times H_9 \right)^2}} \quad \textbf{[3-27.16]}$$

Finally, from **[3-27.12],** the third coefficient of the first row of the rotation matrix can be calibrated as follows:

$$r_{13} = \frac{H_6 \times H_9 - H_5 \times H_{10}}{\sqrt{\left(H_6 \times H_{11} - H_7 \times H_{10} \right)^2 + \left(H_7 \times H_9 - H_5 \times H_{11} \right)^2 + \left(H_5 \times H_{10} - H_6 \times H_9 \right)^2}} \quad \textbf{[3-27.17]}$$

Elevating the left and right sides of equations **[3-27.15], [3-27.16],** and **[3-27.17]** to the quadratic power and then adding the respective results leads to the following:

$$r_{11}^2 + r_{12}^2 + r_{13}^2 = \frac{\left(H_6 \times H_{11} - H_7 \times H_{10} \right)^2 + \left(H_7 \times H_9 - H_5 \times H_{11} \right)^2 + \left(H_5 \times H_{10} - H_6 \times H_9 \right)^2}{\left(H_6 \times H_{11} - H_7 \times H_{10} \right)^2 + \left(H_7 \times H_9 - H_5 \times H_{11} \right)^2 + \left(H_5 \times H_{10} - H_6 \times H_9 \right)^2} = 1 \quad \textbf{[3-27.18]}$$

The rotation matrix axis represented by the first row of the rotation matrix also satisfies the orthonormality property of the rotation matrix axes with its norm equal to one. Substituting **[3-26.14]** and **[3-27.14]** into **[3-23.9]** enables us to calibrate the third rotation angle as follows:

$$\tan\kappa = \frac{(H_2 \times H_{11} - H_3 \times H_{10})\sqrt{(H_6 \times H_{11} - H_7 \times H_{10})^2 + (H_7 \times H_9 - H_5 \times H_{11})^2 + (H_5 \times H_{10} - H_6 \times H_9)^2}}{(H_6 \times H_{11} - H_7 \times H_{10})\sqrt{(H_3 \times H_{10} - H_2 \times H_{11})^2 + (H_1 \times H_{11} - H_3 \times H_9)^2 + (H_2 \times H_9 - H_1 \times H_{10})^2}} \quad \textbf{[3-27.19]}$$

G. Calibrating the first two coefficients of the translation vector

From **[3-19.4],** the first coefficient of the translation vector can be calibrated as follows:

$$t_x = \frac{H_4\left(H_9^2 + H_{10}^2 + H_{11}^2\right) - \left(H_1 \times H_9 + H_2 \times H_{10} + H_3 \times H_{11}\right)}{\left(H_9^2 + H_{10}^2 + H_{11}^2\right)\sqrt{(H_3 \times H_{10} - H_2 \times H_{11})^2 + (H_1 \times H_{11} - H_3 \times H_9)^2 + (H_2 \times H_9 - H_1 \times H_{10})^2}} \quad \textbf{[3-28.1]}$$

From **[3-19.8],** the second coefficient of the translation vector can be calibrated as follows:

$$t_y = \frac{H_8\left(H_9^2 + H_{10}^2 + H_{11}^2\right) - \left(H_6 \times H_{10} + H_7 \times H_{11} + H_5 \times H_9\right)}{\left(H_9^2 + H_{10}^2 + H_{11}^2\right)\sqrt{(H_6 \times H_{11} - H_7 \times H_{10})^2 + (H_7 \times H_9 - H_5 \times H_{11})^2 + (H_5 \times H_{10} - H_6 \times H_9)^2}} \quad \textbf{[3-28.2]}$$

H. Calibrating the coordinates of the camera position in 3D space.

From matrices **[3-7]** and **[3-8],** one can derive the following transformation:

$$\begin{bmatrix} t_x \\ t_y \\ t_z \end{bmatrix} = \begin{bmatrix} r_{11} & r_{12} & r_{13} \\ r_{21} & r_{22} & r_{23} \\ r_{31} & r_{32} & r_{33} \end{bmatrix} \begin{bmatrix} -X_0 \\ -Y_0 \\ -Z_0 \end{bmatrix} \quad \textbf{[3-29]}$$

It can be observed from the above transformation that the central matrix is the rotation matrix in **[3-5].** From the inverse property of a rotation matrix, we can multiply both sides of **[3-29]** by its transpose to achieve the following:

$$\begin{bmatrix} -X_0 \\ -Y_0 \\ -Z_0 \end{bmatrix} = \begin{bmatrix} r_{11} & r_{21} & r_{31} \\ r_{12} & r_{22} & r_{32} \\ r_{13} & r_{23} & r_{33} \end{bmatrix} \begin{bmatrix} t_x \\ t_y \\ t_z \end{bmatrix} \quad \textbf{[3-30]}$$

From **[3-30],** the following three equations can be derived:

$$X_0 = -r_{11}t_x - r_{21}t_y - r_{31}t_z \quad \textbf{[3-31.1]}$$

$$Y_0 = -r_{12}t_x - r_{22}t_y - r_{32}t_z \quad \textbf{[3-31.2]}$$

$$Z_0 = -r_{13}t_x - r_{23}t_y - r_{33}t_z \quad \textbf{[3-31.3]}$$

Since the parameters t_x , t_y ,t_z, r_{11}, r_{12} , $r_{13} \ldots r_{33}$, have already been independently calibrated, as a consequence, the derived parameters of camera location in a 3D scene are also independently estimated through the algorithms in **[3-31.1]– [3-31.3].**

3.2.6 Modelling the DLT solution for the projective transformation matrix.

DLT is a linear formulation of the transformation of point coordinates from the 3D scene to their respective 2D image coordinates. The formulation of the DLT algorithm can vary, with some algorithms not considering the principal point coordinates and radial lens distortion for camera pose estimation. Some formulations of the algorithm consider the coordinates of the principal point, the three rotation angles, as well as the focal length or effective focal lengths; other formulations go further by adding radial and tangential lens distortions into the algorithm. However, it has been reported that performing a full camera calibration through the DLT would result in inaccurate estimates of the parameters (**Kim, 2021**). For this reason, in this section, the DLT solution is formulated solely for the purpose of obtaining the twelve coefficients of the projective transformation matrix. These coefficients are needed to independently solve each parameter of the camera's location and orientation in a 3D scene, as well as calibrate the effective focal lengths and the coordinates of the principal point. From the matrix **[3-14],** the transformation from 3D camera coordinates to 2D image coordinates in pixels can be established as follows:

$$u - u_0 = f_x \frac{r_{11}\left(X_\omega - X_0\right) + r_{12}\left(Y_\omega - Y_0\right) + r_{13}\left(Z_\omega - Z_0\right)}{r_{31}\left(X_\omega - X_0\right) + r_{32}\left(Y_\omega - Y_0\right) + r_{33}\left(Z_\omega - Z_0\right)} \quad \textbf{[3-32.1]}$$

$$v - v_0 = f_y \frac{r_{21}\left(X_\omega - X_0\right) + r_{22}\left(Y_\omega - Y_0\right) + r_{23}\left(Z_\omega - Z_0\right)}{r_{31}\left(X_\omega - X_0\right) + r_{32}\left(Y_\omega - Y_0\right) + r_{33}\left(Z_\omega - Z_0\right)} \quad \textbf{[3-32.2]}$$

Expanding the expressions in the numerator and denominators from both equations produces the following after some rearrangements:

$$u = \frac{X_\omega f_x r_{11} + Y_\omega f_x r_{12} + Z_\omega f_x r_{13} - f_x\left(X_0 r_{11} + Y_0 r_{12} + Z_0 r_{13}\right) + u_0\left(X_\omega r_{31} + Y_\omega r_{32} + Z_\omega r_{33} - \left(X_0 r_{31} + r_{32} Y_0 + Z_0 r_{33}\right)\right)}{X_\omega r_{31} + Y_\omega r_{32} + Z_\omega r_{33} - \left(X_0 r_{31} + r_{32} Y_0 + Z_0 r_{33}\right)} \quad \textbf{[3-32.3]}$$

$$v = \frac{X_\omega f_y r_{21} + Y_\omega f_y r_{22} + Z_\omega f_y r_{23} + f_y\left(-X_0 r_{21} - Y_0 r_{22} - Z_0 r_{23}\right) + v_0\left(X_\omega r_{31} + Y_\omega r_{32} + Z_\omega r_{33} + \left(-X_0 r_{31} - r_{32} Y_0 - Z_0 r_{33}\right)\right)}{X_\omega r_{31} + Y_\omega r_{32} + Z_\omega r_{33} + \left(-X_0 r_{31} - r_{32} Y_0 - Z_0 r_{33}\right)} \quad \textbf{[3-32.4]}$$

Let's pose the following:

$$H_1 = f_x r_{11} \quad \textbf{[3-33.1]}$$

$$H_2 = f_x r_{12} \quad \textbf{[3-33.2]}$$

$$H_3 = f_x r_{13} \quad \textbf{[3-33.3]}$$

$$H_4 = -f_x\left(X_0 r_{11} + Y_0 r_{12} + Z_0 r_{13}\right) + u_0\left(X_\omega r_{31} + Y_\omega r_{32} + Z_\omega r_{33} - \left(X_0 r_{31} + r_{32} Y_0 + Z_0 r_{33}\right)\right) \quad \textbf{[3-33.4]}$$

$$H_5 = f_y r_{21} \quad \textbf{[3-33.5]}$$

$$H_6 = f_y r_{22} \quad \textbf{[3-33.6]}$$

$$H_7 = f_y r_{23} \quad \textbf{[3-33.7}$$

$$H_8 = f_y\left(-X_0 r_{21} - Y_0 r_{22} - Z_0 r_{23}\right) + v_0\left(X_\omega r_{31} + Y_\omega r_{32} + Z_\omega r_{33} + \left(-X_0 r_{31} - r_{32} Y_0 - Z_0 r_{33}\right)\right) \quad \textbf{[3-33.8]}$$

$$H_9 = r_{31} \quad \textbf{[3-33.9]}$$

$$H_{10} = r_{32} \quad \textbf{[3-33.10]}$$

$$H_{11} = r_{33} \quad \textbf{[3-33.11]}$$

$$H_{12} = r_{33} \quad \textbf{[3-33.12]}$$

From **[3-33.1]** to **[3-33.12]** equations **[3-32.1]** and **[3-32.2]** can be reformulated as follows:

$$u = \frac{X_\omega H_1 + Y_\omega H_2 + Z_\omega H_3 + H_4}{X_\omega H_9 + Y_\omega H_{10} + Z_\omega H_{11} + H_{12}} \quad \textbf{[3-34.1]}$$

$$v = \frac{X_\omega H_5 + Y_\omega H_6 + Z_\omega H_7 + H_8}{X_\omega H_9 + Y_\omega H_{10} + Z_\omega H_{11} + H_{12}} \quad \textbf{[3-34.2]}$$

The transformations in **[3-34.1]** and **[3-34.2]** can be formulated as a matrix transformation as follows:

$$\begin{bmatrix} u \\ v \\ 1 \end{bmatrix} = \begin{bmatrix} H_1 & H_2 & H_3 & H_4 \\ H_5 & H_6 & H_7 & H_8 \\ H_9 & H_{10} & H_{11} & H_{12} \end{bmatrix} \begin{bmatrix} X_\omega \\ Y_\omega \\ Z_\omega \\ 1 \end{bmatrix} \quad \textbf{[3-34.3]}$$

From **[3-34.1]– [3-34.2]** it can be observed that the DLT parameters are made of parameters of camera orientation, camera location, effective focal lengths, as well as the coordinates of the principal point. From **[3-34.3],** a solution for the parameters of the direct linear transformation can be formulated as follows:

$$\begin{bmatrix} u_1 \\ v_1 \\ 1 \\ u_2 \\ v_2 \\ 1 \\ u_3 \\ v_3 \\ 1 \\ u_4 \\ v_4 \\ 1 \end{bmatrix} = \begin{bmatrix} X_{\omega-1} & Y_{\omega-1} & Z_{\omega-1} & 1 & 0 & 0 & 0 & 0 & 0 & 0 & 0 & 0 \\ 0 & 0 & 0 & 0 & X_{\omega-1} & Y_{\omega-1} & Z_{\omega-1} & 1 & 0 & 0 & 0 & 0 \\ 0 & 0 & 0 & 0 & 0 & 0 & 0 & 0 & X_{\omega-1} & Y_{\omega-1} & Z_{\omega-1} & 1 \\ X_{\omega-2} & Y_{\omega-2} & Z_{\omega-2} & 1 & 0 & 0 & 0 & 0 & 0 & 0 & 0 & 0 \\ 0 & 0 & 0 & 0 & X_{\omega-2} & Y_{\omega-2} & Z_{\omega-2} & 1 & 0 & 0 & 0 & 0 \\ 0 & 0 & 0 & 0 & 0 & 0 & 0 & 0 & X_{\omega-2} & Y_{\omega-2} & Z_{\omega-2} & 1 \\ X_{\omega-3} & Y_{\omega-3} & Z_{\omega-3} & 1 & 0 & 0 & 0 & 0 & 0 & 0 & 0 & 0 \\ 0 & 0 & 0 & 0 & X_{\omega-3} & Y_{\omega-3} & Z_{\omega-3} & 1 & 0 & 0 & 0 & 0 \\ 0 & 0 & 0 & 0 & 0 & 0 & 0 & 0 & X_{\omega-3} & Y_{\omega-3} & Z_{\omega-3} & 1 \\ X_{\omega-4} & Y_{\omega-4} & Z_{\omega-4} & 1 & 0 & 0 & 0 & 0 & 0 & 0 & 0 & 0 \\ 0 & 0 & 0 & 0 & X_{\omega-4} & Y_{\omega-4} & Z_{\omega-4} & 1 & 0 & 0 & 0 & 0 \\ 0 & 0 & 0 & 0 & 0 & 0 & 0 & 0 & X_{\omega-4} & Y_{\omega-4} & Z_{\omega-4} & 1 \end{bmatrix} \begin{bmatrix} H_1 \\ H_2 \\ H_3 \\ H_4 \\ H_5 \\ H_6 \\ H_7 \\ H_8 \\ H_9 \\ H_{10} \\ H_{11} \\ H_{12} \end{bmatrix} \quad \textbf{[3-35]}$$

Unlike some currently proposed algorithms that require a minimum of six to eight point-correspondences, one advantage of the proposed solution in matrix **[3-35]** is that it only requires a minimum of four point-correspondences to solve the twelve parameters of the DLT through a least squares solution or an orthogonal decomposition provided that the calibration control points are not coplanar with the origin of the 3D scene coordinate system to minimize the number of zero column vectors in the solution.

3.2.7 Calibrating the Coefficients of the Projective Transformation matrix from 3D and 2D points Coordinates

To determine the parameters of the Direct Linear Transformation (DLT), a minimum of four-point correspondences is required. However, to enhance the accuracy of the solution, two additional points were included. For this purpose, a checkerboard calibration pattern composed of two flat planes joined at an angle of 90^0 was used. The pattern consisted of 32 black and 32 yellow squares, yielding a total of 128 well defined corner points. The 3D scene coordinate system was defined such that its origin was located at the bottom intersection point of the two planar surfaces. The coordinate system was oriented with the Z-axis pointing upwards. This configuration was deliberately chosen to ensure that the selected corners exhibited significant

and varied height (Z-axis) values. As a result, this approach helped minimize the presence of zero elements in the coefficient matrix used for DLT parameter estimation. **Figure 3-1** illustrates a selected calibration image along with the extracted feature points used in the evaluation of camera calibration accuracy. The feature points are defined as the intersection corners of the black and yellow squares of a standard chessboard calibration pattern. These corner points were chosen due to their suitability for subpixel refinement and high localization precision. These chessboard corners have strong and predictable gradient patterns that enable robust detection using the Harris Corner detection algorithm.

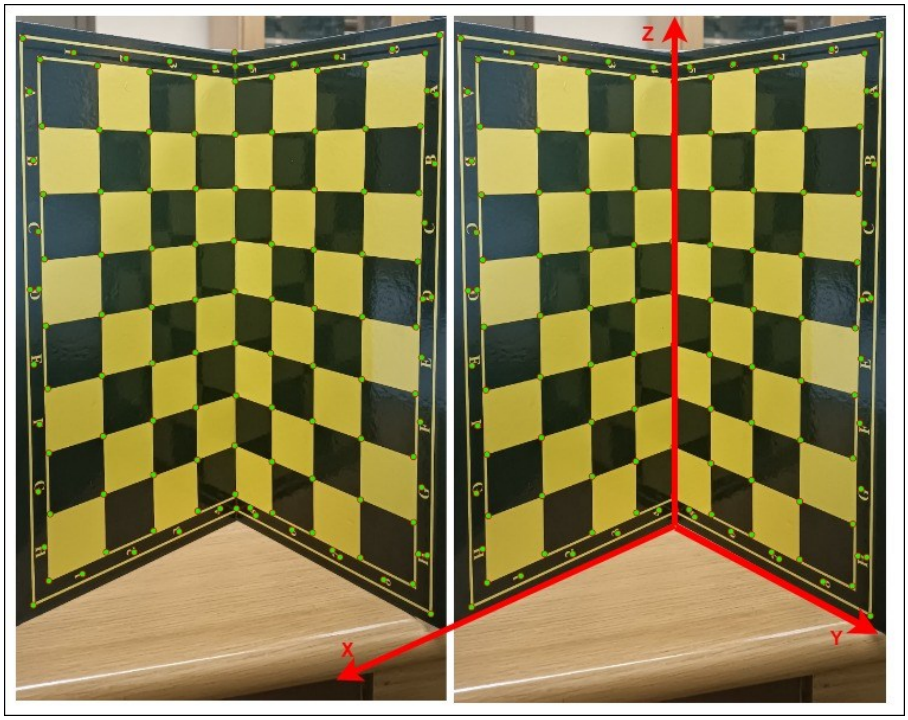

Figure 0-1: Calibration control points identified using the Harris Corner detector needed to run the DLT algorithm

The control points were photographed using a high-hand mobile phone. The mobile phone was fixed on an aluminium tripod at an altitude of 1000mm above the ground at an unknown distance from the calibration pattern. The photograph was then transferred to the post computer for the 2D corner detection using the Harris Corner detector algorithm implemented in the open source software FIVEKO. Once the corners of the black square patterns detected the image was then uploaded into the GIMP software workstation for coordinates measurement. GIMP software provides automatic coordinates measurement and unit conversion tools, and the image coordinates were converted from pixel measures to millimetres for consistency during the computation of the coefficients of the projective transformation matrix. To measure the 3D coordinates a Trimble C3 total station was used to determine the scene coordinates of the corners of the black squares throughout the calibration pattern. The total station offers an accuracy of close to 2 mm. **Table 3.1** presents a sample of the measured ground control points' coordinates and their respective image coordinates directly converted to millimetres.

Table 0.1:A sample of 3D calibration point coordinates and their respective image coordinates

Ground control points	Image coordinates

$X_\omega(\text{mm})$	$Y_\omega(\text{mm})$	$Z_\omega(\text{mm})$	$u(\text{mm})$	$v(\text{mm})$
21.5	21.5	43	10	82
107.5	21.5	57	10	61
278.5	21.5	91	10	22
21.5	109.5	72	30	82
151.5	64.5	60	20	50
151.5	21.5	4	10	51

Substituting the points 3D and 2D coordinates into the extended transformation in **[3-45]** to accommodate six-point point correspondences produces the following:

$$\begin{bmatrix} 10 \\ 82 \\ 1 \\ 10 \\ 61 \\ 1 \\ 10 \\ 22 \\ 1 \\ 30 \\ 82 \\ 1 \\ 20 \\ 50 \\ 1 \\ 10 \\ 51 \\ 1 \end{bmatrix} = \begin{bmatrix} 21.5 & 21.5 & 43 & 1 & 0 & 0 & 0 & 0 & 0 & 0 & 0 & 0 \\ 0 & 0 & 0 & 0 & 21.5 & 21.5 & 43 & 1 & 0 & 0 & 0 & 0 \\ 0 & 0 & 0 & 0 & 0 & 0 & 0 & 0 & 21.5 & 21.5 & 43 & 1 \\ 107.5 & 21.5 & 57 & 1 & 0 & 0 & 0 & 0 & 0 & 0 & 0 & 0 \\ 0 & 0 & 0 & 0 & 107.5 & 21.5 & 57 & 1 & 0 & 0 & 0 & 0 \\ 0 & 0 & 0 & 0 & 0 & 0 & 0 & 0 & 107.5 & 21.5 & 57 & 1 \\ 278.5 & 21.5 & 91 & 1 & 0 & 0 & 0 & 0 & 0 & 0 & 0 & 0 \\ 0 & 0 & 0 & 0 & 278.5 & 21.5 & 91 & 1 & 0 & 0 & 0 & 0 \\ 0 & 0 & 0 & 0 & 0 & 0 & 0 & 0 & 278.5 & 21.5 & 91 & 1 \\ 21.5 & 109.5 & 72 & 1 & 0 & 0 & 0 & 0 & 0 & 0 & 0 & 0 \\ 0 & 0 & 0 & 0 & 21.5 & 109.5 & 72 & 1 & 0 & 0 & 0 & 0 \\ 0 & 0 & 0 & 0 & 0 & 0 & 0 & 0 & 21.5 & 109.5 & 72 & 1 \\ 151.5 & 64.5 & 60 & 1 & 0 & 0 & 0 & 0 & 0 & 0 & 0 & 0 \\ 0 & 0 & 0 & 0 & 151.5 & 64.5 & 60 & 1 & 0 & 0 & 0 & 0 \\ 0 & 0 & 0 & 0 & 0 & 0 & 0 & 0 & 151.5 & 64.5 & 60 & 1 \\ 151.5 & 21.5 & 4 & 1 & 0 & 0 & 0 & 0 & 0 & 0 & 0 & 0 \\ 0 & 0 & 0 & 0 & 151.5 & 21.5 & 4 & 1 & 0 & 0 & 0 & 0 \\ 0 & 0 & 0 & 0 & 0 & 0 & 0 & 0 & 151.5 & 21.5 & 4 & 1 \end{bmatrix} \begin{bmatrix} H_1 \\ H_2 \\ H_3 \\ H_4 \\ H_5 \\ H_6 \\ H_7 \\ H_8 \\ H_9 \\ H_{10} \\ H_{11} \\ H_{12} \end{bmatrix} \quad \textbf{[3-36]}$$

Applying the Graham-Smidt orthogonalization of the central matrix in **[3-36]** gives the following orthogonal and upper triangular matrices:

$$Q = \begin{bmatrix}
0.0583 & 0.151 & 0.4463 & 0.6922 & 0 & 0 & 0 & 0 & 0 & 0 & 0 & 0 \\
0 & 0 & 0 & 0 & 0.0583 & 0.151 & 0.4463 & 0.6922 & 0 & 0 & 0 & 0 \\
0 & 0 & 0 & 0 & 0 & 0 & 0 & 0 & 0.0583 & 0.151 & 0.4463 & 0.6922 \\
0.2916 & 0.0206 & 0.3681 & 0.3504 & 0 & 0 & 0 & 0 & 0 & 0 & 0 & 0 \\
0 & 0 & 0 & 0 & 0.2916 & 0.0206 & 0.3681 & 0.3504 & 0 & 0 & 0 & 0 \\
0 & 0 & 0 & 0 & 0 & 0 & 0 & 0 & 0.2916 & 0.0206 & 0.3681 & 0.3504 \\
0.7553 & -0.2388 & 0.3202 & -0.3601 & 0 & 0 & 0 & 0 & 0 & 0 & 0 & 0 \\
0 & 0 & 0 & 0 & 0.7553 & -0.2388 & 0.3202 & -0.3601 & 0 & 0 & 0 & 0 \\
0 & 0 & 0 & 0 & 0 & 0 & 0 & 0 & 0.7553 & -0.2388 & 0.3202 & -0.3601 \\
0.0583 & 0.9025 & 0.0337 & -0.1444 & 0 & 0 & 0 & 0 & 0 & 0 & 0 & 0 \\
0 & 0 & 0 & 0 & 0.0583 & 0.9025 & 0.0337 & -0.1444 & 0 & 0 & 0 & 0 \\
0 & 0 & 0 & 0 & 0 & 0 & 0 & 0 & 0.0583 & 0.9025 & 0.0337 & -0.1444 \\
0.4109 & 0.321 & -0.1941 & -0.1414 & 0 & 0 & 0 & 0 & 0 & 0 & 0 & 0 \\
0 & 0 & 0 & 0 & 0.4109 & 0.321 & -0.1941 & -0.1414 & 0 & 0 & 0 & 0 \\
0 & 0 & 0 & 0 & 0 & 0 & 0 & 0 & 0.4109 & 0.321 & -0.1941 & -0.1414 \\
0.4109 & -0.0462 & -0.7238 & 0.477 & 0 & 0 & 0 & 0 & 0 & 0 & 0 & 0 \\
0 & 0 & 0 & 0 & 0.4109 & -0.0462 & -0.7238 & 0.477 & 0 & 0 & 0 & 0 \\
0 & 0 & 0 & 0 & 0 & 0 & 0 & 0 & 0.4109 & -0.0462 & -0.7238 & 0.477
\end{bmatrix} \quad \textbf{[3-37]}$$

$$R = \begin{bmatrix}
368.7106 & 65.4836 & 118.3571 & 1.9853 & 0 & 0 & 0 & 0 & 0 & 0 & 0 & 0 \\
0 & 117.0957 & 69.9945 & 1.1102 & 0 & 0 & 0 & 0 & 0 & 0 & 0 & 0 \\
0 & 0 & 57.196 & 0.2504 & 0 & 0 & 0 & 0 & 0 & 0 & 0 & 0 \\
0 & 0 & 0 & 0.8738 & 0 & 0 & 0 & 0 & 0 & 0 & 0 & 0 \\
0 & 0 & 0 & 0 & 368.7106 & 65.4836 & 118.3571 & 1.9853 & 0 & 0 & 0 & 0 \\
0 & 0 & 0 & 0 & 0 & 117.0957 & 69.9945 & 1.1102 & 0 & 0 & 0 & 0 \\
0 & 0 & 0 & 0 & 0 & 0 & 57.196 & 0.2504 & 0 & 0 & 0 & 0 \\
0 & 0 & 0 & 0 & 0 & 0 & 0 & 0.8738 & 0 & 0 & 0 & 0 \\
0 & 0 & 0 & 0 & 0 & 0 & 0 & 0 & 368.7106 & 65.4836 & 118.3571 & 1.9853 \\
0 & 0 & 0 & 0 & 0 & 0 & 0 & 0 & 0 & 117.0957 & 69.9945 & 1.1102 \\
0 & 0 & 0 & 0 & 0 & 0 & 0 & 0 & 0 & 0 & 57.196 & 0.2504 \\
0 & 0 & 0 & 0 & 0 & 0 & 0 & 0 & 0 & 0 & 0 & 0.8738
\end{bmatrix} \quad \textbf{[3-38]}$$

Let's denote by M the central matrix in **[3-36]** and H the column vector containing the parameters of the DLT matrix and p the column vector containing homogenous coordinates of image points. The transformation in **[3-36]** can be simplified as follows:

$$p = MH \qquad \textbf{[3-39]}$$

From **[3-37]** and **[3-38],** equation **[3-39]** can be reformulated as follows:

$$p = QRH \qquad \textbf{[3-40]}$$

Since the matrix Q is orthogonal, multiplying both sides of **[3-40]** by its transpose results in the following:

$$Q^T p = RH \qquad \textbf{[3-41]}$$

From **[3-36], [3-37], [3-38],** and **[3-41],** the following equations are formulated:

$$368.7106H_1 + 65.4836H_2 + 118.3571H_3 + 1.9853H_4 = 25.128 \qquad \textbf{[3-42.1]}$$

$$117.0957H_2 + 69.9945H_3 + 1.1102H_4 = 32.361 \qquad \textbf{[3-42.2]}$$

$$57.196H_3 + 0.2504H_4 = 1.237 \qquad \textbf{[3-42.3]}$$

$$0.8738H_4 = 4.435 \qquad \textbf{[3-42.4]}$$

$$368.7106H_5 + 65.4836H_6 + 118.3571H_7 + 1.9853H_8 = 85.4663 \qquad \textbf{[3-42.5]}$$

$$117.0957H_6 + 69.9945H_7 + 1.1102H_8 = 96.0838 \qquad \textbf{[3-42.6]}$$

$$57.196H_7 + 0.2504H_8 = 22.2247 \qquad \textbf{[3-42.7]}$$

$$0.8738H_8 = 75.6288 \quad \textbf{[3-42.8]}$$

$$368.7106H_9 + 65.4836H_{10} + 118.3571H_{11} + 1.9853H_{12} = 1.9853 \quad \textbf{[3-42.9]}$$

$$117.0957H_{10} + 69.9945H_{11} + 1.1102H_{12} = 1.1101 \quad \textbf{[3-42.10]}$$

$$57.196H_{11} + 0.2504H_{12} = 0.2504 \quad \textbf{[3-42.11]}$$

$$0.8738H_{12} = 0.8737 \quad \textbf{[3-42.12]}$$

3.3. Experimental Results

3.3.1. Calibration of Coefficients of the Projective Transformation Matrix

From **[3-42.12],** the parameter H_{12} was estimated as follows:

$$H_{12} = 1.000 \quad \textbf{[3-43.1]}$$

Substituting **[3-43.1]** into **[3-42.11]** enables us to estimate the value of the coefficient H_{11} as follows:

$$H_{11} = -0.000006993 \quad \textbf{[3-43.2]}$$

Substituting **[3-43.1]** and **[3-43.2]** into **[3-42.10]** led to the following:

$$H_{10} = 0.000003326 \quad \textbf{[3-43.3]}$$

Substituting **[3-43.1]- [3-43.3]** into **[3-42.9]** led to the following:

$$H_9 = 0.000001654 \quad \textbf{[3-43.4]}$$

From **[3-42.8],** the coefficient H_8 was estimated as follows:

$$H_8 = 86.5516 \quad \textbf{[3-43.5]}$$

Substituting **[3-43.5]** into **[3-42.7]** led to the following:

$$H_7 = 0.0096542 \quad \textbf{[3-43.6]}$$

Substituting **[3-43.5]** and **[3-43.6]** into **[3-42.6]** led to the following:

$$H_6 = -0.005820258 \quad \textbf{[3-43.7]}$$

Substituting **[3-43.5]-[3-43.7]** into **[3-42.5]** led to the following:

$$H_5 = -0.2384 \quad \textbf{[3-43.8]}$$

From **[3-42.4],** the coefficient H_4 was estimated as follows:

$$H_4 = 5.07553 \quad \textbf{[3-43.9]}$$

Substituting **[3-43.9]** into **[42.3]** led to the following:

$$H_3 = -0.000592921 \quad \textbf{[3-43.10]}$$

Substituting **[3-43.9]** and **[3-43.10]** into **[3-42.2]** produced the following:

$$H_2 = 0.228596 \quad \textbf{[3-43.11]}$$

From **[3-43.9]-[3-43.11],** the first coefficient of the projective transformation matrix was estimated as follows:

$$H_1 = 0.000413434 \quad \textbf{[3-43.12]}$$

From **[3-43.1]-[3-43.12],** the projective transformation matrix H was formulated as follows:

$$H = \begin{bmatrix} 0.000413434 & 0.228596 & -0.000592921 & 5.07553 \\ -0.2384 & -0.005820258 & 0.0096542 & 86.5516 \\ 0.000001654 & 0.000003326 & -0.000006993 & 1 \end{bmatrix} \quad \textbf{[3-44]}$$

3.3.2. Calibration of parameters of Extrinsic and Intrinsic camera parameters

Table 3.2 presents the calibration results of nineteen camera parameters estimated through the proposed analytical approach. The third row of the table presents the numerical estimates of exterior orientation parameters that include the three rotation angles and the three coefficients of the translation vector under which the camera was subjected at the time of image capture. The sixth row of the table presents the calibrated estimates of the coordinates of the principal point as well as the numerical estimates of the two effective focal lengths. To end, the last three rows of the table present the calibrated estimates of the nine coefficients of the rotation matrix at the time of image capture.

Table 0.2: Camera parameters calibration results

Exterior orientation parameters					
ϕ	φ	κ	$t_x\,(\mathrm{mm})$	$t_y\,(\mathrm{mm})$	$t_z\,(\mathrm{mm})$
-12.056859	-25.436624	89.743485	0.465264	0.264316	1262.891638
Intrinsic camera parameters					
$u_0\,(\mathrm{mm})$		$v_0\,(\mathrm{mm})$	$f_a\,(\mathrm{mm/pixel})$	$f_b\,(\mathrm{mm/pixel})$	

0.096571		-0.060683		0.207114	0.231863
Coefficients of the rotation matrix					
r_{11}	0.004360	r_{21}	0.973781	r_{31}	0.208882
r_{12}	-0.900273	r_{22}	-0.000610	r_{32}	0.422005
r_{13}	-0.436512	r_{23}	-0.229878	r_{33}	-0.883140

Among the mostly used camera calibration assessment metrics is the reprojection error (**Semeniuta, 2016; Hagemann et al., 2022**). The numerical accuracies of calibrated camera parameters are directly related to the performance of the developed geometric calibration algorithms. This performance of the algorithms can be evaluated through a back-projection transformation to recover the coefficients of a conjugate projective transformation matrix using equations **[3-33-1]-[3-33.12].** Robust and reliable calibration algorithms are supposed to produce numerical estimates of coefficients of a conjugate transformation matrix that are very close to those achieved in **[3-44]. Table 3.3** presents a comparison between the original matrix coefficients and their re-projected counterparts with the last coefficient H_{12} normalized. The data in the fifth and eleventh rows of the table presents the standard deviation errors between numerical estimates of the original coefficients and their re-projected counterparts. In addition, the sixth and twelfth rows of the table describe the degree of similarity between numerical estimates of the original coefficients and their re-projected counterparts. It can be observed from the similarity measures that there is a reasonable agreement in terms of numerical estimates between the original and reprojected coefficients of the matrices, and this confirms the robustness and reliability of the proposed calibration models. The standard deviation errors in the fifth and eleventh rows suggest a very good performance of the proposed algorithms, as all the coefficients achieved very small standard deviation errors below 10% (**Luhmann et al., 2016).**

Table 0.3: An accuracy comparison between the calibrated camera pose parameters and their reprojected counterparts

	Coefficients of projective transformation matrix per image					
	H_1	H_2	H_3	H_4	H_5	H_6
Calibrated	0.000413	0.228596	-0.000593	5.075530	-0.238400	-0.005820
Reprojected	0.000408	0.227559	-0.000589	5.054240	-0.237400	-0.005809
Standard deviation	0.000003	0.000519	0.000002	0.010645	0.000500	0.000005
Similarity	0.999900	0.999500	0.999900	0.989400	0.999500	0.999900
	Coefficients of projective transformation matrix per image					
	H_7	H_8	H_9	H_{10}	H_{11}	
Calibrated	0.009654	86.551600	0.000002	0.000003	0.000007	
Reprojected	0.009666	86.547900	0.000002	0.000003	-0.000007	
Standard deviation	0.000006	0.001850	0.00	0.00	0.00	
Similarity	0.999900	0.998150	1.00	1.00	1.00	

3.3.3. Calibration Algorithms Performance Analysis

The performance analysis of the proposed calibration algorithms was extended to compute conjugate estimates of individual camera parameters describing the camera pose. When used with coefficients of conjugate projective transformation matrices, robust calibration algorithms are also expected to reproduce numerical estimates of associated camera parameters that are very close to those achieved with original coefficients. **Table 3.4** presents an accuracy comparison between the initially calibrated camera parameters, and their reprojected conjugate counterparts. It is observed that all the reprojected parameters of camera pose achieved very low standard deviation errors with reference to original measures.
These results are in line with the high degree of similarity between the respective parameters with most of the indices reaching levels very close to 10%. To estimate the parameter similarity index, the following model was proposed:

$$\text{Coefficients similarity} = 1 - \frac{c_i - c_j}{c_i} \qquad \textbf{[3-45]}$$

Where, c_i represents the initial estimate of the camera parameter while c_j represents the reprojected estimate of the parameter. The model returns values close to or equal to one for high-accuracy calibration results, while lower values of the index would suggest a poor performance of the calibration algorithm.

Table 0.4: Comparison between the calibrated estimates of camera pose parameters and their re-projected counterparts

Calibration reprojection error per exterior orientation parameter						
	$\phi(^0)$	$\varphi(^0)$	$\kappa(^0)$	$t_x(\text{mm})$	$t_y(\text{mm})$	$t_z(\text{mm})$
Calibrated values	-12.056859	-25.436624	89.743485	-0.465264	0.264316	1262.891640
Reprojected values	-12.054130	-25.430270	89.741341	-0.465264	0.265388	1262.609990
Standard deviation	0.001365	0.003177	0.001072	0.00	0.000536	0.140825
Similarity	0.998600	0.996800	0.998900	1.00	0.999500	0.859200

Calibration reprojection error per intrinsic camera parameter				
	$u_0(\text{mm})$	$v_0(\text{mm})$	$f_a(\text{mm/pixel})$	$f_b(\text{mm/pixel})$
Calibrated values	0.096571	-0.060683	0.207114	-0.231863
Reprojected values	0.096059	-0.060427	0.206184	0.229868
Standard deviation	0.000256	0.000128	0.000465	0.000998
Similarity	0.999700	0.999900	0.999500	0.999000

It can be observed that the standard deviation associated with the parameter t_z is slightly larger than those associated with the parameters t_x and t_y of the translation matrix. This is because the parameter t_z of the translation vector was derived from the coefficients c_9, c_{10} and c_{11} of the projective transformation matrix. It is well-documented that the Direct Linear Transformation (DLT) algorithm tends to produce smaller numerical estimates for these coefficients relative to others within the matrix. This characteristic leads to comparatively larger absolute values for the derived parameter t_z. Furthermore, between successive images of the same calibration target, the DLT algorithm introduces slight variations in the estimates of c_9, c_{10} and c_{11}. Given their inherently smaller magnitudes, these fluctuations have a proportionally greater effect on the computed value of t_z, thereby contributing to a higher numerical standard deviation for this parameter. In contrast, the parameters t_x, and t_y are typically derived from coefficients with larger magnitudes and are less sensitive to minor numerical perturbations. As a result, their associated standard deviations tend to be lower than that of t_z. This disparity can be attributed to the inherent numerical instability and sensitivity of the DLT algorithm when estimating coefficients of smaller magnitude within the projective transformation matrix.

Repeatability analysis has also been used as an assessment tool to study the robustness of camera pose calibration strategies (**Zhan et al., 2021**). To conduct the analysis, four additional images of the calibration object were captured with the same camera, at approximately the same object distance while maintaining the camera at approximately the same height above the ground. The repeatability analysis of a robust, stable calibration strategy is expected to produce estimates of camera parameters that are numerically very close between successive calibrations. It was suggested that multiple images of the same calibration object be photographed using the same camera under the same geometric constraints **(Gonzales et al.,2005)**. **Table 3.5** presents the coefficients of respective projective transformation matrices, estimated from coordinates extracted from the associated photographs of the calibration object. It can be observed that the derived coefficients are very close in terms of numerical values, and this is in line with the observations in the work of **Hassan et al. (2014).** This suggests a high repeatability of the calibration strategy. Although all the standard deviation errors are acceptable for photogrammetry applications, the coefficients c_4 and c_8 were associated with slightly larger standard deviation errors. This is because the coefficients c_4 and c_8 of the projective transformation matrix are directly influenced by the coefficients c_9, c_{10} and c_{11}, specifically through their dependence on the coefficient t_z of the translation matrix through equations **[3-19.4]** and **[3-19.8].** As the estimates of the parameters c_9, c_{10} and c_{11} decrease, the numerical values of coefficients c_4 and c_8 tend to increase, highlighting an inverse correlation governed by the parameter t_z. In practice, slight numerical variations in the estimates of c_9, c_{10} and c_{11} across projective transformation matrices derived from successive images of the same calibration

pattern lead to magnified variations in the estimates of c_4 and c_8. This sensitivity amplifies the standard deviation errors associated with c_4 and c_8 as observed in rows 8 and 16 of **Table 3.5.**

Table 0.5: Estimates of coefficients of projective transformation matrices associated with each image of the calibration pattern

	Coefficients of projective transformation matrix per image					
Images	c_1	c_2	c_3	c_4	c_5	c_6
Image1	0.000413	0.228596	-0.000593	5.075530	-0.238400	-0.005820
Image2	0.000413	0.228589	-0.000590	5.066950	-0.238400	-0.005820
Image3	0.000409	0.228495	-0.000588	5.170680	-0.238200	-0.005903
Image4	0.000414	0.228598	-0.000591	5.081628	-0.238400	-0.005823
Image5	0.000410	0.227558	-0.000593	5.078680	-0.238300	-0.005820
Stdv	0.000002	0.000406	0.000002	0.038329	0.000080	0.000033
	Coefficients of projective transformation matrix per image					
Images	c_7	c_8	c_9	c_{10}	c_{11}	
Image1	0.009654	86.551600	0.000002	0.000003	-0.000007	
Image2	0.009657	86.548230	0.000002	0.000003	-0.000007	
Image3	0.009662	86.526710	0.000002	0.000003	-0.000007	
Image4	0.009655	86.551830	0.000002	0.000003	-0.000007	
Image5	0.009746	87.013860	0.000002	0.000003	-0.000007	
Stdv	0.000042	0.187938	0.00	0.00	0.00	

Table 3.6 shows the results of repeatability analysis performed on camera exterior and interior parameters, per captured photograph. As anticipated earlier, most of the computed estimates are very close to one another with the exception of the third rotation angle κ and the third coefficient of the translation vector t_z that achieved slightly high standard deviation errors. However, this is in line with the observations made in the work of **Gonzales et al. (2005)** that suggested that larger standard deviation errors in estimates of the parameter t_z should be expected in a repeatability analysis. Furthermore, great attention should be given to the estimates of the coordinates of the principal point (u_0, v_0) and the effective focal lengths (f_a, f_b), which achieved very small standard deviation errors of about 0.000195317mm, 0.0000628318mm, 0.000356581mm, and -0.00057804mm, respectively. It was recently revealed that achieving high calibration repeatability for these four parameters is very difficult (**Leizea et al., 2023**). The achieved small standard deviation errors are indications of the high repeatability of the proposed calibration strategy. The closeness of numerical estimates associated with each exterior and interior orientation camera parameter is in line with the observations in **Gonzales et al. (2005)** that suggest between successive calibrations, estimates of camera parameters are expected to achieve near similar values, respectively. The above also extends to the two rotation angles ϕ and φ, as well as the first two coefficients of the translation vector t_x, and t_y that also achieved very small standard deviation (Stdv) errors.

Table 0.6: Camera exterior and interior orientation parameters repeatability analysis results

Calibration of exterior orientation parameters per image						
	ϕ	φ	κ	$t_x\,(\mathrm{mm})$	$t_y\,(\mathrm{mm})$	$t_z\,(\mathrm{mm})$
Image1	-12.0569	-25.4366	89.7435	-0.4653	0.2643	1262.8916
Image2	-12.0500	-25.4346	89.7424	-0.4652	0.2655	1262.9450
Image3	-12.0576	-25.4194	89.7098	-0.4647	0.2652	1262.8881
Image4	-12.0604	-25.4383	89.7425	-0.4650	0.2654	1262.4964
Image5	-12.0709	-25.4380	89.7422	-0.4648	0.2662	1262.8116
Stdv	0.0068	0.0071	0.0131	-0.0002	0.0006	0.1608

Calibration results of intrinsic camera parameters per image				
	$u_0\,(\mathrm{mm})$	$v_0\,(\mathrm{mm})$	$f_a\,(\mathrm{mm/pixel})$	$f_b\,(\mathrm{mm/pixel})$
Image1	0.0966	-0.0607	0.2071	-0.2319
Image2	0.0966	-0.0607	0.2072	-0.2308
Image3	0.0964	-0.0606	0.2072	-0.2306
Image4	0.0965	-0.0607	0.2072	-0.2309
Image5	0.0961	-0.0608	0.2063	-0.2301
Stdv	0.0002	0.0001	0.0004	-0.0006

3.4. Results Interpretations

To validate the performance of the proposed calibration strategy, it is necessary to assess the accuracy achieved through the new method against some of the existing state-of-the-art analytical calibration techniques. For this purpose, the decomposition strategy proposed in **Ganapathy (1984),** as well as the QR factorization proposed in **Labuz et al. (1991)**, the decomposition solution proposed in **Roumie et al. (2018)**, the Cholesky factorization described in **Wang et al. (2022),** and the Ordinary Direct Linear Transform proposed in **Kim et al. (2023)** were implemented. **Table 3.7** presents a comparison of the calibration results for ten camera exterior and interior orientation parameters.

Table 0.7:Calibration performance of the proposed method against existing calibration approaches

	Exterior orientation parameter calibration results per calibration strategy					
Methods	$\phi\,(^0)$	$\varphi\,(^0)$	$\kappa\,(^0)$	$t_x\,(\mathrm{mm})$	$t_y\,(\mathrm{mm})$	$t_z\,(\mathrm{mm})$
Ganapathy(1984)	-12.0569	-25.4366	89.3083	-0.4662	-1.0311	1262.8900
QR Decomposition (Labuz,1991)	-14.9998	-31.0163	-89.9820	0.5601	-0.1929	1800.2700
Roumie et al.,(2018)	-12.0569	-25.4366	93.2016	0.1082	0.0136	1262.8900
Cholesky Method (Wang et al.,2022)	-19.9996	-37.8564	89.9006	0.5636	-0.1023	1995.0900
ODLT (Kim et al.,2023)	-12.0569	+25.4366	90.1064	0.4135	-0.4166	-1262.8900

Proposed Method	-12.0569	-25.4366	89.7435	0.4653	0.2643	1262.8900

	Interior orientation parameter calibration results per calibration strategy			
Methods	$u_0\,(\text{mm})$	$v_0\,(\text{mm})$	$f_x\,(\text{mm/pixel})$	$f_y\,(\text{mm/pixel})$
Ganapathy(1984)	+/- 0.0967	+/-0.2387	+/-0.2072	+/-0.2308
QR Decomposition (Labuz,1991)	-0.1088	-0.0523	0.1956	0.2324
Roumie et al.,(2018)	0.0966	-0.0607	0.0959	0.0505
Cholesky Method (Wang et al.,2022)	-0.3374	-0.0509	0.2286	0.2358
ODLT (Kim et al.,2023)	0.0966	-0.0507	0.2229	-0.2332
Proposed Method	0.0966	-0.0607	0.2071	-0.2319

The decomposition approaches proposed in **Ganapathy (1984), Roumie et al. (2018)** and **Kim et al. (2023)** made use of the three coefficients H_9, H_{10} and H_{11} of the projective transformation matrix in **[3-54]** to estimate the coefficient t_z of the translation vector. However, the strategy proposed in **Kim et al. (2023)** assigned a negative sign to this coefficient, while the approach proposed by **Ganapathy (1984), Roumie et al. (2018),** and the proposed analytical approach maintained a positive sign of the parameter. From the estimate of this coefficient, the coefficients of the third row of the rotation matrix r_{31}, r_{32} and r_{33} were recovered in a straightforward manner using equations **[3-19.9]-[3-19.11]**. The QR and **Cholesky** factorizations computed the coefficient t_z simultaneously with coefficients t_x and t_y through systems of linear equations from the coefficients of the camera and rotation matrices as well as the location coordinates of the camera in the 3D scene.

The calibration of the first coordinate of the principal point u_0, through the approach proposed by **Ganapathy (1984),** substituted the calibrated estimates of the coefficients $r_{21}, r_{22}, r_{23}, r_{31}, r_{32}$ and r_{33} into equations **[3-19.1]-[3-19.3],** then squared both sides of the respective resulting expressions before adding them and then isolating this coordinate from the square root of the obtained sum. The algorithm to compute this coordinate in the newly proposed strategy did not involve any square root, thus not involving any sign ambiguity. Moreover, **Ganapathy**'s approach to calibrating this coordinate did not take full advantage of the geometric relationships that associate this coordinate to other camera parameters as described in equations **[3-19.1]-[3-19.3].** Since **Ganapathy**'s calibration strategy failed to produce a perfect orthonormal matrix through the three coefficients r_{21}, r_{22} and r_{23}, it can be argued that the estimated magnitude of this coefficient calibrated at 0.0967 mm did not achieve its optimal measure. The above result makes sense since the algorithm proposed by **Ganapathy** enabled the magnitudes of the

coefficients r_{12} and r_{13} to dominate within the numerical magnitude of the output coefficient u_0. Since these two coefficients of the rotation matrix have large enough numerical magnitudes, the calibrated output coordinate through Ganapathy's approach would achieve a larger value than the optimal measure obtained through the new proposed strategy. The algorithm proposed in the new strategy made use of the coefficients of the second and third rows of the projective transformation matrix without involving any parameter coupling or square root and achieved a similar formulation to those proposed in **Roumie et al. (2018)** and **Kim et al. (2023).** This similarity resulted in a common estimate of this coordinate achieved at 0.096571mm. The failures of the QR and Cholesky decomposition approaches to produce perfect homogeneous camera matrices have resulted in numerical estimates of this coordinate achieved at -1088mm and -0.3374mm respectively, as being inaccurate measures.

The method proposed by **Ganapathy (1984)** to calibrate the effective focal length f_x used the cofactor properties of the rotation matrix. Although the strategy differs from ours, both methods achieved similar formulations of the computation algorithm for this effective focal length and achieved a common estimate of the parameter at 0.2072 mm per pixel. To retrieve this parameter, the method proposed by **Roumie et al. (2018)** first computed the norm of the vector product between the first and third rows of the projective transformation matrix, then scaled the result by the product between the parameter t_z and the cosine of the angle between the image x and y axes. In contrast, the method described in **Kim et al. (2023)** computed this internal orientation coefficient as the numerical deviation between the first coordinate of the principal point u_0 and the sum of the squared coefficients H_1, H_2 and H_3 of the projective transformation matrix, scaled by the coefficient of the translation vector t_z. Finally, the QR and Cholesky factorization strategies recovered this interior orientation parameter from the decomposition of the matrix made of the first three columns of the 3×4 projective transformation matrix.

From the above, it was expected that numerical estimates of parameters t_z, f_x, r_{31}, r_{32} and r_{33} calibrated through the approaches proposed in **Ganapathy (1984)** and **Roumie et al. (2018)** would achieve values very close to those computed through the newly proposed strategy, as confirmed in rows 3, 5, 8, 11, 13, and 16 of **table 3.7**. It is observed from **[3-19.5]-[3-19.8]** that four geometric constraints relate the second coordinate of the principal point v_0 and the effective focal length f_y to the coefficients of the rotation matrix $r_{21}, r_{22}, r_{23}, r_{31}, r_{32}, r_{33}$ as well as the coefficients of the translation vector t_y and t_z.The strategy proposed by **Ganapathy (1984)** only considered two of these constraints to estimate the coordinate v_0 and the effective focal length f_y through a system of two linear equations. In contrast, the strategy proposed in **Roumie et al. (2018)** offered an algorithm similar to the newly proposed method to calibrate the coordinate v_0. However, the algorithm proposed in their strategy to compute the second effective focal length f_y did not consider any of the above four constraints but rather estimated the parameter as a ratio described as the product of the pixel dimension in the y direction and the camera focal length measure, divided by the sinus of the angle between the image x and y axes. In addition to the fact that the proposed algorithm does not hold any geometric meaning with reference to the internal structure of the projective transformation matrix, it also created a parameter dependency of this interior orientation parameter on the orthonormality of the rotation matrix.

An analysis of the calibration estimates of coefficients r_{21}, r_{22} and r_{23} of the rotation matrix achieved at -0.20575, -0.01995, -0.14793**,** suggests that the calibration result of 0.0959mm per pixel for this effective focal length through the strategy proposed by **Roumie et al. (2023)** did not achieve its optimal magnitude. In the same way, the algorithm proposed in **Kim et al. (2023)** to calibrate the second coordinate of the principal point v_0 achieved a formulation very close to that proposed in the new approach. However, to compute the second effective focal length f_y, the authors computed the deviation between the second coordinate of the principal point v_0 and the sum of the squared coefficients H_5, H_6 and H_7 of the projective transformation matrix, scaled by the coefficient of the translation vector t_z. As a consequence of the above, any sign ambiguity or sub estimation associated with the coordinate v_0 or the coefficient t_z would compromise the accuracy of this second effective focal length. Since the calibration strategy proposed in **Kim et al. (2023)** associated a negative sign to the coefficient t_z, it could be suggested that the calibrated estimate of -0.2332mm per pixel for this effective focal length may have been subjected to numerical instabilities. The QR and Cholesky factorization methods retrieved these two interior orientation parameters through the derived upper triangular matrices. However, the fact that these two factorization approaches did not produce perfect homogeneous upper triangular camera matrices, with the last coefficient of the third column of the computed upper triangular camera matrices achieving respective estimates of -0.0702 and 0.0337, suggests that the numerical instabilities under which all the coefficients of these camera matrices were subjected also undermined the accuracy of the coordinate v_0 and the effective focal length f_y. These later results are in line with the observation in the work of **Leite et al. (2008)** that argued that factorization of the projective transformation matrix through methods such as the QR and Cholesky factorization always results in inaccurate parameter calibration because of the numerical instabilities characterising these approaches. In contrast, the calibrated estimate of the coefficient v_0 through the approach proposed in **Roumie et al. (2018)** achieved an optimal magnitude very close to that achieved through the newly proposed method as presented in rows 13 and 16 of **Table 3.7**. From the above, it is suggested from the limitations pointed out earlier that the numerical estimates of -0.2387mm, -0.0507mm, -0.0523mm and -0.0509mm achieved through strategies proposed in **Ganapathy (1984), Kim et al. (2023**) and the two factorization approaches, respectively, failed to reach optimal magnitudes. The algorithm proposed in the new approach to estimate this coefficient v_0 is straightforward and accounts for all the geometric constraints in **[3-19.5]-[3-19.8],** while the algorithm to calibrate the second effective focal length only requires coefficients of the computed projective transformation matrix H, resulting in optimal estimates of both parameters achieved at -0.0607mm and -0.2319mm per pixel.

When it comes to the calibration of the coefficients of the second row of the rotation matrix r_{21}, r_{22} and r_{23}, the approach proposed by **Ganapathy (1984)** recovered these parameters directly from the numerical estimate of the second effective focal length f_y through a first-degree linear equation. However, since it was earlier revealed that the proposed calibration strategy failed to account for all the geometric constraints associated with the second effective focal length f_y when calibrating this parameter, it can be suggested that the estimated measures of 0.97327, -

0.00062 and -0.22965 achieved through the calibration are either smaller or larger than the optimal magnitudes they would have achieved. In contrast, the approach proposed by **Roumie et al. (2018)** calibrated these three coefficients by scaling the vector product between the second and third rows of the projective transformation matrix, by a trigonometric function associated with the sinus of the angle between the image x and y axes. However, the calibration of this angle led to a numerical value of 92.8240^0 which is larger than the optimal value of 90^o characterizing the orthogonality between the image x and y axes. From this limitation it is suggested that the estimates of -0.20575, -0.01995 and -0.14793 achieved through the later strategy are of suboptimal magnitudes. The ODLT proposed in **Kim et al. (2023)** computed these three coefficients from the coefficients of the projective transformation matrix H_5, H_6, H_7, the second coordinate of the principal point v_0, the second effective focal length f_y and the last three coefficients of the rotation matrix r_{31}, r_{32} and r_{33}. However, the row 23 of **table3.8** revealed that this calibration strategy failed to optimally recover the coefficients r_{31}, r_{32} and r_{33}. Following this, it is suggested that the calibrated estimates of these coefficients found at 0.97794, -0.09140, -0.18784 are of suboptimal accuracies despite this axis of the rotation matrix achieving a norm of one. Since the QR and Cholesky factorization approaches failed to derive perfect homogeneous camera matrices respectively, it was expected that the numerical instabilities introduced into the respective camera matrices would propagate into the coefficients r_{21}, r_{22} and r_{23}. As a consequence, the estimates of 0.96592,0.13066, -0.22343 and 0.93969, 0.21126, -0.26897 achieved through these two strategies respectively, suffered from numerical instabilities and failed to achieve their optimal magnitudes. Since the calibration algorithm proposed to estimate the first effective focal length f_x in the new method did not suffer from sign ambiguity or parameter coupling and considered all four geometrical constraints that associate this coefficient to other camera parameters, it is suggested that the achieved estimates of 0.97378, -0.00061 and -0.22988 for the coefficients r_{21}, r_{22} and r_{23} are descriptive of their near optimal or optimal magnitudes. From the equation **[3-19.4]** describing the first coefficient of the translation vector t_x, it can be observed that the product between the first coordinate of the principal point u_0 and the third coefficient of the translation vector t_z dominates the output results due to the large numerical magnitudes of these two parameters. In addition, large estimates of the coefficient u_0 would magnify the numerical influence of the coefficient t_z on the output coefficient t_x. Considering that the value of the effective focal length f_x is of small magnitude and that the calibration approach proposed by **Ganapathy (1984)** achieved an estimate of the coordinate u_0 larger than that obtained through the newly proposed strategy, it was expected that the output estimate of the parameter t_x calibrated through Ganapathy's method would achieve a larger value than that achieved through the new strategy. An analysis of the results in rows 3 and 8 of **table 3.8** confirmed that the calibrated estimate of the coefficient t_x achieved a larger magnitude when estimated through Ganapathy's algorithm than that achieved through the newly proposed method. Since **Ganapathy**'s approach failed to reach an optimal measure of the

coefficient u_0, it can be argued that this estimate of the coefficient t_x found at -0.4662mm is suboptimal. In contrast, the approach proposed in **Kim et al. (2023)** achieved an estimate of the coefficient u_0 very close to that achieved by the newly proposed strategy. However, considering that the approach associated a negative sign to the coefficient t_z, it was expected that the output measure of the coefficient t_x would not only be of small magnitude but also subjected to numerical instabilities. Rows 7 and 8 of **table 3.8** confirm the numerical inferiority of the estimate of the calibrated parameter t_x at 0.4135mm, when computed through the strategy proposed in **Kim et al. (2023),** compared to the value of 0.4653mm achieved through the new approach. The approach proposed in **Roumie et al. (2018**) made provision to estimate this coefficient of the translation vector through a system of linear equations involving the coefficients of the rotation matrix and the coordinates of the camera location in a 3D scene retrieved from the 12 coefficients of the projective transformation matrix. It was revealed earlier that this calibration approach failed to produce an orthonormal rotation matrix through its failure to accurately recover the coefficients r_{21}, r_{22}, r_{23} as presented in row 13 of **table 3.8**. As a consequence, the calibrated estimate of 0.1082mm computed through this approach is suggested to be suboptimal. In the same way, the calibrated measures of this coefficient achieved at 0.5601mm and 0.5636mm through the QR and Cholesky factorization approaches, respectively, are not reflections of optimal estimates since these strategies introduced numerical instabilities to the derived coefficients of the rotation matrix.

Equation **[3-29.8]** reveals that the accuracy of the coefficient of the translation vector t_y depends on the accuracy of the effective focal length f_y,the coordinate of the principal point v_0 and the coefficient of the translation vector t_z. The calibration procedure proposed by **Ganapathy (1984)** failed to accurately recover the coordinate of the principal point v_0 while the approach proposed in **Roumie et al. (2018)** failed to optimally recover the effective focal length f_y. The strategy proposed in **Kim et al. (2023)** associated a negative sign to the coefficient $t_z$of the translation vector and this was earlier revealed to have introduced numerical instabilities to any camera parameters associated with this coefficient within the internal structure of the projective transformation matrix. The QR (**Labuz et al., 1991**) and Cholesky factorization (**Wang et al., 2022**), failed to accurately recover the coefficients of their respective camera matrices and consequently also failed to recover the coefficients of associated rotation matrices from which the coefficient t_y was extracted through systems of three linear equations. From the above. It is suggested that the estimates of the coefficient t_y achieved at -1.0311mm, 0.0136mm,-0.4166mm,-0.1929mm, and -0.1023mm, through the approaches proposed in **Ganapathy (1984), Roumie et al. (2018), Kim et al. (2023),** QR method (**Labuz et al.,1991**) and Cholesky factorization (**Wang et al., 2022**), have not achieved their optimal numerical magnitudes.

Table 0.8: Calibration results of coefficients of the rotation matrix per calibration strategy

	Coefficients of the rotation matrix per calibration strategy			
Calibration Strategy Methods	r_{11}	r_{12}	r_{13}	$\sum_{i=1}^{3}(r_{1i})^2$
Ganapathy(1984)	+0.09646	-0.81167	+0.40906	0.850
QR Decomposition (Labuz,1991)	-0.00030	-0.85743	-0.51458	0.990
Roumie et al.,(2018)	-0.98500	-0.04750	-0.16750	1.000
Cholesky Method (Wang et al.,2022)	0.00163	-0.78919	-0.61415	0.990
ODLT (Kim et al.,2023)	-0.00185	-0.90289	0.42986	1.000
Proposed Method	+0.00436	-0.90027	-0.43651	1.000
	Coefficients of the rotation matrix per calibration strategy			
Calibration Strategy Methods	r_{21}	r_{22}	r_{23}	$\sum_{i=1}^{3}(r_{2i})^2$
Ganapathy(1984)	+0.97327	-0.00062	-0.22965	0.990
QR Decomposition (Labuz,1991)	+0.96592	+0.13066	-0.22343	1.000
Roumie et al.,(2018)	-0.20575	-0.01995	-0.14793	0.070
Cholesky Method (Wang et al.,2022)	+0.93969	+0.21126	-0.26897	1.000
ODLT (Kim et al.,2023)	+0.97794	-0.09140	-0.18784	1.000
Proposed Method	+0.97378	-0.00061	-0.22988	1.000
	Coefficients of the rotation matrix per calibration strategy			
Calibration Strategy Methods	r_{31}	r_{32}	r_{33}	$\sum_{i=1}^{3}(r_{3i})^2$
Ganapathy(1984)	+0.20888	0.42004	-0.88314	1.000
QR Decomposition (Labuz,1991)	+0.25882	-0.49773	+0.82782	1.000
Roumie et al.,(2018)	+0.20888	+0.42004	-0.88314	1.000

Cholesky Method (Wang et al.,2022)	+0.34201	-0.57668	+0.74194	0.990
ODLT (Kim et al.,2023)	+0.20888	+0.42004	+0.88314	0.990
Proposed Method	+0.20888	+0.42201	-0.88314	1.000

Finally, the calibration of the three rotation angles ϕ, φ and κ through the new approach, those proposed in **Ganapathy (1984)**, **Roumie et al. (2018),** and **Kim et al. (2023),** made use of the coefficients r_{31}, r_{32}, r_{33} as well as r_{11} and r_{21}.However, it was revealed earlier that Ganapathy's method failed to accurately retrieve the coefficients r_{21} and r_{11}, compromising the accuracy of the angle κ estimated at 89.3083^0. In contrast, the approach proposed in **Roumie et al. (2018)** failed to calibrate the coefficient r_{21} which undermined the accuracy of this rotation angle excessively calibrated at 93.2016^0. Furthermore, the calibration scheme proposed in **Kim et al. (2023)** computed the coefficient r_{11} from the coordinate of the principal point u_0 as well as the effective focal length f_x. Since the algorithm proposed by the authors to calibrate the coefficient u_0 is prone to numerical instabilities originating from the negated coefficient t_z, it is argued that the numerical instability originating from the coefficient r_{11} undermined the estimated measure of the angle κ calibrated at 90.1064^0. The newly proposed calibration method achieved a measure of this rotation angle at 89.7435^0. This measure is in line with the observation in the work of **Wakai and Yamashita (2021)** that suggests that a normal roll angle would be within the range of $\left[-\frac{\pi}{2} \quad \frac{\pi}{2}\right]$. Ganapathy's achieved measure, although falling within this range could be a case of a false solution to the parameter.

3.5. Results Discussion

The calibration of the coordinates of camera location in a 3D scene X_0, Y_0 and Z_0 requires accurate measures of twelve among the nineteen camera parameters calibrated. These twelve parameters include the nine coefficients of the rotation matrix and the three coefficients of the translation matrix. However, the accuracy of the remaining parameters, which include the two coordinates of the principal point and the two effective focal lengths, with the exception of the three rotation angles, is also significant since they are geometrically related to these considered twelve parameters. The calibrated coordinates are numerically compared again a set of reference coordinates of the camera location carefully measured using a measuring tape at the time of image capture. **Table 3.9** presents root mean square errors for the calibration of parameters of camera location in 3D scene X_0, Y_0 and Z_0 per calibration method.

Table 0.9: The reprojection error associated with each calibration strategy for the estimation of coordinates of camera location in a 3D scene

Camera Location Coordinates per calibration method			
	$X_0\,(\mathrm{mm})$	$\mathrm{Y}_0\,(\mathrm{mm})$	$\mathrm{Z}_0\,(\mathrm{mm})$
Reference Estimates	-264.05475	-533.36529	+1115.57398

Calibration Methods			
Ganapathy(1984)	-262.83712	-530.08495	+1115.73778
Reprojection error	1.21763	3.28034	0.16380
Average reprojection error	**1.554mm**		
QR Decomposition(Labuz,1991)	-465.75299	+896.54634	-1490.05506
Root Mean Square Error	+201.69824	+363.18105	+374.48108
Average reprojection error	**313.120mm**		
Roumie et al.(2018)	-263.79564	-530.46217	+1115.31030
Reprojection error	+0.25821	+2.90312	+0.26368
Average reprojection error	**1.142mm**		
Cholesky Method (Wang et al.,2022)	-682.25333	+115.09080	-1479.97388
Reprojection error	+418.19858	+418.27449	364.39990
Average reprojection error	**400.291mm**		
ODLT(Kim et al.,2023)	-263.38845	-530.12595	+1115.05413
Reprojection error	+0.66630	+3.23934	+0.51985
Average reprojection error	**1.475mm**		
Proposed Method	-263.93887	-533.34596	+1115.37015
Reprojection error	+0.11589	+0.02233	+0.20383
Average reprojection error	**0.114mm**		

Rows 10 and 16 of **Table 3.9** reveal that the QR and Cholesky factorization methods produced the largest average reprojection errors, with respectively 313.120mm and 400.291 mm for the calibration of the coordinates of camera location in a 3D scene. These results reveal that the failures to recover the parameters X_0, Y_0 and Z_0 were mostly caused by numerical instabilities and alterations of the original coefficients of the projective transformation matrix used for the factorization. This is because many geometric constraints that interconnected the camera parameters within the internal structure of the projective transformation matrix were broken. Indeed, the numerical instabilities associated with the non-homogeneous camera matrices, respectively, were likely propagated to the coefficients of the orthogonal rotation matrices. The inaccurate coordinates of the principal point u_0, v_0 and the effective focal lengths f_x and f_y were found all derived from numerically unstable camera matrices produced by each of these two strategies, and because the parameters X_0, Y_0 and Z_0 were mainly computed from the nine coefficients of the rotation matrix, their estimated values indicate some occurrences of false solutions. These results are in line with the assessment made by **Heikkila (2000)** that suggests that although QR and Cholesky factorization methods are both analytical approaches that can provide close form solutions, individual camera parameters calibrated through these strategies are not of optimal magnitude.

The third largest average reprojection error of 1.554mm, which is equivalent to 6.047 pixels and achieved by **Ganapathy**'s calibration strategy, exposed the failure of the algorithm proposed

to recover the first coefficient of the rotation matrix r_{11}, despite a successful calibration of the approach to calibrate the fourth coefficient of the rotation matrix r_{21}. According to the assessment made in **Frazer (2013),** a reprojection error of 6.047 pixels is very large for photogrammetry and acceptable errors should be between 0.3 and 0.5 pixels. Moreover, the algorithm proposed to calibrate the coefficient t_x failed to achieve an optimal magnitude of the parameter because the large magnitude of the coordinate u_0 could not minimize the influence of the coefficient t_z. This compromised the accuracy of the coordinate X_0, which achieved a magnitude inferior to its optimal value. The fact that the system of two equations proposed by Ganapathy to recover the parameters f_y and v_0 ignored the geometric constraints associated with each of these parameters resulted in a decrease in accuracy for these two parameters. Since these two parameters were geometrically associated with the second coefficient of the translation vector t_y ,this led to a large estimate of the parameter. In addition, despite the small magnitude of the coefficient r_{22}, the instability introduced by the coefficient t_y could not be absorbed and stabilized by this coefficient of the rotation matrix. These led to the parameter of camera location Y_0 not achieving the expected accuracy. This observation appears to align with the assessment made in the work of **Tang and Fritsch (2013)**. The small magnitude of the coefficient r_{23} and the large magnitude of the coefficient r_{33} played a vital role in reducing the numerical instability brought by the parameter t_y when recovering the third coordinate of the camera location Z_0, which achieved a reprojection error of 0.16380mm, which is slightly above half a pixel at 0.6 pixels. The above results confirm an assessment made by **Luhmann et al. (2016)** that suggests that calibration strategies that rely on parameter coupling generally do not produce metrically adequate estimates of parameters.

The ordinary direct linear transformation strategy proposed in **Kim et al. (2023)** achieved an average reprojection error of 5.59 pixels, slightly lower than that achieved by **Ganapahy**'s approach. This result mostly originates from the fact that the parameter t_x and t_y were computed from a suboptimal estimate of the effective focal length f_x and a negated third coefficient of the translation vector t_z. In addition, the large magnitude of the coefficients r_{21} and r_{33} could not compensate for the numerical instabilities introduced by the very small numerical product $t_x r_{11}$, resulting in an estimate of the coordinate X_0 being smaller than its optimal magnitude. Despite a successful calibration of the coefficients r_{21} and r_{31} the numerical instabilities introduced by the coefficients t_x and t_y failed to be absorbed by coefficients r_{11} and r_{21} ,respectively, leading to a reprojection error of 2.53 pixels associated with the coordinate of the camera location X_0. The negative sign associated with the coefficient r_{12} and the positive sign associated with the parameter t_x mainly contributed to drastically decreasing the estimate of the second coordinate of the camera location Y_0. Furthermore, despite the successful calibration of the parameter r_{32} ,its small magnitude and that of the coefficients r_{22} compromised the numerical advantage

offered by the magnitudes of the parameters t_y and t_z in order to increase the numerical estimate of the coordinate to a value closer to the reference measure. The inaccuracy related to the coefficient r_{22} originating from parameter coupling error from suboptimal estimates of coefficients r_{31} and r_{32}, also contributed to the accuracy degradation of the second coordinate of camera location. These led to a large reprojection error of 3.24 mm that corresponds to 12.25 pixels associated with this coordinate. In contrast, the third coordinate of camera location Z_0 achieved a reprojection error slightly smaller than that achieved through the calibration of the first coordinate X_0. This is because the numerical instability introduced by the negative product $t_x r_{13}$ was slightly attenuated by the positive product $t_y r_{23}$, accentuating the influence of the product $t_z r_{33}$ that led to the estimated coefficient slightly increasing towards the numerical magnitude of the reference measure. These resulted in a calibration reprojection error of 0.51985mm that corresponds to 1.965pixels. These results exposed that the numerical instabilities originated from the parameter coupling errors during the calibration of the parameters u_0, f_y, propagated through the coefficients of the second and third rows of the rotation matrix r_{21}, r_{22}, r_{23}, r_{31}, r_{32}, r_{33}, respectively, as well as the first two coefficients of the translation matrix t_x and t_y.

The decomposition solution proposed by **Roumie et al. (2018)** produced the lowest average reprojection error of the five calibration approaches. This strategy achieved two fair enough roots mean square errors associated with the calibration of the first and third coordinates of camera location X_0 and Z_0. The reprojection errors associated with the coordinates X_0 and Z_0 achieved 0.25821mm and 0.26368mm that correspond to 0.98 and 0.997pixels, respectively. The largest reprojection error was associated with the second coordinate of camera location Y_0. The successful calibration of the coordinates X_0 originated from the fact that the small value of the coefficient r_{11} successfully absorbed the numerical instability introduced by the parameter t_x while the small value of the coefficient r_{21} minimized the influence of the parameter t_y. The large magnitude of the coefficient r_{31} also increased the influence of the product $t_z r_{31}$ to drive the estimate of the coordinate X_0 closer to the reference magnitude, resulting in a moderate reprojection error of 0.25821mm that corresponds to 0.976 pixels. In the same way, the successful calibration of the third coordinate of the camera location Z_0 was due to the fact that the large magnitude of the coefficient r_{33} enabled the product $r_{33} t_z$ to compensate for the numerical instabilities introduced by the parameters t_x and t_y. In addition, although the calibration strategy failed to accurately recover the optimal magnitude of the coefficients r_{13} and r_{23} their respective small magnitudes played a pivotal role in reducing the negative influence of the two inaccurate coefficients t_x and t_y, increasing the influence of the product $t_z r_{33}$ which drove the magnitude of this third coordinate to a value closer to the reference measure. These resulted in the parameter achieving a reprojection error of 0.997 pixels. It is to be noted that the

failure by the calibration strategy to achieve optimal estimates of the coefficients of the translation matrix t_x and t_y originating from parameter coupling errors associated with inaccurate estimates of the three coefficients of the second row of the rotation matrix r_{21}, r_{22} and r_{23}. In contrast, the largest reprojection error achieved by this calibration approach was associated with the second coordinate of camera location Y_0. Despite the advantage of the small magnitudes of the inaccurate coefficients r_{12}, r_{22} to absorb the negative influences of the two parameters t_x and t_y, the successful calibration of the coefficient r_{32} could not strengthen the product $t_z r_{32}$ in compensating for the numerical instabilities introduced by the products $t_x r_{12}$ and $t_y r_{22}$. These resulted in a drop in the numerical magnitude of this third coefficient, leading to a larger reprojection error of about 10.97pixels. These results indicate that the numerical instabilities originated from the parameter coupling errors during the calibration of the parameters t_x and t_y contributed to the degradation of the numerical accuracy of coordinates and more importantly, that of the second coordinate Y_0.

The last row of **table 3.9** presents the reprojection errors achieved by the newly proposed calibration system. The proposed strategy achieved three acceptable reprojection errors with the lowest associated with the second coordinate of the camera location Y_0 that reached about 0.084 pixels. This error is followed by that achieved through the calibration of the first coordinate of the camera location X_0 that reached 0.11589 mm, which corresponds to 0.438 pixels. Both these errors are less than half a pixel and fall within the range of 0.3 to 0.5 pixels, which is suggested as the acceptable error range for close-range photogrammetry applications (**Przybilla et al., 2020**). The largest reprojection error was associated with the third coordinate of camera location Z_0 that achieved an error slightly larger than half a pixel at 0.77 pixels. The smallest reprojection error associated with the coefficient Y_0 mainly originated from the successful calibration of the coordinate r_{11} that enabled to stabilize the numerical unbalance that the very small negated coefficient r_{22} imposed on the second coefficient of the translation vector t_y. This numerical stabilization enabled the product $t_z r_{32}$ to increase the numerical magnitude of the output estimate of this coefficient of camera location to a value very close to the magnitude of its reference measure, leading to the very small reprojection error achieved. The second lowest reprojection error associated with the first coordinate of camera location X_0 was firstly due to the small magnitude of the coefficient r_{31} that absorbed most of the magnitude potential of the coefficient t_z to an estimate almost twice lower than that achieved by the numerical unbalanced imposed by the coefficient r_{32} on this same parameter when calibrating the second coordinate of camera location Y_0. Secondly, the very small magnitude of the first coefficient of the rotation matrix r_{11} also further diminished the numerical influence of the parameter t_x, while the large magnitude of the coefficient r_{21} levelled these numerical unbalances to drive the final magnitude of this first coefficient of camera location to a value smaller than the reference measure. This resulted in a

decrease of the computed magnitude of this coordinate to an estimate slightly lower than the reference measure, with a deviation of 0.438 pixels. This also confirms the robustness of the calibration algorithms developed for the estimation of the parameters t_x, f_x, u_0 and t_z. The negative signs associated with the coefficients r_{23} and r_{33} have played a pivotal role in slightly increasing the reprojection error magnitude of the coefficient of camera location Z_0, which achieved a value 0.77 pixels. The large magnitude of the parameters r_{13} and t_x were not enough to compensate for the numerical magnitude unbalance created by the product $t_z r_{23}$. In addition, the opposite signs held by the parameters t_y and r_{23} further contributed to decreasing the numerical estimate of the calibrated coefficient Z_0, driving its value to a magnitude lower than the reference measure. The fact that the parameter t_y held a numerical value smaller than that of the parameter t_x and that the large magnitude of the coefficient r_{23} failed to stabilize the instability introduced by the product $t_x r_{11}$ highly contributed to the "large" reprojection error. This result seems to indicate that there may be a correlation between the coefficient of the second coordinate of the principal point v_0 and the third coordinate of the camera location Z_0. The reprojection errors of 0.438, 0.0843 and 0.770 pixels are actually acceptable measures and are characteristics of a stable and robust calibration system, as suggested in the work of Heikkila **(2000).** These also confirm the robustness of the algorithms developed to calibrate the parameters f_y, t_y and v_0.

Table 3.10 shows a comparison of the calibration reprojection errors of some of the existing state-of-the art camera pose estimation calibration methods based on a single image and using a checkerboard calibration pattern.

Table 0.10: Comparison of some of the best reprojection errors achieved for the calibration of camera pose parameters per calibration approach

Camera pose calibration methods	**Geiger et al.,2012**	**Placht et al.,2014**	**Ha et al.,2017**	**Sels et al.,2019**	**Lu et al. (2022)**	**The New method**
Reprojection errors(pixel)	0.135	0.137	0.128	0.250	0.370	0.084

The pose estimation strategy proposed in **Ha et al. (2017)** produced the lowest reprojection error with 0.0128 pixels. The approaches proposed by **Geiger et al. (2012)** and **Placht et al., (2014)** achieved nearly equal calibration performance, while the method proposed by **Sels et al. (2019)** achieved the second largest error after that achieved by the strategy proposed in **Lu et al. (2022)**. The last column of the table shows the reprojection error achieved through the newly proposed decomposition solution to the projective transformation matrix. This error of magnitude of 0.0843 pixels demonstrates the robustness and reliability of the newly proposed analytical calibration algorithms. These results are in line with the assessment made in the work of **Schmaltz et al. (2011)** that suggests that an average reprojection error of about 0.05 pixels is very good and achievable through a robust camera pose calibration strategy. These reprojection errors are also superior to 0.61pixel achieved by the iterative camera calibration approach

proposed by **Heikkila (2000)** and the proposed strategy's best error achieved an estimate very close to the $\frac{1}{10}$ pixels suggested for close range photogrammetry (**Yuan et al. (2021)**.

3.6. Concluding Remarks

This chapter successfully presented an improved concept of a fully analytical decomposition calibration solution for camera pose parameters. The proposed strategy relied on strategic formulations of linear and nonlinear mathematical models to isolate and independently calibrate each camera parameter while preserving their geometric attributes. This proposed calibration approach extends and improves the method described in the works of **Ganapathy (1984)**, **Labuz et al. (1991), Roumie et al. (2018), Wang et al. (2022), and Kim et al. (2023)** that suffer the limitations of parameter coupling, weak geometric constraints, sign ambiguity, and subjective selection of optimal solutions, to name a few. The newly proposed method provides a comprehensive approach to understanding the decomposition of the projective transformation matrix and the accuracy advantages of such decomposition in analytically recovering camera parameters with very good standard deviation and reprojection errors for close-range photogrammetry. The analytical calibration strategy developed in this chapter is not limited to non-metric systems. They are designed to be broadly applicable to any close-range setup, including those involving calibrated metric cameras, drone-mounted systems at low altitudes, or industrial imaging platforms. In such contexts, the proposed method can either provide a primary calibration solution or act as a validation and refinement tool for existing calibration parameters. By addressing both intrinsic (the effective focal lengths and coordinates of the principal points) and extrinsic parameters in a fully analytical and structurally independent manner, the approach supports diverse imaging geometries and camera types typically encountered in engineering, architectural, archaeological, forensic, and UAV-based photogrammetric projects. The proposed strategy was proven robust, reliable, and repeatable and could be integrated in a close-range photogrammetry production environment.

CHAPTER 4
ANALYTICAL FORMULAE FOR INVERSE RADIAL DISTORTION COEFFICIENTS COMPUTATIONS FOR HIGH-ORDER DISTORTION POLYNOMIAL MODELS

4.1. Introduction

Radial distortion is common in most off-the-shelf lenses often used for photogrammetry applications. Several polynomial functions have been adopted to model such distortions, and suggestions have been made to use polynomials with several terms when dealing with severe radial distortions (**Bukhari and Dailey, 2013**). However, among the challenges of using such functions is that their inverse polynomials cannot be computed analytically (**Beauchemin and**

Bajcsy, 2001; Devernay and Faugeras, 2001; Kumar et al., 2020; Kaufman and Gurfil, 2021). Inverse modelling of radial distortion polynomials involves the estimation of inverse distortion coefficients accurate enough from the original coefficients to reduce the distortion effects introduced by lenses. **Kumar et al. (2022)** even described this lack of analytical inverse modelling formulae as a "major computational problem" in camera calibration. Following the above limitations, **Ma et al. (2003)** suggested two coefficients of inverse polynomial function to undistort altered image point coordinates by formulating an inverse polynomial with negated first and second radial distortion coefficients. The problem with the proposed approach is that the highest degree the polynomial can hold is three with two radial distortion coefficients only. Most of the current camera calibration software packages, such as MATLAB, Photoscan, Micmac, and PhotoModeler, to name a few, use up to three coefficients in polynomial models of higher degrees, such as the fifth, sixth, or eighth degree (**Griffiths and Burningham, 2019; Kabadayi et al., 2020**).

The radial distortion polynomial inversion strategy proposed by **Drap and Lefevre (2016)** can be considered a valuable semi-analytical method since the proposed algorithms enable the estimation of inverse distortion coefficients recursively before refining their estimates through an iteration process. The proposed approach, however, suffers from certain limitations in its formulation and implementation. In terms of the algorithm formulation, the technique was derived from a general polynomial function. This means the first inverse radial distortion coefficient would retain dominance within the inverse distortion function only if the power associated with the term attached to the second inverse coefficient is closer to the power of the term attached to the first inverse radial distortion coefficient. However, for high-degree polynomials, especially depressed polynomials, the proposed algorithm would poorly perform because of the possible numerical dominance of some of the inverse radial distortion coefficients over the first inverse distortion coefficient within the formulation of the high-order inverse polynomial. In addition, although it is an advantage to estimate inverse coefficients recursively, the stability of the proposed inverse radial distortion models can be compromised because all radial distortion coefficients present in the original polynomials are not represented in the formulation of their respective inverse models.

To alleviate this challenge, **Ernould et al. (2021)** suggested only considering truncated versions of inverse coefficients proposed by **Drap and Lefevre (2016)**. However, this option can lead to further instabilities since some of the terms being dropped may have high numerical relevance for the remaining terms of the inverse coefficients. Furthermore, **Lee et al. (2018)** and **Jaroš (2021)** suggested the use of the first three inverse coefficients to correct distortion modelled by a depressed six-degree polynomial. **Zhu (2021)** also suggested the use of the first three inverse coefficients proposed in **Drap and Lefevre (2016)** to formulate an inverse radial distortion function in order to correct moustache radial distortions modelled by a three-term six-order polynomial function. Although the author reported satisfactory radial distortion correction results, the error report provided did not offer enough evidence to support that the formulations of the inverse coefficients were adequate to handle the moustache radial distortion profile. Conversely, **Hamed et al. (2021)** suggested the use of the first four inverse coefficients proposed in **Drap and Lefevre (2016)** to formulate a five-term, eight-degree inverse radial distortion function to deal with severe barrel radial distortions. Although the residual error was reported to be very small after applying an iteration algorithm to refine the inverse coefficients, there was not enough numerical evidence to support that the formulated inverse model was stable and could efficiently deal with severe barrel radial distortions. The fact that the fourth radial distortion coefficient κ_4 was not part of the formulation of the forward model but appeared in the formulation of the inverse model could undermine the effectiveness of the derived inverse model to deal with the barrel distortions. In terms of its implementation, the strategy proposed by **Drap and Lefevre** is difficult to customize in order to match the expressions of high-order depressed

polynomials. Moreover, the proposed algorithms may also suffer from numerical instabilities due to exaggerations of coefficients associated with each term of the respective inverse coefficients. This is because the optimal number of iterations supposed to produce optimal magnitudes of coefficients is not known a priori.
This chapter attempts to develop a fully analytical, robust, flexible, reliable, and stable radial distortion polynomial reversion strategy that enables the computation of accurate inverses of radial distortion coefficients needed to formulate inverse radial distortion polynomial models. The key assumptions under which this technique operates include radial symmetry of the distortion function around the principal point, the distortion function is monotonically increasing or decreasing within the region of interest, the polynomial model is known and fixed, and all coefficients are real-valued. To the best of my knowledge, there is currently no analogue to such a strategy available among the photogrammetry and computer vision literature.

4.2. Material and Methods

4.2.1. Non-metric Digital Cameras Used

The first non-metric digital camera used in this chapter was a DSLR Sony Alpha 200 presented in Figure 4-1 with its characteristics presented in Table 4.1.

Figure 4-1:DSLR Sony Alpha 200 Camera

The camera possesses a pixel size of 6.2 µm and a focal length of 24mm, as presented in **Table 4.1**.

Table 4.1: DSLR Alpha 200 Camera Main Characteristics

Camera Model	**DSLR Sony Alpha 200**
Body type	Compact SLR
Sensor resolution	10.2 megapixels
Maximum resolution	3872×2592 pixels
Sensor dimension	$23.6\,mm \times 15.8\,mm$
Pixel size	6.2µm
Focal length	24 mm
Image type	jpeg
Sensor type	CCD

The second non-metric camera used in this chapter was a DSLR Nikon D3100 camera presented in Figure 4-2. The camera possesses a sensor resolution of 14.2 megapixels with a pixel size of 5µm and a focal length of 35mm as presented in Table 4.2.

Figure 4-2: DSLR Nikon D3100 camera

Table 4.2: DSLR Nikon D3100 camera main specifications

Camera Model	**DSLR Nikon D3100**
Body type	Compact SLR
Sensor resolution	14.2 megapixels
Maximum resolution	4608×3072 pixels
Sensor dimension	23.1mm×15.4 mm
Pixel size	5 µm
Focal length	35 mm
Image type	jpeg
Sensor type	CMOS

To test the effectiveness of the proposed algorithms in correcting severe barrel distortions, a Xiaomi Redmi Pro mobile phone camera was used. The mobile phone offers the possibility to capture imagery with an ultra-wide-angle camera of 118^0 field of view, which is enough to introduce severe barrel radial distortions. The camera's ultra-wide lens characteristics are summarized in Table 4.3.

Table 4.3: Xiaomi Redmi ultra-wide camera main specifications

Camera Model	**XIOMI Redmi 11 Pro Mobile phone**
Sensor resolution by default	108 megapixels
Sensor resolution in wide angle mode	8 megapixels
Maximum resolution	1080×2400 pixels
Sensor dimension	6.058 mm×4.415mm
Pixel size	0.7µm
Focal length	26 mm
Image type	jpeg
Sensor type	Sony IMX 355

4.2.2. Computing radial distortion coefficients

Radial distortion coefficients were computed using three strategies. The first strategy used was the least squares method to solve for the four radial distortion coefficients of a general quintic due to the limitations of available software packages in solving more than 3 coefficients. The

second radial distortion coefficient computation was done through a simple automatic camera calibration done in the PhotoModeler software workstation. The approach only needed a few photographs of the planar calibration pattern that contains 100 equally spaced black dots painted on a white background. The third method to compute radial distortion coefficients was through a camera calibration script. This tool needed several images of a well-defined checkerboard pattern made of successions of black and white squares of 30mm side, that contained a total of 7×5 squares. The computation of radial distortion coefficients from images captured by the above-mentioned consumer-grade digital cameras is motivated by two primary objectives. The first objective is to characterize the nature and extent of radial distortion specific to each camera lens by estimating the associated distortion coefficients using established calibration techniques. This characterization aimed to identify the dominant types of radial distortion (e.g., moderate or severe barrel or pincushion) exhibited by each consumer-grade lens, as these distortions can vary significantly between devices due to manufacturing variability and lens quality. The second objective is to use these empirically derived distortion coefficients as reference functions for evaluating the performance of the newly developed fully analytical inverse radial distortion models. Specifically, the computed coefficients will be substituted into both the proposed analytical inversion models and existing iterative inversion schemes. The resulting inverse distortion functions will then be compared against the original distortion curves to assess their accuracy, shape conformity, and numerical stability. This comparative analysis is critical in validating the ability of the analytical inverse models to effectively approximate the inverse of the original radial distortion function, particularly in scenarios where high-order polynomial terms are present. Figure 4-3 presents the two calibration patterns used in this chapter.

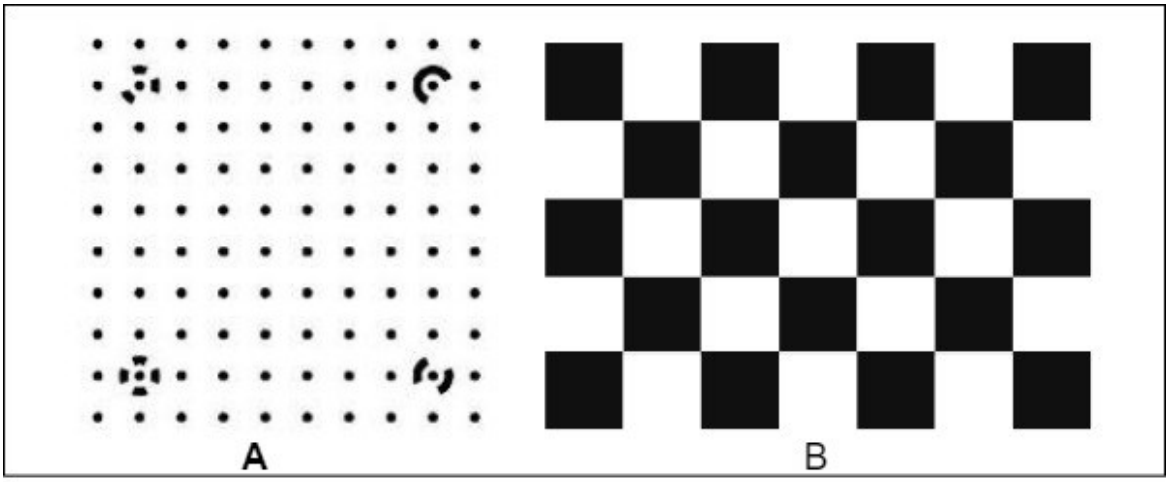

Figure 4-3: Distortion-free images of calibration patterns with (A) representing the calibration pattern used by the Photomodeler calibration toolbox and (B) the checkerboard pattern used by the MATLAB camera calibration script.

A. Least Squares Estimation of Radial Distortion Coefficients.

To estimate the coefficients of radial distortion polynomials using the least squares method, a carefully structured image acquisition procedure was conducted using a DSLR Sony Alpha 200 camera mounted on a tripod to ensure geometric stability and reduce motion blur. The calibration target consisted of a high-contrast grid of equally spaced black and white squares, affixed to a fixed, vertical, planar surface to maintain consistency across all views. The image capture

process began with a central photograph taken with the camera positioned orthogonally to the pattern. To introduce variation in radial displacement across the image plane, additional images were captured by incrementally moving the camera to the right and left of the central position. At each new viewpoint, both the height of the tripod and the orientation of the camera (azimuth and elevation angles) were altered to vary perspective. This systematic variation in camera pose was critical for sampling different parts of the lens's field of view and capturing the nonlinearity of radial distortion effects. All images were acquired under consistent lighting conditions to enhance the visibility of the calibration pattern and support accurate feature detection.

Since the versions of MATLAB and PhotoModeler available at the time of this experiment did not support solving for four or more radial distortion coefficients directly, a point correspondence strategy based on the least squares method was employed. This approach required both distorted and distortion-free 2D image coordinates of specific points. Nine well-defined image points were selected from the various captured images of the checkerboard calibration pattern in Figure 4-3(A) to improve the stability and accuracy of the coefficient estimates. The calibration image points were first identified using the Harris corner detector tool implemented in the open-source software FiveKo. The distortion-free coordinates of these points were extracted using the open-source GIMP software from a geometrically correct image of the calibration target, downloaded from the PhotoModeler website. The distorted coordinates associated with the identified corners were similarly obtained by importing the DSLR Sony Alpha 200 camera-captured photographs into the GIMP workstation. The combination of a carefully executed image acquisition setup and a robust Gram-Schmidt-based least squares computational strategy enabled the accurate estimation of the higher-order radial distortion coefficients beyond the limitations of the default software packages. The following equations were used to form the least squares system of linear equations that enabled us to estimate each of the coefficients of radial distortion:

$$x_d = x_u + x_u \left(\sum_{j=i+1}^{5} \sum_{i=1}^{5} \kappa_i r_u^j \right) \quad \textbf{[4-1]}$$

$$y_d = y_u + y_u \left(\sum_{j=i+1}^{5} \sum_{i=1}^{5} \kappa_i r_u^j \right) \quad \textbf{[4-2]}$$

With nine-point correspondences with measured x_u, y_u, x_d and y_d coordinates, the four coefficients of radial distortion $\kappa_1, \kappa_2, \kappa_3$ and κ_4 were computed. Figure 4-4 presents the calibration workflow used to estimate the coefficients of radial distortion.

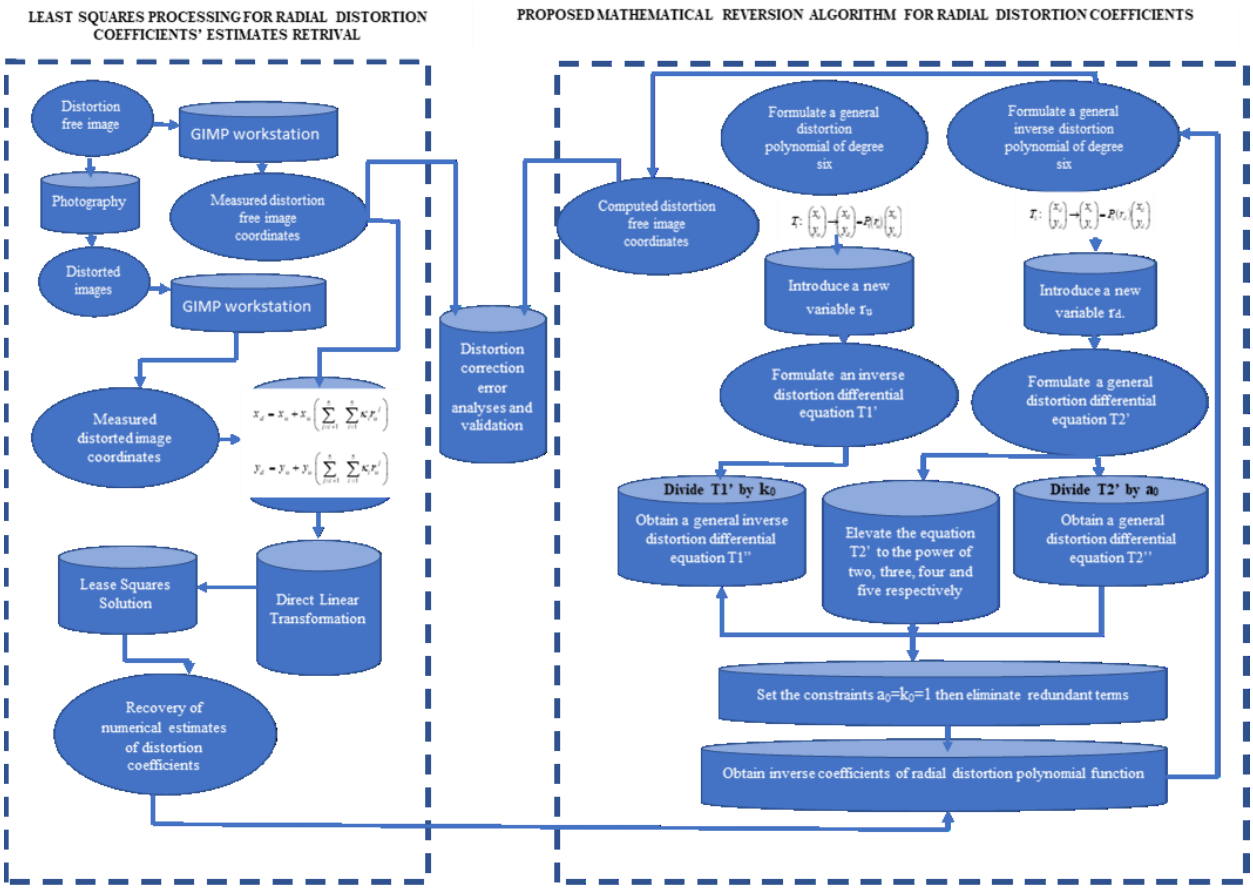

Figure 4-4: Least Squares Radial Distortion Coefficients Calibration Workflow on the left side of the figure. The polynomial reversion workflow on the right side of the figure is elaborated in section 4.2.3.B of this chapter. Equations on the left side of the diagram are presented in [4-1] and [4-2], while equations on the right side of the diagram are presented in [4-6.1] and [4-6.2].

Table 4.4 presents the computed estimates of radial distortion coefficients for the general quintic to analyse and model radial distortions introduced by the Sony Alpha camera.

Table 4.4: Radial Distortion Coefficients Calibrated through the Least Squares Approach

Radial Distortion Coefficients	Numerical estimates of coefficients
κ_1	$1.379\times10^{-4}\,(mm)^{-2}$
κ_2	$-8.690\times10^{-8}\,(mm)^{-3}$
κ_3	$6.521\times10^{-11}\,(mm)^{-4}$
κ_4	$2.3\times10^{-18}\,(mm)^{-5}$

B. PhotoModeler Estimation of Radial Distortion Coefficients

To calibrate the DSLR Nikon D3100 camera using PhotoModeler, a structured image acquisition procedure was conducted to ensure robust geometric coverage and high calibration accuracy. The calibration pattern used was the standard PhotoModeler target sheet, which was printed and mounted onto the flat surface of a light book cover using transparent adhesive tape. The book was then placed on a horizontal table surface to maintain a stable and planar reference for all

photographs. The camera was operated in landscape orientation and securely mounted on a tripod to maintain consistent framing and to minimize motion blur. The initial set of three images was captured with the camera in a level position directly above the calibration sheet. To vary the image geometry and enrich the data for calibration, the camera was then rotated 90^0 about its optical axis (roll) to the left, and three additional images were taken. Finally, the camera was rotated by an equivalent roll angle to the right to acquire the last three images. This controlled variation introduced perspective changes necessary for accurate computation of the camera's internal parameters and radial distortion coefficients. All photographs were captured under stable and diffuse lighting conditions to minimize reflections, glare, and shadows that could interfere with target recognition. All nine photographs were transferred to a computer and imported into a multi-sheet field calibration project within PhotoModeler. After setting the correct inner diameter for the circular coded targets and adjusting the printed calibration sheet's physical size, the software's automatic calibration process was initiated. PhotoModeler automatically detected and labeled the coded targets across the image set and then computed the camera's intrinsic parameters, including focal length, principal point, and three radial distortion coefficients, through a bundle adjustment process. The calibration successfully converged after only four iterations, yielding the coefficients used to formulate a depressed sixth-order radial distortion polynomial. Compared to other tools such as OpenCV, PhotoModeler provided a streamlined and efficient calibration workflow with minimal manual intervention. Figure 4-5 shows the radial distortion coefficient calibration workflow:

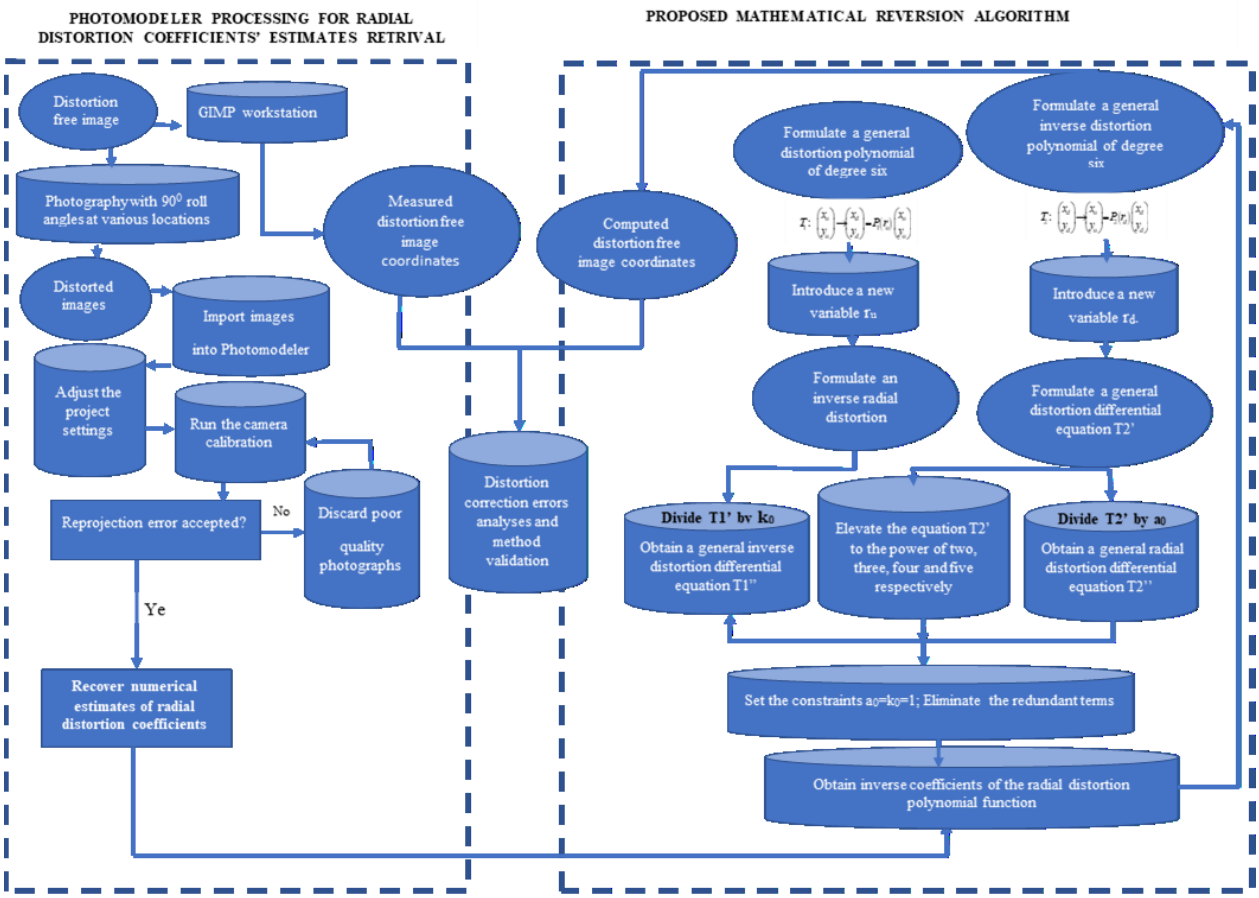

Figure 4-5: The PhotoModeler Radial Distortion Coefficients Calibration Workflow is shown on the left side of the figure. The associated polynomial reversion workflow on the right side of the figure is elaborated in section 4.2.3.C. of this chapter. Equations on the right side of the diagram are presented in [4-6.1] and [4-6.2].

Table 4.5 presents the estimates of calibrated radial distortion coefficients. The three coefficients describe the curves of radial distortion modelled by a depressed six-degree polynomial function.

Table 4.5: Radial Distortion Coefficients Calibrated through the Photomodeler Calibration Toolbox

Radial Distortion Coefficients	Numerical estimates of coefficients
κ_1	$1.27\times10^{-3}\,(mm)^{-2}$
κ_2	$-3.23\times10^{-5}\,(mm)^{-4}$
κ_3	$8.29\times10^{-8}\,(mm)^{-6}$

C. MATLAB Estimation of Radial Distortion Coefficients

To calibrate the Xiaomi Redmi, Note 11 Pro smartphone camera using MATLAB's Camera Calibration Toolbox, a carefully designed image acquisition procedure was carried out to ensure both geometric diversity and reliable feature extraction. A black-and-white checkerboard calibration pattern, with each black square measuring 30 mm per side, was printed and firmly mounted on a whiteboard, which was in turn fixed to a flat, vertical wall to provide a stable, planar reference surface. The smartphone camera was used to capture a total of 27 images of the pattern from various viewpoints. During the image capture process, the checkerboard remained stationary while the camera was repositioned at different heights, distances, and orientations, varying pitch, yaw, and roll angles to sample a wide portion of the lens's field of view and introduce necessary perspective distortion. These varied poses are essential for accurately estimating the intrinsic camera parameters and radial distortion coefficients. Efforts were made to ensure the entire pattern was visible within each frame, with good focus and uniform lighting to support precise corner detection. Importantly, a non-square checkerboard pattern was used to enable consistent identification of the origin corner across all images, which is critical for maintaining a consistent 3D coordinate reference in MATLAB's calibration process. Following image acquisition, the photographs were transferred to a desktop computer and imported into MATLAB. All 27 images were loaded into the calibration toolbox, and the automated corner detection algorithm was applied. Out of the 27 input images, 21 were successfully processed, while six were rejected. The rejected images exhibited either excessive glare resulting from direct overhead office lighting or extreme oblique angles, which caused distant corners to become too distorted for reliable detection. For calibration, the standard polynomial distortion model was selected instead of the fisheye model, as it allowed explicit specification of three radial distortion coefficients suitable for general-purpose lenses. The calibration toolbox then used a nonlinear least squares optimization routine to estimate the intrinsic camera parameters, including focal length, coordinates of the principal point, and radial distortion coefficients. The final calibration output was based on the 21 validated images and provided stable, accurate estimates of radial lens distortion coefficients. This process is summarized in Figure 4-6, which outlines the complete radial distortion calibration workflow used in MATLAB.

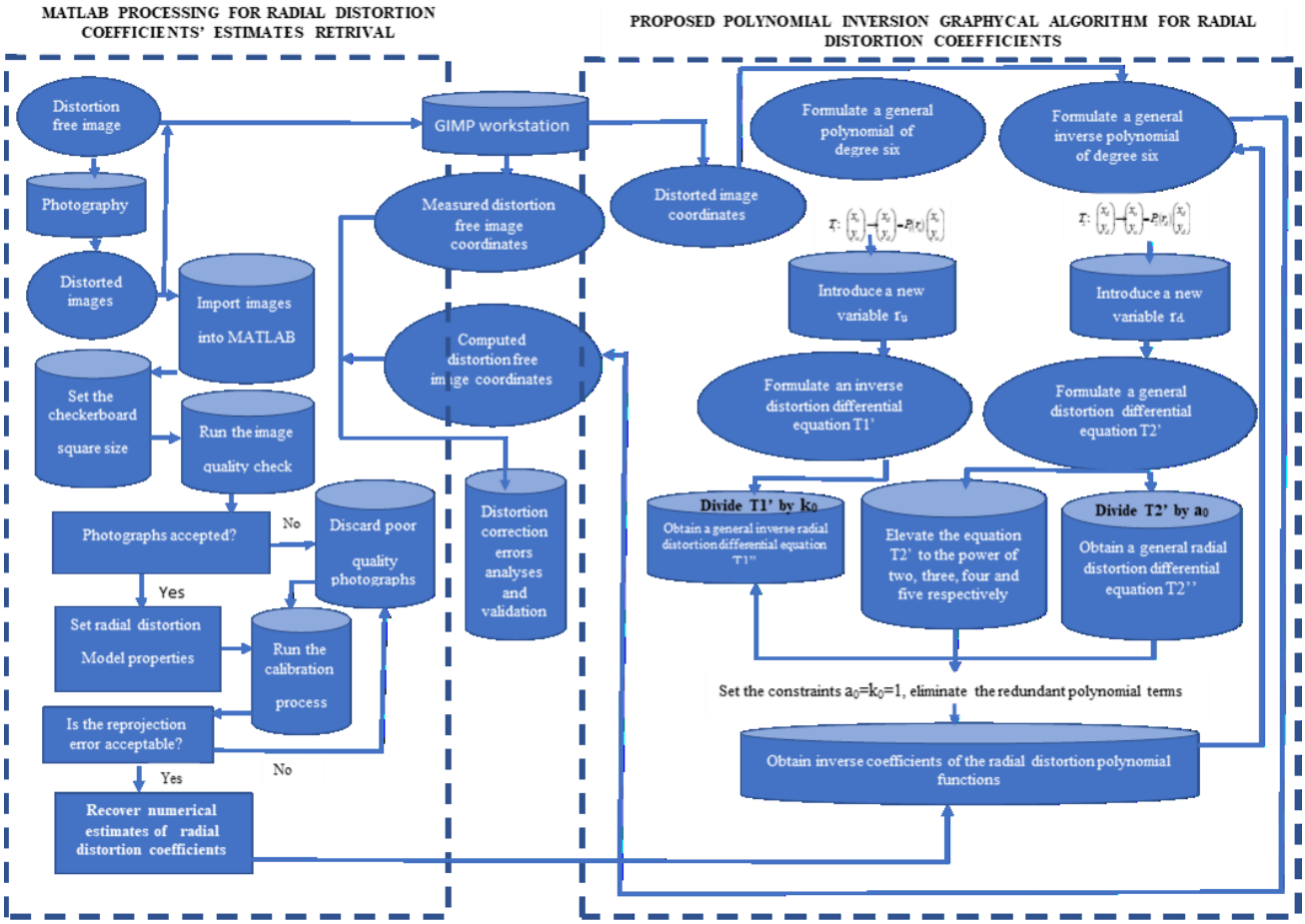

Figure 4-6: MATLAB Radial Distortion Coefficients Calibration Workflow on the left side of the figure. The associated polynomial reversion workflow on the right side of the figure is elaborated in section 4.2.3.D of this chapter. Equations on the right side of the diagram are presented in [4-6.1] and [4-6.2].

Table 4-6 presents radial distortion coefficients computed through the MATLAB camera calibration script.

Table 4.6: Radial Distortion Coefficients calibrated through MATLAB Calibration Toolbox

Radial Distortion Coefficients	Numerical estimates of coefficients
κ_1	$1.38\times10^{-3}\,(mm)^{-2}$
κ_2	$-8.69\times10^{-7}\,(mm)^{-5}$
κ_3	$6.52\times10^{-11}\,(mm)^{-8}$

4.2.3. Inverse Modelling of Radial Lens Distortion Polynomials

A. Semi Analytical Inverse Modelling of Radial Lens Distortions

The semi-analytic derivation of inverse radial distortion coefficients is similar to that proposed in the work of **Drap and Lefevre (2016)**. The strategy formulates the expressions of inverse radial distortions in a recursive manner where the expression of an inverse coefficient is derived

from that of the previous coefficient, and then an intensive iterative process is applied to refine the numerical estimates of all coefficients simultaneously. In this approach, the radial distance was first estimated under the assumption that the principal is located at the centre of the image. The estimated radial distance is then minimized through an optimization function. The first stage of the approach that refines the radial distortion magnitude is coded as follows:

$$\begin{cases} require: p_n \\ p_c = p_n \\ repeat \\ r = \|p_c\| \\ dr = 1 + \kappa_2 r^2 + \kappa_4 r^4 + \ldots \\ p_c = \dfrac{p_n}{dr} \\ until\ converge\ of\ p_c \\ return\ p_c \end{cases} \quad \textbf{[4-3]}$$

Where p_c is the distorted point while p_n is its distortion-free counterpart such that the distance $\|p_c - p_n\|$ is minimized using the repeat loop until the function **[4-3]** converges. The constraint $r = \|p_c\|$ means that the radial distance r is equal to the distance from the principal point, which is considered the image centre, to the distorted point p_c. Once the first coefficient of the series is computed, the next coefficients are recovered recursively, and the proposed first nine inverse coefficients of a general polynomial model are given as follows:

$$\alpha_1 = -\beta_1 \quad \textbf{[4-4.1]}$$

$$\alpha_2 = 3\varphi_1^2 - \varphi_2 \quad \textbf{[4-4.2]}$$

$$\alpha_3 = -12\varphi_1^3 + 8\varphi_1\varphi_2 - \varphi_3 \quad \textbf{[4-4.3]}$$

$$\alpha_4 = 55\varphi_1^4 - 55\varphi_1^2\varphi_2 + 5\varphi_2^2 + 10\varphi_1\varphi_3 - \varphi_4 \quad \textbf{[4.4.4]}$$

$$\alpha_5 = -273\varphi_1^5 + 364\varphi_1^3\varphi_2 - 78\varphi_1\varphi_2^2 - 78\varphi_1^2\varphi_3 + 12\varphi_2\varphi_3 + 12\varphi_1\varphi_4 \quad \textbf{[4-4.5]}$$

$$\begin{aligned} \alpha_6 = {} & 1428\varphi_1^6 - 2380\varphi_1^4\varphi_2 + 840\varphi_1^2\varphi_2^2 - 35\varphi_2^3 + 560\varphi_1^3\varphi_3 - 210\varphi_1\varphi_2\varphi_3 \\ & + 7\varphi_3^2 - 105\varphi_1^2\varphi_4 + 14\varphi_2\varphi_4 \end{aligned} \quad \textbf{[4-4.6]}$$

$$\begin{aligned} \alpha_7 = {} & -7752\varphi_1^7 + 15504\varphi_1^5\varphi_2 - 7752\varphi_1^3\varphi_2^2 + 816\varphi_1\varphi_2^3 - 3876\varphi_1^4\varphi_3 + 2448\varphi_1^2\varphi_2\varphi_3 \\ & - 136\varphi_2^2\varphi_3 - 136\varphi_1\varphi_3^2 + 816\varphi_1^3\varphi_4 - 272\varphi_1\varphi_2\varphi_4 + 16\varphi_3\varphi_4 \end{aligned} \quad \textbf{[4-4.7]}$$

$$\begin{aligned} \alpha_8 = {} & 43263\varphi_1^8 - 100947\varphi_1^6\varphi_2 + 65835\varphi_1^4\varphi_2^2 - 11970\varphi_1^2\varphi_2^3 + 285\varphi_2^4 + 26334\varphi_1^5\varphi_3 \\ & - 23940\varphi_1^3\varphi_2\varphi_3 + 3420\varphi_1\varphi_2^2\varphi_3 + 1710\varphi_1^2\varphi_3^2 - 171\varphi_2\varphi_3^2 - 5985\varphi_1^4\varphi_4 + 3420\varphi_1^2\varphi_2\varphi_4 \\ & - 171\beta\varphi_2^2\beta\varphi_4 - 342\beta\varphi_1\beta\varphi_3\beta\varphi_4 + 9\beta\varphi_4^2 \end{aligned} \quad \textbf{[4-4.8]}$$

$$\begin{aligned} \alpha_9 = {} & -246675\varphi_1^9 + 657800\varphi_1^7\varphi_2 - 531300\varphi_1^5\varphi_2^2 + 141680\varphi_1^3\varphi_2^3 - 8855\varphi_1\varphi_2^4 \\ & - 177100\varphi_1^6\varphi_3 + 212520\varphi_1^4\varphi_2\varphi_3 - 53130\varphi_1^2\varphi_2^2\varphi_3 + 1540\varphi_2^3\varphi_3 - 17710\varphi_1^3\varphi_3^2 \\ & + 4620\varphi_1\varphi_2\varphi_3^2 - 70\varphi_3^3 + 42504\varphi_1^5\varphi_4 - 35420\varphi_1^3\varphi_2\varphi_4 + 4620\varphi_1\varphi_2^2\varphi_4 \\ & + 4620\varphi_1^2\varphi_3\varphi_4 - 420\varphi_2\varphi_3\varphi_4 - 210\varphi_1\varphi_4^2 \end{aligned} \quad \textbf{[4-4.9]}$$

Where φ_n are the radial distortion coefficients of an invertible general polynomial model formulated as follows:

$$g(r) := \sum_{n=0}^{+\infty} \varphi_n r^{2n} \quad \textbf{[4-5.1]}$$

Let α_n be the coefficients of the inverse polynomial of $g(r)$ denoted $h(r)$ defined as follows:

$$h(r) := \sum_{n=0}^{+\infty} \alpha_n r^{2n} \quad \textbf{[4-5.2]}$$

As it can be observed from **[4-5.1]** and **[4-5.2],** the inverse distortion coefficients α_n were derived from a general polynomial formulation.

B. Analytical Inverse Modelling of a General Quintic Radial Distortion Polynomial.

Provided a general quintic radial distortion polynomial P_1 with coefficients $\kappa_0, \kappa_1, \kappa_2, \kappa_3$ and κ_4 that maps the undistorted coordinates (x_u, y_u) to their distorted counterparts (x_d, y_d) ,it is desired to formulate an inverse transformation polynomial P_2 of degree five with coefficients a_0 , a_1, a_2, a_3, a_4 that transforms the distorted coordinates (x_d, y_d) to undistorted counterparts (x_u, y_u) such that:

$$T_1: \quad \begin{pmatrix} x_u \\ y_u \end{pmatrix} \rightarrow \begin{pmatrix} x_d \\ y_d \end{pmatrix} = P_1(r_u) \begin{pmatrix} x_u \\ y_u \end{pmatrix} \quad \textbf{[4-6.1]}$$

$$T_2: \quad \begin{pmatrix} x_d \\ y_d \end{pmatrix} \rightarrow \begin{pmatrix} x_u \\ y_u \end{pmatrix} = P_2(r_d) \begin{pmatrix} x_d \\ y_d \end{pmatrix} \quad \textbf{[4-6.2]}$$

Where P_1 and P_2 are power series such that:

$$P_1(r_u): \quad = \sum_{n=2}^{5} \sum_{m=1}^{4} \left(k_m r_u^n + 1\right) \quad \textbf{[4-6.3]}$$

$$P_2(r_d): \quad = \sum_{n=2}^{5} \sum_{m=1}^{4} \left(\alpha_m r_d^n + 1\right) \quad \textbf{[4-6.4]}$$

It can be observed that equations **[4.1]** and **[4.2]** correspond to the equation **[4-6.3]** and **[4-6.4]** with $P_1(r_u)$ being an invertible polynomial. Since $P_1(r_u)$ is invertible, then $P_2(r_d)$ would transform a distorted point to its corresponding undistorted location through the following:

$$x_u = x_d \left(1 + \sum_{m=2}^{5} \sum_{n=1}^{4} \alpha_n r_d^m\right) \quad \textbf{[4-7.1]}$$

$$y_u = y_d \left(1 + \sum_{m=2}^{5} \sum_{n=1}^{4} \alpha_n r_d^m\right) \quad \textbf{[4-7.2]}$$

With the coefficients a_n being the inverse coefficients of κ_n . Let $f(r_u)$ be a general quintic polynomial defined in $\Re$ and formulated as follows:

$$f\left(r_u\right)=1+\sum_{m=1}^{5}\sum_{n=0}^{4}\kappa_n r_u^m \qquad \textbf{[4-8]}$$

Subtracting one from both sides of **[4-8]** leads to the following:

$$f\left(r_u\right)-1=\sum_{m=1}^{5}\sum_{n=0}^{4}\kappa_n r_u^m \qquad \textbf{[4-9]}$$

By introducing a new variable r_d by posing $f\left(r_u\right)-1=r_d$ the equation **[4-9]** was reformulated as follows:

$$r_d=\sum_{m=1}^{5}\sum_{n=0}^{4}\kappa_n r_u^m \qquad \textbf{[4-10]}$$

The inverse function of **[4-8]** must be a quintic model and must contain the variable r_u in its formulation so that its coefficients can easily be derived from those of **[4-8].** Let $g\left(r_u\right)$ be that inverse function formulated as follows:

$$g\left(r_u\right)=1+\sum_{m=1}^{5}\sum_{n=0}^{4}\alpha_n r_d^m \qquad \textbf{[4-11]}$$

Introducing a new variable r_u by posing $g\left(r_u\right)-1=r_u$, the equation **[4-11]** was reformulated as follows:

$$r_u=\sum_{m=1}^{5}\sum_{n=0}^{4}\alpha_n r_d^m \qquad \textbf{[4-12]}$$

Dividing both sides of equation **[4-10]** by the coefficient κ_0 leads to the following:

$$r_u=\frac{r_d}{\kappa_0}-\frac{1}{\kappa_0}\left(\sum_{m=2}^{5}\sum_{n=1}^{4}\kappa_n r_u^m\right) \qquad \textbf{[4-13]}$$

An observation of **[4-12]** and **[4-13]** reveals that both polynomials can be related. Elevating **[4-12]** to the quadratic, cubic, quartic, and quintic powers and then substituting these into the right side of **[4-13]** leads to the following:

$$r_u=\frac{r_d}{\kappa_0}-\frac{1}{\kappa_0}\left(\begin{array}{l}\kappa_4\left(\sum_{m=1}^{5}\sum_{n=0}^{4}\alpha_n r_d^m\right)^5+\kappa_3\left(\sum_{m=1}^{5}\sum_{n=0}^{4}\alpha_n r_d^m\right)^4\\ +\kappa_2\left(\sum_{m=1}^{5}\sum_{n=0}^{4}\alpha_n r_d^m\right)^3+\kappa_1\left(\sum_{m=1}^{5}\sum_{n=0}^{4}\alpha_n r_d^m\right)^2\end{array}\right) \qquad \textbf{[4-14]}$$

Substituting **[4-12]** into the left side of **[4-14]** leads to the following after some rearrangements of terms:

$$\left(\sum_{m=2}^{5}\sum_{n=1}^{4}\alpha_n r_d^m\right)+\alpha_0 r_d=\frac{r_d}{\kappa_0}-\frac{1}{\kappa_0}\left(\begin{array}{l}\kappa_4\left(\sum_{m=1}^{5}\sum_{n=0}^{4}\alpha_n r_d^m\right)^5+\kappa_3\left(\sum_{m=1}^{5}\sum_{n=0}^{4}\alpha_n r_d^m\right)^4\\ +\kappa_2\left(\sum_{m=1}^{5}\sum_{n=0}^{4}\alpha_n r_d^m\right)^3+\kappa_1\left(\sum_{m=1}^{5}\sum_{n=0}^{4}\alpha_n r_d^m\right)^2\end{array}\right) \qquad \textbf{[4-15]}$$

Dividing both sides of **[4-12]** by α_0 and after some reformulations produces the following:

$$r_d=\frac{r_u}{\alpha_0}-\frac{1}{\alpha_0}\left(\sum_{m=2}^{5}\sum_{n=1}^{4}\alpha_n r_d^m\right) \qquad \textbf{[4-16]}$$

For expressions **[4-13]** and **[4-16]** to match formulations of radial distortion polynomial models, the following constraints must be satisfied:

$$\alpha_0 = 1 \text{ and } \kappa_0 = 1 \quad \textbf{[4-17]}$$

Considering the constraints in **[4-17]** into **[4-15],** then after discarding terms with powers greater than five in the expressions in parentheses on the right side of the equality sign leads to the extraction of the following equations:

$$-\left(\kappa_0^{-1}\kappa_1\alpha_0^2\right)r_d^2 = \alpha_1 r_d^2 \quad \textbf{[4-18]}$$

$$-\left(\kappa_0^{-1}\kappa_2\alpha_0^3 + 2\kappa_0^{-1}\kappa_1\alpha_0\alpha_1\right)r_d^3 = \alpha_2 r_d^3 \quad \textbf{[4-19]}$$

$$-\left(2\kappa_0^{-1}\kappa_1\alpha_0\alpha_2 + \kappa_0^{-1}\kappa_3\alpha_0^4 + \kappa_0^{-1}\kappa_1\alpha_1^2 + 3\kappa_0^{-1}\kappa_2\alpha_0^2\alpha_1\right)r_d^4 = \alpha_3 r_d^4 \quad \textbf{[4-20]}$$

$$-\left(\kappa_4\kappa_0^{-1}\alpha_0^5 + \kappa_3\kappa_0^{-1}4\alpha_0^3\alpha_1 + 2\kappa_0^{-1}\kappa_1\alpha_0\alpha_3 + 2\kappa_0^{-1}\kappa_1\alpha_1\alpha_2 + 3\kappa_0^{-1}\kappa_2\alpha_0\alpha_1^2 + 3\kappa_0^{-1}\kappa_2\alpha_0^2\alpha_2\right)r_d^5 = \alpha_4 r_d^5 \quad \textbf{[4-21]}$$

From **[4-18] to [4-21],** the inverse radial distortion coefficients of the inverse quintic distortion model can analytically be estimated as follows:

$$\alpha_1 = -\kappa_1 \quad \textbf{[4-22.1]}$$

$$\alpha_2 = 2\kappa_1^2 - \kappa_2 \quad \textbf{[4-22.2]}$$

$$\alpha_3 = 5\kappa_1\kappa_2 - 5\kappa_1^3 - \kappa_3 \quad \textbf{[4-22.3]}$$

$$\alpha_4 = 14\kappa_1^4 + 6\kappa_1\kappa_3 - 21\kappa_1^2\kappa_2 + 3\kappa_2^2 - \kappa_4 \quad \textbf{[4-22.4]}$$

From **[4-22.1]- [4-22.4],** the inverse quintic radial distortion model required to correct radial distortions modelled by a general quintic can be formulated as follows:

$$x_u = x_d + x_d\left(\sum_{m=2}^{5}\sum_{n=1}^{4}\alpha_n r_d^m\right) \quad \textbf{[4-23.1]}$$

$$y_u = y_d + y_d\left(\sum_{m=2}^{5}\sum_{n=1}^{4}\alpha_n r_d^m\right) \quad \textbf{[4-23.2]}$$

A comparison between the formulations in **[4-22.1]- [4-22.4]** and **[4-4.1]- [4-4.4]** is presented in **Table 4.7**. It can be observed from the table that both methods share not only the same coefficients but also the same number of terms when formulating their respective individual inverse radial distortion coefficients. The formulation of the first inverse coefficient is similar for both approaches. In the formulation of the second inverse distortion coefficient, the numerical coefficient associated with the first term is greater for the semi-analytical algorithm in comparison to that of the proposed fully analytical algorithm. A similar trend can be observed for the estimation of the third and fourth inverse radial distortion coefficients.

Table 4.7: Formulations comparison for the inverse radial distortion coefficients of a general quintic polynomial distortion model derived from the semi-analytical and the fully analytical methods

Inverse radial distortion coefficients	Semi-analytical inverse modelling algorithms	Fully analytical inverse modelling algorithms
α_1	$-\kappa_1$	$-\kappa_1$
α_2	$3\kappa_1^2 - \kappa_2$	$2\kappa_1^2 - \kappa_2$
α_3	$8\kappa_1\kappa_2 - 12\kappa_1^3 - \kappa_3$	$5\kappa_1\kappa_2 - 5\kappa_1^3 - \kappa_3$

α_4	$55\kappa_1^4+10\kappa_1\kappa_3-55\kappa_1^2\kappa_2+5\kappa_2^2-\kappa_4$	$14\kappa_1^4+6\kappa_1\kappa_3-21\kappa_1^2\kappa_2+3\kappa_2^2-\kappa_4$

From algorithms in **[4-4.1]-[4-4.4]** presented in the second column of **table 4-7,** the semi-analytically derived inverse of a general quintic radial distortion polynomial can be formulated as follows:

$$x_u = x_d + x_d\begin{pmatrix}-\kappa_1 r_d^2+\left(3\kappa_1^2-\kappa_2\right)r_d^3+\left(8\kappa_1\kappa_2-12\kappa_1^3-\kappa_3\right)r_d^4\\+\left(55\kappa_1^4+10\kappa_1\kappa_3-55\kappa_1^2\kappa_2+5\kappa_2^2-\kappa_4\right)r_d^5\end{pmatrix} \quad \textbf{[4-24.1]}$$

$$y_u = y_d + y_d\begin{pmatrix}-\kappa_1 r_d^2+\left(3\kappa_1^2-\kappa_2\right)r_d^3+\left(8\kappa_1\kappa_2-12\kappa_1^3-\kappa_3\right)r_d^4\\+\left(55\kappa_1^4+10\kappa_1\kappa_3-55\kappa_1^2\kappa_2+5\kappa_2^2-\kappa_4\right)r_d^5\end{pmatrix} \quad \textbf{[4-24.2]}$$

Likewise, from the algorithms in **[4-22.1]-[4-22.4],** the analytically derived inverse of a general quintic radial distortion polynomial can be formulated as follows:

$$x_u = x_d + x_d\begin{pmatrix}-\kappa_1 r_d^2+\left(2\kappa_1^2-\kappa_2\right)r_d^3+\left(5\kappa_1\kappa_2-5\kappa_1^3-\kappa_3\right)r_d^4\\+\left(14\kappa_1^4+6\kappa_1\kappa_3-21\kappa_1^2\kappa_2+3\kappa_2^2-\kappa_4\right)r_d^5\end{pmatrix} \quad \textbf{[4-25.1]}$$

$$y_u = y_d + y_d\begin{pmatrix}-\kappa_1 r_d^2+\left(2\kappa_1^2-\kappa_2\right)r_d^3+\left(5\kappa_1\kappa_2-5\kappa_1^3-\kappa_3\right)r_d^4\\+\left(14\kappa_1^4+6\kappa_1\kappa_3-21\kappa_1^2\kappa_2+3\kappa_2^2-\kappa_4\right)r_d^5\end{pmatrix} \quad \textbf{[4-25.2]}$$

To correct radial distortion introduced by the DSLR Sony Alpha 200 lens system and modelled by a general quintic polynomial, using the semi-analytical derived inverse radial distortion coefficients, the numerical values of coefficients estimated through least squares were substituted into the algorithms in **[4-4.1]-[4-4.4],** and this led to the following formulations:

$$x_u = x_d + x_d\left(-1.379\times10^{-4}r_d^2+1.43\times10^{-7}r_d^3-1.93\times10^{-10}r_d^4+2.4\times10^{-13}r_d^5\right) \quad \textbf{[4-26.1]}$$

$$y_u = y_d + y_d\left(-1.379\times10^{-4}r_d^2+1.43\times10^{-7}r_d^3-1.93\times10^{-10}r_d^4+2.4\times10^{-13}r_d^5\right) \quad \textbf{[4-26.2]}$$

Similarly, to correct radial distortion introduced by the DSLR Sony Alpha 200 lens system and modelled by a general quintic polynomial using analytically developed algorithms, numerical values of radial distortion coefficients in **Table 4-4** were substituted into the algorithms in **[4-22.1]-[4-22.4]** to achieve the following inverse models:

$$x_u = x_d + x_d\left(-1.379\times10^{-4}r_d^2+1.24\times10^{-7}r_d^3-1.38\times10^{-10}r_d^4+1.17\times10^{-13}r_d^5\right) \quad \textbf{[4-27.1]}$$

$$y_u = y_d + y_d\left(-1.379\times10^{-4}r_d^2+1.24\times10^{-7}r_d^3-1.38\times10^{-10}r_d^4+1.17\times10^{-13}r_d^5\right) \quad \textbf{[4-27.2]}$$

C. Analytical Inverse Modelling of a Depressed Six-degree Radial Distortion Polynomial

The objective of this task is to determine three coefficients β_1, β_2 and β_3 such that the correction of radial distortion modelled by a depressed six-degree polynomial is done through the following algorithms:

$$x_u = x_d + x_d\left(\sum_{m=2,4,6}\sum_{n=1}^{3}\beta_n r_d^m\right) \quad \textbf{[4-28.1]}$$

$$y_u = y_d + y_d\left(\sum_{m=2,4,6}\sum_{n=1}^{3}\beta_n r_d^m\right) \quad \textbf{[4-28.2]}$$

For this purpose, let's consider the following six-degree radial distortion polynomial:

$$h(r_u) = \sum_{m=1}^{6} \sum_{n=0}^{3} \kappa_n r_u^m + 1 \qquad \textbf{[4-29]}$$

A reformulation of **[4-29]** can be given as follows:

$$h(r_u) - 1 = \sum_{m=1}^{6} \sum_{n=0}^{3} \kappa_n r_u^m \qquad \textbf{[4-30]}$$

Introducing a new variable by posing $h(r_u) - 1 = r_d$, the expression in **[4-30]** becomes the following:

$$r_d = \sum_{m=1}^{6} \sum_{n=0}^{3} \kappa_n r_u^m \qquad \textbf{[3-31]}$$

Since the original distortion model in **[4-29]** is a sixth-order polynomial, its corresponding inverse must also be a sixth-order polynomial and its formulation must contain the variable r_u. Let's define $J(r_d)$ as this inverse sixth-order radial distortion polynomial formulated as follows:

$$J(r_u) = \sum_{m=1}^{6} \sum_{n=0}^{3} \beta_n r_d^m + 1 \qquad \textbf{[4-32]}$$

By introducing a new variable r_u by posing $J(r_d) - 1 = r_u$, the equation **[4-32]** can be formulated as follows:

$$r_u = \sum_{m=1}^{6} \sum_{n=0}^{3} \beta_n r_d^m \qquad \textbf{[4-33]}$$

Dividing both sides of equation **[4-31]** by the coefficient κ_0 and then isolating r_u on one side of the equality sign leads to the following:

$$r_u = \frac{r_d}{\kappa_0} - \frac{1}{\kappa_0}\left(\sum_{m=2,4,6} \sum_{n=1}^{3} \kappa_n r_u^m \right) \qquad \textbf{[4-34]}$$

Substituting **[4-33]** into the left side of **[4-34]** leads to the following:

$$\sum_{m=1}^{6} \sum_{n=0}^{3} \beta_n r_d^m = \frac{r_d}{\kappa_0} - \frac{1}{\kappa_0}\left(\sum_{m=2,4,6} \sum_{n=1}^{3} \kappa_n r_u^m \right) \qquad \textbf{[4-35]}$$

Elevating **[4-33]** to the quadratic, quartic, and sixth powers, respectively, and substituting the results in the right side of **[4-35]** leads to the following equation:

$$\sum_{m=1}^{6} \sum_{n=0}^{3} \beta_n r_d^m = \frac{r_d}{\kappa_0} - \frac{1}{\kappa_0}\left(\begin{array}{l} \kappa_4 \left(\sum_{m=1}^{6} \sum_{n=0}^{3} \beta_n r_d^m \right)^5 + \kappa_3 \left(\sum_{m=1}^{6} \sum_{n=0}^{3} \beta_n r_d^m \right)^4 \\ + \kappa_2 \left(\sum_{m=1}^{6} \sum_{n=0}^{3} \beta_n r_d^m \right)^3 + \kappa_1 \left(\sum_{m=1}^{6} \sum_{n=0}^{3} \beta_n r_d^m \right)^2 \end{array} \right) \qquad \textbf{[4-36]}$$

Similarly, after consideration of the constraints in **[4-17]** and discarding all terms with powers greater than six on the right side of **[4-36],** the following five equations can be derived**:**

$$\beta_1 r_d^2 = -\kappa_1 \beta_0^2 r_d^2 \qquad \textbf{[4-37.1]}$$

$$-2\beta_0 \beta_1 \kappa_1 r_d^3 = 0 \qquad \textbf{[4-37.2]}$$

$$\beta_2 r_d^4 = \left(-\kappa_2 \beta_0^4 - \kappa_1 \beta_1^2 \right) r_d^4 \qquad \textbf{[4-37.3]}$$

$$-2\beta_0 \beta_2 \kappa_1 r_d^5 - 4\beta_0^3 \beta_1 \kappa_2 r_d^5 = 0 \qquad \textbf{[4-37.4]}$$

$$\beta_3 r_d^6 = -2\beta_1\beta_2\kappa_1 r_d^6 - 6\beta_0^2\beta_1^2\kappa_2 r_d^6 - \beta_0^6\kappa_3 r_d^6 \quad \textbf{[4.37.5]}$$

Constraints **[4-37.2]** and **[4-37.4]** are not needed; thus, from **[4-37.4], [4-37.3],** and **[4-37.5],** the following three inverse coefficients are formulated:

$$\beta_1 = -\kappa_1 \quad \textbf{[4-38.1]}$$

$$\beta_2 = -\kappa_1^3 - \kappa_2 \quad \textbf{[4-38.2]}$$

$$\beta_3 = -8\kappa_1^2\kappa_2 - 2\kappa_1^5 - \kappa_3 \quad \textbf{[4-38.3]}$$

A comparison between **[4-38.1]-[4.38.3]** and **[4-4.1]-[4.4.9]** is presented in **table 4.8**. Although the presented inverse coefficient β_2 contains the same original radial distortion coefficients κ_1 and κ_2 as well as the same number of terms in both algorithms, the main difference can be observed in the formulation of the first term of the second inverse coefficient. Although both first terms are made of the radial distortion coefficient κ_1, the numerical coefficient associated with it is three times larger and positive for the semi-analytical algorithm, while it is associated with a negated unity coefficient in the analytically derived expression. The power attached to this coefficient κ_1 is quadratic for the semi-analytical model while it has a cubic power in the analytically derived inverse coefficient. Regarding the formulation of the third inverse radial distortion coefficient β_3, the main differences concern the first and second terms, respectively. Although the first term of the inverse coefficient holds the same numerical coefficient of eight in both strategies, it has a positive sign in the semi-analytically derived formulation while it has a negative sign in the analytically derived formulation. In addition, the parameter κ_1 holds a quadratic power in the analytically derived formulation, while it holds a power of one in the semi-analytically derived formulation. The second term of the inverse coefficient β_3 shares a negative sign from both formulations; however, the numerical coefficient associated with the term is six times larger in the semi-analytically derived formulation than the analytically derived inverse coefficient. Although the powers associated with the parameter κ_1 are odd powers, that of the semi-analytically derived algorithm is cubic, while in the analytically derived formulation it is a quintic power. Both semi-analytically and analytically derived formulations share the same third term, which is the negated radial distortion coefficient κ_3.

Table 4.8: Formulations comparison for the inverse coefficients of a depressed six-degree polynomial model respectively derived from the semi-analytical and fully analytical approaches

Inverse radial distortion coefficients	Semi-analytical inversion algorithms for the six-order radial distortion polynomial	Proposed analytical inversion algorithms for the six-order radial distortion polynomial
β_1	$-\kappa_1$	$-\kappa_1$
β_2	$3\kappa_1^2 - \kappa_2$	$-\kappa_1^3 - \kappa_2$
β_3	$8\kappa_1\kappa_2 - 12\kappa_1^3 - \kappa_3$	$-8\kappa_1^2\kappa_2 - 2\kappa_1^5 - \kappa_3$

From the inverse radial distortion coefficients **[4-4.1]- [4-4.3]** presented in the second column of table 8 the expression of the inverse radial distortion function that corrects radial distortions modelled by a depressed six-degree polynomial is formulated as follows:

$$x_u = x_d + x_d\left(-\kappa_1 r_d^2 + \left(3\kappa_1^2 - \kappa_2\right) r_d^4 + \left(8\kappa_1\kappa_2 - 12\kappa_1^3 - \kappa_3\right) r_d^6\right) \quad \textbf{[4-39.1]}$$

$$y_u = y_d + y_d\left(-\kappa_1 r_d^2 + \left(3\kappa_1^2 - \kappa_2\right) r_d^4 + \left(8\kappa_1\kappa_2 - 12\kappa_1^3 - \kappa_3\right) r_d^6\right) \quad \textbf{[4-39.2]}$$

Similarly, the correction of radial distortions modelled by a depressed six-order polynomials can be done through the analytically modelled inverse functions as follows:

$$x_u = x_d + x_d\left(-\kappa_1 r_d^2 - \left(\kappa_1^3 + \kappa_2\right) r_d^4 - \left(2\kappa_1^5 + 8\kappa_1^2\kappa_2 + \kappa_3\right) r_d^6\right) \quad \textbf{[4-40.1]}$$

$$y_u = y_d + y_d\left(-\kappa_1 r_d^2 - \left(\kappa_1^3 + \kappa_2\right) r_d^4 - \left(2\kappa_1^5 + 8\kappa_1^2\kappa_2 + \kappa_3\right) r_d^6\right) \quad \textbf{[4-40.2]}$$

The correction of radial distortions introduced by the Nikon D3100 non-metric camera lens system can be done using the semi-analytically derived inverse coefficients through the following inverse polynomial models:

$$x_u = x_d + x_d\left(-1.27\times10^{-3} r_d^2 + 3.71\times10^{-5} r_d^4 - 4.37\times10^{-7} r_d^6\right) \quad \textbf{[4-41.1]}$$

$$y_u = y_d + y_d\left(-1.27\times10^{-3} r_d^2 + 3.71\times10^{-5} r_d^4 - 4.37\times10^{-7} r_d^6\right) \quad \textbf{[4-41.2]}$$

Likewise, the correction of radial distortions produced by the lens system of the Nikon D3100 non-metric camera and modelled by a six-order depressed polynomial model can be done through the analytically derived inverse models as follows:

$$x_u = x_d + x_d\left(-1.27\times10^{-3} r_d^2 + 3.23\times10^{-5} r_d^4 - 8.2\times10^{-8} r_d^6\right) \quad \textbf{[4-42.1]}$$

$$y_u = y_d + y_d\left(-1.27\times10^{-3} r_d^2 + 3.23\times10^{-5} r_d^4 - 8.2\times10^{-8} r_d^6\right) \quad \textbf{[4-42.2]}$$

D. Analytical Inverse Modelling of a Depressed Eight-degree Radial Distortion Polynomial

Let's now consider the following invertible eight-degree radial distortion model:

$$L\left(r_u\right) = \sum\nolimits_{q=1,2,5,8} \sum_{p=0}^{3} \kappa_p r_u^q + 1 \quad \textbf{[4-43]}$$

A reformulation of **[4-43]** can be made as follows:

$$L\left(r_u\right) - 1 = \sum\nolimits_{q=1,2,5,8} \sum_{p=0}^{3} \kappa_p r_u^q \quad \textbf{[4-44]}$$

Introducing a new variable r_d by posing $L\left(r_u\right) - 1 = r_d$ the expression in **[4-44]** becomes the following:

$$r_d = \sum\nolimits_{q=1,2,5,8} \sum_{p=0}^{3} \kappa_p r_u^q \quad \textbf{[4-45]}$$

Let's define $M\left(r_d\right)$ as the inverse six-order polynomial formulated as follows:

$$M\left(r_d\right) = \sum\nolimits_{q=1,2,5,8} \sum_{p=0}^{3} \rho_p r_d^q + 1 \quad \textbf{[4-46]}$$

Introducing a new variable r_u by posing $M\left(r_d\right)-1=r_u$, the equation **[4-46]** was formulated as follows:

$$r_u=\sum\nolimits_{q=1,2,5,8}\ \sum_{p=0}^{3}\rho_p r_d^q \qquad \textbf{[4-47]}$$

Dividing both sides of equation **[4-45]** by the coefficient κ_0 leads to the following:

$$r_u=\frac{r_d}{\kappa_0}-\frac{1}{\kappa_0}\left(\begin{array}{l}\kappa_3\left(\sum\nolimits_{q=1,2,5,8}\ \sum_{p=0}^{3}\rho_p r_d^q\right)^8+\kappa_2\left(\sum\nolimits_{q=1,2,5,8}\ \sum_{p=0}^{3}\rho_p r_d^q\right)^5\\ +\kappa_1\left(\sum\nolimits_{q=1,2,5,8}\ \sum_{p=0}^{3}\rho_p r_d^q\right)^2\end{array}\right) \qquad \textbf{[4-48]}$$

Dividing both sides of **[4-47]** by ρ_0 leads to the following equality:

$$r_d=\frac{r_u}{\rho_0}-\frac{1}{\rho_0}\left(\sum_{q=2,5,8}\ \sum_{p=1}^{3}\rho_p r_d^q\right) \qquad \textbf{[4-49]}$$

For the models in **[4-48]** and **[4-49]** to match the formulation of a radial distortion function, the following constraint must hold true:

$$\kappa_0=\rho_0=1 \qquad \textbf{[4-50]}$$

Substituting **[4-47]** in the left side of the equality sign in **[4-48]** leads to the following after consideration of the constraint in **[4-50]:**

$$\sum_{q=2,5,8}\ \sum_{p=1}^{3}\rho_p r_d^q+r_d=r_d+\left(\begin{array}{l}-\kappa_3\left(\sum\nolimits_{q=1,2,5,8}\ \sum_{p=0}^{3}\rho_p r_d^q\right)^8\\ -\kappa_2\left(\sum\nolimits_{q=1,2,5,8}\ \sum_{p=0}^{3}\rho_p r_d^q\right)^5\\ -\kappa_1\left(\sum\nolimits_{q=1,2,5,8}\ \sum_{p=0}^{3}\rho_p r_d^q\right)^2\end{array}\right) \qquad \textbf{[4-51]}$$

Subtracting r_d from both sides of **[4-51]** leads to the following equality:

$$\sum_{q=2,5,8}\ \sum_{p=1}^{3}\rho_p r_d^q=\left(\begin{array}{l}-\kappa_3\left(\sum\nolimits_{q=1,2,5,8}\ \sum_{p=0}^{3}\rho_p r_d^q\right)^8-\kappa_2\left(\sum\nolimits_{q=1,2,5,8}\ \sum_{p=0}^{3}\rho_p r_d^q\right)^5\\ -\kappa_1\left(\sum\nolimits_{q=1,2,5,8}\ \sum_{p=0}^{3}\rho_p r_d^q\right)^2\end{array}\right) \qquad \textbf{[4-52]}$$

Elevating **[4-47]** to the quadratic, quintic, and eighth powers and then substituting the results into the right side of **[4-52]** produces the following equations after discarding all terms with powers greater than eight:

$$\rho_1 r_d^2=-\left(\kappa_1\rho_0^2\right)r_d^2 \qquad \textbf{[4-53.1]}$$

$$\rho_2 r_d^5=-\left(\kappa_2\right)r_d^5 \qquad \textbf{[4-53.2]}$$

$$\rho_3 r_d^7=-\left(\kappa_3+10\kappa_2\rho_1^3\right)r_d^7 \qquad \textbf{[4-53.3]}$$

$$\left(10\kappa_2\rho_0^3\rho_1^2 + 2\kappa_1\rho_1\rho_2\right)r_d^6 + \left(2\kappa_1\rho_0\rho_2 + 5\kappa_2\rho_0^4\rho_1\right)r_d^5 + \left(2\kappa_1\rho_0\rho_1\right)r_d^2 = 0 \qquad \textbf{[4-53.4]}$$

From **[4-53.1]** to **[4-53.3]** the following three inverse coefficients were derived since the constraint in **[4-53.4]** was not needed:

$$\rho_1 = -\kappa_1 \qquad \textbf{[4-54.1]}$$

$$\rho_2 = -\kappa_2 \qquad \textbf{[4-54.2]}$$

$$\rho_3 = 10\kappa_1^3\kappa_2 - \kappa_3 \qquad \textbf{[4-54.3]}$$

A comparison between **[4-4.1]- [4-4.3]** and **[4-54.1]- [4-54.3]** is presented in **Table 4.9**. An analysis of columns two and three shows that both inverse coefficient calibration strategies share the same first inverse radial distortion coefficient ρ_1. Regarding the second inverse distortion coefficient ρ_2, the main formulation difference between the semi-analytical and analytically derived methods is that the semi-analytical algorithm possesses an additional term composed of the distortion parameter κ_1 elevated to the quadratic power and associated with a numerical coefficient of three. The formulations of ρ_2 by both strategies share a negated radial distortion parameter κ_2. Regarding the formulation of the third inverse radial distortion coefficient ρ_3 the semi-analytical strategy possesses one additional term compared to the number of terms in the analytically derived approach. The first term of the coefficient from both strategies is composed of the product of radial distortion coefficients κ_1 and κ_2. However, in the semi analytic expression, the coefficients product is associated with a positive numerical coefficient of eight, while for the analytical approach, the coefficient κ_1 is elevated to the cubic power, and the coefficients product is associated with a positive coefficient of 10. The second term of the inverse coefficient is made of the coefficients κ_1 elevated to the cubic power and associated with a negative numerical coefficient of twelve for the semi-analytical approach. This second term does not appear in the inverse coefficient algorithm derived analytically. Regarding the last term, both strategies share the negated radial distortion coefficient κ_3.

Table 4.9: Comparison between inverse radial distortion coefficients derived from the semi analytical and the fully analytical approaches

Inverse radial distortion coefficients	Semi-analytical inversion formulations	Analytical inversion formulations
ρ_1	$-\kappa_1$	$-\kappa_1$
ρ_2	$3\kappa_1^2 - \kappa_2$	$-\kappa_2$
ρ_3	$8\kappa_1\kappa_2 - 12\kappa_1^3 - \kappa_3$	$10\kappa_1^3\kappa_2 - \kappa_3$

From the inverse coefficients **[4-4.1]- [4-4.3]** presented in the second column in **Table 4-9,** one can formulate the inverse radial distortion models to correct radial distortions modelled by a depressed eight-degree polynomial function as follows:

$$x_u = x_d + x_d\left(\left(-\kappa_1\right)r_d^2 + \left(3\kappa_1^2 - \kappa_2\right)r_d^5 + \left(8\kappa_1\kappa_2 - 12\kappa_1^3 - \kappa_3\right)r_d^8\right) \qquad \textbf{[4-55.1]}$$

$$x_u = x_d + x_d\left(\left(-\kappa_1\right)r_d^2 + \left(3\kappa_1^2 - \kappa_2\right)r_d^5 + \left(8\kappa_1\kappa_2 - 12\kappa_1^3 - \kappa_3\right)r_d^8\right) \qquad \textbf{[4-55.2]}$$

Similarly, from inverse coefficients analytically derived in **[4-54.1]- [4-54.2]** the correction of radial distortions modelled by a depressed eight-degree polynomial can be done through the following transformations:

$$x_u = x_d - x_d\left(\kappa_1 r_d^2 + \kappa_2 r_d^5 - \left(10\kappa_1^3\kappa_2 - \kappa_3\right) r_d^8\right) \quad \textbf{[4-56.1]}$$

$$y_u = y_d - y_d\left(\kappa_1 r_d^2 + \kappa_2 r_d^5 - \left(10\kappa_1^3\kappa_2 - \kappa_3\right) r_d^8\right) \quad \textbf{[4-56.2]}$$

To correct radial distortions introduced by the Xiaomi Redmi Pro 11 lens system using semi-analytically derived inverse radial distortion coefficients, the following modeling can be used:

$$x_u = x_d + x_d\left(-1.38\times10^{-3} r_d^2 + 6.57\times10^{-6} r_d^5 - 4\times10^{-8} r_d^8\right) \quad \textbf{[4-57.1]}$$

$$y_u = y_d + y_d\left(-1.38\times10^{-3} r_d^2 + 6.57\times10^{-6} r_d^5 - 4\times10^{-8} r_d^8\right) \quad \textbf{[4-57.2]}$$

Similarly, the correction of radial distortions introduced by the Xiaomi Redmi Pro 11 lens system and modelled by an eight-order depressed radial distortion polynomial can be done through the following transformations when using the analytically derived inverse radial distortion coefficients:

$$x_u = x_d + x_d\left(-1.38\times10^{-3} r_d^2 + 8.69\times10^{-7} r_d^5 - 6.52\times10^{-11} r_d^8\right) \quad \textbf{[4-58.1]}$$

$$y_u = y_d + y_d\left(-1.38\times10^{-3} r_d^2 + 8.69\times10^{-7} r_d^5 - 6.52\times10^{-11} r_d^8\right) \quad \textbf{[4-58.2]}$$

4.2.4. Applications of the developed theories in radial distortions corrections

A. Correcting moderate barrel radial distortions modelled by a general quintic polynomial function

The effects of radial lens distortions on distortion-free image points are generally modelled by equation **[4-59]** as follows.

$$r_d = \sum_{m=0}^{n}\sum_{n=0}^{n} \kappa_n r_u^m \quad \textbf{[4-59]}$$

However, from the formulation in **[4-59],** it is not possible to predict the type of radial distortion that would affect points in an image. Generally, only numerical estimates of individual radial distortion coefficients can give an idea of the type of radial distortions that alter the distortion-free image coordinates. Substituting radial distortion coefficients estimated through least squares into equation **[4-59]** gives the following modelling:

$$x_d = x_u + x_u\left(1.379\times10^{-4} r_u^2 - 8.690\times10^{-8} r_u^3 + 6.521\times10^{-11} r_u^4 + 2.3\times10^{-18} r_u^5\right) \quad \textbf{[4-60.1]}$$

$$y_d = y_u + y_u\left(1.379\times10^{-4} r_u^2 - 8.690\times10^{-8} r_u^3 + 6.521\times10^{-11} r_u^4 + 2.3\times10^{-18} r_u^5\right) \quad \textbf{[4-60.2]}$$

An analysis of equations **[4-60.1]– [4-60.2]** reveals that the radial distortion function is mainly a positive function because of the very small negative coefficient associated with the second term of the function, and this suggests that the lens system of the DSLR Sony Alpha 200 camera introduced barrel radial lens distortions into the photographed images. To assess the effectiveness of the inverse radial distortion models in correcting barrel radial distortion, it is needed to obtain measures of distortion-free coordinates and their distorted counterparts. To

achieve these, a synthetic distortion-free image of the PhotoModeler calibration pattern was imported into the GIMP open-source software in order to collect distortion-free coordinates of 100 image points in millimetres. To have their respective distorted counterparts, the PhotoModeler calibration pattern was printed, then one picture of the pattern was taken using the Sony Alpha 200 camera, and then transferred the image into the computer before importing it into the GIMP workstation. From the digital photograph, distorted coordinates of the same 100 image points were measured in millimetres. **Table 4.10** presents a subset of the distortion-free point coordinates and their distorted counterparts measured from the GIMP workstation.

Table 4.10: Subset of distortion free image point coordinates measured from the synthetic distortion free digital image of a calibration pattern and their respective distorted coordinates measured after the photograph

Measured distortion free points coordinates(mm)		Measured distorted points coordinates(mm)	
$x_u\,(mm)$	$y_u\,(mm)$	$x_d\,(mm)$	$y_d\,(mm)$
7.34	6.96	7.44	7.06
8.20	5.96	8.32	6.05
5.23	6.76	5.28	6.83
4.60	5.10	4.63	5.13
6.90	7.39	7.00	7.49
1.75	6.54	1.76	6.58
3.26	2.98	3.27	2.99
2.85	8.35	2.88	8.44
9.92	3.80	10.07	3.86
4.56	2.75	4.58	2.76

A comparison between the first two columns and the last two columns in **Table 4-10** reveals that the radial distortion effect has altered the original locations of points by pushing them outwardly to create the barrel distortion effect. To remove radial distortions from the distorted coordinates in the last two columns using inverse radial distortion models formulated in **(30.1)** and **(30.2),** the radial distance r_d for each distorted point was computed and then elevated to the powers of two, three, four, and five. **Table 4.11** shows the computed radial distances elevated to the required powers.

Table 4.11: Radial distortion radii estimated from distorted image points coordinates measured from the photograph of the calibration pattern in Figure 4-4(A)

Distorted points coordinate		distorted radii elevated to the power two, three, four and five			
$x_d\,(mm)$	$y_d\,(mm)$	$r_d^2\,(mm)^2$	$r_d^3\,(mm)^3$	$r_d^4\,(mm)^4$	$r_d^5\,(mm)^5$
7.44	7.06	105.27	1080.05	11081.27	113693.81
8.32	6.05	105.88	1089.55	11211.44	115365.75
5.28	6.83	74.48	642.74	5546.81	47868.96
4.63	5.13	47.75	329.94	2279.88	15753.98
7.00	7.49	105.06	1076.89	11038.13	113140.82

1.76	6.58	46.38	315.82	2150.74	14646.56
3.27	2.99	19.63	86.94	385.14	1706.16
2.88	8.44	79.57	709.73	6330.81	56470.84
10.07	3.86	116.21	1252.73	13504.39	145577.35
4.58	2.76	28.62	153.13	819.25	4382.97

Substituting the data in the third, fourth, fifth, and sixth columns of **table 4-11** into the inverse radial distortion models in **[4-24.1], [4-24.2],** and **[4-25.1], [4-25.2]** leads to the corrected coordinates of image points in columns one and two of **Table 4.11.** After the removal of radial distortion effects from affected points, the corrected coordinates are expected to fall as close as possible to their respective distortion-free reference coordinate measures presented in the first two columns of **Table 4.10.**

B. Correcting moustache radial distortions modelled by a sixth-degree polynomial.

Radial distortion coefficients estimated using PhotoModeler and presented in **Table 4-5** show more than one sign held by the coefficients, which according to some current literature is proof of the presence of moustache radial distortions in the photographed imagery. Only a comparison between distortion-free coordinates and their respective distorted counterparts can give a clue about the distortion profile(s) that dominate the distortion function since the assumption that more than one sign among radial distortion coefficients was enough to describe moustache distortions did not hold true in the previous experiment. Substituting the estimates of radial distortion coefficients into the radial distortion functions can also provide some information about the dominant distortion profile in the imagery. Substituting distortion coefficients estimated through the PhotoModeler calibration toolbox and presented in **Table 4-5** into equations **[4.1]** and **[4.2]** leads to the following:

$$x_d = x_u + x_u\left(1.27\times10^{-3}r_u^2 - 3.23\times10^{-5}r_u^4 + 8.29\times10^{-8}r_u^6\right) \qquad \textbf{[4-61.1]}$$

$$x_d = x_u + x_u\left(1.27\times10^{-3}r_u^2 - 3.23\times10^{-5}r_u^4 + 8.29\times10^{-8}r_u^6\right) \qquad \textbf{[4-61.2]}$$

An analysis of **[4-61.1]** and **[4-61.2]** shows that for small values of the radial distortion radius, r_u these equations may model only barrel radial distortions. In contrast, for larger values of the parameter, the second term of the function with the negative numerical coefficient may turn out to be the most dominant within the distortion function numerical estimate. The power of four associated with the second term of the above models makes it possible to obtain negative values of the distortion function, which will lead to pincushion and barrel radial distortions among the distorted coordinates. To further investigate the possibilities of having barrel and pincushion distortions affecting the image points, a synthetic distortion-free image of the PhotoModeler calibration pattern was downloaded, and then 70 distortion-free points were extracted in the GIMP workstation. To extract the corresponding distorted coordinates, the same calibration pattern was printed and then photographed by the Nikon D3100 non-metric camera. The photographed image of the pattern was transferred to the computer desktop, and then imported into GIMP to have the distorted image coordinates measured in millimetres. **Table 4.12** presents a subset of the measured distortion-free coordinates and their associated distorted coordinates extracted from the digital photograph of the calibration pattern.

Table 4.12: Manually measured distortion free image points coordinates and their measured distorted counterparts

Distortion free points coordinates		Distorted coordinates by the first set of coefficients	
$x_u\,(mm)$	$y_u\,(mm)$	$x_d\,(mm)$	$y_d\,(mm)$
6.34	5.60	6.06	5.35
7.20	4.96	6.80	4.69
4.22	5.75	4.19	5.70
3.59	4.10	3.63	4.15
5.90	6.39	5.59	6.05
2.72	7.54	2.64	7.32
4.26	3.98	4.30	4.02
2.84	8.34	2.68	7.86
8.91	2.79	8.20	2.57
3.56	1.74	3.61	1.76

After analysing the measured distortion-free coordinates extracted from the image of the calibration pattern and their distorted counterparts, it can be observed that some point coordinates were increased due to the outward displacements while others were reduced due to the inward displacement caused by the lens system of the Nikon D3100 camera. The above seems to indicate that the lens system created a moustache radial distortion profile on the image points. With the distorted coordinates of image points now measured, it is possible to evaluate the effectiveness of the analytically derived inverse radial distortion models proposed to correct moustache radial distortions. To remove or reduce the amounts of moustache distortions from image points in the last two columns of **Table 4.12,** the radial distance r_d was computed for each point and then elevated them to the quadratic, quartic, and sixth powers needed by the inverse radial distortion models. Table 4.13 shows a subset of the different distorted radii computed from individual measured distorted image coordinates.

Table 4.13: Distorted radii computed from distorted image points measured on the photographed printout of the synthetic image of the calibration pattern

Distorted points coordinate		distorted radii elevated to the power two, four and six			
$x_d\,(mm)$	$y_d\,(mm)$	$r_d\,(mm)$	$r_d^2\,(mm)^2$	$r_d^4\,(mm)^4$	$r_d^6\,(mm)^6$
6.06	5.35	8.09	65.45	4283.46	280343.91
6.80	4.69	8.26	68.23	4655.01	317599.85
4.19	5.70	7.07	49.99	2498.49	124886.78
3.63	4.15	5.52	30.47	928.45	28290.10
5.59	6.05	8.24	67.90	4610.08	313013.65
2.64	7.32	7.78	60.53	3663.69	221757.13
4.30	4.02	5.89	34.69	1203.54	41753.40
2.68	7.86	8.30	68.89	4745.83	326940.37
8.20	2.57	8.59	73.79	5444.68	401752.87

3.61	1.76	4.02	16.16	261.16	4220.43

With the radial distortion radii now computed, the effect of radial moustache distortion can be corrected. To evaluate the newly proposed inverse distortion models, the parameters in the fourth, fifth, and sixth columns were substituted into each one of the models in **[4-42.1]** and **[4-42.2].** Similarly, to evaluate the performance of the semi-analytical inverse radial distortion models, the same data was substituted into the models formulated in **[4-41.1]** and **[4-41.2].**

C. Correcting severe barrel radial distortions modelled by an eight-degree polynomial.

From the estimates of radial distortion coefficients computed through the MATLAB calibration script and presented in **Table 4.6,** it can be observed that the coefficients hold more than one sign, and from the earlier experiments, it was observed that the unique criterion of having more than one sign among distortion coefficients does not guarantee the presence of moustache radial distortions alone. To remove this ambiguity, the respective range of estimates of the coefficients κ_1, κ_2 and κ_3 were rescaled to 10^{-3} range, by multiplying the estimate of the second coefficient κ_2 by 10^2 and that of the third coefficient κ_3 by 10^8 and the results are presented in **Table 4.14**.

Table 4.14: Scaled radial distortion coefficients calibrated through MATLAB calibration toolbox

Radial Distortion Coefficients	Numerical estimates of coefficients
κ_1	$1.38\times10^{-3}\left[(mm)^{-2}\right]$
κ_2	$-0.00869\times10^{-3}\left[(mm)^{-5}\right]$
κ_3	$0.00652\times10^{-3}\left[(mm)^{-8}\right]$

Substituting the newly scaled radial distortion coefficients into an eight-degree depressed radial distortion model gives the following:

$$x_d = x_u + x_u\left(1.38\times10^{-3}r_u^2 - 0.00869\times10^{-3}r_u^5 + 0.00652\times10^{-3}r_u^8\right) \quad \textbf{[4-62.1]}$$

$$y_d = y_u + y_u\left(1.38\times10^{-3}r_u^2 - 0.00869\times10^{-3}r_u^5 + 0.00652\times10^{-3}r_u^8\right) \quad \textbf{[4-62.2]}$$

From the above equations, it can be observed that the negative powers associated with the numerical coefficients of the last two terms are equal and taken in absolute values; their numerical estimates are very close to each other. However, since the last term holds a radial distance elevated to a higher power of eight, it dominates over the negative second term. This numerical superiority of the third positive term added to the magnitude of the first positive term would lead to a positive and larger numerical estimate of the radial distortion function. To evaluate the performance of the proposed new inverse radial distortion models in reducing the effect of severe barrel radial distortions, a similar process as in the previous experiments was followed by downloading a distortion-free synthetic image of a checkerboard calibration pattern that was imported into the GIMP software workstation. Fifty-four (54) points were selected on

the digital image of the checkerboard pattern by identifying three points per small black square, their respective coordinates in millimetres were measured. The same checkerboard pattern was printed, and then one picture of the pattern was captured using the Xiaomi Redmi 11 Pro mobile phone with the ultra-wide lens option activated. The captured image was transferred from the mobile phone memory to the computer desktop, then imported into the GIMP environment to measure the distorted image coordinates of the previously identified 54 image points. **Table 4.15** presents a subset of the measured distortion-free coordinates and their associated distorted coordinates measured from the photograph.

Table 4.15: Subset of measured distortion free and their respective distorted image point coordinates

Distortion free points coordinates		Distorted coordinates by the first set of coefficients	
$x_u\,(mm)$	$y_u\,(mm)$	$x_d\,(mm)$	$y_d\,(mm)$
5.70	4.53	6.02	4.79
6.48	4.47	6.87	4.74
3.80	5.18	3.98	5.44
3.24	3.69	3.34	3.81
5.31	5.75	5.63	6.10
2.45	6.79	2.60	7.17
3.84	3.58	3.97	3.71
2.56	7.50	2.73	7.97
8.02	2.51	8.53	2.67
3.20	1.57	3.25	1.61

To evaluate the effectiveness of our newly developed analytical inverse radial distortion models in correcting severe barrel radial distortions, it is necessary to compute the distorted radius associated with each individual distorted point defined by coordinates in the last two columns of **table 4.15**. The computed radii must be elevated to the powers two, five, and eight, as presented in **table 4.16**.

Table 4.16: Subset of distorted radii computed for each distorted image point

Distorted points coordinate		distorted radii elevated to the power two, five and eight			
$x_d\,(mm)$	$y_d\,(mm)$	$r_d\,(mm)$	$r_d^2\,(mm)^2$	$r_d^5\,(mm)^5$	$r_d^8\,(mm)^8$
6.02	4.79	7.69	59.14	26892.53	12229556.8
6.87	4.74	8.35	69.72	40591.25	23631528.01
3.98	5.44	6.74	45.44	13909.12	4258720.83
3.34	3.81	5.08	25.81	3383.13	443516.42
5.63	6.10	8.30	68.89	39390.41	22522922.32
2.60	7.17	7.64	58.37	26029.57	11607718.53
3.97	3.71	5.44	29.59	4764.26	766992.64
2.73	7.97	8.43	71.07	42573.36	25504722.17
8.53	2.67	8.94	79.92	57106.77	40803756.8
3.25	1.61	3.64	13.26	639.02	30818.48

Substituting the estimated radii in columns four, five, and six into models **(55.1)** and **(55.2)** enables to remove the effects of radial lens distortion using iteratively derived inverse distortion models. Similarly, substituting the data computed in columns four, five, and six into the newly proposed inverse distortion models in **(56.1)** and **(56.2)** enables us to remove the effects of radial lens distortions on the image point coordinates in the first two columns of **table 4.16.**

4.2.5. Applications Results and Interpretations

A. Evaluation of the Derived Inverse General Quintic Distortion Polynomial Function

Figure 4-7 illustrates a graphical representation of inverse radial distortion curves produced by inverse distortion coefficients estimated from the semi-analytical and analytical calibration approaches. For a better projection, the individual coefficients were equally scaled since the actual values are very small to produce a meaningful projection. For this purpose, the estimates of the first inverse distortion coefficient were respectively scaled by 10^4 while the estimates of the second inverse radial distortion coefficient were respectively scaled by 10^7. The third inverse distortion coefficient estimates were respectively scaled by 10^{10} while the respective estimates of the fourth inverse radial distortion coefficient were scaled by 10^{13} .
From the figure, it can be observed that the iterative and analytically estimated curves are following a sinusoidal curve. Between the first and second coefficients, the semi-analytical curve is following a trajectory slightly above the trajectory of the analytical curve, while shortly after the second coefficient, almost half way between the third and fourth coefficients, the analytical curve follows a trajectory slightly above that of the semi-analytical curve. However, at the third coefficient, the gap between the analytical curve on top and the semi-analytic curve beneath is larger compared to the one observed at the second inverse coefficient. From half way between the third and the fourth inverse radial distortion coefficient, the semi-analytic curve portrays a trajectory above that of the analytical curve. In addition, the gap between the semi-analytic curve above and the analytical curve below is larger than that observed at the third inverse radial distortion coefficient. From these at this level of the analysis, it seems as if both strategies would equally correct radial lens distortion modelled by a general quintic distortion function.

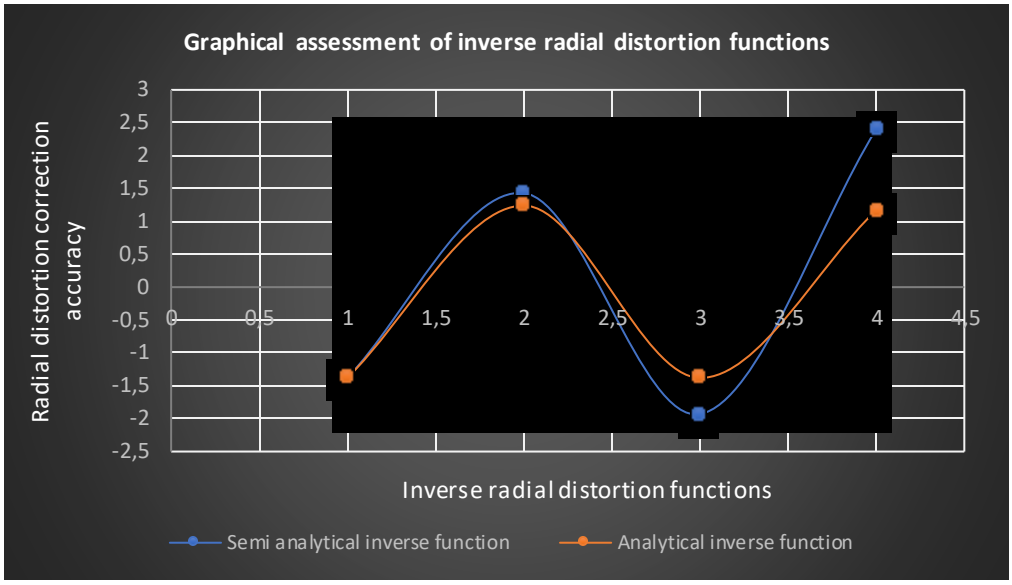

Figure 4-7: A comparison between the semi analytical and fully analytical derived inverse radial distortion models' respective curves

B. Evaluation of the Derived Inverse Six-degree Distortion Polynomial Function

Figure 4-8 presents a graphical projection of the curve of the semi-analytically estimated inverse radial distortion coefficients as well as the curve of the analytically estimated inverse radial distortion coefficients modelled by a six-degree depressed polynomial model. For a better interpretation, individual estimates of inverse radial distortion coefficients were equally scaled as in the previous experiment since their true estimates are of very small values. As such, the estimates of the first inverse distortion coefficient were respectively scaled by 10^3 while the estimates of the second inverse distortion coefficient were respectively scaled by 10^5. The estimates of the third inverse radial distortion coefficient were equally scaled by 10^8 .

An analysis of **Figure 4-8** shows that between the first and second inverse radial distortion coefficients, both the semi-analytical and analytical curves follow the same trajectory and are almost overlapping. Nearly before the second inverse distortion coefficient, both curves follow downward trajectories; the analytical curve passes the zero-horizontal axis nearly halfway the distance between the second and third inverse distortion coefficients, and the gap between the semi-analytical curve on top and the analytical curve below is gradually increasing till both curves reach negative values, with the analytical curve reaching a value further below zero. It can be added that the semi-analytical curve kept a positive value within a longer coefficient span than the analytically estimated curve. However, after the second inverse coefficient, the analytically estimated curve kept a negative value within a larger inverse coefficient span. At the third inverse distortion coefficient, both curves have negative values, with the semi- analytical curve keeping the greater negative estimates closer to zero compared to the analytically estimated curve. In terms of modelling the inverse of the original radial distortion function, it seems that the analytically derived and the original radial distortion curves are almost symmetrical with reference to the horizontal zero axis, and this could mean the analytical inverse radial distortion curve could more efficiently eliminate radial distortions modelled by a depressed six-order polynomial compared to the semi-analytical inverse function.

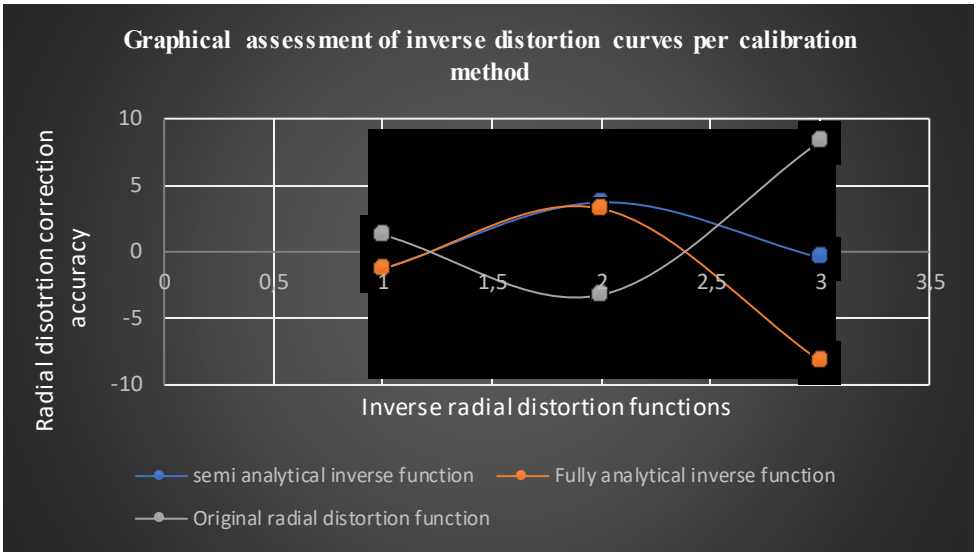

Figure 4-8: A comparison between the semi analytical and fully analytical derived inverse radial distortion models' respective curves

C. Evaluation of the Inverse Eight-degree Distortion Polynomial Function

Figure 4-9 shows in orange colour the inverse radial distortion curve estimates through the semi-analytical strategy to correct the effects of radial distortion modelled by a depressed eight-degree radial distortion polynomial function. On the other hand, the curve in blue represents the shape of the inverse radial distortion function modelled to correct the same radial distortion effects modelled by an eight-degree depressed polynomial. For an optimal projection of both inverse functions, their respective inverse coefficients were equally scaled. The estimates of the first inverse radial distortion coefficient were scaled by 10^3, respectively. The second inverse distortion coefficient estimates were scaled by 10^7 ,respectively, while the estimates of the third inverse coefficient were equally scaled by 10^{11} .

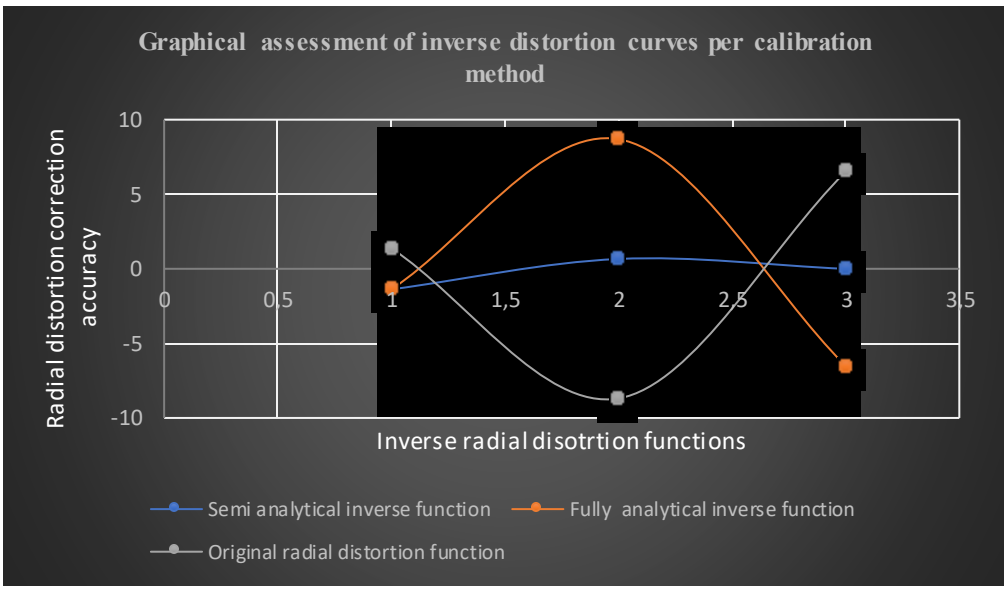

Figure 4-9: Comparison between the semi analytical inverse distortion function curve in blue and the fully analytical inverse radial distortion function curve in orange against the original forward radial distortion model curve in grey

Within the interval between the first and second inverse coefficients, both curves are increasing, with a higher increase observed with the analytically estimated curve. Inside the interval between these two coefficients, the analytically estimated curve maintains a positive value within a larger interval compared to the semi-analytic curve. In contrast, between the second and third inverse radial distortion coefficients, the semi-analytic curve holds a positive value within a larger interval compared to the analytically estimated curve. After the second inverse coefficient, the semi-analytic curve in blue follows a trajectory slightly parallel to the zero axis within a small interval before decreasing to zero value at the third inverse coefficient. On the other hand, the analytically estimated curve drastically decreases from the second inverse coefficient and reaches a negative value after passing half the distance between the second and third inverse radial distortion coefficients. In terms of effectiveness to correct radial distortions, it can be observed that the analytically estimated inverse radial distortion curve and the original radial distortion curve are nearly symmetrical with reference to the horizontal zero axis, and this could mean that the proposed strategy is a near-perfect inverse of the original radial distortion function, and the analytically developed inverse coefficients would outperform the semi-analytical inverse radial distortion coefficients when dealing with radial lens distortion modelled by a high-order eight-degree depressed polynomial.

4.2.6. Corrections Results for Radial Distortions

A. Correction of Moderate Barrel Radial Distortions Modelled by a General Quintic Polynomial

Table 4.17 presents in the first two columns a sample of reference distortion-free image coordinates measured from the distortion-free image of the calibration pattern, while the two middle columns present the x_u and y_u image coordinates computed using the semi-analytical inverse radial distortion models proposed in **[4-25.1]** and **[4-25.2].** The last two columns of the table show the distortion-free x_u and y_u image coordinates computed through the analytically derived inverse radial distortion models proposed in **[4-27.1]** and **[4-27.2].** It can be observed that the semi-analytical and fully analytical inverse radial distortion models have considerably reduced the effects of barrel radial distortion from distorted image point coordinates. These results are not surprising, as both calibration methods displayed near-similar profiles in **figure 4-8**. Both techniques seem to be able to satisfactorily correct moderate radial barrel lens distortions modelled by a general quintic polynomial function. It is candid to point out that when considering the computed estimates of distortion-free coordinates beyond three decimal values, the estimates computed through the analytically derived models in **[4-27.1]** and **[4-27.2]** were slightly smaller than those computed through **[4-26.1]** and **[4-26.2]** models, but the differences in terms of magnitudes were very small as the rounded-off estimates still equal those estimated through the semi-analytical model.

Table 4.17: Moderate barrel radial distortion correction results per calibration strategy

Measured reference distortion free image coordinates		Computed distortion free coordinates through iteratively derived inverse models		Computed distortion free coordinates through analytically derived inverse models	
$x_u\,(mm)$	$y_u\,(mm)$	$x_u\,(mm)$	$y_u\,(mm)$	$x_u\,(mm)$	$y_u\,(mm)$
7.34	6.96	7.33	6.96	7.33	6.96
8.20	5.96	8.20	5.96	8.20	5.96

5.23	6.76	5.23	6.76	5.23	6.76
4.60	5.10	4.60	5.10	4.60	5.10
6.90	7.39	6.90	7.38	6.90	7.38
1.75	6.54	1.75	6.54	1.75	6.54
3.26	2.98	3.26	2.98	3.26	2.98
2.85	8.35	2.85	8.35	2.85	8.35
9.92	3.80	9.91	3.80	9.91	3.80
4.56 *	2.75	4.56	2.75	4.56	2.75

Techniques proposed in the literature to assess the level of accuracy of the calibration of radial distortion coefficients make use of the reprojection error. The general principle of the approach is that inverse radial distortion coefficients are used with the projective transformation matrix to compute coordinates of projected 3D points from their respective image points, and the obtained coordinates are used to calculate the deviations between the measured 3D control point coordinates and their respective computed coordinates. However, the use of such an assessment method was discouraged by some authors because, under circumstances such as inaccurate camera pose estimation and lens distortion errors that could not perfectly be modelled, this reprojection error is generally never equal to zero (**Remondino et al., 2017).** In the same way, since the calibration process aims at improving the quality of the distorted image(s), it is more realistic to use image point coordinates to formulate the reprojection error (**Poulin-Girard et al., 2016; Cvišić et al., 2022**). To compute a more reliable assessment metric, the reprojection error was considered as the distance between the measured distortion-free image coordinates extracted from the distortion-free synthetic image of the calibration pattern and their associated distortion-free counterparts computed through inverse radial distortion models proposed in **[4-26.1]-[4-26.2]** and **[4-27.1]-[4-27.2]**. The smaller the computed distance, the more efficient the inverse model is to deal with associated lens distortions. The following formula was used in this chapter:

$$reprojection\ error = \lambda_{ref} - \lambda_{comp} \qquad \textbf{[4-63]}$$

Where the parameter λ_{ref} represents the measured reference distortion-free image coordinates of an image point while λ_{comp} represents the corresponding computed distortion-free image coordinates of the same point. From the reference distortion-free coordinates and their mathematically modelled counterparts in **table 4.17,** the reprojection errors presented in **table 4.18** were estimated. The largest reprojection errors achieved after correcting the measured distorted image point coordinates with inverse models in **[4-26.1]** and **[4-26.2]** were 0.04 pixel and zero pixel for the x and y coordinates, respectively. A similar outcome was achieved using the analytically derived inverse calibration models in **[4-27.1]** and **[4-27.2].**

Table 4.18: Reprojection errors computed per radial distortion correction approach

Reprojection errors for the iterative algorithm		Reprojection errors for the analytical algorithm	
$x_u\,(mm)$	$y_u\,(mm)$	$x_u\,(mm)$	$y_u\,(mm)$
0.010	0.000	0.010	0.000
0.000	0.000	0.000	0.000
0.000	0.000	0.000	0.000
0.000	0.000	0.000	0.000
0.000	0.010	0.000	0.010

0.000	0.000	0.000	0.000
0.000	0.000	0.000	0.000
0.000	0.000	0.000	0.000
0.000	0.000	0.010	0.000
0.000	0.000	0.000	0.000

The average reprojection error for both the semi-analytical and fully analytical correction methods was around 0.008 pixels for the x_u coordinates, while for the y_u coordinates the techniques achieved about 0.004 pixels reprojection error. Although the estimated reprojection errors were very negligible from **Table 4.18**, further investigation of the performance of the inverse radial distortion calibration algorithms was conducted by estimating the relative residual error metric for each corrected image point. In this chapter, the formulation proposed in the works of **Strand and Hayman (2005)** and **Buquet et al. (2021)** was adopted and formulated as follows:

$$relative\ residual\ error = \frac{\lambda_{ref} - \lambda_{comp}}{\lambda_{ref}} \quad \textbf{[4-64]}$$

With λ_{ref} the measured distortion-free reference coordinate and λ_{comp} its calibrated distortion-free counterpart estimated through inverse radial distortion functions. From the measured distorted image point coordinates in **table 4.10,** it can be observed that image points have been displaced outwardly with comparison of the measured distortion-free coordinates recorded in the first two columns of the table. This is supported by positive relative residual errors recorded in the first two columns of **Table 4.19**. From the subset of corrected image points recorded in the middle two columns of the table, it can be observed and confirmed that the semi-analytically derived correction algorithms reduced most of these errors by projecting corrected image points closer to their respective measured distortion-free references. An observation of the last two columns of the table reveals a similar outcome, as the analytically derived inverse radial distortion algorithms have also projected the distorted image points to estimates very close to those of measured distortion-free references.

Table 4.19: Residual error computation results per radial distortion correction method

Measured radial distortion magnitudes		Relative residual error computed from iteratively derived inverse models		Relative residual error computed from analytically derived inverse models	
Error(x_u)	Error(y_u)	Rel-res(x_u)	Rel-res(y_u)	Rel-res(x_u)	Rel-res(y_u)
0.014	0.015	0.0014	0.000	0.0014	0.000
0.015	0.015	0.000	0.000	0.000	0.000
0.010	0.011	0.000	0.000	0.000	0.000
0.007	0.006	0.000	0.000	0.000	0.000
0.015	0.014	0.000	0.001	0.000	0.001
0.006	0.006	0.000	0.000	0.000	0.000
0.003	0.004	0.000	0.000	0.000	0.000
0.011	0.011	0.000	0.000	0.000	0.000
0.015	0.016	0.001	0.000	0.001	0.000
0.005	0.004	0.000	0.000	0.000	0.000

The computed average relative residual errors for both semi-analytical and fully analytical correction models were estimated to be less than half a pixel, with 0.001 pixel for the x_u coordinates and 0.0004 pixel for the y_u coordinates. Since image points were selected all over the imagery without following a certain geometric pattern such as a line, the estimation of the standard deviation error or the root mean square would not yield more realistic results as the computed average coordinates needed for the metrics may be too large or too small and lead to false representations of the errors. Instead, the root mean square error was adopted, since the measure is estimated with respect to a reference measurement achieved through an independent method (**Remondino et al., 2017**). This is in line with the nature of the data used in this experiment because the reference distortion-free coordinates were measured through a software workstation, while the computed distortion-free coordinates were estimated through inverse modelling algorithms. The root-mean-square error for the x and y coordinates are respectively modelled as follows:

$$\text{rmse}_x = \sqrt{\frac{1}{n} \times \sum_{1}^{n} \left(x_{u-ref} - x_{u-comp} \right)^2} \qquad \textbf{[4-65.1]}$$

$$\text{rmse}_y = \sqrt{\frac{1}{n} \times \sum_{1}^{n} \left(y_{u-ref} - y_{u-comp} \right)^2} \qquad \textbf{[4-65.2]}$$

The overall RMSE is computed from **[4-67.1]** and **[4-67.2]** as follows:

$$\text{RMSE} = \sqrt{\left(\text{rmse}_x\right)^2 + \left(\text{rmse}_y\right)^2} \qquad \textbf{[4-65.3]}$$

It can be observed that the algorithms in **[4-65.1]- [4-65.3]** are different from the traditional root mean square RMS, which is the square root of the mean of the squared differences between the computed distortion-free coordinates and the mean of these computed distortion- free coordinates. From the data in **table 4.17**, the RMSE were computed, and the results are presented in **table 4.20**.

Table 4.20: Results of the root mean square errors computation per radial distortion calibration method

Radial distortion correction algorithms	$\text{rmse}_x\,(\text{mm})$	$\text{rmse}_y\,(\text{mm})$	RMSE(mm)
Iterative	0.005	0.003	0.006
Analytical	0.005	0.003	0.006

B. Correction of Moustache Radial Distortions Modelled by a Depressed Six-degree Polynomial Function.

Table 4.21 presents the outcomes of moustache radial distortion correction using semi-analytical models in **[4-41.1]-[4-41.2]** and analytically derived models in **[4-42.1]** and **[4-42.2].** The analysis of the results in the two middle columns of the table shows that the semi-analytic inverse radial distortion models seem to have projected the distorted image points further inwardly and further outwardly with respect to the reference measured distortion-free coordinates, respectively. The correction algorithms seem to have added more barrel and pincushion

distortions to the original distorted point coordinates. In contrast, an analysis of the subset of corrected image point coordinates in the last two columns of the table shows that the analytically derived inverse radial distortion correction models in **[4-42.1]** and **[4-42.2]** have drastically reduced the amount of moustache radial distortions present in the original distorted data presented in the last two columns of Table **4.12.**

Table 4.21: Moustache radial distortion correction results per calibration approach

Reference measured distortion free coordinates		Computed distortion free coordinates achieved through semi analytical inverse models.		Computed distortion free coordinates achieved through analytically derived inverse models.	
$x_u\,(mm)$	$y_u\,(mm)$	$x_u\,(mm)$	$y_u\,(mm)$	$x_u\,(mm)$	$y_u\,(mm)$
6.34	5.60	5.78	5.10	6.26	5.53
7.20	4.96	7.29	5.03	7.06	4.88
4.22	5.75	4.08	5.57	4.22	5.75
3.59	4.10	3.58	4.08	3.59	4.10
5.90	6.39	5.30	5.74	5.81	6.28
2.72	7.54	2.54	7.05	2.70	7.49
4.26	3.98	4.22	3.95	4.26	3.98
2.84	8.34	2.54	7.43	2.79	8.18
8.91	2.79	7.65	2.40	8.60	2.72
3.56	1.74	3.37	1.64	3.56	1.74

The above results were further investigated by generating moustache radial distortion correction curves per calibration strategy for the x_d coordinates as presented in **Figure 4-10.** An observation of the three curves reveals that the distortion-free correction curve in blue and the moustache radial distortion correction curve derived from the analytical inverse model in red are almost overlapping, while the correction curve derived from the semi-analytical model in orange follows a separate trajectory that overlaps with the other two curves at some discontinued intervals. This suggests that values of image coordinates corrected through the inverse radial distortion model in **[4-42.1]** seem to converge towards distortion-free respective reference coordinate measures presented in the first column of **table 4.21**. It contrasts; it can be observed that coordinates computed through the semi-analytical inverse radial distortion model in **[4-41.1]** produced more diverging coordinate measures, which explains the deviation of the orange curve with respect to the blue curve, which describes the distortion-free profile.

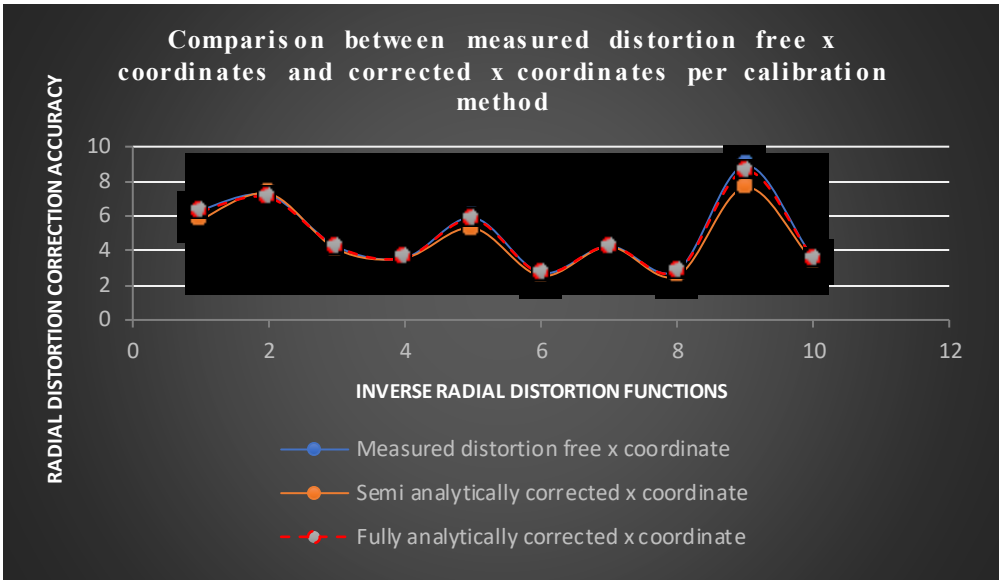

Figure 4-10: Moustache radial distortion correction curves for image point's x coordinates per calibration method

Table 4.22 presents a further analysis of the results in **Figure 4-10**. It evaluates the nearness of the corrected x_u coordinates with reference to the distortion-free reference coordinates and their measured distorted counterparts. The first column of the table contains the measured distortion-free point coordinates extracted from the synthetic distortion-free image of the PhotoModeler calibration pattern. The last column of the table contains the same points, but distorted, that were measured from the printed photoModeler calibration pattern that was photographed by the Nikon 3100 non-metric camera. The second column of the table contains the correction results of moustache radial distortions on distorted image points' x_d coordinates using the semi-analytical inverse correction model in **[4-41.1].** The third column of the table presents the correction results of the moustache radial distortion on distorted x_d coordinates using the analytically derived distortion correction model in **[4-42.1].** An analysis of the first, second, and last columns of the table reveals that some image points' x_d coordinates that were affected by barrel radial distortions were under-corrected by the semi-analytical inverse distortion correction model, as the calibrated x_u coordinates reached values lower than their respective measured distortion-free reference coordinates presented in the first column of the table, with the worst correction highlighted on row 10 and the best correction highlighted on row 5. In addition, some point coordinates that were affected by pincushion radial distortions were now subjected to larger amounts of radial barrel distortion effects, while others were subjected to more acute effects of radial pincushion distortions. In contrast, a study of the first, third, and fourth columns of the table shows that corrections done using analytically derived inverse distortion functions led to better results than the semi-analytic models. Indeed, image coordinates subjected to pincushion distortion effects were now showing an increase of their respective x coordinates to values very close to measured distortion-free reference coordinates, respectively, with the worst correction achieving a deviation error of 0.31mm in row 10, while the best correction of the strategy achieved a deviation error of 0.00mm. It seems as if the inverse models in **[4-42.1]** produced a counterbalance effect of barrel distortions that drastically reduced the opposite effect of pincushion distortions. In the same way, point coordinates that were affected by barrel distortions

showed decreased estimates of their respective coordinates to values close to their respective distortion-free reference coordinates after running the correction process using the analytically derived correction model in **[4-42.1].**

Table 4.22: Radial distortion correction results for the x image coordinates per calibration method with the second and fifth columns showing the deviation errors associated with each method.

Reference measured distortion free x_u coordinates	Semi analytical deviation error	Corrected distortion free x_u coordinates using semi analytical method	Computed distortion free x_u coordinates using analytically derived method	Fully analytical deviation error	Reference measured distortion free x_d coordinates
6.34	0.56	5.78	6.26	0.08	6.06
7.20	0.09	7.29	7.06	0.14	6.80
4.22	0.14	4.08	4.22	0.00	4.19
3.59	**0.01**	3.58	3.59	0.00	3.63
5.90	0.60	5.30	5.81	0.09	5.59
2.72	0.18	2.54	2.70	0.02	2.64
4.26	0.04	4.22	4.26	0.00	4.30
2.84	0.30	2.54	2.79	0.05	2.68
8.91	**1.26**	7.65	8.60	**0.31**	8.20
3.56	0.19	3.37	3.56	0.00	3.61

Figure 4-11 shows the moustache radial distortion correction curves for the image points' y_d coordinates. It can be noticed that the semi-analytical moustache distortion correction curve in green follows a trajectory slightly below that of the analytically derived correction curve as well as that of the distortion-free curve. It can also be observed that the analytically derived moustache distortion correction curve in yellow and the distortion-free curve in red are nearly overlapping throughout their respective trajectories. One can deduce from these results that corrections of distorted image points' y_d coordinates through the inverse model in **[4-42.1]** produced estimates of coordinates very close to the distortion-free reference measures. In contrast, corrections of the distorted coordinates through the inverse model in **[4-42.2]** seem to have produced in one hand image point coordinates that are mostly diverging with respect to their original locations and on the other hand with respect to the distortion-free reference measures.

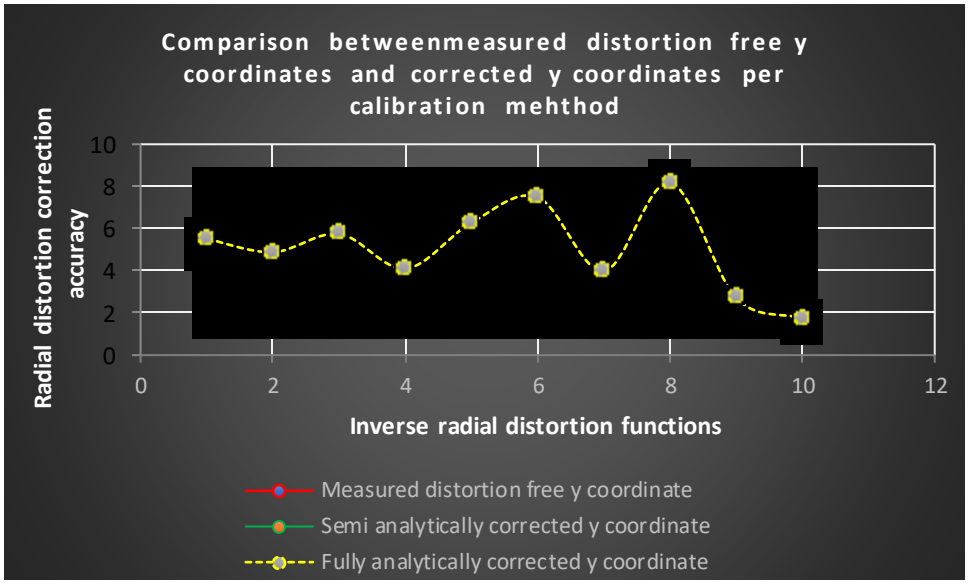

Figure 4-11: Moustache radial distortion correction curves for the image point y coordinates per calibration method

Table 4.23 presents a projection of the corrected image y_u coordinates within the numerical boundaries between the reference distortion-free coordinates and the associated measured distorted counterparts. A look at the third column of Table **4.23** shows that distorted y_d coordinates that were subjected to the effects of pincushion radial distortions portrayed an increase of their coordinate estimates to values closer to their respective distortion-free reference coordinates. Similarly, distorted y_d coordinates that were subjected to the effects of barrel radial distortions showed a decrease of their respective coordinates to values closer to their respective distortion-free reference coordinates. In contrast, after distortion corrections using the semi-analytical model in **[4-41.2],** several image points' y_d coordinates that were subjected to barrel distortion effects showed a decrease of their respective estimates to values falling far below the values of their respective distortion-free reference coordinates, and these seem to indicate that the model in **[4-41.2]** has introduced more acute pincushion distortions while trying to reduce the effects of barrel distortions. In the same way, image y_d coordinates that were subjected to pincushion radial distortions displayed a decrease of their respective coordinates to values below their respective distortion-free reference coordinate measures. Some image points' y_d coordinates that were subjected to pincushion distortion effects also displayed an increase of their original coordinates to values larger than their respective distortion-free reference estimates.

Table 4.23: Reprojection errors for the correction of the distorted y coordinates of each measured distorted point per calibration method

Reference measured distortion free y_u coordinates	Computed distortion free y_u coordinates using the semi analytical method	Computed distortion free y_u coordinates using the analytical method	Reference measured distortion free y_d coordinates
5.60	5.10	5.53	5.35
4.96	5.03	4.88	4.69
5.75	5.57	5.75	5.70
4.10	4.08	4.10	4.15

6.39	5.74	6.28	6.05
7.54	7.05	7.49	7.32
3.98	3.95	3.98	4.02
8.34	7.43	8.18	7.86
2.79	2.40	2.72	2.57
1.74	1.64	1.74	1.76

From the reference distortion-free x_u and y_u coordinates in the first columns of **table 4.22** and **table 4.23,** respectively, as well as the corrected x_u and y_u coordinates in the two middle columns of **table 4.22** and **table 4.23,** the reprojection error was estimated. **Table 4-24** presents a sample of the obtained computed errors. The average reprojection errors for the correction of x_d and y_d coordinates using the semi-analytical model were estimated at about 2.12mm and 0.33mm, which corresponds to about 8.01 and 1.25 pixels, respectively. The largest reprojection errors estimated after distortion removals using the analytically developed models for the corrections of x_d and y_d coordinates were computed at about 0.069 mm and 0.05mm, which correspond to about 0.26 and 0.19 pixels, respectively.

Table.4.24: Reprojection errors computed from the semi-analytical and fully analytical correction approaches

Reprojection errors for the iterative algorithm		Reprojection errors for the analytical algorithm	
x_u	y_u	x_u	y_u
0.56	0.50	0.08	0.07
–0.09	–0.07	0.14	0.08
0.14	0.18	0.00	0.00
0.01	0.02	0.00	0.00
0.60	0.65	0.09	0.11
0.18	0.49	0.02	0.05
0.04	0.03	0.00	0.00
0.30	0.91	0.05	0.16
1.26	0.39	0.31	0.07
0.19	0.10	0.00	0.00

Computing the relative residual errors from the data in **table 4.24** produced the results in **table 4.25**. The first two columns show that many image points' coordinates hold positive residual errors. This means that most image points affected by pincushion distortions were undercorrected since their final corrected coordinate estimates fell below the distortion-free reference values, and these led to positive relative residual errors. Moreover, some negative residual errors were found associated with some image points that were also subjected to pincushion radial distortions. These negative residuals suggest that the first three inverse radial distortion coefficients presented in **[4-4.1]-[4-4.3]** failed to perfectly model the opposite effects of moustache radial distortions present in the photographs. The models' formulations may have introduced some numerical instabilities that resulted in each inverse radial distortion coefficient failing to model the correct distortion profile introduced by the coefficients κ_1, κ_2 and κ_3 in the

original six-degree radial distortion polynomial. In contrast, residual errors computed from image point coordinates corrected by the analytically derived models in **[4-42.1]** and **[4-42.2]** showed positive signs as presented by the subset of point data in **table 4.25**. This suggests that inverse coefficients formulated in **[4-38.1]-[4-38.3]** successfully modelled the opposite effects of moustache radial distortions introduced by the three radial distortion coefficients κ_1, κ_2 and κ_3 in the original depressed radial distortion polynomial. Furthermore, the fact that the analytically derived inverse distortion coefficients were directly derived from this original six-degree polynomial may have played a positive role in the successful modelling of distortions present in the photograph. Deriving the formulations of inverse radial distortion coefficients directly from customized distortion models rather than a general rigid model may offer some flexibility advantages in such a way that they "correctly" capture the opposite distortion effects introduced by associated radial distortion polynomials. This is supported by the residual error magnitudes in the last two columns of **table 4.25** that show that the moustache radial distortion effects have been considerably minimized to magnitudes very close to zero by the analytically derive inverse models in **[4-42.1]** and **[4-42.2].**

Table 4.25: Residual errors after radial distortion corrections per calibration method

After semi-analytical corrections		After analytical corrections	
Error(x_u)	Error(y_u)	Error(x_u)	Error(y_u)
0.088	0.089	0.013	0.013
–0.013	–0.014	0.019	0.016
0.033	0.032	0.000	0.000
0.003	0.005	0.000	0.000
0.102	0.102	0.015	0.017
0.066	0.065	0.007	0.007
0.009	0.008	0.000	0.000
0.106	0.109	0.018	0.019
0.141	0.140	0.035	0.025
0.053	0.058	0.000	0.000

Although the residual error metric was very crucial to assess the good performance of the analytically derived inverse distortion correction models in **[4-42.1]** and **[4-42.2],** lower values of the metric do not always mean that the algorithms have efficiently dealt with radial distortions since any corrected coordinate estimates lower than their respective reference distortion-free coordinates may also achieve a positive residual error. In cases of pincushion distortion, for instance, where the corrected values fall lower than the distorted values of coordinates or grow larger than the distortion-free reference values, as observed in **tables 4.22** and **4.23,** the use of residual error as a performance evaluation tool can reveal its limits. As an example, the estimates of residual errors in the four columns of **table 4.25** can be misleading and may give the false impression that the semi-analytically derived inverse correction algorithms have achieved acceptable results that are very close to those obtained from analytically derived algorithms. From these limitations, the performances of both methods were further evaluated through the root mean square error. The root-mean square error for the correction of the x_d coordinates using the semi-analytically derived model in **[4-41.1]** was estimated at 0.495mm which corresponds to 1.87 pixels, while the error for the correction of the y_d coordinate using the model in **[4-41.2]**

was estimated at 0.441mm, which corresponds to 1.67 pixels, as shown in **table 4.26**. These led to an overall root mean square error of 0.482mm which corresponds to 1.82 pixels, which is very large for photogrammetry applications that require accurate measurements from photographs. In contrast, the root-mean square error for the correction of the x_d image coordinates using the analytically derived model in **[4-42.1]** was estimated at 0.43 pixels, and the error for the correction of the y_d image coordinates through the analytical model in **[4-42.2]** was estimated at 0.28 pixels. These estimates led to the overall root mean square error of 0.52 pixels which is acceptable for photogrammetry applications.

Table 4.26: root mean square error computation results per radial distortion correction method

Radial distortion correction algorithms	$\text{RMSE}_y(\text{mm})$	$\text{RMSE}_y(\text{mm})$	$\text{RMSE}(\text{mm})$
Semi analytical	0.495	0.441	0.482
Fully analytical	0.115	0.075	0.137

From results in **figures 4.11**, **4.12**, **table 4.21, table 4.22, table 4.23**, **table 4.24**, **table 4.25,** and **table 4.26,** it can be concluded that the analytically derived models have been proven to outperform the semi-analytically derived six-degree inverse polynomial models in reducing the amount of moustache radial distortions.

C. Correction of Severe Barrel Radial Distortions Modelled by a Depressed Eight-degree Polynomial Function.

Corrections of severe barrel radial distortions were performed using the semi-analytically derived models in **[4-57.1], [4-57.2],** and the analytically derived models in **[4-58.1] and [4-58.2].** The corrections were done on 54 distorted image point coordinates that were measured from the image of a checkerboard calibration pattern photographed using a Xiaomi Redmi 11 Pro mobile phone's camera. **Table 4.27** presents the distortion correction outcome in the last four columns.

Table 4.27: Severe barrel radial distortion correction results per calibration approach

Original distortion free coordinates		Undistorted data points computed using the semi analytically derived inverse model.		Undistorted data points computed using analytically derived inverse model.	
x_u	y_u	x_u	y_u	x_u	y_u
5.70	4.53	3.65	2.90	5.67	4.51
6.48	4.47	1.55	1.07	6.44	4.45
3.80	5.18	3.42	4.67	3.78	5.17
3.24	3.69	3.24	3.69	3.24	3.69
5.31	5.75	1.48	1.60	5.28	5.73
2.45	6.79	1.63	4.49	2.45	6.75
3.84	3.58	3.81	3.56	3.84	3.58
2.56	7.51	0.44	1.29	2.56	7.48
8.02	2.51	–3.13	–0.98	8.00	2.50
3.20	1.57	3.20	1.59	3.20	1.58

The first two columns of the above table describe the coordinates measured from the distortion-free image of the calibration pattern. From the comparison between the middle two columns and the first two columns, it can be observed that the image x_u and y_u coordinates corrected through the semi-analytically derived models in **[4-57.1]** and **[4-57.2]** hold numerical estimates that have dropped far below the estimates of their respective distortion-free references. In contrast, a comparison between the last two columns and the first two columns reveals that the distorted coordinates corrected through the analytically derived models in **[4-58.1]** and **[4-58.2]** hold corrected image coordinates very close to their respective distortion-free references. From the above, it appears that the semi-analytically derived inverse radial distortion correction models presented in equations **[4-4.1]-[4-4.3]** failed to efficiently model the opposite effects of severe barrel radial distortions introduced by the lens system of the Xiaomi Redmi 11 Pro mobile phone. In contrast, the fact that the corrected coordinates x_u and y_u in columns five are very close to the associated distortion-free references in the first column of **Table 4.27** suggests that the inverse radial distortion coefficients analytically derived presented in equations **[4-54.1]– [4-54.3]** have better modelled the opposite effects of severe barrel radial distortions introduced by the coefficients κ_1, κ_2 and κ_3. Projecting the coordinates in the first, third, and fourth columns of **Table 4-27** in a graphical feature space enables us to demonstrate the under- corrected effects applied to the distorted image coordinates. **Figure 4-12** presents a graphical projection of the measured distortion-free x_u coordinates curve in red, the curve of the distortion-free x_u coordinates corrected by the semi-analytically derived coefficients in yellow, and the curve of the distortion-free x_u coordinates corrected through the analytically derived coefficients in green**.** An analysis of **Figure 4.12** shows that the reference distortion-free coordinates curve and that of the analytically derived coefficients are almost overlapping along a near identical trajectory. In contrast, the curve of the distortion-free coordinates corrected through semi-analytically derived coefficients is following a trajectory drifting away from the other two curves while randomly crossing four times the other two curves along its isolated trajectory.

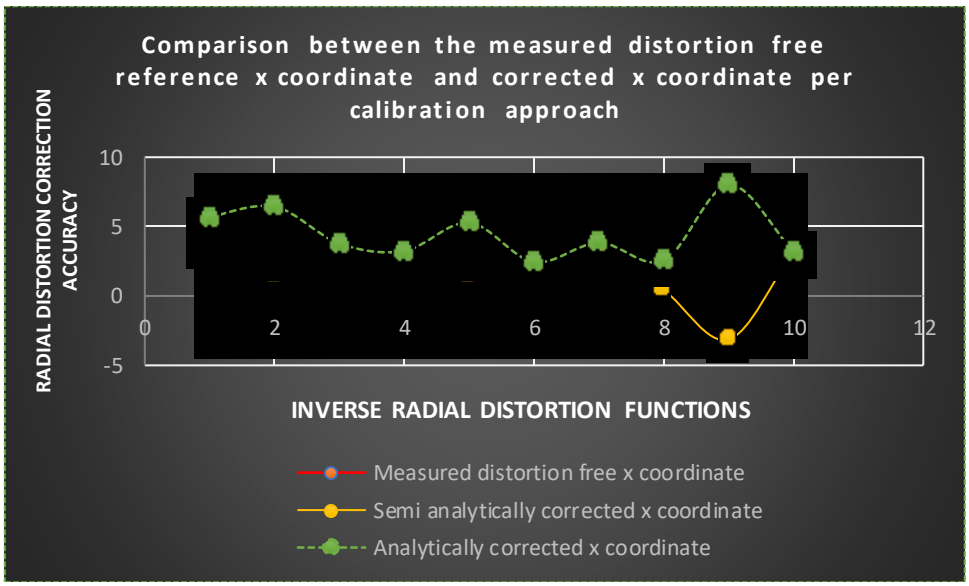

Figure 4-12: Severe barrel radial distortion correction curves per calibration method for the correction of image x coordinates

Table 4.27 and **Figure 4.12** give an idea of the nearness between distortion-free x_u image coordinate of each image point computed using the two correction strategies with respect to their associated measured distortion-free reference coordinates. However, these do not provide enough information about the locations of these corrected point coordinates with regards to their respective distorted locations. **Table 4.28** presents the corrected distortion-free x_u coordinates per calibration method projected within two boundaries defined by the measured distortion-free reference x_u coordinates and their associated distorted counterparts.

Table.4.28: Corrected x_u coordinates projected within the boundary defined between the measured distortion-free reference x_u coordinate and their respective measured distorted x_d counterparts.

Reference measured distortion free x_u coordinates	Computed distortion free x_u coordinates using the semi analytical method	Computed distortion free x_u coordinates using the analytical method	Reference measured distorted x_d coordinates
5.70	3.65	5.67	6.02
6.48	1.55	6.44	6.87
3.80	3.42	3.78	3.98
3.24	3.24	3.24	3.34
5.31	1.48	5.28	5.63
2.45	1.63	2.45	2.60
3.84	3.81	3.84	3.97
2.56	0.44	2.56	2.73
8.02	–3.13	8.00	8.53
3.20	3.20	3.20	3.25

A comparison between the second and fourth columns in **table 4.28** shows that image point coordinates corrected through the semi-analytically developed algorithm have all fallen inside the respective defined boundaries. However, a comparison between the same corrected image point coordinates and their respective measured distortion-free references in the first column reveals that these corrected points have fallen outside of the defined boundaries. Similarly, projecting the corrected y_u coordinates in the second, fourth, and sixth columns of **Table 4.27** in a graphical feature space enables us to observe the agreements or discrepancies between the measured distortion-free y_u coordinates and the corrected coordinates y_u. **Figure 4-13** seems to expose a near overlap between the measured distortion-free coordinates curve in red and the curve representing image points corrected by the analytically derived inverse coefficients in yellow**.** In contrast, the graph seems to suggest that the semi-analytically derived coefficient formulations failed to model the opposite effects of severe barrel radial lens distortion introduced by the lens system of the Xiaomi Redmi 11 camera.

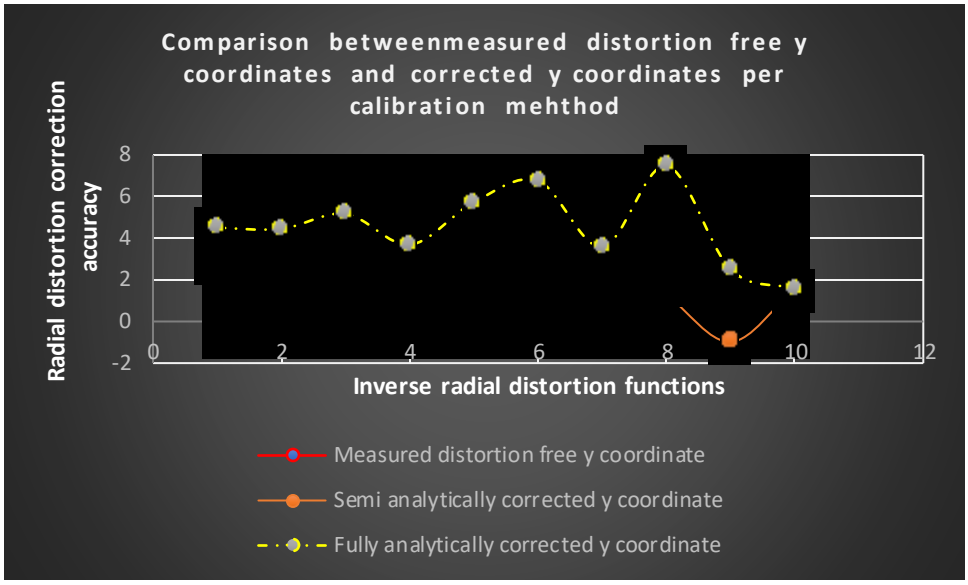

Figure 4-13: Severe radial distortion correction curves per calibration method for the correction of image y coordinates

To further investigate how accurately the corrected y_u image coordinates fell within the boundaries defined by the measured distortion-free y_u coordinates and their measured distorted counterparts, the data contained in the second, fourth, and sixth columns of **table 4.27** was projected within the defined boundaries as presented in **table 4.29**. A comparison between the corrected coordinates in the second column of the table and those in the last column shows that all corrected points fell within the defined coordinate boundary. Similarly, the comparison between the corrected y_u coordinates in the second column of the table and the data in the first column reveals that the majority of corrected coordinates fell below their respective distortion-free references. In contrast, the comparison between the corrected coordinates in the third column and those in the fourth column shows that all the corrections fell below their respective boundaries set by the measured distorted coordinates in the fourth column. Similarly, the comparison between the data in the third column and that in the first column reveals that some corrected points fell slightly outside their respective boundaries while others fell inside their respective boundaries set by the measured distortion-free coordinates. It is observed that the deviations between the correction of y_u coordinates done through the analytical inverse coefficients and their references are very negligible, compared to the deviations associated with semi-analytically derived coefficients.

Table 4.29: Corrected y_u coordinates projected within the boundary defined between the measured distortion-free y_u coordinates and their respective measured distorted y_d counterparts.

Reference measured distortion free y_u coordinates	Computed distortion free y_u coordinates using semi-analytically derived method	Computed distortion free y_u coordinates using analytically derived method	Reference measured distortion free y_d coordinates

4.53	2.90	4.51	4.79
4.47	1.07	4.45	4.74
5.18	4.67	5.17	5.44
3.69	3.69	3.69	3.81
5.75	1.60	5.73	6.10
6.79	4.49	6.75	7.17
3.58	3.56	3.58	3.71
7.51	1.29	7.48	7.97
2.51	–0.98	2.50	2.67
1.57	1.59	1.58	1.61

To quantify the reprojection errors, the equation **[4-65]** was used**. Table 4.30** presents the computation results per calibration approach. The first two columns of the table contain the errors estimated through the models in **[4-57.1]** and **[4-57.2],** while the last two columns present the reprojection errors estimated with the coordinates corrected through the analytically derived inverse models**.** The analysis of the errors in the first two columns suggests that the semi-analytically derived inverse distortion models introduced more acute pincushion errors while trying to reduce the effects of severe barrel radial distortions. From the last two columns of the table, the errors' magnitudes have been found to be very small, and these suggest that the analytically derived barrel distortion correction algorithms have drastically reduced the effects of the severe barrel radial distortions. The average reprojection error for the correction of the x_d coordinates through the semi-analytically derived inverse functions was estimated at about 2.53mm, which corresponds to about 9.56 pixels. The largest reprojection error for the correction of the y_d coordinates was estimated at 11.15mm, which corresponds to 42.14 pixels, which is an extremely large error in photogrammetry. The average reprojection error for the correction of the y_d coordinates through the semi-analytically derived inverse function was estimated at about 2.17 mm, which corresponds to about 8.20 pixels. In contrast, the average reprojection error for the correction of x_d coordinates through the analytically derived inverse model was estimated at about 0.014mm which corresponds to 0.053 pixels, while the average reprojection error for the correction of the y_d coordinates was estimated at 0.016 mm, which corresponds to about 0.061 pixels.

Table 4.30: Computed reprojection errors after radial distortion corrections per calibration method

Reprojection errors for the semi analytical algorithm in mm		Reprojection errors for the analytical algorithm in mm	
x_u	y_u	x_u	y_u
2.05	1.63	0.03	0.02
4.93	3.4	0.04	0.02
0.38	0.51	0.02	0.01
0.00	0.00	0.00	0.00
3.83	4.15	0.03	0.02
0.82	2.3	0.00	0.04
0.03	0.02	0.00	0.00

2.12	6.22	0.00	0.03
11.15	3.49	0.02	0.01
0.00	–0.02	0.00	–0.01

Table 4.31 shows the computation results of relative residual errors for each corrected image point. The first two columns show the residual errors computed from image coordinates corrected through the semi-analytical inverse models. The last two columns present the residual errors estimated through analytically derived inverse radial distortion functions. The largest residual error for the correction of x_d and y_d coordinates through the semi-analytically derived algorithm was estimated at 1.39 mm respectively, which corresponds to about 5.25 pixels. In the same way, the largest residual errors for the correction of the x_d and y_d coordinates modelled through the analytically derived correction algorithms were estimated to about 0.006mm, respectively, which correspond to about 0.023 pixels. The average relative residual errors for the correction of the x_d and y_d coordinates using the semi-analytically derived algorithm were estimated at about 0.450mm and 0.46mm which are equivalent to about 1.70 pixels and 1.74 pixels, respectively. Similarly, the average relative residual error for the correction of the x_d and the y_d coordinates through the analytically derived inverse radial distortion models was estimated at 0.003mm and 0.004 mm which correspond to 0.011 pixels and 0.015 pixels, respectively.

Table 4.31: Residual errors computed after radial distortion corrections per calibration method

After semi analytical corrections		After analytical corrections	
Error(x_u)	Error(y_u)	Error(x_u)	Error(y_u)
0.360	0360	0.006	0.004
0.761	0.761	0.006	0.005
0.100	0.099	0.005	0.002
0.000	0.000	0.000	0.000
0.721	0.722	0.006	0.005
0.335	0.339	0.000	0.006
0.008	0.007	0.000	0.000
0.828	0.828	0.000	0.004
1.390	1.390	0.003	0.004
0.000	–0.013	0.000	–0.006

Table 4.31 presents radial barrel distortion correction success for each individual image point with regards to their associated reference estimates. However, these results do not give a measure of how well each correction algorithm performed throughout the entire set of points. To investigate the overall distortion correction success, the root mean square error was computed using the formulae provided in equations **[4-65.1]-[4-65.2]** and **table 4.32** provides the outcome of the error computation process. It can be observed that the root means square error for the correction of all the x_d coordinates through the semi-analytical inverse radial distortion model was estimated at about 4.16mm, that corresponds to about 15.72 pixels, which is a very large error but is in line with the results reported in the first and second columns of **table 4.30**. Conversely, from a numerical point of view, the root mean square error computed for the

corrections of all the y_d coordinates through the inverse correction model in **[4-57.2]** was slightly lower and found at about 2.96mm, which is equivalent to about 11.19 pixels. The overall performance of the semi-analytical inverse radial distortion models with respect to reducing the effects of severe barrel radial distortions was evaluated at about 5.11mm, which corresponds to 19.31 pixels, which is a very large error for photogrammetry applications. In contrast, the third row of the table shows the root mean square errors estimated for the correction of x_d and y_d coordinates using the analytical inverse radial distortion models**.** The correction error for the x_d and y_d coordinates was estimated at about 0.02mm respectively, which is equivalent to about 0.08 pixels. The overall radial distortion correction success of the analytical inverse radial distortion correction models in **[4-58.1]** and **[4-58.2]** was described by a root mean square error of about 0.03 pixels which is a very small and acceptable error.

Table 4.32: root mean square error computation results per calibration strategy

Radial distortion correction algorithms	$RMSE_x$	$RMSE_y$	RMSE
Semi analytical	4.16	2.96	5.11
Analytical	0.02	0.02	0.028

From the results in **tables 4.27**, **4.28, 4.29, 4.30**, **4.31**, **4.32,** and **figures 4-13** and **4-14,** it can be argued that the analytically derived inverse radial distortion coefficients enabled better modelling of inverse radial distortion functions and can efficiently reduce the effects of severe barrel radial distortions. In contrast, the semi-analytically derived inverse radial distortion coefficients are not suitable to correct severe barrel radial distortions modelled by a high-degree polynomial such as a depressed eight-degree polynomial.

4.3. Results Discussion

Table 4.33 presents the average reprojection error in millimeters and in pixels for radial distortion corrections of moderate, severe barrel, and moustache radial distortions. Moderate barrel radial distortions have perfectly been modeled by a general quintic polynomial function. As presented in the fourth column of the table, this type of distortion profile was successfully dealt with by the inverse radial distortion coefficients derived through the proposed fully analytical approach. Similarly, the semi-analytical approach also successfully corrected the moderate radial distortions on the distorted image point coordinates. This equal performance may be associated with the fact that the difference in magnitude between the second inverse coefficients modeled by each approach was enough to compensate for the difference in magnitude between the third coefficients produced by each approach. Indeed, the numerical magnitude of the second inverse coefficient derived from the semi-analytical strategy was larger than the second inverse coefficient derived from the new fully analytical approach. On the other hand, the magnitude of the third inverse coefficient derived from the fully analytical approach was larger than that derived from the semi-analytical approach.
The fact that both strategies showed equal performance suggests that the second coefficient of the semi-analytical approach dealt better with moderate barrel radial distortions than the second inverse coefficient derived from the fully analytical approach. In contrast, the third coefficient derived from the fully analytical approach seems to have handled moderate radial distortions better than the third coefficient derived from the semi-analytical approach. These tradeoffs between inverse coefficients resulted in a nearly equal performance between the two strategies.

Modeling of severe barrel radial distortions was proven effective using a depressed eight-degree polynomial function. Corrections of such severe radial distortion profiles were successfully done using inverse radial distortion coefficients derived through the newly proposed analytical approach, as the average reprojection error achieved was 0.108246 pixels, which is less than one pixel. In contrast, the very large average reprojection error of 19.2967 pixels achieved by inverse coefficients derived through the semi-analytical approach confirms the failure of the strategy to model accurate inverse coefficients that can remove the effects of radial distortions modeled by a depressed eight-degree polynomial function. Such large error magnitude is generally not suitable for close-range photogrammetry applications. The successful correction of severe barrel radial distortion by inverse distortion coefficients derived from the proposed strategy may first be associated with the absence of the first coefficient of radial distortion κ_1 within the concatenated formulation of the second term of the second inverse coefficient. Secondly, the influence of the redundant parameter κ_1 elevated to the cubic power in the third inverse coefficient was absorbed by the small numerical magnitude of the parameter κ_2, leading to a very good estimate of the third inverse coefficient derived through the new strategy. In contrast, the redundancy of the coefficient κ_1 within the semi-analytic formulation of the second term of the second inverse coefficient may have introduced some numerical instabilities into the estimate of this inverse coefficient. In addition, the absence of the coefficient κ_2 in the second term $-12\kappa_1^3$ of the third inverse coefficient derived from the semi-analytical strategy enabled to increase the numerical influence of the coefficient κ_1 in this inverse coefficient. Furthermore, the presence of an additional redundant coefficient κ_1 in the formulation of this third inverse coefficient as well as the negative sign associated with the first term of the coefficient may have added further numerical instabilities, resulting in inaccuracy of the coefficient's estimate.

Table 4.33: Radial distortion correction accuracy comparison per distortion profile and per correction strategy

Reprojection errors for the correction of moderate, severe, and moustache radial distortions per calibration method				
	Semi analytical calibration		Fully analytical calibration	
	mm	Pixels	mm	pixels
Moderate radial distortions	0.005477	0.0207004724	0.005477	0.0207004724
Severe radial distortions	5.10558	19.296680315	0.02864	0.1082456693
Moustache radial distortions	0.66261	2.5043527559	0.1377	0.5204409449

One would think that complex radial distortion profiles such as moustache distortions could perfectly be modeled by depressed polynomial functions with degrees higher than eight. However, the conducted experiments have exposed that a depressed sixth-degree polynomial was actually enough to accurately model such distortions. The small reprojection error of about half a pixel presented in the fifth column of the table confirms that the inverse distortion coefficients derived from the fully analytical approach were accurate enough to model the

opposite effect of moustache radial distortions modeled by a depressed sixth-degree polynomial. The inverse coefficients derived from the semi-analytical approach failed to model the opposite effect of moustache radial distortion, resulting in a large reprojection error of about 2.5 pixels, which is a gross error for photogrammetry applications. The success of the inverse coefficients derived from the proposed analytical method may be associated with the power of 3 attached to the coefficient κ_1 in the formulation of the second inverse coefficient.

Such parameter's power advantage also extended to the formulation of the third inverse distortion coefficient. Within the formulation of this coefficient, the parameter κ_1 held respective powers of two and five in the first and second terms of this inverse coefficient. In addition, the negative sign associated with the first term of this coefficient may also have played an important role in ensuring the accuracy and numerical stability of the coefficient.

Table 4.34 presents the root mean square error computed from each correction method for moderate, severe, and moustache radial distortion profiles.

Table 4.34: Root mean square error per radial distortion correction approach

Radial distortion profiles	Moderate barrel radial distortions		Severe barrel radial distortions		Moustache barrel distortions	
Distortion correction methods	Semi analytical	Fully analytical	Semi analytical	Fully analytical	Semi analytical	Fully analytical
Root Mean Square Error(mm)	0.006	0.006	5.11	0.028	0.482	0.137

The largest root mean square error was achieved by the semi-analytic distortion correction method when dealing with severe radial distortions. This confirms that the approach failed to model the inverse effect of severe barrel radial distortions modelled by an eight-degree depressed polynomial. The proposed analytical approach achieved a very small error magnitude of 0.028mm, which corresponds to0.10583 pixels. A root means square error of 5.11 mm that corresponds to 19.3134 pixels achieved with the semi-analytical approach is very large when information derived from the photographs is needed for metric and 3D modelling or 3D reconstruction purposes. This large error may originate from the fact that inverse coefficients derived from the semi-analytical algorithms failed to efficiently reduce the effect of barrel distortions to some reasonable magnitudes. The inverse coefficient formulations may also have been responsible for introducing pincushion distortions while trying to reduce the effects of severe barrel distortions from distorted image points. The newly proposed fully analytical strategy also achieved a small root mean square error of 0.0137 mm, which corresponds to 0.05178 pixel, for the corrections of moustache radial distortions. The root mean square error of 0.482mm, which corresponds to 1.8217 pixel, is a very large error for close-range photogrammetry applications. The small magnitude of the root mean square error of 0.0137mm suggests that the inverse radial distortion correction function modelled from the inverse coefficients derived from the analytical approach successfully reduced the effects of barrel radial distortions to acceptable magnitudes without introducing additional effects of pincushion

distortions. The inverse model also reduced the effects of pincushion radial distortion without introducing further barrel radial distortions.
Table 4.35 presents a comparison between the newly proposed approach and some of the best root mean square errors achieved by some of the state-of-the-art approaches when calibrating radial distortions. These strategies also used a checkerboard calibration pattern similar to the new approach to extract coordinates of image points.

Table 4.35: Comparison of radial distortion correction root mean square error per calibration method

Calibration approaches	Albarelli et al.,2010	Geiger et al., (2012)	Placht et al., 2014	Ha et al., 2017	Drap and Lefevre 2016	New method
RMSE (pixel)	0.0891	0.1140	0.492	0.096	3.63	0.057

The table reveals that the calibration approach proposed by **Placht et al. (2014)** produced the largest root mean square error for radial lens distortion correction. The strategy developed by **Ha et al. (2017)** achieved an acceptable error of 0.096 pixels which is slightly higher than that earlier achieved by **Albarelli et al. (2010).** The proposed analytical approach based on inverse radial distortion coefficients outperformed these four previous studies. Radial distortion correction through inverse distortion coefficients offers more accuracy advantages than compensation and iterative correction-based methods currently implemented in available radial distortion correction software.

4.4. Conclusion Remarks

This chapter presented an improved concept of a fully analytical mathematical system to compute inverses of any radial distortion polynomial model. The developed system offers the potential to derive any inverse coefficients associated with a high-order radial distortion polynomial model. Currently, there is no fully analytical strategy that enables to compute inverse coefficients of radial distortion polynomial functions. This proposed new strategy first relied on the concept of forced differential equations since current series reversion techniques are not suitable to reverse the formulation structure of radial distortion functions. Furthermore, the current semi-analytical distortion polynomial reversion strategy assumes the same first four inverse coefficients for all the high-order radial distortion polynomials, regardless of their formulation structure. To fill the scientific gap of current series reversion algorithms not being suitable for radial distortion polynomials, unique and robust mathematical algorithms that can successfully derive inverse coefficients of any radial distortion polynomial function were developed in this study. These algorithms do not require any optimization to refine the inverse coefficients' estimates. From the inverse coefficients, inverse polynomial models were formulated for radial distortion corrections. The newly developed calibration system extended and improved the method proposed in **Drap and Lefevre (2016).** The proposed strategy provides a comprehensive outline to understand the fully analytical inverse modelling of radial distortion polynomial functions, which are structurally different in formulations from commonly known general polynomial models. The approach can produce inverse radial distortion models

capable of simultaneously modelling the inverse profiles of more than one radial distortion type with high accuracy. Empirically, the experiments conducted using distorted points demonstrated that the proposed analytical inversion method not only converged reliably but also produced more accurate undistorted point estimates than conventional iterative polynomial inversion methods. This suggests that within the bounds of the adopted distortion model, the proposed approach is not only valid but also significantly more efficient and stable. While the radial distortion polynomial model may not fully characterize all optical aberrations in off-the-shelf lenses, the enhanced inversion accuracy contributed to reducing the overall error propagation in downstream geometric estimations, particularly when higher-order radial terms are included.

CHAPTER5
RESEARCH SUMMARY AND CONCLUSION

5.1. Comparative and Critical Analysis of Conventional and Polynomial-Based Camera Calibration Approaches

The literature reveals that numerous camera calibration methods, particularly those based on conventional calibration tools, have been widely applied to estimate camera internal geometry parameters and determine the camera's spatial position and orientation within a 3D scene. Despite their prevalence, a detailed examination of these approaches highlights critical limitations in leveraging the intrinsic geometric properties embedded within the projective transformation matrix. Specifically, these methods do not fully utilize the individual geometric constraints that characterize the transformation. Consequently, these calibration methods are often susceptible to certain methodological challenges, including parameter coupling, sign ambiguity, and multiple roots among some calibration parameters, each of which can introduce significant inaccuracies. Such issues are notably problematic as they tend to create dependencies between parameters that can obscure accurate solutions, leading to errors in calibration output.
The examination of a second group of calibration approaches, particularly those that address radial lens distortion through inverse polynomial modelling, further underscores the comparative advantages and limitations of these techniques. Radial distortion, a common non-linear aberration in camera lenses, significantly impacts the fidelity of 3D reconstructions if not properly addressed. Among radial distortion models, polynomial functions generally offer superior performance over rational and division models, as they more effectively capture complex distortion profiles such as barrel, pincushion, and moustache distortions. Analytical approaches to radial distortion modelling and correction, which rely on explicit formulations rather than iterative adjustments, have demonstrated practical advantages over traditional iterative methods. Iterative approaches typically involve estimating inverse radial distortion coefficients concurrently with the calibration of other intrinsic and extrinsic camera parameters in a single minimization process. However, this integrated batch processing approach introduces error compensation, where inaccuracies in one parameter estimation may propagate and influence other parameters, leading to cumulative calibration errors. For practical applications,

such as 3D scene reconstruction, even slight inaccuracies in the calibration of radial distortion can manifest as significant imperfections in the reconstructed model, regardless of the accuracy of the camera pose estimation. This sensitivity to radial distortion calibration underscores a key drawback in iterative methodologies, which, despite their simplicity, may compromise the accuracy of the overall calibration process, particularly when applied in complex distortion scenarios.

In recent studies aimed at addressing these challenges within the computer vision community, recursive series reversion techniques have been explored as potential alternatives. These techniques aim to calculate inverse radial distortion coefficients directly through recursive formulations, thus allowing for radial distortion corrections via inverse modelling. This approach presents a promising step towards a non-iterative framework for radial distortion correction. However, several aspects of recursive series reversion remain inadequately developed and validated, particularly in terms of its robustness against severe distortion profiles like barrel, pincushion, and moustache. As a result, its practical efficacy in handling complex distortions has yet to be clearly demonstrated in comprehensive studies.

Moreover, while the computer vision community has explored non-iterative methods for inverse radial distortion correction, the photogrammetry discipline currently lacks an equivalent analytical solution specifically tailored for photogrammetric applications. This knowledge gap reflects a critical need for further research within photogrammetry that focuses on non-iterative inverse modelling techniques for radial lens distortion correction. Such work could substantially improve the accuracy and practicality of photogrammetric calibration processes, offering an alternative to the error-prone iterative methods. Addressing this gap could potentially enhance the precision of 3D reconstructions by mitigating distortions at the fundamental level, thereby supporting more robust applications across remote sensing, cartography, and related geospatial fields.

In summary, the review of existing calibration approaches reveals that while conventional methods provide valuable insights, they fail to exploit certain intrinsic geometric properties necessary for accurate calibration of camera pose parameters as well as the coordinates of the principal point and the effective focal lengths. Likewise, iterative methods for radial distortion correction are limited by error propagation issues, making them suboptimal for high-precision applications. These strategies typically achieve root mean square (RMS) reprojection errors in the range of 2.5 to 3.63 pixels under scenarios involving severe radial distortions (e.g., barrel, pincushion, and moustache). This level of error is substantial in photogrammetric applications, where sub-pixel accuracy is often required for reliable 3D reconstruction and metric analysis. The development of analytical, non-iterative methods for radial distortion correction through inverse modelling represents a promising avenue for future research, with the potential to overcome current limitations and elevate the standard of camera calibration in photogrammetry.

5.2. Summary of the Analytical Projective Decomposition calibration

The primary objective of this doctoral research is to address critical limitations in current camera calibration techniques for accurately estimating both intrinsic camera geometry parameters and extrinsic parameters that define camera pose within a 3D scene. Many existing camera calibration methods, especially those relying on nonlinear optimization, are susceptible to issues such as parameter coupling (where changes in one parameter incorrectly influence another), sign ambiguity (e.g., in rotation matrix estimation where multiple sign configurations may satisfy the same projection constraints), false solutions (numerically valid but physically implausible outcomes due to under-constrained systems of equations), and multiple roots (where multiple mathematically valid solutions exist, making it difficult to identify the correct physical

configuration). These issues often lead to unreliable or non-unique estimation of some intrinsic camera parameters, such as the coordinates of the principal point and the effective focal lengths, and extrinsic camera parameters that describe the camera location and orientation in a 3D scene, thereby limiting the robustness and repeatability of calibration outcomes. To overcome these challenges, this study introduced a fully analytical calibration framework by systematically decomposing the twelve coefficients of the projective transformation matrix into nineteen mathematically independent and robust equations. This decomposition approach introduces a novel solution by enforcing structural independence among equations, which eliminates coupling between parameters and ensures unambiguous solution convergence. The analytical decomposition formulates the calibration problem in a way that each camera parameter is estimated without the interference of cross-parameter dependencies, producing a unique solution set that accurately represents the camera's spatial configuration and pose. Unlike iterative or optimization-based methods that are prone to convergence on local minima or ambiguous solutions, the proposed methodology uses deterministic, independent equations to yield a highly accurate, globally optimal parameter set. The calibration algorithms developed within this strategy, termed the Analytical Projective Decomposition (APD) approach, were rigorously validated through extensive experimentation and testing across various real datasets. Experimental validation demonstrated the algorithms' capabilities to achieve superior accuracy in parameter estimation, with substantially reduced reprojection errors that outperform many existing state-of-the-art camera pose estimation methods. By resolving issues inherent in traditional camera calibration methods and achieving reliable, precise estimation of parameters of camera internal geometry and camera pose in a 3D scene, the developed APD calibration system makes a significant advancement in photogrammetry and computer vision. The analytical framework developed here is not only robust against the challenges typically encountered in camera internal geometry and pose calibration but also establishes a scalable model that can be applied across diverse imaging scenarios requiring high-accuracy calibration solutions. Through the elimination of false solutions and parameter ambiguities, this work contributes a foundational advancement in calibration methodologies, providing a dependable basis for further development in related computational imaging fields.

5.3. Summary of Analytical Inverse Modelling and Correction of Radial Distortions

This thesis also addresses significant challenges in the field of camera calibration, particularly in correcting radial distortions through inverse modelling of radial distortion polynomials. Radial distortion, a common issue in camera lenses, can greatly affect the precision of photogrammetric measurements. While polynomial models have proven effective in capturing complex distortion profiles such as barrel, pincushion, and moustache distortions, the inverse modelling and correction of these distortions remain challenging. One limitation of traditional radial distortion polynomial models is the lack of an easily computable inverse, which hinders the efficiency and accuracy of distortion correction. Recursive methods, although widely used, often rely on iterative processes that are computationally expensive and susceptible to inaccuracies. Moreover, these methods may fail to account for complex distortion profiles and tend to have rigid inverse coefficients, making them unsuitable for handling a variety of polynomial models or varying distortion characteristics. This research introduces a novel solution through the development of a fully analytical camera calibration system that utilizes forced differential equations for computing the inverse of radial distortion polynomials. The key contribution of this work is the creation of a new method for analytically computing inverse radial distortion coefficients for polynomial models of any degree. This method overcomes the limitations of existing recursive approaches by offering a more accurate and flexible solution that can handle a wide range of

distortion profiles, including those modelled by high-degree polynomials such as quintic, depressed sextic, and depressed octic. The proposed method eliminates the need for iterative processes and provides an analytical solution that significantly reduces reprojection errors compared to state-of-the-art techniques. The accuracy improvements are particularly notable when correcting severe radial distortions, which had previously been challenging for traditional methods. By providing a general solution that can be applied to polynomials of varying degrees, this approach offers a promising calibration tool for applications that require precise imaging and measurements. Therefore, this research successfully achieves its second primary objective by presenting a significant advancement in the field of radial distortion correction, improving accuracy over previous solutions while offering a more general, efficient, and robust calibration methodology.

5.4. Applicability of Developed Calibration Strategies.

The research outcomes of this study pave the way for applications across diverse industries where precise camera calibration is essential. Key applications include photogrammetric measurements, urban and environmental planning, cultural heritage preservation, accident scene reconstruction, autonomous vehicle navigation, computer vision, and aerial or drone-based mapping. In photogrammetry, accurate correction of radial lens distortions is critical for precise 3D modelling and topographic mapping. This is fundamental for high-accuracy cartography and surveying. In urban planning, precise camera calibration enables the creating of accurate models of buildings, roads, and other infrastructure, which are crucial for planning and development. Accurate 3D mapping, enabled by precise camera pose estimation and distortion correction, is also highly beneficial for monitoring land-use and land-cover changes. By enhancing the detection of subtle shifts in vegetation and terrain, this method aids in tracking environmental changes over time. For archaeological documentation, reliable camera pose calibration allows the digital preservation of cultural heritage sites. It enables the creation of detailed 3D models of historical structures and artworks, capturing their features with high fidelity. In forensic applications, particularly accident reconstruction, accurate camera pose calibration allows experts to recreate scenes with great precision, providing essential insights into the sequence of events and critical details of the scene. In the field of autonomous navigation, precise on-board camera calibration is crucial for accurate spatial awareness and safety. The inverse radial distortion correction algorithms developed in this research enhance depth perception by providing undistorted real-time 3D scene mapping and improved obstacle detection. This enhanced spatial accuracy supports key safety features in autonomous systems, such as collision avoidance and automated navigation. Similarly, in computer vision applications, inverse modelling of radial distortions is vital for object recognition and tracking, as undistorted imagery improves feature detection and alignment. The refined inverse polynomial modelling of radial distortions achieved in this study supports high-accuracy georeferencing of imagery, an essential capability for precision agriculture, urban planning, and wildlife monitoring. These advancements in distortion correction directly translate into improved image accuracy, benefiting sectors that rely on precise geographic information for decision-making and monitoring. This research, therefore, contributes significantly to enhancing both the precision and applicability of camera-based measurement systems across multiple high-stakes domains.

In addition to the improvements in calibration accuracy, the developed analytical strategies also offer significant advantages in terms of computational efficiency. Traditional camera calibration and radial distortion correction methods often rely on iterative optimization or recursive algorithms, which can be computationally intensive and prone to convergence issues, especially for high-degree polynomial models or large datasets. In contrast, the Analytical Projective

Decomposition (APD) and the inverse polynomial modelling approaches developed in this research are fully analytical and deterministic, eliminating the need for iterative computation. This results in a substantially reduced computational cost. For example, in the case of radial distortion correction, the proposed method uses forced differential equations to analytically compute inverse polynomial coefficients, which bypasses the recursive approximation loops used in traditional methods. Time complexity assessments showed that the analytical inversion requires only a single pass symbolic solution, while iterative methods require multiple evaluation cycles to converge, often with diminishing improvements after a certain number of iterations. As a result, the analytical approach achieves faster execution times and is more predictable in its performance. These improvements make the proposed methods particularly suitable for real-time or large-scale calibration tasks in time-sensitive applications such as autonomous navigation or drone-based imaging, where computational overhead must be minimized.

5.5. Research Findings

The application of a forced differential equation within close-range photogrammetry and computer vision to address the inversion of radial distortion functions is novel. The proposed study introduced an analytical polynomial reversion method capable of deriving inverse models for any given radial distortion polynomial with high accuracy, eliminating the need for iterative computation. This approach is computationally efficient relative to conventional iterative methods. The developed inverse radial distortion coefficients accurately represent the inverse profile of any radial distortion pattern, including moderate to severe barrel, pincushion, and moustache distortions.

Radial distortion, though often assumed to exhibit global symmetry, can in fact exhibit significant local variations. Residual error analyses conducted in Chapter 4 reveal that the observed symmetry in radial distortion tends to be localized, with variations in distortion becoming more prominent in certain areas of the image. This raises a key question regarding the suitability of adhering to a radially symmetric model in the presence of such localized effects. The choice to use a radial symmetric distortion model was made with the intention of providing a computationally efficient and generalized solution that could be applied across a variety of distortion types. However, it is acknowledged that local asymmetries in distortion may still remain. The power terms of the polynomial model, particularly the even-powered terms, appear to capture these localized effects more consistently than the odd-powered terms, as evidenced by the residual error analysis. Despite this, residual errors produced by the new model remain minimal when compared to traditional iterative calibration methods, suggesting that the radial model, while not exhaustive, performs well in reducing the most significant distortions present in the data. It is important to note that all models, including the radial model, will inevitably have some residual errors, especially when the distortion exhibits complex or non-radial behaviour. However, the results presented in this research demonstrate that the radial symmetric model, with its reduced residual errors, offers a highly effective and practical solution in the majority of imaging scenarios. Future work may explore the introduction of non-radial components or a hybrid distortion model to further improve the accuracy of calibration, particularly in the case of lenses with more complex distortion profiles.

Existing literature frequently claims that a multi-sign configuration in radial distortion coefficients suffices to describe moustache distortions. However, the conducted experiments demonstrate that multiple coefficient signs can also characterize pincushion distortions and, in certain configurations, barrel distortions as well. Thus, the profile of a radial distortion effect depends not only on the sign distribution but also on the specific magnitudes of the coefficients involved.

Notably, attempts to derive inverse radial distortion coefficients based on a general polynomial form led to inaccurate distortions when applied to inverse models structured as either depressed or truncated polynomials of the same degree.

The results achieved in this study further indicate that a sixth-degree depressed polynomial can simultaneously model both barrel and pincushion distortions, while an eighth-degree depressed polynomial effectively captures the effects of moustache radial distortions.

A novel camera pose calibration method that addresses critical issues inherent in traditional models was devised, such as parameter coupling, sign ambiguity, and the challenge of multiple roots, while preserving essential geometric constraints between camera parameters and the projective transformation matrix. This calibration strategy yields a reliable model, characterized by a second effective focal length f_y larger than the first f_x and a principal point's first coordinate u_0 greater than its second coordinate v_0.

Inversely, the sequencing and arrangement of radial distortion coefficients in an inverse model are dependent on the structural formulation of the original polynomial model.

Additionally, imposing coplanarity constraints on the 3D coordinate system's origin and calibration points may compromise the accuracy of the newly proposed camera pose estimation method. The resulting introduction of numerous zero elements under coplanarity constraints can diminish the accuracy of coefficients within the projective transformation matrix, which underscores the sensitivity of the proposed calibration model to initial setup constraints.

5.6. Limitations of the Study

In photogrammetry, achieving accurate radial distortion correction is vital to high-precision applications. However, it has been observed that certain sign configurations in the radial distortion coefficients can challenge correction accuracy. Specifically, when the first, second, and third radial distortion coefficients κ_1, κ_2 and κ_3 are calculated and assume positive, negative, and positive signs, respectively, a notable decrease in the efficacy of distortion correction arises. The underlying reasons for this difficulty remain unclear despite extensive analysis, presenting a challenging aspect for accurate modelling.

This analysis employed high-order depressed six- and eight-degree polynomial models rather than general polynomial forms, a choice informed by their frequent application in photogrammetric literature for radial distortion correction, typically limited to three terms. Notably, most radial distortion correction research available utilizes depressed polynomials comprising up to three terms due to their relative simplicity and efficacy in capturing lower-order distortions while minimizing computational complexity, and existing photogrammetry software at the start of this study predominantly relied on three-term radial distortion coefficients.

Due to constraints in software engineering expertise, this research did not culminate in a standalone application that integrates the developed calibration strategies within a single computational tool. Instead, the two developed calibration methodologies were implemented and evaluated independently, utilizing established statistical tools and calibration accuracy metrics. This modular approach ensured that each strategy could be rigorously tested and validated prior to potential integration in future work.

Furthermore, to maintain rigorous control over distortion-free and distorted image coordinates, the study employed manual coordinate measurement after automatic corner detection processing. Unlike automated coordinate measurements, which introduce variables that can obscure subtle distortion effects, manual measurement using the measurement tools in GIMP software provided precise and repeatable coordinates for comparative analyses. This

methodology, while time-intensive, enabled precise data acquisition, ensuring robust evaluation of each calibration strategy's accuracy in isolation.

The consideration of a 3D test field or simulated 3D environments with depth measures is usually recommended for the evaluation of the Z-dimension and provides a more comprehensive validation of the calibration accuracy, as recommended in the literature. However, in chapter4, the evaluation primarily focuses on 2D image reprojection errors to validate the accuracy of the calibration framework. While these errors provide insight into the precision of the intrinsic parameters and the corrected distortion, the Z-coordinate (depth) of the reconstructed 3D coordinates was not assessed in this phase. This limitation stems from the use of 2D calibration targets (printed checkerboard patterns), which did not offer 3D ground-truth depth data.

5.7. Future Studies

- The accuracy of inverse radial distortion coefficients is intricately linked to the precision of the original distortion polynomial. However, in current calibration systems, polynomial reduction, the strategic omission or simplification of certain polynomial terms, has been used to achieve computational efficiency. While effective in reducing calculation time, these omissions can impact accuracy, especially in complex models. Polynomial reduction through techniques such as Tschirnhaus transformations provides a mathematical foundation for achieving term-specific reductions without arbitrary term exclusion, thus preserving the coefficient integrity in the resulting inverse polynomial. Further research is needed to refine polynomial reduction methods, focusing on maintaining coherence in the distortion coefficient estimates while maximizing computational efficiency. Such advances could enhance accuracy in photogrammetric applications where minor errors can propagate significantly.
- Conventional approaches to compute radial distortion coefficients rely on estimating an optimal radial distortion radius. However, this radius often has multiple roots, leading to subjectivity in root selection and potential inconsistency across solutions. Developing methods that directly estimate distortion coefficients, bypassing the need to compute the radial distortion radius, could improve calibration accuracy. Tools like Newton power sums could be employed to facilitate the direct computation of distortion coefficients, ensuring more stable radial distortion corrections. Such advancements would provide a robust foundation for applications in which precise distortion modelling is central.
- A promising future direction is to integrate both analytical systems into a comprehensive software platform capable of executing two-stage fully analytical camera calibration. This tool would offer significant advancements over traditional calibration software by allowing precise, parameter-specific control, minimizing distortions through optimized polynomial models, and automating inverse coefficient computations. Such software could streamline calibration for photogrammetric and computer vision applications, providing a reliable, consistent solution for both standard and specialized imaging systems.
- With the developed analytical models capable of parameter-specific coefficient retrieval, machine learning (ML) techniques offer potential to enhance the calibration process by identifying and adjusting for nuances in distortion patterns. For example, ML systems could learn from previous calibration data to predict approximate radial distortion coefficients under varying lighting conditions or for different camera types, expediting calibration in dynamic environments. Additionally, deep learning approaches may be

utilized to predict calibration parameters in real-time, offering solutions for applications that demand high adaptability, such as robotic vision and autonomous navigation.

- The versatility of the analytical radial distortion calibration method allows for potential adaptation to non-standard lenses, such as fisheye and panoramic lenses. Unlike conventional lenses, these specialized lenses exhibit unique and often extreme distortion profiles. Future research could focus on extending the model to accommodate these lenses, ensuring accurate calibration across diverse optical systems. Such adaptations would support a broad array of imaging technologies and enhance performance in applications with unconventional field-of-view requirements.
- Accurate camera calibration is essential in computer vision tasks like object detection, 3D reconstruction, and autonomous navigation. The use of polynomials for modelling and correcting radial distortions holds promise for improving calibration in applications with wide-angle or fisheye lenses, which inherently exhibit more pronounced distortions. Robust calibration of these lenses can improve object localization accuracy and depth estimation, directly impacting applications in autonomous vehicles and robotics. Future studies could aim at optimizing these polynomial models to further refine camera positioning and orientation in complex, real-world scenes.
- While the primary focus has been on radial distortion, lenses also suffer from tangential distortions, chromatic aberrations, and affine distortions. Extending the current analytical model to simultaneously address these types of distortion could yield a more comprehensive calibration solution. Research into unified models that incorporate multiple distortion types would increase calibration accuracy in general-purpose and high-precision cameras alike, supporting a broader range of optical configurations.
- Current inverse coefficient calculations assume a fixed lens model, which can lead to inaccuracies in scenarios where optical properties vary over time due to environmental changes. Adaptive calibration methods, which can dynamically adjust to account for temperature fluctuations, mechanical stresses, or wear, would significantly improve calibration robustness in long-term or high-stress applications. Such systems would be invaluable in applications where the camera setup cannot be frequently recalibrated, such as space exploration or high-precision industrial settings.
- Advances in distortion modelling could also inform future lens design by enabling precise adjustments during manufacturing to minimize distortion. This approach could streamline the production of specialized lenses with minimal inherent distortion, reducing the need for extensive post-capture calibration. Further research could explore the integration of these techniques into the lens design process, potentially influencing the next generation of lenses used in high-stakes imaging applications.

5.8. Conclusion

This doctoral research presents a critical re-evaluation and advancement of camera calibration methods, addressing some limitations that have hindered precise parameter estimation in conventional calibration frameworks. Through a rigorous literature review, key issues were identified in the predominant camera calibration approaches, focusing particularly on the challenges inherent in parameter coupling, sign ambiguity, and convergence to false solutions. Traditional calibration methodologies often struggle to independently estimate camera intrinsic parameters and pose due to the complexity and interaction of parameters within the projective transformation matrix. Moreover, iterative techniques commonly used in radial distortion correction were found to be limited by computational expense, error compensation, and dependency on the specific form of polynomial distortion models. These methodological

limitations in both intrinsic and extrinsic parameter calibration highlight the need for improved, analytically robust calibration systems.

In response to these gaps, this research developed the Analytical Projective Decomposition (APD) method, an innovative and comprehensive calibration framework that enhances accuracy by decomposing the projective transformation matrix into nineteen independent, mathematically robust equations. This decomposition creates a calibration model where intrinsic and extrinsic parameters are derived independently, effectively eliminating parameter coupling and ensuring convergence to unique solutions. The APD approach demonstrated considerable improvements in calibration accuracy, particularly in reducing reprojection error, positioning it as a superior alternative to traditional and state-of-the-art calibration methods. Additionally, this research advanced the field of radial distortion correction by introducing a novel, fully analytical approach for inverse modelling of radial distortion through forced differential equations. Radial distortion, which commonly manifests in complex forms like barrel, pincushion, and moustache patterns, has posed significant challenges to inverse modelling due to the inherent complexity of distortion profiles and limitations of existing iterative and semi-analytic approaches. Polynomial radial distortion models, while capable of capturing complex distortions, have traditionally required recursive estimation methods, leading to issues of computational inefficiency and reliance on batch processing. The forced differential equations method developed in this research eliminates these issues by deriving inverse radial distortion coefficients analytically, allowing for accurate and flexible correction of radial distortions across polynomial models of varying degrees. The novel analytical inverse model presented here offers several technical advantages. First, it provides a generalizable solution applicable to any polynomial distortion model, enabling it to handle distortions of varying severity with high accuracy and reduced reprojection error. Second, this method accommodates complex distortion patterns, surpassing existing techniques in accuracy and eliminating the need for iterative correction processes. Third, through a forced differential equation approach, it achieves computational efficiency and resilience against error propagation, addressing a long-standing challenge in camera calibration for high-stakes applications in 3D modelling and photogrammetric measurements.

The technical contributions of this research culminate in a scalable, efficient, and accurate camera calibration system suitable for a wide range of practical applications. This research also added two accredited conference publications to the body of knowledge in photogrammetry. The two research papers were presented at the 2019 ISPRS Geospatial Week conference at ITC in the Netherlands and published in the 2019 ISPRS archives series. In conclusion, this thesis has successfully achieved its objectives and addressed key gaps in camera calibration and distortion correction, presenting a robust analytical framework that transcends the limitations of some of the existing conventional methodologies. By introducing non-iterative, independent equation-based calibration and an analytical solution for radial distortion inversion, this research contributes significantly to the precision and applicability of camera-based measurement systems in photogrammetry, remote sensing, and computer vision. This work lays a solid foundation for further advancements in computational imaging, establishing a scalable model that meets the high accuracy requirements across diverse imaging scenarios and solidifying its applicability in fields that depend on reliable, distortion-free imaging and accurate 3D measurements. In conclusion, the fully analytical methods introduced in this research provide a significant step forward in camera calibration and distortion correction, offering higher precision, greater stability, and improved adaptability compared to existing iterative techniques. The numerical results clearly demonstrate the practical advantages of these methods in real-world applications.

REFERENCES

Abdullah, S., Tahar, K.N., Rashid, M.F.A. and Osoman, M.A., 2019. Camera Calibration Performance on Different Non-metric Cameras. *Pertanika Journal of Science & Technology,* 27(3).

Abeles, P., 2018. Inverse radial distortion formula. Less Than Optimal. Available online: http://peterabeles. com/blog.

Abdel-Aziz, Y.I., Karara, H.M. and Hauck, M., 2015. Direct linear transformation from comparator coordinates into object space coordinates in close-range photogrammetry. *Photogrammetric engineering & remote sensing*, 81(2), pp.103-107.

Aicardi, I., Chiabrando, F., Lingua, A.M. and Noardo, F., 2018. Recent trends in cultural heritage 3D survey: The photogrammetric computer vision approach. *Journal of Cultural Heritage,* 32, pp.257-266.

Allmendinger, R.W., 2015. Modern structural practice. *A structural geology laboratory manual for the 21st Century*, *1*(0).

Alturki, A.S. and Loomis, J.S., 2016, July. Camera principal point estimation from vanishing points. In *2016 IEEE National Aerospace and Electronics Conference (NAECON) and Ohio Innovation Summit (OIS)* (pp. 307-313). IEEE.

An, G.H., Lee, S., Seo, M.W., Yun, K., Cheong, W.S. and Kang, S.J., 2018. Charuco board-based omnidirectional camera calibration method. *Electronics*, *7*(12), p.421.

Andaru, R., Rau, J.Y., Chuang, L.Z.H. and Jen, C.H., 2022. Multitemporal UAV photogrammetry for sandbank morphological change analysis: evaluations of camera calibration methods, co-registration strategies, and the reconstructed DSMs. *IEEE Journal of Selected Topics in Applied Earth Observations and Remote Sensing*, 15, pp.5924-5942.

ASPRS Camera calibration report, 2015, accessed at http://www.asprs.org/a/news/archive/final_report.html.

Babaei, A. and Saadat Seresht, M., 2019. Optimal selection of distortion model parameters for projection lenses ssing phasogrammetric self-calibration. *Earth Observation and Geomatics Engineering*, *3*(2), pp.39-50.

Barbero-García, I., Cabrelles, M., Lerma, J.L. and Marqués-Mateu, Á., 2018. Smartphone-based close-range photogrammetric assessment of spherical objects. *The Photogrammetric Record*, *33*(162), pp.283-299.

Barrett, J.M., Viggiani, D., Park, J. and Callaghan, J.P., 2020. Expressing angles relative to reference postures: A mathematical comparison of four approaches. *Journal of biomechanics*, *104*, p.109733.

Bartl, V., Špaňhel, J., Dobeš, P., Juranek, R. and Herout, A., 2021. Automatic camera calibration by landmarks on rigid objects. *Machine Vision and Applications*, *32*(1), pp.1-13.

Beauchemin, S.S. and Bajcsy, R., 2001. Modelling and removing radial and tangential distortions in spherical lenses. In *Multi-Image Analysis* (pp. 1-21). Springer, Berlin, Heidelberg.

Bell, T., Xu, J. and Zhang, S., 2016. Method for out-of-focus camera calibration. *Applied optics*, *55*(9), pp.2346-2352.

Boby, R.A. and Saha, S.K., 2016, May. Single image-based camera calibration and pose estimation of the end-effector of a robot. In *2016 IEEE International Conference on Robotics and Automation (ICRA)* (pp. 2435-2440). IEEE.

Brauer-Burchardt, C., Voss K., 2001. A new algorithm to correct fish-eye- and strong wide-angle-lens-distortion from single images. In: *IEEE International Conference on Image Processing*. Volume 1. (2001) 225 – 228

Brown DC, 1971. "Close-range camera calibration", *Photogrammetric Engineering and Remote Sensing* 1971; 42:855–66.

Bukhari, F. and Dailey, M.N., 2013. Automatic radial distortion estimation from a single image. *Journal of mathematical imaging and vision*, *45*(1), pp.31-45.

Buquet, J., Zhang, J., Roulet, P., Thibault, S. and Lalonde, J.F., 2021. Evaluating the Impact of Wide-Angle Lens Distortion on Learning-based Depth Estimation. In *Proceedings of the IEEE/CVF Conference on Computer Vision and Pattern Recognition* (pp. 3693-3701).

Burger, W., 2019. Zhang's camera calibration algorithm: In-Depth tutorial and implementation (Technical report HGB16-05). *School of Informatics, Communications and Media, Department of Digital Media, University of Applied Sciences Upper Austria, Hagenberg, Austria*.

Cai, H., Pang, W., Chen, X., Wang, Y. and Liang, H., 2020. A novel calibration board and experiments for 3D LiDAR and camera calibration. *Sensors*, *20*(4), p.1130.

Cai, H., Song, Y., Shi, Y., Cao, Z., Guo, Z., Li, Z. and He, A., 2020. Flexible multicamera calibration method with a rotating calibration plate. Optics Express, 28(21), pp.31397-31413.

Cao, M.W., Jia, W., Zhao, Y., Li, S.J. and Liu, X.P., 2018. Fast and robust absolute camera pose estimation with known focal length. *Neural Computing and Applications*, *29*, pp.1383-1398.

Capolupo, A., Saponaro, M., Borgogno Mondino, E. and Tarantino, E., 2020. Combining Interior Orientation Variables to Predict the Accuracy of Rpas–Sfm 3D Models. *Remote Sensing*, *12*(17), p.2674.

Chen, B. and Pan, B., 2020. Camera calibration using synthetic random speckle pattern and digital image correlation. *Optics and Lasers in Engineering*, *126*, p.105919.

Chen, C., Chen, B. and Pan, B., 2021. Telecentric camera calibration with virtual patterns. *Measurement Science and Technology*, *32*(12), p.125004.

Chen, J., Li, S., Liu, D. and Lu, W., 2021. Indoor camera pose estimation via style-transfer 3D models. *Computer-Aided Civil and Infrastructure Engineering*.

Chen, J., Zhang, J., Liang, B. and Yang, D., 2021. A General Method of Series Reversion for Synthetic Aperture Radar Imaging. *IEEE Geoscience and Remote Sensing Letters*, 19, pp.1-5.

Chen, J., Zhu, F. and Little, J.J., 2018, March. A two-point method for PTZ camera calibration in sports. In *2018 IEEE Winter Conference on Applications of Computer Vision (WACV)* (pp. 287-295). IEEE.

Cheng, M.L. and Matsuoka, M., 2021. Extracting three-dimensional (3D) spatial information from sequential oblique unmanned aerial system (UAS) imagery for digital surface modelling. *International Journal of Remote Sensing*, *42*(5), pp.1643-1663.

Chu, C. and Yang, S., 2020. Keyframe-based RGB-D visual-inertial odometry and camera extrinsic calibration using extended Kalman filter. *IEEE Sensors Journal*, 20(11), pp.6130-6138.

Clédat, E., Cucci, D.A. and Skaloud, J., 2020. Camera calibration models and methods for corridor mapping with UAVS. ISPRS Annals of the Photogrammetry, *Remote Sensing and Spatial Information Sciences*, 1, pp.231-238.

Cornic, P., Illoul, C., Cheminet, A., Le Besnerais, G., Champagnat, F., Le Sant, Y. and Leclaire, B., 2016. Another look at volume self-calibration: calibration and self-calibration within a pinhole model of Scheimpflug cameras. *Measurement Science and Technology*, *27*(9), p.094004.

Cvišić, I., Marković, I. and Petrović, I., 2022. Enhanced calibration of camera setups for high-performance visual odometry. *Robotics and Autonomous Systems*, *155*, p.104189.

Dai, R., Li, W., Tang, X., Li, Y. and Liu, Y.H., 2023. High-Accuracy Calibration for a Multiview Microscopic 3-D Measurement System. IEEE/ASME Transactions on Mechatronics.

Darvatkar, S. and Bhandari, S.U., 2017, August. Implementation of barrel distortion correction on FPGA. In 2017 International Conference on Computing, Communication, Control and Automation (ICCUBEA) (pp. 1-6). *IEEE*.

Dehkharghani, S.S. and Pleshkova, S., 2014. Geometric thermal infrared camera calibration for target tracking by a mobile robot. *Comptes rendus de l'Academie bulgare des Sciences*, *67*(1), pp.109-114.

Devernay, F. and Faugeras, O., 2001. Straight lines have to be straight. *Machine vision and applications*, 13, pp.14-24.

Diaz-Ramirez, V.H., 2021, July. Numerical Solution for Radial Distortion Rectification in Optical Systems. In Maple in Mathematics Education and Research: *4th Maple Conference, MC* 2020, Waterloo, Ontario, Canada, November 2–6, 2020, Revised Selected Papers (Vol. 1414, No. 10, p. 319). Springer Nature.

Drap, P., Lefevre, J., 2016. An exact formula for calculating inverse radial lens distortions. Sensors, Vol. 16(6).

Duan, Y., Yu, Y. and Liang, M., 2024. A weighted camera calibration algorithm with global solution of homography. *Optics & Laser Technology*, 174, p.110585.

El-Ashmawy, K., 2021. Block Adjustment Using Control Distances Constraint. *International Journal of Innovation Scientific Research and Review (IJISRR)*, *3*, pp.948-953.

El-Ashmawy, K.L., 2015. A comparison study between collinearity condition, coplanarity condition, and direct linear transformation (DLT) method for camera exterior orientation parameters determination. *Geodesy and Cartography*, *41*(2), pp.66-73.

Elnima, E.E., 2015. A solution for exterior and relative orientation in photogrammetry, a genetic evolution approach. *Journal of King Saud University-Engineering Sciences*, *27*(1), pp.108-113.

Ernould, C., Beausir, B., Fundenberger, J.J., Taupin, V. and Bouzy, E., 2021. Integrated correction of optical distortions for global HR-EBSD techniques. *Ultramicroscopy*, *221*, p.113158.

Fang, W. and Zheng, L., 2016. Distortion correction modelling method for zoom lens cameras with bundle adjustment. *Journal of the Optical Society of Korea*, 20(1), pp.140-149.

Faraji, M., 2021. Active Sensors: Calibration & Applications.

Faugeras OD and Toscani G, 1986. "The calibration problem for stereo," *Proceedings of IEEE Computer Vision and Pattern Recognition, pp. 15–20, 1986.*

Feng, X.F. and Pan, D.F., 2018. A camera calibration method based on plane mirror and vanishing point constraint. *Optik*, *154*, pp.558-565.

Fitzgibbons A.W., 2001, "Simultaneous linear estimation of multiple view geometry and lens distortion," in Proc. *IEEE Conf. Computer Vision and Pattern Recognition*, 2001.

Fraser, C.S., 2013. Automatic camera calibration in close range photogrammetry. *Photogrammetric Engineering & Remote Sensing*, 79(4), pp.381-388.

Fryskowska, A., Kedzierski, M., Grochala, A. and Braula, A., 2016. CALIBRATION OF LOW COST RGB AND NIR UAV CAMERAS. *International Archives of the Photogrammetry, Remote Sensing & Spatial Information Sciences*, *41*.

Ganapathy, S., 1984. Decomposition of transformation matrices for robot vision. *Pattern Recognition Letters*, *2*(6), pp.401-412.

Gavin, H.P., 2019. The Levenberg-Marquardt algorithm for nonlinear least squares curve-fitting problems. *Department of Civil and Environmental Engineering, Duke University*, *19*.

Gao, D. and Yin, F., 2013. Computing a complete camera lens distortion model by planar homography. *Optics & Laser Technology*, *49*, pp.95-107.

Guo, F., He, Y. and Guan, L., 2017, November. RGB-D camera pose estimation using deep neural network. In 2017 *IEEE global conference on signal and information processing* (GlobalSIP) (pp. 408-412). IEEE.

Griffiths, D. and Burningham, H., 2019. Comparison of pre-and self-calibrated camera calibration models for UAS-derived nadir imagery for a SfM application. *Progress in physical geography: earth and environment*, *43*(2), pp.215-235.

Halloran, B., Premaratne, P. and Vial, P.J., 2020. Robust one-dimensional calibration and localization of a distributed camera sensor network. *Pattern Recognition*, 98, p.107058.

Hamad R., Sattar S.A., Al-Azawi. R., 2017. Calculation the inverse radial distortion model based on Zhang method. *Advances in Natural and Applied Sciences*. 11(3); Pages: 86-90.

Hamed, B.K., Hamad, R.K. and Hassonny, H.A., 2021, September. High Order Inverse Radial Lens Distortion. In Journal of Physics: Conference Series (Vol. 1999, No. 1, p. 012126). IOP Publishing.

Hamed, B.K., Hamad, R.K. and Hassonny, H.A., 2021, September. High Order Inverse Radial Lens Distortion. In *Journal of Physics: Conference Series* (Vol. 1999, No. 1, p. 012126). IOP Publishing.

Hassan, M.F.A., Ma'arof, I. and Samad, A.M., 2014, March. Assessment of camera calibration towards accuracy requirement. In 2014 *IEEE 10th International Colloquium on Signal Processing and its Applications* (pp. 123-128). IEEE.

He, H., Li, H., Huang, Y., Huang, J. and Li, P., 2020. A novel efficient camera calibration approach based on K-SVD sparse dictionary learning. *Measurement,* 159, p.107798.

Henrichsen, A., 2000. *3D reconstruction and camera calibration from 2D images* (Master's thesis, University of Cape Town).

Hiba, A., Sántha, L.M., Zsedrovits, T., Hajder, L. and Zarandy, A., 2020. Onboard Visual Horizon Detection for Unmanned Aerial Systems with Programmable Logic. *Electronics*, *9*(4), p.614.

Hirmiz, N., Tsikouras, A., Osterlund, E.J., Richards, M., Andrews, D.W. and Fang, Q., 2019. Cross-talk reduction in a multiplexed synchroscan streak camera with simultaneous calibration. *Optics express*, *27*(16), pp.22602-22614.

Hong, Y., Ren, G. and Liu, E., 2015. Non-iterative method for camera calibration. Optics Express, 23(18), pp.23992-24003.

Huang, P., Meng, Z., Guo, J. and Zhang, F., 2018. Chapter 3-pose measurement based on vision perception. *Tethered Space Robot*, pp.75-119.

Hugemann W, 2010," Correcting lens distortion in digital photographs" *EVU,* 2010.

Hu, H., Zhang, R., Fong, T., Rhodin, H. and Murphy, T.H., 2023. Standardized 3D test object for multi-camera calibration during animal pose capture. *Neurophotonics, 10(4)*, pp.046602-046602.

Hu, J., Liu, E. and Yu, J., 2021. Application of Structural Deformation Monitoring Based on Close-Range Photogrammetry Technology. Advances in Civil Engineering, 2021.

Huo, J., Zhang, H., Meng, Z., Yang, F. and Yang, G., 2022. A flexible calibration method based on small planar target for defocused cameras. *Optics and Lasers in Engineering*, *157*, p.107125.

Ibrahim, M., Wagdy, M., AlHarithi, F.S., Qahtani, A.M., Elkilani, W.S. and Zarif, S., 2022. An Efficient Method for Document Correction Based on Checkerboard Calibration Pattern. *Applied Sciences*, *12*(18), p.9014.

Imakura, A. and Yamamoto, Y., 2019. Efficient implementations of the modified Gram–Schmidt orthogonalization with a non-standard inner product. *Japan Journal of Industrial and Applied Mathematics*, *36*(2), pp.619-641.

Janos, I. and Benesova, W., 2021. Single Image Automatic Radial Distortion Compensation Using Deep Convolutional Network. *arXiv preprint arXiv:2112.08198*.

Jaroš, M., 2021. *Calibration of multiple cameras for autonomous driving*, Bachelor of Cybernetics and robotics,Czech Technical University in Prague(M Jaroš - 2021 - wiki.control.fel.cvut.cz, accessed on 15th October 2022)

Jiang, J., Zeng, L., Chen, B., Lu, Y. and Xiong, W., 2019. An accurate and flexible technique for camera calibration. *Computing*, *101*(12), pp.1971-1988.

Jin, L., Zhang, J., Hold-Geoffroy, Y., Wang, O., Blackburn-Matzen, K., Sticha, M. and Fouhey, D.F., 2023. Perspective Fields for Single Image Camera Calibration. In *Proceedings of the IEEE/CVF Conference on Computer Vision and Pattern Recognition* (pp. 17307-17316).

Jin, Z., Li, Z., Gan, T., Fu, Z., Zhang, C., He, Z., Zhang, H., Wang, P., Liu, J. and Ye, X., 2022. A Novel Central Camera Calibration Method Recording Point-to-Point Distortion for Vision-Based Human Activity Recognition. *Sensors*, *22*(9), p.3524.

Juarez-Salazar, R., Zheng, J. and Diaz-Ramirez, V.H., 2020. Distorted pinhole camera modelling and calibration. *Applied Optics*, *59*(36), pp.11310-11318.

Ju, M.H. and Kang, H.B., 2014. Stitching images with arbitrary lens distortions. *International Journal of Advanced Robotic Systems*, *11*(1), p.2.

Kabadayi, A., Yunus, K. and Yiğit, A.Y., 2020. Comparison of documentation cultural artifacts using the 3D model in different software. *Mersin Photogrammetry Journal*, *2*(2), pp.51-58.

Kannala, J. and Brandt, S.S., 2006. A generic camera model and calibration method for conventional, wide-angle, and fish-eye lenses. *IEEE transactions on pattern analysis and machine intelligence*, *28*(8), pp.1335-1340.

Kaufman, O. and Gurfil, P., 2021. Spacecraft relative navigation with an omnidirectional vision sensor. *Acta Astronautica*, *188*, pp.334-351.

Khalil, A.M., 2011. Two-dimensional displacement measurement using static close-range photogrammetry and a single fixed camera. *Alexandria Engineering Journal*, *50*(3), pp.219-227.

Khomutenko, B., Garcia, G. and Martinet, P., 2015. An enhanced unified camera model. IEEE Robotics and Automation Letters, 1(1), pp.137-144.

Kim, T.E., 2021. Study on Comparative Analysis of Camera Calibration. *Ilkogretim Online*, *20*(3), pp.1136-1143.

Kumar, V.R., Eising, C., Witt, C. and Yogamani, S., 2022. Surround-view Fisheye Camera Perception for Automated Driving: Overview, Survey and Challenges. *arXiv preprint arXiv:2205.13281*.

Kumar, V.R., Yogamani, S., Bach, M., Witt, C., Milz, S. and Mäder, P., 2020, January. Unrectdepthnet: Self-supervised monocular depth estimation using a generic framework for handling common camera distortion models. In *2020 IEEE/RSJ International Conference on Intelligent Robots and Systems (IROS)* (pp. 8177-8183). IEEE.

Kurillo, G., Li, Z. and Bajcsy, R., 2008, September. Wide-area external multi-camera calibration using vision graphs and virtual calibration object. In *2008 Second ACM/IEEE International Conference on Distributed Smart Cameras* (pp. 1-9). IEEE.

Labuz, J., Thaker, M. and Venkateswaran, B., 1991, January. Decomposition of the camera calibration matrix. In the Twenty-Third South-eastern Symposium on System Theory (pp. 89-90). IEEE Computer Society.

Lai, M., Shan, C. and de With, P.H., 2018, September. Hand-eye camera calibration with an optical tracking system. In *Proceedings of the 12th International Conference on Distributed Smart Cameras* (pp. 1-6).

Lari, Z., Habib, A., Mazaheri, M. and Al-Durgham, K., 2014. Multi-camera system calibration with built-in relative orientation constraints (Part 1) theoretical principle. *Journal of the Korean Society of Surveying, Geodesy, Photogrammetry and Cartography*, *32*(3), pp.191-204.

Larsson, V., Sattler, T., Kukelova, Z. and Pollefeys, M., 2019. Revisiting radial distortion absolute pose. In *Proceedings of the IEEE/CVF International Conference on Computer Vision* (pp. 1062-1071).

Lava, P., Van Paepegem, W., Coppieters, S., De Baere, I., Wang, Y. and Debruyne, D., 2013. Impact of lens distortions on strain measurements obtained with 2D digital image correlation. *Optics and Lasers in Engineering*, *51*(5), pp.576-584.

Lee, J.K. and Jung, W.C., 2019. Comparison between Two Coordinate Transformation-Based Orientation Alignment Methods. *Journal of Sensor Science and Technology*, *28*(1), pp.30-35.

Lee, T.E., Tremblay, J., To, T., Cheng, J., Mosier, T., Kroemer, O., Fox, D. and Birchfield, S., 2020, May. Camera-to-robot pose estimation from a single image. In 2020 *IEEE International Conference on Robotics and Automation* (ICRA) (pp. 9426-9432). IEEE.

Leite, N., Bue, A.D. and Gaspar, J., 2008. Calibrating a network of cameras based on visual odometry. in Proc. of IV *Jornadas de Engenharia Electrónica e Telecomunicaçoes e de Computadores*, Lisbon, Portugal, pp.174-179.

Lei, W., Xu, M., Hou, F., Jiang, W., Wang, C., Zhao, Y., Xu, T., Li, Y., Zhao, Y. and Li, W., 2020. Calibration Venus: An Interactive Camera Calibration Method Based on Search Algorithm and Pose Decomposition. *Electronics*, 9(12), p.2170.

Leizea, I., Herrera, I. and Puerto, P., 2023. Calibration Procedure of a Multi-Camera System: Process Uncertainty Budget. *Sensors*, 23(2), p.589.

Lelowicz, K., 2019, August. Camera model for lens with strong distortion in automotive application. In 2019 24th *International Conference on Methods and Models in Automation and Robotics* (MMAR) (pp. 314-319). IEEE.

Li, A., Wu, Y., Xia, X., Huang, Y., Feng, C. and Zheng, Z., 2015. Computational method for correcting complex optical distortion based on FOV division. *Applied optics*, *54*(9), pp.2441-2449.

Li, H., Zhang, X., Wu, H. and Gan, J., 2017. Line-based calibration of a micro-vision motion measurement system. *Optics and Lasers in Engineering*, *93*, pp.40-46.

Li, K., Bu, J. and Zhang, D., 2016. Lens distortion elimination for improving measurement accuracy of fringe projection profilometry. *Optics and Lasers in Engineering*, *85*, pp.53-64.

Li, W., Zhang, Y. and Zhao, Y., 2015, February. Camera calibration based on parallel lines. In *Intelligent Robots and Computer Vision XXXII: Algorithms and Techniques* (Vol. 9406, pp. 194-201). SPIE.

Liang, G., Chen, F., Liang, Y., Feng, Y., Wang, C. and Wu, X., 2020. A Manufacturing-Oriented Intelligent Vision System Based on Deep Neural Network for Object Recognition and 6D Pose Estimation. *Frontiers in Neurorobotics*, *14*, p.102.

Lichti, D.D., Jarron, D., Tredoux, W., Shahbazi, M. and Radovanovic, R., 2020. Geometric modelling and calibration of a spherical camera imaging system. *The Photogrammetric Record*, *35*(170), pp.123-142.

Liao, K., Lin, C., Zhao, Y. and Gabbouj, M., 2019. DR-GAN: Automatic radial distortion rectification using conditional GAN in real-time. *IEEE Transactions on Circuits and Systems for Video Technology*, *30*(3), pp.725-733.

Liao, K., Lin, C., Zhao, Y., Gabbouj, M. and Zheng, Y., 2019. OIDC-Net: Omnidirectional image distortion correction via coarse-to-fine region attention. *IEEE Journal of Selected Topics in Signal Processing*, 14(1), pp.222-231.

Liu, C., Wang, L., Liu, X. and Xu, Z., 2021. Iterative mapping for high-precision calibration and displacement measurements. *Optik*, *248*, p.168195.

Liu, S., Guo, P., Feng, L. and Yang, A., 2019. Accurate and Robust Monocular SLAM with Omnidirectional Cameras. Sensors, 19(20), p.4494.

Liu, W., Li, F., Jing, C., Wan, Y., Su, B. and Helali, M., 2021. Recognition and location of typical automotive parts based on the RGB-D camera. Complex & Intelligent Systems, 7(4), pp.1759-1765.Sapirstein, P., 2018. A high-precision photogrammetric recording system for small artefacts. *Journal of Cultural Heritage*, 31, pp.33-45.

Liu, Y., Al-Obaidi, A., Jakas, A. and Li, L., 2008. Accurate camera calibration and correction using rigidity and radial alignment constraints. In Proc. 3DPVT (pp. 145-152).

Liu, Y., Lv, Z., Zhang, Q., Zhao, J., Fang, Z., Gao, Z. and Su, Y., 2023. Comparison Study of Three Camera Calibration Methods Considering the Calibration Board Quality and 3D Measurement Accuracy. *Experimental Mechanics*, *63*(2), pp.289-307.

Liu, Y., Tian, C. and Huang, Y., 2016. Critical Assessment of Correction Methods for FishEye lens Distortion. *International Archives of the Photogrammetry, Remote Sensing & Spatial Information Sciences*, *41*.

Liu, Z., Wu, Q., Wu, S. and Pan, X., 2017. Flexible and accurate camera calibration using grid spherical images. *Optics express*, *25*(13), pp.15269-15285.

Lopez, M., Mari, R., Gargallo, P., Kuang, Y., Gonzalez-Jimenez, J. and Haro, G., 2019. Deep single image camera calibration with radial distortion. In Proceedings of the IEEE Conference on Computer Vision and Pattern Recognition (pp. 11817-11825).

Lowe, D.G., 1987. Three-dimensional object recognition from single two-dimensional images. *Artificial intelligence*, *31*(3), pp.355-395.

Luhmann, T., Fraser, C. and Maas, H.G., 2016. Sensor modelling and camera calibration for close-range photogrammetry. *ISPRS Journal of Photogrammetry and Remote Sensing*, *115*, pp.37-46.

Lü, X., Meng, L., Long, L. and Wang, P., 2022. Comprehensive improvement of camera calibration based on mutation particle swarm optimization. *Measurement*, 187, p.110303.

Lu, X.X., 2018, September. A review of solutions for perspective-n-point problem in camera pose estimation. In *Journal of Physics: Conference Series* (Vol. 1087, No. 5, p. 052009). IOP Publishing.

Lu, Z. and Cai, L., 2020. Camera calibration method with focus-related intrinsic parameters based on the thin-lens model. *Optics Express*, *28*(14), pp.20858-20878.

Madeira S, Gonçalves JA and Bastos L, 2009. "Fast Camera Calibration for Low Cost Mobile Mapping", *the sixth International Symposium on Mobile Mapping Technology* - MMT09, Presidente Prudente, Brasil.

Ma, Z., Zhong, X., Xie, H., Zhou, Y., Chen, Y. and Wang, J., 2023. A Combined Physical and Mathematical Calibration Method for Low-Cost Cameras in the Air and Underwater Environment. *Sensors*, 23(4), p.2041.

Ma, L., Chen Y.Q. and Moore K.L. 2003., A new analytical radial distortion model for camera calibration. http://arxiv.org/pdf/cs/0307046.pdf, 2003.

Miyata, S., Saito, H., Takahashi, K., Mikami, D., Isogawa, M. and Kojima, A., 2017. Extrinsic camera calibration without visible corresponding points using omnidirectional cameras. *IEEE Transactions on Circuits and Systems for Video Technology*, 28(9), pp.2210-2219.

Mokhtar, M.R.M., Wahab, S.N.A., Husain, M.N. and Hashim, H., 2021. LANDSLIDE MONITORING USING CLOSE RANGE PHOTOGRAMMETRY. *PLANNING MALAYSIA*, *19*.

Moravec, J., 2020. A polynomial-division based correction model for camera calibration: a large comparative study. *Sādhanā*, *45*(1), pp.1-17.

Moru, D.K. and Borro, D., 2020. A machine vision algorithm for quality control inspection of gears. *The International Journal of Advanced Manufacturing Technology*, *106*(1), pp.105-123.

Narazaki, Y., Gomez, F., Hoskere, V., Smith, M.D. and Spencer, B.F., 2021. Efficient development of vision-based dense three-dimensional displacement measurement algorithms using physics-based graphics models. *Structural Health Monitoring*, *20*(4), pp.1841-1863.

Nave, T. and Francos, J.M., 2008, December. Global featureless estimation of radial distortions. In *2008 2nd International Conference on Signal Processing and Communication Systems* (pp. 1-11). IEEE.

Nocerino, E., Menna, F. and Grün, A., 2021. Bundle adjustment with polynomial point-to-camera distance dependent corrections for underwater photogrammetry. *International Archives of the Photogrammetry, Remote Sensing and Spatial Information Sciences-ISPRS Archives*, *43*(B2-2021), pp.673-679.

Olague, G. and Dunn, E., 2007. Development of a practical photogrammetric network design using evolutionary computing. *The Photogrammetric Record*, 22(117), pp.22-38.

Oniga, V.E. and Oniga, M.B., 2015. Testing the accuracy of different calibration methods. *J. Geod. Cartogr. Cadastre*, 2, pp.8-17.

Paiz-Reyes, E., Brédif, M. and Christophe, S., 2020. Geometric Distortion of Historical Images for 3d Visualization. *ISPRS Annals of the Photogrammetry, Remote Sensing and Spatial Information Sciences*.

Pan, J., Appia, V. and Bovik, A.C., 2016, March. Virtual top-view camera calibration for accurate object representation. In *2016 IEEE Southwest Symposium on Image Analysis and Interpretation (SSIAI)* (pp. 21-24). IEEE.

Pan, L., Pollefeys, M. and Larsson, V., 2022. Camera pose estimation using implicit distortion models. *In Proceedings of the IEEE/CVF Conference on Computer Vision and Pattern Recognition* (pp. 12819-12828).

Park, J., Bhat, P.C. and Kak, A.C., 2006, October. A look-up table-based approach for solving the camera selection problem in large camera networks. In *Proceedings of the International Workshop on Distributed Smart Cameras (DCS'06)* (pp. 72-76).

Park, S.W. and Hong, K.S., 2001. Practical ways to calculate camera lens distortion for real-time camera calibration. *Pattern Recognition*, *34*(6), pp.1199-1206.

Perez, A.J., Perez-Cortes, J.C. and Guardiola, J.L., 2020. Simple and precise multi-view camera calibration for 3D reconstruction. *Computers in Industry*, 123, p.103256.

Pierré, J.E., Passieux, J.C., Périé, J.N., Bugarin, F. and Robert, L., 2016. Unstructured finite element-based digital image correlation with enhanced management of quadrature and lens distortions. *Optics and Lasers in Engineering*, *77*, pp.44-53.

Poulin-Girard, A.S., Thibault, S. and Laurendeau, D., 2016. Influence of camera calibration conditions on the accuracy of 3D reconstruction. *Optics express*, *24*(3), pp.2678-2686.

Przybilla, H.J., Bäumker, M., Luhmann, T., Hastedt, H. and Eilers, M., 2020. Interaction between direct georeferencing, control point configuration and camera self-calibration for RTK-based UAV photogrammetry. The *International Archives of the Photogrammetry, Remote Sensing and Spatial Information Sciences*, 43, pp.485-492.

Rodehorst, V., Heinrichs, M. and Hellwich, O., 2008. Evaluation of relative pose estimation methods for multi-camera setups. *International Archives of Photogrammetry and Remote Sensing* (ISPRS'08), pp.135-140.

Syafiq, M., Rau, J.Y. and Jhan, J.P., 2022. 3D indoor corridor mapping with calibrated rops of multi-Fisheye camera-rig. *The International Archives of the Photogrammetry, Remote Sensing and Spatial Information Sciences*, 48, pp.237-242.

Qi, W., Li, F. and Zhenzhong, L., 2010, May. Review on camera calibration. In *2010 Chinese control and decision conference* (pp. 3354-3358). IEEE.

Rabin, J., Delon, J., Gousseau, Y. and Moisan, L., 2010. MAC-RANSAC: a robust algorithm for the recognition of multiple objects. In *Fifth International Symposium on 3D Data Processing, Visualization and Transmission (3DPTV 2010)* (p. 051).

Ramírez-Hernández, L.R., Rodríguez-Quiñonez, J.C., Castro-Toscano, M.J., Hernández-Balbuena, D., Flores-Fuentes, W., Rascón-Carmona, R., Lindner, L. and Sergiyenko, O., 2020. Improve three-dimensional point localization accuracy in stereo vision systems using a novel camera calibration method. *International Journal of Advanced Robotic Systems*, *17*(1), p.1729881419896717.

Rojtberg, P. and Kuijper, A., 2018, October. Efficient pose selection for interactive camera calibration. In 2018 IEEE International Symposium on Mixed and Augmented Reality (ISMAR) (pp. 31-36). IEEE.

Remondino, F., Nocerino, E., Toschi, I. and Menna, F., 2017. A critical review of automated photogrammetric processing of large datasets. *The International Archives of Photogrammetry, Remote Sensing and Spatial Information Sciences*, *42*, pp.591-599.

Ruszczynski, A., 2011. *Nonlinear optimization*. Princeton university press.

Ryberg, A., Lennartson, B., Christiansson, A.K., Ericsson, M. and Asplund, L., 2011. Analysis and evaluation of a general camera model. *Computer Vision and Image Understanding*, *115*(11), pp.1503-1515.

Santana-Cedrés, D., Gomez, L., Aleman-Flores, M., Salgado, A., Esclarín, J., Mazorra, L. and Alvarez, L., 2017. Estimation of the lens distortion model by minimizing a line reprojection error. *IEEE Sensors Journal*, *17*(9), pp.2848-2855.

Santana-Cedrés, D., Gomez, L., Alemán-Flores, M., Salgado, A., Esclarín, J., Mazorra, L. and Alvarez, L., 2016. An iterative optimization algorithm for lens distortion correction using two-parameter models. *Image Processing On Line*, *6*, pp.326-364.

Sanz-Ablanedo E, Rodríguez-Pérez JR, Armesto J, Taboada M.Á, 2010, "Geometric stability and lens decentring in compact digital cameras", *Sensor 10: 1553–1572*.

Sapirstein, P., 2018. A high-precision photogrammetric recording system for small artifacts. *Journal of Cultural Heritage*, 31, pp.33-45.

Sasián, J., 2019. Introduction to lens design. Cambridge University Press**.**

Schmalz, C., Forster, F. and Angelopoulou, E., 2011. Camera calibration: active versus passive targets. *Optical Engineering*, 50(11), pp.113601-113601.

Schramm, S., Ebert, J., Rangel, J., Schmoll, R. and Kroll, A., 2021. Iterative feature detection of a coded checkerboard target for the geometric calibration of infrared cameras. *Journal of Sensors and Sensor Systems*, *10*(2), pp.207-218.

Seedahmed, G.H. and Habib, A.F., 2006. Linear recovery of the exterior orientation parameters in a planar object space. International archives of Photogrammetry Remote sensing and Spatial information sciences, 34(3/B), pp.245-248.

Semeniuta, O., 2016. Analysis of camera calibration with respect to measurement accuracy. *Procedia Cirp*, *41*, pp.765-770.

Sels, S., Ribbens, B., Vanlanduit, S. and Penne, R., 2019. Camera calibration using gray code. *Sensors*, *19*(2), p.246.

Shih, M.H. and Tung, S.H., 2017. A method for correcting radial distortion based on verifying the planarity of specimens. *Sadhana* 42, Issue 11, pp. 1943-1952, November 2017.

Shi, Y., Zhang, D., Wen, J., Tong, X., Ying, X. and Zha, H., 2018, August. Radial lens distortion correction by adding a weight layer with inverted foveal models to convolutional neural networks. In *2018 24th International Conference on Pattern Recognition (ICPR)* (pp. 1-6). IEEE.

Sims-Waterhouse, D., Isa, M., Piano, S. and Leach, R., 2020. Uncertainty model for a traceable stereo-photogrammetry system. *Precision engineering*, *63*, pp.1-9.

Stankiewicz, O., Lafruit, G. and Domański, M., 2018. Multiview video: Acquisition, processing, compression, and virtual view rendering. In *Academic Press Library in Signal Processing, Volume 6* (pp. 3-74). Academic Press.

Stapleton, M.P. and Bajic, I.V., 2016, December. Robust domain-filling plumb-line lens distortion correction. In *2016 IEEE International Symposium on Multimedia (ISM)* (pp. 507-514). IEEE.

Stehel, S., Vertal', P. and Demčáková, L., 2021. Application of close-range photogrammetry in documenting the location of an accident. *Transportation research procedia*, *55*, pp.1657-1664.

Strand, R. and Hayman, E., 2005, September. Correcting Radial Distortion by Circle Fitting. In *BMVC*.

Sun, Q., Wang, X., Xu, J., Wang, L., Zhang, H., Yu, J., Su, T. and Zhang, X., 2016. Camera self-calibration with lens distortion. *Optik*, *127*(10), pp.4506-4513.

Swaminathan R and Nayar SK, 2000. "Nonmetric calibration of wide-angle lenses and polycameras" *PAMI*, 22(10):1172–1178.

Tanackov, I., Pavkov, I. and Stević, Ž., 2020. The New New-Nacci Method for Calculating the Roots of a Univariate Polynomial and Solution of Quintic Equation in Radicals. *Mathematics*, *8*(5), p.746.

Tang, L., Wang, Y., Yu, H. and Zhu, J., 2017. Automatic camera calibration using active displays of a virtual pattern. *Sensors*, *17*(4), p.685.

Tang, S., Dong, Z., Feng, W., Li, Q. and Nie, L., 2021, February. Fast and Accuracy Camera Calibration Based on Tsai Two-Step Method. *In 2021 7th International Conference on Mechatronics and Robotics Engineering* (ICMRE) (pp. 190-194). IEEE.

Tang, Z., Lin, Y.S., Lee, K.H., Hwang, J.N. and Chuang, J.H., 2019. ESTHER: Joint camera self-calibration and automatic radial distortion correction from tracking of walking humans. *IEEE Access*, *7*, pp.10754-10766.

Tang, Z., von Gioi, R.G., Monasse, P. and Morel, J.M., 2017. A precision analysis of camera distortion models. *IEEE Transactions on Image Processing*, *26*(6), pp.2694-2704.

Tardif JP and Sturm P, 2006, "Self-Calibration of a General Radially Symmetric Distortion Model," *Proc. Ninth European Conf. Computer Vision*, 2006.

Thall, E.H., 2018. Wavefront Optics and Aberrations of the Eye. *Ophthalmology E-Book*, p.67.

Tjahjadi, M.E., Handoko, F. and Sai, S.S., 2017. Novel image mosaicking of UAV's imagery using collinearity condition. *International Journal of Electrical and Computer Engineering (IJECE)*, *7*(3), pp.1188-1196.

Tjahjadi, M.E., Sai, S.S. and Handoko, F., 2019. Assessing a 35mm Fixed-Lens Sony Alpha-5100 Intrinsic Parameters Prior to, During, and Post UAV Flight Mission. *KnE Engineering*, pp.372-383.

Tsai R. Y., 1987. "A Versatile Camera Calibration Technique for High- Accuracy 3D Machine Vision Metrology Using Off-the-Shelf TV Cameras and Lenses,'' *IEEE Journal of Robotics and Automation*, Vol. RA–3, No. 4, August 1987, pp. 323–344.

Usamentiaga, R. and García, D.F., 2019. Multi-camera calibration for accurate geometric measurements in industrial environments. *Measurement*, *134*, pp.345-358.

Uygur, S.Ö., Aydin, C. and Akyilmaz, O., 2020. Retrieval of Euler rotation angles from 3D similarity transformation based on quaternions. *Journal of Spatial Science*, pp.1-18.

Vakhitov, A., Funke, J. and Moreno-Noguer, F., 2016, October. Accurate and linear time pose estimation from points and lines. In *European Conference on Computer Vision* (pp. 583-599). Springer, Cham.

Vera, P., Icasio-Hernández, O. and Salas, J., 2020. Determination of the Center of Radial Distortion for a Camera Lens. *IEEE Transactions on Instrumentation and Measurement*, *69*(9), pp.7015-7027.

Vieira, L.H., Pagnoca, E.A., Milioni, F., Barbieri, R.A., Menezes, R.P., Alvarez, L., Déniz, L.G., Santana-Cedrés, D. and Santiago, P.R., 2017. Tracking futsal players with a wide-angle lens camera: accuracy analysis of the radial distortion correction based on an improved Hough transform algorithm. *Computer Methods in Biomechanics and Biomedical Engineering: Imaging & Visualization*, 5(3), pp.221-231.

Vladimirov, A. and Koceski, S., 2019. Attitude Determination of Unmanned Aerial Vehicle using Single Camera Vector Observations. *International Journal of Computer Applications*, *178*(41), pp.15-21.

Wackrow R and Chandler, JH. 2008. A convergent image configuration for DEM extraction that minimizes the systematic effects caused by an inaccurate lens model. *Photogrammetric Record*, 23(121): 6–18.

Wang, Y., Jiang, W., Huang, K., Schwertfeger, S. and Kneip, L., 2022, May. Accurate calibration of multi-perspective cameras from a generalization of the hand-eye constraint. In 2022 *International Conference on Robotics and Automation* (ICRA) (pp. 1244-1250). IEEE.

Wang, Y., Yuan, F., Jiang, H. and Hu, Y., 2016. Novel camera calibration based on cooperative target in attitude measurement. *Optik*, *127*(22), pp.10457-10466.

Wang, Y., Qiu, J., Liu, C., He, D., Kang, X., Li, J. and Shi, L., 2018. Virtual image points based geometrical parameters' calibration for focused light field camera. *IEEE Access*, *6*, pp.71317-71326.

Wang, X., Zhang, H. and Liu, S., 2013. Reliable ransac using a novel preprocessing model. *Computational and mathematical methods in medicine*, *2013*.

Wegman, E.J. and Said, Y.H., 2010. Natural homogeneous coordinates. *Wiley Interdisciplinary Reviews: Computational Statistics*, *2*(6), pp.678-685.

Weng, J., Zhou, W., Ma, S., Qi, P. and Zhong, J., 2021. Model-Free Lens Distortion Correction Based on Phase Analysis of Fringe-Patterns. *Sensors*, *21*(1), p.209.

Wierzbicki, D., 2018. Calibration low-cost cameras with wide-angle lenses for measurements. *Journal of Automation Mobile Robotics and Intelligent Systems*, *12*.

Wierzbicki, D., 2018. Multi-camera imaging system for UAV photogrammetry. *Sensors*, *18*(8), p.2433.

Wu, F., Wei, H. and Wang, X., 2017. Correction of image radial distortion based on division model. Optical Engineering, 56(1), p.013108.

Xiao, D., Li, J. and Li, K., 2019. Robust precise dynamic point reconstruction from multi-view. *IEEE Access*, 7, pp.22408-22420.

Xing, S. and Guo, H., 2020. Iterative calibration method for measurement system having lens distortions in fringe projection profilometry. *Optics express*, *28*(2), pp.1177-1196.

Xu, D., Chen, L., Mou, X., Wu, Q. and Sun, G., 2021, May. 3D Reconstruction of Camellia Oleifera Fruit Recognition and Fruit Branch based on Kinect Camera. In *2021 2nd International Conference on Artificial Intelligence and Information Systems* (pp. 1-6).

Xu, Y., Gao, F., Ren, H., Zhang, Z. and Jiang, X., 2017. An iterative distortion compensation algorithm for camera calibration based on phase target. *Sensors*, *17*(6), p.1188.

Xu, W., Hu, L., Tsakiris, M.C. and Kneip, L., 2019, September. Online stability improvement of Gröbner basis solvers using deep learning. In *2019 International Conference on 3D Vision (3DV)* (pp. 544-552). IEEE.

Yan, K., Tian, H., Liu, E., Zhao, R., Hong, Y. and Zuo, D., 2016. A decoupled calibration method for camera intrinsic parameters and distortion coefficients. *Mathematical Problems in Engineering*, *2016*.

Yuan, G., Zheng, L., Ding, Y., Zhang, H., Zhang, X., Liu, X. and Sun, J., 2021. A precise calibration method for line scan cameras. *IEEE Transactions on Instrumentation and Measurement*, 70, pp.1-9.

Zahneisen, B. and Ernst, T., 2016. Homogeneous coordinates in motion correction. *Magnetic resonance in medicine*, 75(1), pp.274-279.
Zhang, J., Yu, H., Deng, H., Chai, Z., Ma, M. and Zhong, X., 2018. A robust and rapid camera calibration method by one captured image. IEEE Transactions on Instrumentation and Measurement, 68(10), pp.4112-4121.
Zhang, L., Shang, H., Wu, F., Wang, R., Sun, T. and Xie, J., 2019. Robust Line-Based Radial Distortion Estimation from a Single Image. *IEEE Access*, *7*, pp.180373-180382.
Zhang, J., Zhu, J., Deng, H., Chai, Z., Ma, M. and Zhong, X., 2019. Multi-camera calibration method based on a multi-plane stereo target. *Applied optics*, 58(34), pp.9353-9359.
Zhao, Z., Zhu, Y., Li, Y., Qiu, Z., Luo, Y., Xie, C. and Zhang, Z., 2020. Multi-camera-based universal measurement method for 6-DOF of rigid bodies in world coordinate system. *Sensors*, *20*(19), p.5547.
Zheng, M., Wang, S., Xiong, X. and Zhu, J., 2020. A fast and accurate iterative method for the camera pose estimation problem. *Image and Vision Computing*, 94, p.103860.
Zhu, Y., Li, C. and Zhang, Y., 2020, May. Online camera-lidar calibration with sensor semantic information. In *2020 IEEE International Conference on Robotics and Automation (ICRA)* (pp. 4970-4976). IEEE.
Zhu, Y., Wu, Y., Zhang, Y. and Qu, F., 2021, December. Multi-camera System Calibration of Indoor Mobile Robot Based on SLAM. *In 2021 3rd International Conference on Machine Learning, Big Data and Business Intelligence* (MLBDBI) (pp. 240-244). IEEE.
Zhu, Z., Wang, X., Liu, Q. and Zhang, F., 2019. Camera calibration method based on optimal polarization angle. *Optics and Lasers in Engineering*, *112*, pp.128-135.
Zwillinger, D. and Dobrushkin, V., 2021. Handbook of differential equations. *CRC Press*.

APPENDICES

Appendix A: MATLAB calibration algorithm to retrieve the coefficients of radial distortions needed to test the newly developed inverse polynomial models.

```
RADIAL DISTORTION COEFFICIENTS RETRIVAL MATLAB SCRIPT AND CALIBRATION
                    RESULTS SUMMARY-PHD GB IKOKOU


% Auto-generated by cameraCalibrator app on 12-Jan-2023
%-------------------------------------------------------

% Define images to process
imageFileNames = {'F:\CAMERA CALIBRATION GROUP IMAGES PhD
ResearchGBIKOKOU\PhD Calibration ImagesGBIKOKOU\IMG-20231102-WA0062.jpg',...
    'F:\CAMERA CALIBRATION GROUP IMAGES PhD ResearchGBIKOKOU\PhD Calibration
ImagesGBIKOKOU\IMG-20231102-WA0063.jpg',...
    'F:\CAMERA CALIBRATION GROUP IMAGES PhD ResearchGBIKOKOU\PhD Calibration
ImagesGBIKOKOU\IMG-20231102-WA0064.jpg',...
```

```
    'F:\CAMERA CALIBRATION GROUP IMAGES PhD ResearchGBIKOKOU\PhD Calibration
ImagesGBIKOKOU\IMG-20231102-WA0065.jpg',...
    'F:\CAMERA CALIBRATION GROUP IMAGES PhD ResearchGBIKOKOU\PhD Calibration
ImagesGBIKOKOU\IMG-20231102-WA0066.jpg',...
    'F:\CAMERA CALIBRATION GROUP IMAGES PhD ResearchGBIKOKOU\PhD Calibration
ImagesGBIKOKOU\IMG-20231102-WA0067.jpg',...
    'F:\CAMERA CALIBRATION GROUP IMAGES PhD ResearchGBIKOKOU\PhD Calibration
ImagesGBIKOKOU\IMG-20231102-WA0068.jpg',...
    'F:\CAMERA CALIBRATION GROUP IMAGES PhD ResearchGBIKOKOU\PhD Calibration
ImagesGBIKOKOU\IMG-20231102-WA0069.jpg',...
    'F:\CAMERA CALIBRATION GROUP IMAGES PhD ResearchGBIKOKOU\PhD Calibration
ImagesGBIKOKOU\IMG-20231102-WA0070.jpg',...
    'F:\CAMERA CALIBRATION GROUP IMAGES PhD ResearchGBIKOKOU\PhD Calibration
ImagesGBIKOKOU\IMG-20231102-WA0071.jpg',...
    'F:\CAMERA CALIBRATION GROUP IMAGES PhD ResearchGBIKOKOU\PhD Calibration
ImagesGBIKOKOU\IMG-20231102-WA0072.jpg',...
    'F:\CAMERA CALIBRATION GROUP IMAGES PhD ResearchGBIKOKOU\PhD Calibration
ImagesGBIKOKOU\IMG-20231102-WA0073.jpg',...
    'F:\CAMERA CALIBRATION GROUP IMAGES PhD ResearchGBIKOKOU\PhD Calibration
ImagesGBIKOKOU\IMG-20231102-WA0074.jpg',...
    'F:\CAMERA CALIBRATION GROUP IMAGES PhD ResearchGBIKOKOU\PhD Calibration
ImagesGBIKOKOU\IMG-20231102-WA0075.jpg',...
    'F:\CAMERA CALIBRATION GROUP IMAGES PhD ResearchGBIKOKOU\PhD Calibration
ImagesGBIKOKOU\IMG-20231102-WA0076.jpg',...
    'F:\CAMERA CALIBRATION GROUP IMAGES PhD ResearchGBIKOKOU\PhD Calibration
ImagesGBIKOKOU\IMG-20231102-WA0077.jpg',...
    'F:\CAMERA CALIBRATION GROUP IMAGES PhD ResearchGBIKOKOU\PhD Calibration
ImagesGBIKOKOU\IMG-20231102-WA0078.jpg',...
    'F:\CAMERA CALIBRATION GROUP IMAGES PhD ResearchGBIKOKOU\PhD Calibration
ImagesGBIKOKOU\IMG-20231102-WA0079.jpg',...
    'F:\CAMERA CALIBRATION GROUP IMAGES PhD ResearchGBIKOKOU\PhD Calibration
ImagesGBIKOKOU\IMG-20231102-WA0080.jpg',...
    'F:\CAMERA CALIBRATION GROUP IMAGES PhD ResearchGBIKOKOU\PhD Calibration
ImagesGBIKOKOU\IMG-20231102-WA0082.jpg',...
    'F:\CAMERA CALIBRATION GROUP IMAGES PhD ResearchGBIKOKOU\PhD Calibration
ImagesGBIKOKOU\IMG-20231102-WA0083.jpg',...
    'F:\CAMERA CALIBRATION GROUP IMAGES PhD ResearchGBIKOKOU\PhD Calibration
ImagesGBIKOKOU\IMG-20231102-WA0084.jpg',...
    'F:\CAMERA CALIBRATION GROUP IMAGES PhD ResearchGBIKOKOU\PhD Calibration
ImagesGBIKOKOU\IMG-20231102-WA0085.jpg',...
    };
% Detect checkerboards in images
[imagePoints, boardSize, imagesUsed] =
detectCheckerboardPoints(imageFileNames);
imageFileNames = imageFileNames(imagesUsed);

% Read the first image to obtain image size
originalImage = imread(imageFileNames{1});
[mrows, ncols, ~] = size(originalImage);

% Generate world coordinates of the corners of the squares
squareSize = 30;  % in units of 'millimeters'
worldPoints = generateCheckerboardPoints(boardSize, squareSize);

% Calibrate the camera
[cameraParams, imagesUsed, estimationErrors] =
estimateCameraParameters(imagePoints, worldPoints, ...
    'EstimateSkew', false, 'EstimateTangentialDistortion', false, ...
    'NumRadialDistortionCoefficients', 3, 'WorldUnits', 'millimeters', ...
    'InitialIntrinsicMatrix', [], 'InitialRadialDistortion', [], ...
    'ImageSize', [mrows, ncols]);
```

```
% View reprojection errors
h1=figure; showReprojectionErrors(cameraParams);

% Visualize pattern locations
h2=figure; showExtrinsics(cameraParams, 'CameraCentric');

% Display parameter estimation errors
displayErrors(estimationErrors, cameraParams);

% Use the calibration data to remove effects of lens distortion.
undistortedImage = undistortImage(originalImage, cameraParams);
```

.....END.....

SUMMARY OF CAMERA CALIBRATION RESULTS

Using "C:\Users\ikokougb\Documents\MATLAB" as the initial working folder.

>> CameraCalibrationScriptPhDGBIKOKOU

Intrinsic

Focal length (pixels): [0.7553764 +/- 0.026228 0.7541377 +/- 0.026679]

Principal point (pixels): [0.4953959 +/- 0.04847 0.3668464 +/- 0.06360]

Radial distortion: [0.00138 +/- 0.0070 -0.000000869 +/- 0.000000451 0.0000000000652+/- 0.0000000000867]

Extrinsic

Rotation vectors:

[0.1132 +/- 0.0013 -0.0360 +/- 0.0018 -3.1107 +/- 0.0002]

[-0.1634 +/- 0.0014 -0.8213 +/- 0.0020 3.0003 +/- 0.0006]

[0.0667 +/- 0.0012 0.3214 +/- 0.0019 -3.1125 +/- 0.0003]

[0.0862 +/- 0.0013 0.2986 +/- 0.0019 -3.0982 +/- 0.0003]

[0.0516 +/- 0.0012 0.2690 +/- 0.0019 -3.1202 +/- 0.0003]

[0.0446 +/- 0.0013 0.2713 +/- 0.0019 -3.1202 +/- 0.0003]

[0.0464 +/- 0.0013 0.2690 +/- 0.0019 -3.1226 +/- 0.0003]

[0.0652 +/- 0.0013 0.2706 +/- 0.0019 -3.1139 +/- 0.0003]

[0.0651 +/- 0.0013 0.2710 +/- 0.0019 -3.1152 +/- 0.0003]

[-0.1094 +/- 0.0013 -0.5191 +/- 0.0020 3.0642 +/- 0.0004]

[0.0562 +/- 0.0012 0.2752 +/- 0.0019 -3.1176 +/- 0.0003]

[0.0665 +/- 0.0012 0.3415 +/- 0.0019 -3.1053 +/- 0.0003]

[0.0611 +/- 0.0012 0.3592 +/- 0.0019 -3.1056 +/- 0.0003]

[0.1534 +/- 0.0023 -0.1151 +/- 0.0031 -3.1257 +/- 0.0003]

[0.1455 +/- 0.0024 0.3379 +/- 0.0035 -3.1026 +/- 0.0005]

[0.1143 +/- 0.0017 -0.3539 +/- 0.0023 -3.0954 +/- 0.0004]

[0.1771 +/- 0.0021 0.1536 +/- 0.0028 -3.1256 +/- 0.0003]

[0.1158 +/- 0.0024 -0.0257 +/- 0.0032 -3.1182 +/- 0.0003]

[-0.1564 +/- 0.0023 -0.4074 +/- 0.0032 3.1043 +/- 0.0005]

[0.1397 +/- 0.0016 0.3193 +/- 0.0024 -3.0988 +/- 0.0004]

[0.1539 +/- 0.0014 -0.1860 +/- 0.0020 -3.1167 +/- 0.0003]

[0.1196 +/- 0.0013 -0.0607 +/- 0.0018 -3.1006 +/- 0.0002]

[0.2071 +/- 0.0015 -0.1201 +/- 0.0019 -3.1191 +/- 0.0003]

Translation vectors (millimetres):

[132.2749 +/- 0.1752 91.6861 +/- 0.2349 281.5331 +/- 0.9892]

[133.0259 +/- 0.2148 39.8301 +/- 0.3053 356.2257 +/- 1.1295]

[133.2347 +/- 0.1774 78.9328 +/- 0.2379 292.4460 +/- 1.0233]

[139.6565 +/- 0.1801 81.9356 +/- 0.2412 296.6651 +/- 1.0387]

[132.8862 +/- 0.1759 80.2147 +/- 0.2339 287.8307 +/- 1.0117]

[133.0128 +/- 0.1785 81.2738 +/- 0.2372 291.7321 +/- 1.0255]

[131.9635 +/- 0.1773 81.1062 +/- 0.2355 289.7891 +/- 1.0188]

[133.6706 +/- 0.1783 81.8254 +/- 0.2375 292.2180 +/- 1.0263]

[133.9537 +/- 0.1776 80.6123 +/- 0.2366 291.1288 +/- 1.0225]

[154.0757 +/- 0.1969 83.9159 +/- 0.2691 324.6386 +/- 1.1051]

[131.8717 +/- 0.1765 80.9876 +/- 0.2349 289.1570 +/- 1.0157]

[130.7405 +/- 0.1724 79.5528 +/- 0.2318 285.1445 +/- 0.9958]

[130.3666 +/- 0.1747 81.1073 +/- 0.2354 289.1948 +/- 1.0084]

[135.9711 +/- 0.2356 71.1548 +/- 0.3175 376.7372 +/- 1.3193]

[128.4251 +/- 0.2511 29.8679 +/- 0.3408 408.8438 +/- 1.4284]

[132.6363 +/- 0.2031 76.5244 +/- 0.2766 318.5996 +/- 1.1289]

```
[143.5008 +/- 0.2312    69.2159 +/- 0.3093    376.4097 +/- 1.3157]
[154.5048 +/- 0.2450    80.1726 +/- 0.3277    392.0483 +/- 1.3768]
[142.7644 +/- 0.2572    39.7112 +/- 0.3494    418.8171 +/- 1.4443]
[124.9555 +/- 0.2084    71.5925 +/- 0.2800    341.6516 +/- 1.1884]
[135.0102 +/- 0.1779    90.9488 +/- 0.2435    285.7873 +/- 1.0014]
[123.6597 +/- 0.1713    86.6945 +/- 0.2299    274.3905 +/- 0.9625]
[130.9806 +/- 0.1822    79.9885 +/- 0.2476    296.1981 +/- 1.0336]
>> CameraCalibrationScriptPhDGBIKOKOU
                    Standard Errors of Estimated Camera Parameters
                    ----------------------------------------
CameraParams =
  CameraParameters with properties:
   Camera Intrinsics
              IntrinsicMatrix: [3×3 double]
                FocalLength: [0.7553764  0.7541377]
               Principal Point: [0.4953959  0.3668464]
                     Skew: 0
            RadialDistortion: [0.00138 -0.000000869  0.0000000000652]
         TangentialDistortion: [0 0]
   Camera Extrinsics
             RotationMatrices: [3×3×23 double]
           TranslationVectors: [23×3 double]
   Accuracy of Estimation
         MeanReprojectionError: 0.4624
           ReprojectionErrors: [54×2×23 double]
            ReprojectedPoints: [54×2×23 double]
   Calibration Settings
               NumPatterns: 23
               WorldPoints: [54×2 double]
                WorldUnits: 'millimeters'
              EstimateSkew: 0
```

NumRadialDistortionCoefficients: 3

EstimateTangentialDistortion: 0

%END%

Appendix B: Developed Python codes for the calibration of parameters of camera internal geometry and parameters of camera location and orientation in a 3D scene.

```
#Compute the twelve coefficients of the projective transformation matrix needed
for the estimation of camera parameters.

import numpy as np

def compute_transformation_matrix_3d_to_2d(X, Y):
    """
    Compute the linear transformation matrix from 3D points to 2D points.

    Args:
        X (numpy.ndarray): 6x3 matrix of 3D points.
        Y (numpy.ndarray): 6x2 matrix of 2D points.
```

```
    Returns:
        numpy.ndarray: 3x4 linear transformation matrix.
    """
    # Number of points
    n = X.shape[0]

    # Create the matrix A and vector b for the system of equations Ax = b
    A = []
    b = []

    for i in range(n):
        X1, Y1, Z1 = X[i]
        x1, y1 = Y[i]

        # Two rows for each correspondence
        A.append([X1, Y1, Z1, 1, 0, 0, 0, 0, -x1*X1, -x1*Y1, -x1*Z1])
        A.append([0, 0, 0, 0, X1, Y1, Z1, 1, -y1*X1, -y1*Y1, -y1*Z1])

        b.append(x1)
        b.append(y1)

    A = np.array(A)
    b = np.array(b)

    # Solve the system A * coeffs = b
    coeffs = np.linalg.lstsq(A, b, rcond=None)[0]

    # Reshape the coefficients into a 3x4 matrix (linear transformation matrix)
    transformation_matrix = np.zeros((3, 4))
    transformation_matrix[0, :] = coeffs[0:4]
    transformation_matrix[1, :] = coeffs[4:8]
    transformation_matrix[2, :] = coeffs[8:12]

    return transformation_matrix

# Given 3D points (X1, Y1, Z1) and 2D points (x1, y1)
X = np.array([
    [21.5, 21.5, 43],
    [107.5, 21.5, 57],
    [278.5, 21.5, 91],
    [21.5, 109.5, 72],
    [15.5, 64.5, 60],
    [151.5, 21.5, 4]
])

Y = np.array([
    [10, 82],
    [10, 61],
```

```
    [10, 22],
    [30, 82],
    [20, 50],
    [10, 51]
])

# Compute the transformation matrix
transformation_matrix = compute_transformation_matrix_3d_to_2d(X, Y)

# Print the transformation matrix
print("Linear Transformation Matrix (3D to 2D):")
print(transformation_matrix)


# Compute the two coordinates of the principal point and the two effective
focal lengths using the newly developed analytical algorithms.

import math

# Given coefficients of the projective transformation matrix H
H = {
    'H1': 0.000413434,
    'H2': 0.228596,
    'H3': -0.000592921,
    'H4': 5.07553,
    'H5': -0.2384,
    'H6': -0.005820258,
    'H7': 0.0096542,
    'H8': 86.5516,
    'H9': 0.000001654,
    'H10': 0.000003326,
    'H11': -0.000006993,
    'H12': 1
}

# Denominator common term (H9^2 + H10^2 + H11^2)
denominator = H['H9']**2 + H['H10']**2 + H['H11']**2

# Compute principal point (U_o, V_o)
U_o = (H['H1'] * H['H9'] + H['H2'] * H['H10'] + H['H3'] * H['H11']) /
denominator
V_o = (H['H6'] * H['H10'] + H['H7'] * H['H11'] + H['H5'] * H['H9']) /
denominator

# Compute focal lengths (f_x, f_y)
f_x = math.sqrt((H['H3'] * H['H10'] - H['H2'] * H['H11'])**2 +
                (H['H1'] * H['H11'] - H['H3'] * H['H9'])**2 +
                (H['H2'] * H['H9'] - H['H1'] * H['H10'])**2) / denominator
```

```
f_y = math.sqrt((H['H6'] * H['H11'] - H['H7'] * H['H10'])**2 +
                (H['H7'] * H['H9'] - H['H5'] * H['H11'])**2 +
                (H['H5'] * H['H10'] - H['H6'] * H['H9'])**2) / denominator

# Print the results
print(f"Principal point (U_o, V_o): ({U_o:.6f}, {V_o:.6f})")
print(f"Focal lengths (f_x, f_y): ({f_x:.6f}, {f_y:.6f})")



#Compute the three coefficients of the translation vector using the newly
developed analytical algorithms.

import math

# Given coefficients of the projective transformation matrix H
H = {
    'H1': 0.000413434,
    'H2': 0.228596,
    'H3': -0.000592921,
    'H4': 5.07553,
    'H5': -0.2384,
    'H6': -0.005820258,
    'H7': 0.0096542,
    'H8': 86.5516,
    'H9': 0.000001654,
    'H10': 0.000003326,
    'H11': -0.000006993,
    'H12': 1
}

# Denominator common term (H9^2 + H10^2 + H11^2)
denominator = H['H9']**2 + H['H10']**2 + H['H11']**2

# Compute t_x
numerator_t_x = H['H4'] * denominator - (H['H1'] * H['H9'] + H['H2'] * H['H10']
+ H['H3'] * H['H11'])
factors_t_x = math.sqrt((H['H3'] * H['H10'] - H['H2'] * H['H11'])**2 +
                        (H['H1'] * H['H11'] - H['H3'] * H['H9'])**2 +
                        (H['H2'] * H['H9'] - H['H1'] * H['H10'])**2)
t_x = (numerator_t_x / denominator) * factors_t_x

# Compute t_y
numerator_t_y = H['H8'] * denominator - (H['H6'] * H['H10'] + H['H7'] *
H['H11'] + H['H5'] * H['H9'])
factors_t_y = math.sqrt((H['H6'] * H['H11'] - H['H7'] * H['H10'])**2 +
                        (H['H7'] * H['H9'] - H['H5'] * H['H11'])**2 +
```

```
                        (H['H5'] * H['H10'] - H['H6'] * H['H9'])**2)
t_y = (numerator_t_y / denominator) * factors_t_y

# Compute t_z
t_z = 1 / math.sqrt(denominator)

# Print the results
print(f"Camera Location Parameters:")
print(f"t_x = {t_x:.6f}")
print(f"t_y = {t_y:.6f}")
print(f"t_z = {t_z:.6f}")



#Compute the nine coefficients of the rotation matrix using the developed fully
analytical algorithms.

import math

# Given coefficients of the projective transformation matrix H
H = {
    'H1': 0.000413434,
    'H2': 0.228596,
    'H3': -0.000592921,
    'H4': 5.07553,
    'H5': -0.2384,
    'H6': -0.005820258,
    'H7': 0.0096542,
    'H8': 86.5516,
    'H9': 0.000001654,
    'H10': 0.000003326,
    'H11': -0.000006993,
    'H12': 1
}

# Compute D1 using its formula
D1 = math.sqrt((H['H6'] * H['H11'] - H['H7'] * H['H10'])**2 +
               (H['H7'] * H['H9'] - H['H5'] * H['H11'])**2 +
               (H['H5'] * H['H10'] - H['H6'] * H['H9'])**2)

# Compute D2 using its formula
D2 = math.sqrt((H['H3'] * H['H10'] - H['H2'] * H['H11'])**2 +
               (H['H1'] * H['H11'] - H['H3'] * H['H9'])**2 +
               (H['H2'] * H['H9'] - H['H1'] * H['H10'])**2)

# Compute D3 using its formula
D3 = math.sqrt(H['H9']**2 + H['H10']**2 + H['H11']**2) / (H['H9']**2 +
H['H10']**2 + H['H11']**2)
```

```
# Compute r11, r12, r13
r11 = (H['H7'] * H['H10'] - H['H6'] * H['H11']) / D1
r12 = (H['H5'] * H['H11'] - H['H7'] * H['H9']) / D1
r13 = (H['H6'] * H['H9'] - H['H5'] * H['H10']) / D1

# Compute r21, r22, r23
r21 = (H['H3'] * H['H10'] - H['H2'] * H['H11']) / D2
r22 = (H['H1'] * H['H11'] - H['H3'] * H['H9']) / D2
r23 = (H['H2'] * H['H9'] - H['H1'] * H['H10']) / D2

# Compute r31, r32, r33
r31 = H['H9'] * D3
r32 = H['H10'] * D3
r33 = H['H11'] * D3

# Print the results
print("D1 =", D1)
print("D2 =", D2)
print("D3 =", D3)
print("r11 =", r11)
print("r12 =", r12)
print("r13 =", r13)
print("r21 =", r21)
print("r22 =", r22)
print("r23 =", r23)
print("r31 =", r31)
print("r32 =", r32)
print("r33 =", r33)
```

Appendix C: Linear Least Squares algorithm to recover the radial distortion coefficients needed to test the newly developed inverse distortion polynomials.

The transformation from distortion free coordinates to distorted image coordinates is performed as follows:

$$x_u = x_d\left(1+\kappa_1 r_d^2+\kappa_2 r_d^4+\kappa_3 r_d^6+\kappa_4 r_d^8+\kappa_5 r_d^{10}+\kappa_6 r_d^{12}\right) \quad \textbf{(1)}$$

$$y_u = y_d\left(1+\kappa_1 r_d^2+\kappa_2 r_d^4+\kappa_3 r_d^6+\kappa_4 r_d^8+\kappa_5 r_d^{10}+\kappa_6 r_d^{12}\right) \quad \textbf{(2)}$$

Equations (1) and (2) can be expanded as follows:

$$x_u - x_d = \kappa_1 x_d r_d^2+\kappa_2 x_d r_d^4+\kappa_3 x_d r_d^6+\kappa_4 x_d r_d^8+\kappa_5 x_d r_d^{10}+\kappa_6 x_d r_d^{12} \quad \textbf{(3)}$$

$$y_u - y_d = \kappa_1 y_d r_d^2+\kappa_2 y_d r_d^4+\kappa_3 y_d r_d^6+\kappa_4 y_d r_d^8+\kappa_5 y_d r_d^{10}+\kappa_6 y_d r_d^{12} \quad \textbf{(4)}$$

With at least six-point correspondences a system of six linear equations was built as follows:

$$\begin{bmatrix} x_{u1}-x_{d1} \\ y_{u1}-y_{d1} \\ x_{u2}-x_{d2} \\ y_{u2}-y_{d2} \\ x_{u3}-x_{d3} \\ y_{u3}-y_{d3} \end{bmatrix} = \begin{bmatrix} x_{d1}r_{d1}^2 & x_{d1}r_{d1}^4 & x_{d1}r_{d1}^6 & x_{d1}r_{d1}^8 & x_{d1}r_{d1}^{10} & x_{d1}r_{d1}^{12} \\ y_{d1}r_{d1}^2 & y_{d1}r_{d1}^4 & y_{d1}r_{d1}^6 & y_{d1}r_{d1}^8 & y_{d1}r_{d1}^{10} & y_{d1}r_{d1}^{12} \\ x_{d2}r_{d2}^2 & x_{d2}r_{d2}^4 & x_{d2}r_{d2}^6 & x_{d2}r_{d2}^8 & x_{d2}r_{d2}^{10} & x_{d2}r_{d2}^{12} \\ y_{d2}r_{d2}^2 & y_{d2}r_{d2}^4 & y_{d2}r_{d2}^6 & y_{d2}r_{d2}^8 & y_{d2}r_{d2}^{10} & y_{d2}r_{d2}^{12} \\ x_{d3}r_{d3}^2 & x_{d3}r_{d3}^4 & x_{d3}r_{d3}^6 & x_{d3}r_{d3}^8 & x_{d3}r_{d3}^{10} & x_{d3}r_{d3}^{12} \\ y_{d3}r_{d3}^2 & y_{d3}r_{d3}^4 & y_{d3}r_{d3}^6 & y_{d3}r_{d3}^8 & y_{d3}r_{d3}^{10} & y_{d3}r_{d3}^{12} \end{bmatrix} \begin{bmatrix} \kappa_1 \\ \kappa_2 \\ \kappa_3 \\ \kappa_4 \\ \kappa_5 \\ \kappa_6 \end{bmatrix} \quad \textbf{(5)}$$

The transformation in **(5)** is of the form $Ux = b$ where the vector x contains the six radial distortion coefficients and the matrix U contains the products of distorted image coordinates with the distorted radii elevated to the power two, four, six, eight, ten and twelve respectively. Solving (5) amounts to minimize the difference $Ux - b$. Let $\{\vec{u_1} \quad \vec{u_2} \quad .... \quad \vec{u_6}\}$ be a basis of the central matrix U in (5). For each b in R^m where m is the number of rows in U ,the equation $Ux - b = 0$ has a unique Least squares solution expressed in the form of $x = R^{-1}Q^T b$ where QR is an orthogonal decomposition of the matrix U .

The Gram Smidt decomposition produces an orthogonal basis for the matrix U such that:

$$\vec{q_1} = \frac{\vec{u_1}}{\|\vec{u_1}\|} \quad \textbf{(6)}$$

$$\vec{u_2} = \vec{u_2} - \frac{\vec{u_2}}{\|\vec{q_1}\|} \quad \textbf{(7)}$$

From **(7)** we have the following orthogonal vector:

$$\vec{q_2} = \frac{\vec{u_2}}{\|\vec{u_2}\|} \quad \textbf{(8)}$$

From the third column of **(5)** we have the following:

$$\vec{u_3} = \vec{u_3} - \frac{\vec{u_3}}{\|\vec{q_1}\|} \qquad \frac{\vec{u_3}}{\|\vec{q_2}\|} \quad \textbf{(9)}$$

From **(9)** we have the following orthogonal vector:

$$\vec{q_3} = \frac{\vec{u_3}}{\|\vec{u_3}\|} \quad \textbf{(10)}$$

From the fourth column of **(5)** we have the following:

$$\vec{u}_4 = \vec{u}_4 - \frac{}{\|\vec{q}_1\|} \quad \|\vec{q}_2\| \quad \|\vec{q}_3\| \tag{11}$$

From **(11)** we have the following:

$$\vec{q}_4 = \frac{}{\|\vec{v}_4\|} \tag{12}$$

From the fifth column of **(5)** we have the following:

$$\vec{v}_5 = \vec{v}_5 - \frac{}{\|\vec{q}_1\|} \quad \|\vec{q}_2\| \quad \|\vec{q}_3\| \quad \|\vec{q}_4\| \tag{13}$$

From **(13)** we have the following:

$$\vec{q}_5 = \frac{}{\|\vec{u}_5\|} \tag{14}$$

From the last column of **(5)** we can derive the following equation:

$$\vec{u}_6 = \vec{u}_6 - \frac{}{\|\vec{q}_1\|} \quad \|\vec{q}_2\| \quad \|\vec{q}_3\| \quad \|\vec{q}_4\| \quad \|\vec{q}_5\| \tag{15}$$

From **(15)** we have the following:

$$\vec{q}_6 = \frac{}{\|\vec{v}_6\|} \tag{16}$$

From **(6), (8), (10), (12), (14), (16)** we reformulate the matrix U as follows:

$$\vec{U} = \lfloor \vec{q}_1 \quad \vec{q}_2 \quad \vec{q}_3 \quad \vec{q}_4 \quad \vec{q}_5 \quad \vec{q}_6 \rfloor \times \kappa \tag{17}$$

Where the matrix R is an upper triangular matrix. Since the matrix Q is orthogonal, from **(17)** the upper triangular matrix R is retrieved as follows:

$$R = \lceil \vec{q}_1 \quad \vec{q}_2 \quad \vec{q}_3 \quad \vec{q}_4 \quad \vec{q}_5 \quad \vec{q}_6 \rfloor \ \vec{U} \tag{18}$$

From **(5)** and **(17)** an expanded formulation of the upper triangular matrix R is retrieved as follows:

$$R=\begin{bmatrix} (\vec{q_1}\bullet\vec{u_1}) & (\vec{q_1}\bullet\vec{u_2}) & (\vec{q_1}\bullet\vec{u_3}) & (\vec{q_1}\bullet\vec{u_4}) & (\vec{q_1}\bullet\vec{u_5}) & (\vec{q_1}\bullet\vec{u_6}) \\ 0 & (\vec{q_2}\bullet\vec{u_2}) & (\vec{q_2}\bullet\vec{u_3}) & (\vec{q_2}\bullet\vec{u_4}) & (\vec{q_2}\bullet\vec{u_5}) & (\vec{q_2}\bullet\vec{u_6}) \\ 0 & 0 & (\vec{q_3}\bullet\vec{u_3}) & (\vec{q_3}\bullet\vec{u_4}) & (\vec{q_3}\bullet\vec{u_5}) & (\vec{q_3}\bullet\vec{u_6}) \\ 0 & 0 & 0 & (\vec{q_4}\bullet\vec{u_4}) & (\vec{q_4}\bullet\vec{u_5}) & (\vec{q_4}\bullet\vec{u_6}) \\ 0 & 0 & 0 & 0 & (\vec{q_5}\bullet\vec{u_5}) & (\vec{q_5}\bullet\vec{u_6}) \\ 0 & 0 & 0 & 0 & 0 & (\vec{q_6}\bullet\vec{u_6}) \end{bmatrix} \quad \textbf{(19)}$$

From **(5)** and **(19)** we retrieve the numerical estimates of the radial distortion coefficients as follows:

$$\kappa_6=(\vec{p}\bullet\vec{q_6})/(\vec{q_6}\bullet\vec{u_6}) \quad \textbf{(20)}$$

$$\kappa_5=\left[(\vec{p}\bullet\vec{q_5})-\kappa_6(\vec{q_5}\bullet\vec{u_6})\right]/(\vec{q_5}\bullet\vec{u_5}) \quad \textbf{(21)}$$

$$\kappa_4=\left[(\vec{p}\bullet\vec{q_4})-\kappa_6(\vec{q_4}\bullet\vec{u_6})-\kappa_5(\vec{q_4}\bullet\vec{u_5})\right]/(\vec{q_4}\bullet\vec{u_4}) \quad \textbf{(22)}$$

$$\kappa_3=\left[(\vec{p}\bullet\vec{q_3})-\kappa_6(\vec{q_3}\bullet\vec{u_6})-\kappa_5(\vec{q_3}\bullet\vec{u_5})-\kappa_4(\vec{q_3}\bullet\vec{u_4})\right]/(\vec{q_3}\bullet\vec{u_3}) \quad \textbf{(23)}$$

$$\kappa_2=\left[(\vec{p}\bullet\vec{q_2})-\kappa_6(\vec{q_2}\bullet\vec{u_6})-\kappa_5(\vec{q_2}\bullet\vec{u_5})-\kappa_4(\vec{q_2}\bullet\vec{u_4})-\kappa_3(\vec{q_2}\bullet\vec{u_3})\right]/(\vec{q_2}\bullet\vec{u_2}) \quad \textbf{(24)}$$

$$\kappa_1=\left[(\vec{p}\bullet\vec{q_1})-\kappa_6(\vec{q_1}\bullet\vec{u_6})-\kappa_5(\vec{q_1}\bullet\vec{u_5})-\kappa_4(\vec{q_1}\bullet\vec{u_4})-\kappa_3(\vec{q_1}\bullet\vec{u_3})-\kappa_2(\vec{q_1}\bullet\vec{u_2})\right]/(\vec{q_1}\bullet\vec{u_1}) \quad \textbf{(25)}$$

Where the vector $\vec{p}$ is the column vector on the left-hand side of the transformation in **(5).** For consistency with the number of radial distortion coefficients considered in the MATLAB and Photomodeler estimations only the parameters in **(23), (24)** and **(25)** are considered.

Appendix D: Ethics approval form

APPLICATION FORM

Please Note:
Any person planning to undertake research in the Faculty of Engineering and the Built Environment (EBE) at the University of Cape Town is required to complete this form **before** collecting or analyzing data. The objective of submitting this application *prior* to embarking on research is to ensure that the highest ethical standards in research, conducted under the auspices of the EBE Faculty, are met. Please ensure that you have read, and understood the **EBE Ethics in Research Handbook** (available from the UCT EBE, Research Ethics website) prior to completing this application form: http://www.ebe.uct.ac.za/ebe/research/ethics1

APPLICANT'S DETAILS		
Name of principal researcher, student or external applicant:		Guy Blanchard IKOKOU
Department		Geomatics
Preferred email address of applicant:		ikokou@gmail.com
If Student	Your Degree: e.g., MSc, PhD, etc.	PhD
	Credit Value of Research: e.g., 60/120/180/360 etc.	360
	Name of Supervisor (if supervised):	Julian Smit
If this is a research contract, indicate the source of funding/sponsorship		N/A
Project Title		Geometric calibration of non-metric digital cameras for Photogrammetry Applications

I hereby undertake to carry out my research in such a way that:

- there is no apparent legal objection to the nature or the method of research; and
- the research will not compromise staff or students or the other responsibilities of the University;
- the stated objective will be achieved, and the findings will have a high degree of validity;
- limitations and alternative interpretations will be considered;
- the findings could be subject to peer review and publicly available; and
- I will comply with the conventions of copyright and avoid any practice that would constitute plagiarism.

SIGNED BY	Full name	Signature	Date
Principal Researcher/ Student/External applicant	Guy Blanchard Ikokou		**18 Feb 2019**

APPLICATION APPROVED BY	Full name	Signature	Date
Supervisor (where applicable)	Julian Smit		Click here to enter a date. **25 Feb 2019**
HOD (or delegated nominee) Final authority for all applicants who have answered NO to all questions in Section1; and for all Undergraduateresearch (Including Honours).	Click here to enter text.		Click here to enter a date.
Chair : Faculty EiR Committee For applicants other than undergraduate students who have answered YES to any of the above questions.	R Behrens		25 Mar 2019